

JPL Publication 93-26, Vol. 1

Summaries of the Fourth Annual JPL Airborne Geoscience Workshop October 25–29, 1993

Volume 1. AVIRIS Workshop

Robert O. Green
Editor

October 25, 1993

NASA

National Aeronautics and
Space Administration

Jet Propulsion Laboratory
California Institute of Technology
Pasadena, California

This publication was prepared by the Jet Propulsion Laboratory, California Institute of Technology, under a contract with the National Aeronautics and Space Administration.

ABSTRACT

This publication contains the summaries for the Fourth Annual JPL Airborne Geoscience Workshop, held in Washington, D. C. on October 25–29, 1993. The main workshop is divided into three smaller workshops as follows:

- The Airborne Visible/Infrared Imaging Spectrometer (AVIRIS) workshop, on October 25–26. The summaries for this workshop appear in Volume 1.
- The Thermal Infrared Multispectral Scanner (TIMS) workshop, on October 27. The summaries for this workshop appear in Volume 2.
- The Airborne Synthetic Aperture Radar (AIRSAR) workshop, on October 28–29. The summaries for this workshop appear in Volume 3.

FOREWORD

In the text and the figure captions of some of the papers for the AVIRIS and AIRSAR Workshops, reference is made to color slides. A pocket containing a set of all the slides mentioned in those papers appears at the end of this volume.

CONTENTS

Volume 1: AVIRIS Workshop

Use of Spectral Analogy to Evaluate Canopy Reflectance Sensitivity to Leaf Optical Property.....	1
<i>Frédéric Baret, Vern C. Vanderbilt, Michael D. Steven, and Stephane Jacquemoud</i>	
A Tool for Manual Endmember Selection and Spectral Unmixing.....	3
<i>C. Ann Bateson and Brian Curtiss</i>	
Lithologic Discrimination and Alteration Mapping From AVIRIS Data, Socorro, New Mexico.....	7
<i>K. K. Beratan, N. DeLillo, A. Jacobson, R. Blom, and C. E. Chapin</i>	
Automating Spectral Unmixing of AVIRIS Data Using Convex Geometry Concepts.....	11
<i>Joseph W. Boardman</i>	
AVIRIS Calibration Using the Cloud-Shadow Method.....	15
<i>K. L. Carder, P. Reinersman, and R. F. Chen</i>	
Field Observations Using an AOTF Polarimetric Imaging Spectrometer.....	19
<i>Li-Jen Cheng, Mike Hamilton, Colin Mahoney, and George Reyes</i>	
Instantaneous Field of View and Spatial Sampling of the Airborne Visible/Infrared Imaging Spectrometer (AVIRIS).....	23
<i>Thomas G. Chrien and Robert O. Green</i>	
Airborne Visible/Infrared Imaging Spectrometer (AVIRIS): Recent Improvements to the Sensor.....	27
<i>Thomas G. Chrien, Robert O. Green, Charles M. Sarture, Christopher Chovit, Michael L. Eastwood, and Bjorn T. Eng</i>	
Comparison of Three Methods for Materials Identification and Mapping with Imaging Spectroscopy.....	31
<i>Roger N. Clark, Gregg Swayze, Joe Boardman, and Fred Kruse</i>	
Comparison of Methods for Calibrating AVIRIS Data to Ground Reflectance.....	35
<i>Roger N. Clark, Gregg Swayze, Kathy Heidebrecht, Alexander F. H. Goetz, and Robert O. Green</i>	

The U.S. Geological Survey, Digital Spectral Reflectance Library: Version 1: 0.2 to 3.0 μm	37
<i>Roger N. Clark, Gregg A. Swayze, Trude V. V. King, Andrea J. Gallagher, and Wendy M. Calvin</i>	
Application of a Two-Stream Radiative Transfer Model for Leaf Lignin and Cellulose Concentrations From Spectral Reflectance Measurements (Part 1).....	39
<i>James E. Conel, Jeannette van den Bosch, and Cindy I. Grove</i>	
Application of a Two-Stream Radiative Transfer Model for Leaf Lignin and Cellulose Concentrations From Spectral Reflectance Measurements (Part 2).....	45
<i>James E. Conel, Jeannette van den Bosch, and Cindy I. Grove</i>	
Discrimination of Poorly Exposed Lithologies in AVIRIS Data.....	53
<i>William H. Farrand and Joseph C. Harsanyi</i>	
Spectral Decomposition of AVIRIS Data	57
<i>Lisa Gaddis, Laurence Soderblom, Hugh Kieffer, Kris Becker, Jim Torson, and Kevin Mullins</i>	
Remote Sensing of Smoke, Clouds, and Fire Using AVIRIS Data	61
<i>Bo-Cai Gao, Yoram J. Kaufman, and Robert O. Green</i>	
Use of Data from the AVIRIS Onboard Calibrator.....	65
<i>Robert O. Green</i>	
Inflight Calibration of AVIRIS in 1992 and 1993	69
<i>Robert O. Green, James E. Conel, Mark Helmlinger, Jeannette van den Bosch, Chris Chovit, and Tom Chrien</i>	
Estimation of Aerosol Optical Depth and Additional Atmospheric Parameters for the Calculation of Apparent Reflectance from Radiance Measured by the Airborne Visible/Infrared Imaging Spectrometer.....	73
<i>Robert O. Green, James E. Conel, and Dar A. Roberts</i>	
Use of the Airborne Visible/Infrared Imaging Spectrometer to Calibrate the Optical Sensor on board the Japanese Earth Resources Satellite-1.....	77
<i>Robert O. Green, James E. Conel, Jeannette van den Bosch, and Masanobu Shimada</i>	
A Proposed Update to the Solar Irradiance Spectrum Used in LOWTRAN and MODTRAN	81
<i>Robert O. Green and Bo-Cai Gao</i>	

A Role for AVIRIS in the Landsat and Advanced Land Remote Sensing System Program.....	85
<i>Robert O. Green and John J. Simmonds</i>	
Estimating Dry Grass Residues Using Landscape Integration Analysis.....	89
<i>Quinn J. Hart, Susan L. Ustin, Lian Duan, and George Scheer</i>	
Classification of High Dimensional Multispectral Image Data.....	93
<i>Joseph P. Hoffbeck and David A. Landgrebe</i>	
Simulation of Landsat Thematic Mapper Imagery Using AVIRIS Hyperspectral Imagery.....	97
<i>Linda S. Kalman and Gerard R. Peltzer</i>	
The Effects of AVIRIS Atmospheric Calibration Methodology on Identification and Quantitative Mapping of Surface Mineralogy, Drum Mtns., Utah.....	101
<i>Fred A. Kruse and John L. Dwyer</i>	
AVIRIS Spectra Correlated With the Chlorophyll Concentration of a Forest Canopy.....	105
<i>John Kupiec, Geoffrey M. Smith, and Paul J. Curran</i>	
AVIRIS and TIMS Data Processing and Distribution at the Land Processes Distributed Active Archive Center.....	109
<i>G. R. Mah and J. Myers</i>	
Measurements of Canopy Chemistry With 1992 AVIRIS Data at Blackhawk Island and Harvard Forest.....	113
<i>Mary E. Martin and John D. Aber</i>	
Classification of the LCVF AVIRIS Test Site With a Kohonen Artificial Neural Network.....	117
<i>Erzsébet Merényi, Robert B. Singer, and William H. Farrand</i>	
Extraction of Auxiliary Data from AVIRIS Distribution Tape for Spectral, Radiometric, and Geometric Quality Assessment.....	121
<i>Peter Meyer, Robert O. Green, and Thomas G. Chrien</i>	
Preprocessing: Geocoding of AVIRIS Data using Navigation, Engineering, DEM, and Radar Tracking System Data.....	127
<i>Peter Meyer, Steven A. Larson, Earl G. Hansen, and Klaus I. Itten</i>	

The Data Facility of the Airborne Visible/Infrared Imaging Spectrometer (AVIRIS).....	133
<i>Pia J. Nielsen, Robert O. Green, Alex T. Murray, Bjorn T. Eng, H. Ian Novack, Manuel Solis, and Martin Olah</i>	
Mapping of the Ronda Peridotite Massif (Spain) From AVIRIS Spectro-Imaging Survey: A First Attempt.....	137
<i>P. C. Pinet, S. Chabrilat, and G. Ceuleneer</i>	
Spectral Variations in a Collection of AVIRIS Imagery.....	141
<i>John C. Price</i>	
Monitoring Land Use and Degradation Using Satellite and Airborne Data.....	145
<i>Terrill W. Ray, Thomas G. Farr, Ronald G. Blom, and Robert E. Crippen</i>	
The Red Edge in Arid Region Vegetation: 340–1060 nm Spectra.....	149
<i>Terrill W. Ray, Bruce C. Murray, A. Chehbouni, and Eni Njoku</i>	
Temporal Changes in Endmember Abundances, Liquid Water and Water Vapor Over Vegetation at Jasper Ridge.....	153
<i>Dar A. Roberts, Robert O. Green, Donald E. Sabol, and John B. Adams</i>	
Mapping and Monitoring Changes in Vegetation Communities of Jasper Ridge, CA, Using Spectral Fractions Derived From AVIRIS Images.....	157
<i>Donald E. Sabol, Jr., Dar A. Roberts, John B. Adams, and Milton O. Smith</i>	
The Effect of Signal Noise on the Remote Sensing of Foliar Biochemical Concentration.....	161
<i>Geoffrey M. Smith and Paul J. Curran</i>	
Application of MAC-Europe AVIRIS Data to the Analysis of Various Alteration Stages in the Landmannalaugar Hydrothermal Area (South Iceland).....	165
<i>S. Sommer, G. Lörcher, and S. Endres</i>	
Estimation of Crown Closure From AVIRIS Data Using Regression Analysis.....	169
<i>K. Staenz, D. J. Williams, M. Truchon, and R. Fritz</i>	
Optimal Band Selection for Dimensionality Reduction of Hyperspectral Imagery.....	173
<i>Stephen D. Stearns, Bruce E. Wilson, and James R. Peterson</i>	

Objective Determination of Image End-Members in Spectral Mixture Analysis of AVIRIS Data.....	177
<i>Stefanie Tompkins, John F. Mustard, Carle M. Pieters, and Donald W. Forsyth</i>	
Relationships Between Pigment Composition Variation and Reflectance for Plant Species from a Coastal Savannah in California.....	181
<i>Susan L. Ustin, Eric W. Sanderson, Yaffa Grossman, Quinn J. Hart, and Robert S. Haxo</i>	
Atmospheric Correction of AVIRIS Data of Monterey Bay Contaminated by Thin Cirrus Clouds.....	185
<i>Jeannette van den Bosch, Curtiss O. Davis, Curtis D. Mobley, and W. Joseph Rhea</i>	
Investigations on the 1.7 μm Residual Absorption Feature in the Vegetation Reflection Spectrum.....	189
<i>J. Verdebout, S. Jacquemoud, G. Andreoli, B. Hosgood, and A. Sieber</i>	
A Comparison of Spectral Mixture Analysis and NDVI for Ascertaining Ecological Variables.....	193
<i>Carol A. Wessman, C. Ann Bateson, Brian Curtiss, and Tracy L. Benning</i>	
Using AVIRIS for In-Flight Calibration of the Spectral Shifts of Spot-HRV and of AVHRR?.....	197
<i>Veronique Willart-Soufflet and Richard Santer</i>	
Laboratory Spectra of Field Samples as a Check on Two Atmospheric Correction Methods.....	201
<i>Pung Xu and Ronald Greeley</i>	
Determination of Semi-Arid Landscape Endmembers and Seasonal Trends Using Convex Geometry Spectral Unmixing Techniques.....	205
<i>Roberta H. Yuhas, Joseph W. Boardman, and Alexander F. H. Goetz</i>	
Slide Captions.....	209
Volume 2: TIMS Workshop	
Estimation of Spectral Emissivity in the Thermal Infrared.....	1
<i>David Kryskowski and J. R. Maxwell</i>	
The Difference Between Laboratory and in-situ Pixel-Averaged Emissivity: The Effects on Temperature-Emissivity Separation.....	5
<i>Tsuneo Matsunaga</i>	

Mineralogic Variability of the Kelso Dunes, Mojave Desert, California Derived From Thermal Infrared Multispectral Scanner (TIMS) Data.....	9
<i>Michael S. Ramsey, Douglas A. Howard, Philip R. Christensen, and Nicholas Lancaster</i>	
Remote Identification of a Gravel Laden Pleistocene River Bed.....	13
<i>Douglas E. Scholen</i>	
Volume 3: AIRSAR Workshop	
Interferometric Synthetic Aperture Radar Imagery of the Gulf Stream	1
<i>T. L. Ainsworth, M. E. Cannella, R. W. Jansen, S. R. Chubb, R. E. Carande, E. W. Foley, R. M. Goldstein, and G. R. Valenzuela</i>	
MAC-91: Polarimetric SAR Results on Montespertoli Site	5
<i>S. Baronti, S. Luciani, S. Moretti, S. Paloscia, G. Schiavon, and S. Sigismondi</i>	
AIRSAR Views of Aeolian Terrain	9
<i>Dan G. Blumberg and Ronald Greeley</i>	
Glaciological Studies in the Central Andes Using AIRSAR/TOPSAR	13
<i>Richard R. Forster, Andrew G. Klein, Troy A. Blodgett, and Bryan L. Isacks</i>	
Estimation of Biophysical Properties of Upland Sitka Spruce (<i>Picea Sitchensis</i>) Plantations.....	17
<i>Robert M. Green</i>	
Forest Investigations by Polarimetric AIRSAR Data in the Harz Mountains.....	21
<i>M. Keil, D. Poll, J. Raupenstrauch, T. Tares, and R. Winter</i>	
Comparison of Inversion Models Using AIRSAR Data for Death Valley, California.....	25
<i>Kathryn S. Kierein-Young</i>	
Geologic Mapping Using Integrated AIRSAR, AVIRIS, and TIMS Data.....	29
<i>Fred A. Kruse</i>	
Statistics of Multi-look AIRSAR Imagery: A Comparison of Theory With Measurements.....	33
<i>J. S. Lee, K. W. Hoppel, and S. A. Mango</i>	

AIRSAR Deployment in Australia, September 1993: Management and Objectives	37
<i>A. K. Milne and I. J. Tapley</i>	
Current and Future Use of TOPSAR Digital Topographic Data for Volcanological Research.....	41
<i>Peter J. Mouginis-Mark, Scott K. Rowland, and Harold Garbeil</i>	
Preliminary Analysis of the Sensitivity of AIRSAR Images to Soil Moisture Variations.....	45
<i>Rajan Pardipuram, William L. Teng, James R. Wang, and Edwin T. Engman</i>	
Unusual Radar Echoes From the Greenland Ice Sheet.....	49
<i>E. J. Rignot, J. J. van Zyl, S. J. Ostro, and K. C. Jezek</i>	
MAC Europe '91 Campaign: AIRSAR/AVIRIS Data Integration for Agricultural Test Site Classification.....	53
<i>S. Sangiovanni, M. F. Buongiorno, M. Ferrarini, and A. Fiumara</i>	
Measurement of Ocean Wave Spectra Using Polarimetric AIRSAR Data	57
<i>D. L. Schuler</i>	
An Improved Algorithm for Retrieval of Snow Wetness Using C-Band AIRSAR.....	61
<i>Jiancheng Shi, Jeff Dozier, and Helmut Rott</i>	
Polarimetric Radar Data Decomposition and Interpretation.....	65
<i>Guoqing Sun and K. Jon Ranson</i>	
Synergy Between Optical and Microwave Remote Sensing to Derive Soil and Vegetation Parameters From MAC Europe 91 Experiment.....	69
<i>O. Taconet, M. Benallegue, A. Vidal, D. Vidal-Madjar, L. Prevot, and M. Normand</i>	
SAR Terrain Classifier and Mapper of Biophysical Attributes	73
<i>Fawwaz T. Ulaby, M. Craig Dobson, Leland Pierce, and Kamal Sarabandi</i>	
Classification and Soil Moisture Determination of Agricultural Fields.....	77
<i>A. C. van den Broek and J. S. Groot</i>	
Relating P-Band AIRSAR Backscatter to Forest Stand Parameters.....	81
<i>Yong Wang, John M. Melack, Frank W. Davis, Eric S. Kasischke, and Norman L. Christensen, Jr.</i>	

Soil Moisture Retrieval in the Oberpfaffenhofen Testsite Using MAC Europe AIRSAR Data	85
<i>Tobias Wever and Jochen Henkel</i>	
Microwave Dielectric Properties of Boreal Forest Trees.....	89
<i>G. Xu, F. Ahern, and J. Brown</i>	
Slide Captions.....	93

USE OF SPECTRAL ANALOGY TO EVALUATE CANOPY REFLECTANCE SENSITIVITY TO LEAF OPTICAL PROPERTY.

Frédéric Baret¹, Vern C. Vanderbilt², Michael D. Steven³,
Stephane Jacquemoud⁴

¹INRA Bioclimatologie, BP 91, 84 143 Montfavet Cedex, France

²NASA Ames Res. Center, MS 242-4, Moffet Field, CA 94 035, USA

³Nottingham University, Dept. Geography, Nottingham, NG7 2RD, U.K.

⁴IRSA/AT, JRC, 21 020 Ispra, (Varese), Italy.

1-Sep-93

Abstract

The spectral variation of canopy reflectance is mostly governed by the absorption properties of the elements, hence the leaves, since their intrinsic scattering properties show very little spectral variation. The relationship between canopy reflectance and leaf reflectance measured at the red edge over sugar beet canopies was used to simulate canopy reflectance from leaf reflectance spectra measured over the whole spectral domain. The results show that the spectral analogies found allows accurate reconstruction of canopy reflectance spectra. Explicit assumptions about the very low spectral variation of leaf intrinsic scattering properties are thus indirectly justified.

The sensitivity of canopy reflectance (ρ_c) to leaf optical properties can then be investigated from concurrent spectral variations of canopy ($\partial\rho_c / \partial\lambda$) and leaf reflectance ($\partial\rho_l / \partial\lambda$):

$$\frac{\partial\rho_c}{\partial\rho_l} = \frac{\partial\rho_c}{\partial\lambda} \left(\frac{\partial\rho_l}{\partial\lambda} \right)^{-1}$$

This expression is strictly valid only when the optical properties of the soil background or of the other vegetation elements such as bark are either spectrally flat or do not contribute significantly to canopy reflectance. Simulations using the SAIL and PROSPECT models demonstrate that the sensitivity of canopy reflectance to leaf reflectance is significant for large vegetation cover fractions in spectral domains where absorption is low. In these conditions, multiple scattering enhances the leaf absorption features by a factor that can be greater than 2.0. To override the limitations of the SAIL model for the description of the canopy architecture, we tested the previous findings on experimental data. Concurrent canopy and leaf reflectance spectra were measured for a range of sugar beet canopies. The results show good agreement with the theoretical findings. Conclusions are drawn about the applicability of these findings, with particular attention to the potential detectability of leaf biochemical composition from canopy reflectance sensed from space.

4/1/82
4/1/82

**A TOOL FOR MANUAL ENDMEMBER
SELECTION AND SPECTRAL UNMIXING**

C. Ann Bateson and Brian Curtiss

CIRES and Center for the Study of Earth from Space
University of Colorado
Campus Box 449
Boulder, Colorado 80309-0449

1.0. INTRODUCTION

Sampling a continuous radiance spectrum in many narrow contiguous spectral bands results in a high covariance between the bands. Hence, the true dimensionality of imaging spectrometer data is not determined by the number of spectral bands, but by the number of spectrally unique signatures whose mixtures reproduce the spectral variance observed in an image. Methods to unmix high dimensional multispectral data use principal components analysis to reduce the dimensionality. The variance of the spectral data is modeled as a linear combination of a finite set of endmembers in the space of the eigenvectors that account for most of the variance. The number and characteristics of these endmembers are determined not only by the number and characteristics of the spectrally unique materials on the surface but also by processes (e.g., illumination, atmospheric scattering and absorption) affecting the signal received by the sensor.

Selection of endmember spectra has typically been from a library. However, since most libraries are incomplete and do not account for the processes mentioned above, we have devised a computer display that allows researchers to explore interactively the eigenvector space of a representative and mean-corrected subset of the image data in search of extreme spectra to designate as endmembers. This display, which is based on parallel coordinates (Inselberg, 85), is unique in the area of multidimensional visualization in that it includes not only a passive view of higher dimensional data but also the capability to interact and move geometrical objects in higher dimensional spaces.

2.0. UNMIXING RECIPE

After endmember selection, unmixing of the spectral data to compute concentrations is straight forward. If the true dimensionality of the data is n, then there are n+1 endmembers, E_1, \dots, E_{n+1} in the scene. The endmembers and spectral data are offset by E_1 and rotated into the eigenvector space of dimension n. For each spectrum $P = (p_1, \dots, p_n)$ in the data, solution of the matrix equation below yields the concentrations (c_1, \dots, c_{n+1}) :

$$\begin{bmatrix} 0 & e_{12} & \dots & e_{1n} \\ \dots & \dots & \dots & \dots \\ 0 & e_{n2} & \dots & e_{nn} \\ 1 & 1 & 1 & 1 \end{bmatrix} \cdot \begin{bmatrix} c_1 \\ \dots \\ c_n \\ c_{n+1} \end{bmatrix} = \begin{bmatrix} p_1 \\ \dots \\ p_n \\ 1 \end{bmatrix}$$

The vector (e_{1i}, \dots, e_{ni}) is E_i , offset and rotated. Note that the last row of 1's guarantees that the concentrations sum to 1. A spectrum P viewed as a point in n dimensional space

lies within the n-simplex* with E_1, \dots, E_{n+1} as vertices, if and only if each c_i lies between 0 and 1.

3.0. ENDMEMBER SELECTION IN LOWER DIMENSIONS

The endmember selection tool aids the researcher in finding endmembers as vertices of an n-simplex that contains all the spectral data. Figure 1 shows the display for the 3-dimensional case. Initially, the first panel of the four panel endmember selection screen shows the data projected into the space of the first two eigenvectors. As the cursor moves over this panel, the current spectrum window displays the spectrum of the point underneath. By clicking on the mouse, the user may select 3 endmembers in this window. If a fourth endmember is selected, then the plane of the first panel becomes three dimensional space and the fourth endmember is the apex of a tetrahedron whose base is the triangle in the plane. The four panels in figure 1 correspond to the four faces of the tetrahedron. The user may relocate endmembers in the panels in order to encompass the data within a simplex whose vertices are recognizable endmember.

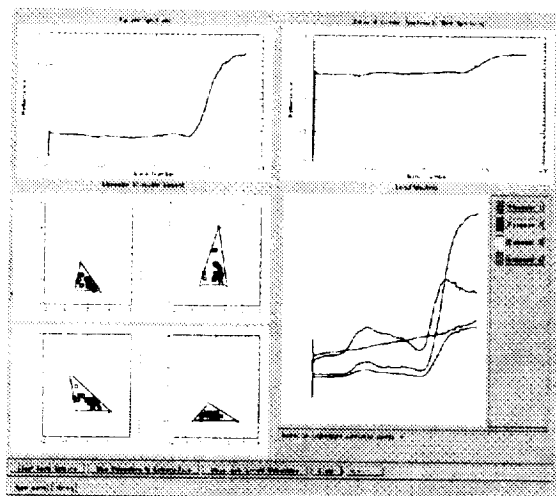


Figure 1. The endmember selection tool for three dimensions.

4.0. Higher Dimensional Endmember Selection

The endmember selection tool does not use the simple projection method above for dimensions exceeding 3 because of the following shortcomings:

a. The coordinate system becomes confusing when the data is projected. That is, it is hard to change an endmember spectrum only in the direction of a specified eigenvector

b. It is difficult to reach all points in a higher dimensional space by adjusting the vertices of the triangular faces of the constructed simplex.

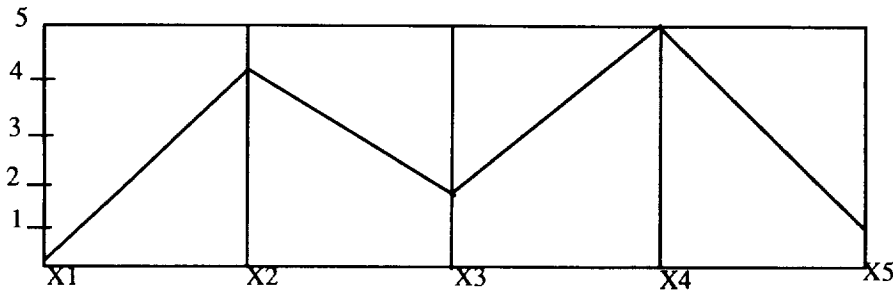
c. The number of planes grows on the order of n^3 , where n is the dimension of the space.

Parallel coordinate systems (Inselberg, 85) allowed the development of a display to overcome these shortcomings.

4.1 BRIEF OVERVIEW OF PARALLEL COORDINATES

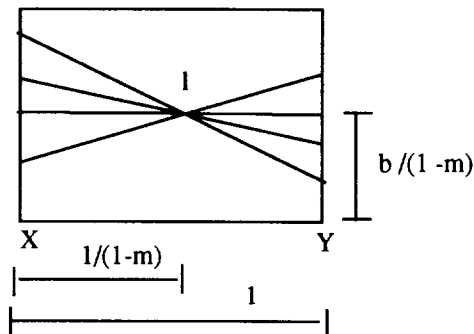
*. That is, a triangle in the plane, a tetrahedron in 3-space and in n-space a polyhedron with $n+1$ vertices and an edge for each vertex pair.

The parallel coordinate representation of the point (0, 4, 2, 5, 1) in fifth dimensional space is:



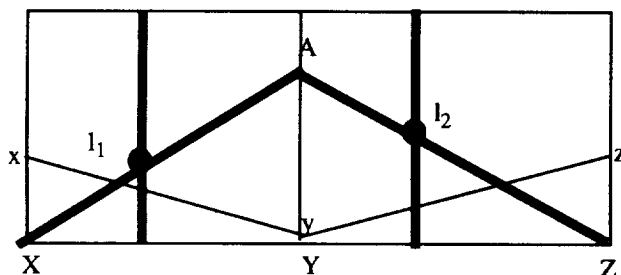
The five equally spaced vertical lines are the axes of the parallel coordinate system and the polygonal line segment is the plotted point. Note that spectra have a very natural representation in parallel coordinates with a parallel axis for each wavelength.

While points are represented by line segments in parallel coordinates, lines are dually represented as a collection of points. Below are points in parallel coordinates lying on the line $y = m \cdot x + b$:



The point l is said to represent the line $y = m \cdot x + b$ in parallel coordinates. Observe that if l_1 and l_2 represent parallel lines then they lie on the same vertical line in parallel coordinate representation.

The parallel coordinate treatment of planes is based on the simple observation that a plane is determined by two lines l_1 and l_2 intersecting at a point A . The plot below shows the two points representing l_1 and l_2 , the polygonal line representing A , and a polygonal line representing another point on the plane. In this plot, we assume that A lies on the y -axis. In the higher dimensional display, the face of an n -simplex may be trans-



lated away from the vertex (endmember) opposite that face by adjusting A . The face may be rotated by adjusting the vertical lines through l_1 or l_2 .

4.2 TOOLS OF THE DISPLAY

The higher dimensional display includes the following tools:

1. The data window (figure 2) shows the selected endmembers and the parallel coordinate representation of the spectra projected into the eigenvector space. The user may adjust coordinate values of the endmembers in this window.

2. The cluster window (figure 2) has a parallel coordinate axis for each endmember. Concentrations are plotted on these axes. The user can look for and select clusters in this window. For example, the user could select the cluster containing all spectra on the wrong side of the hyperplane of the face opposite the first endmember--- i.e, all spectra which have a negative abundance for the first endmember.

3. The face window (figure 3) displays spectra selected in the cluster window. The medium width polygonal lines in the face window below are data on the wrong side of the face opposite a selected endmember. The thinner lines represent points on the hyperplane of the face. The single thickest polygonal line represents an endmember A and the thinner vertical lines are slope lines. Note that A and the thin polygonal lines intersect the second slope line at the same point. To relocate the hyperplane so that the spectra lie on the positive side, the user interactively adjusts A and the slope lines to reverse the relative location of the two sets of polygonal lines representing points on the hyperplane and those on the wrong side.

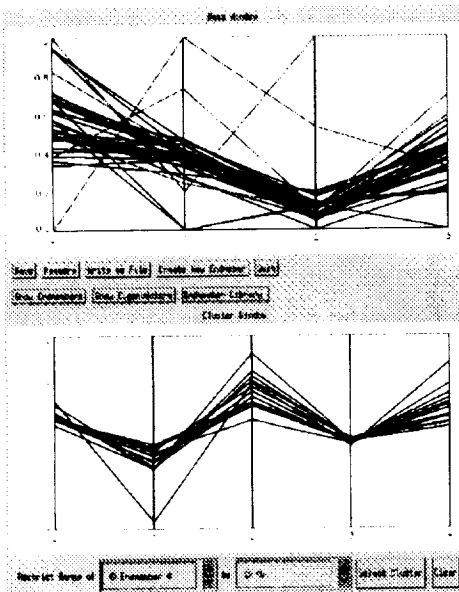


Figure 2. The data and cluster window

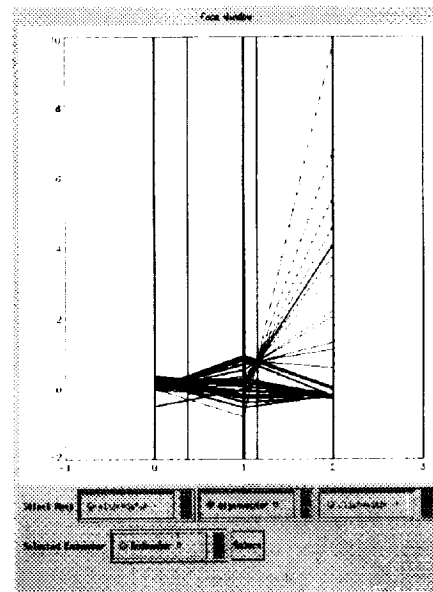


Figure 3. The face window

REFERENCE

Adams, J.B., M.O. Smith and P.E. Johnson, 1986, "Spectral Mixture Modeling: A New Analysis of Rock and Soil Types at the Viking Lander Site," *J. Geophys. Res.*, 91, pp. 8098-8112.

Inselberg, A., 1985, "The Plane with Parallel Coordinates", *Special Issue on Computational Geometry of the Visual Computer* 1, pp.69-97.

53-43
4/10/92

LITHOLOGIC DISCRIMINATION AND ALTERATION MAPPING FROM AVIRIS DATA, SOCORRO, NEW MEXICO

K. K. Beratan and N. DeLillo, Dept. of Geology and Planetary Science,
University of Pittsburgh, Pittsburgh, PA, 15260
A. Jacobson and R. Blom, Jet Propulsion Laboratory, California Institute of
Technology, Pasadena, CA, 91109
C. E. Chapin, New Mexico Bureau of Mines, Socorro, NM, 87801

1. INTRODUCTION

Geologic maps are, by their very nature, interpretive documents. In contrast, images prepared from AVIRIS data can be used as uninterpreted, and thus unbiased, geologic maps. We are having significant success applying AVIRIS data in this non-quantitative manner to geologic problems. Much of our success has come from the power of the Linked Windows Interactive Data System. LinkWinds is a visual data analysis and exploration system under development at JPL which is designed to rapidly and interactively investigate large multivariate data sets. In this paper, we present information on the analysis technique, and preliminary results from research on potassium metasomatism, a distinctive and structurally significant type of alteration associated with crustal extension.

2. LINKWINDS AND MULTISPECTRAL DATA

The AVIRIS instrument collects 224 contiguous spectral channels within the visible and near-infrared. The large number of channels makes analysis difficult; only a few channels can be displayed in image format at one time, and individual rock spectra are hard to distinguish from one another. One approach is to take advantage of the digital nature of the data by comparing spectra from different image elements to laboratory spectra of minerals. However, this approach is hindered when individual minerals are combined into rocks and more than one rock type is averaged into a single image element (pixel). Spatial information, as important as spectral information for geologic interpretation, is not readily included in this type of analysis. Geologists are used to analyzing data in 2-dimensional map format, and the human eye is well-adapted for pattern recognition. However, it is not possible to create an image that simultaneously presents the information from 224 channels.

Spectral information that is important for mapping a specific area or answering a specific geologic question commonly is contained within only a few wavelength channels. However, which channels may not be apparent from theoretical considerations. LinkWinds allows the user to interactively scan through all channels and all combinations of band ratios, with the data presented both graphically (e.g., spectra and statistics) and in image form. Links between the two forms preserve spatial relationships. Visual evaluation allows identification of significant geological information. The advantage of this approach is that a priori selection of spectral regions believed significant is avoided.

LinkWinds is a UNIX-based integrated multi-application execution environment which has a full graphical user interface and presently runs on Silicon Graphics workstations. Data sets and individual tools in the form of data displays and controls for manipulating those displays are coded as objects, each occupying a window on the LinkWinds screen. Messages are passed between objects along one-way paths set up (or broken) by linking (or unlinking) the objects or windows at the discretion of the user. This data-linking paradigm makes the system perform much like a graphics spreadsheet, and is a powerful way of organizing the data for analysis while providing an intuitive and easy-to-learn interface.

3. POTASSIUM METASOMATISM

Potassium-metasomatism (K-metasomatism) is a form of alteration in which large amounts of potassium are added to rocks. In this process, rocks of diverse composition tend to be homogenized to a mixture of potassium feldspar (adularia) + hematite \pm quartz \pm illite-montmorillonite. Rock textures are preserved. Potassium-bearing phenocrysts, such as sanidine and biotite, are generally not affected and give the illusion that the rocks are unaltered (Chapin and Lindley, 1986). K-metasomatism is commonly associated with crustal extension. Examples of K-metasomatism are found associated with detachment faulting (extension along large-scale, low-angle normal faults) in California and in the Rio Grande Rift of New Mexico.

Two models have been proposed for the origin of metasomatizing fluids. In one, the fluids travel from depth along faults and play an important role in the mechanically difficult process of initiation of low-angle normal faults (Bartley and Glazner, 1985). In the second model, the fluids are surficial alkaline, saline brines, and metasomatism results from long-duration brine circulation through basins formed by extension-related subsidence (Chapin and Lindley, 1986). The two models have very different tectonic and structural implications. It should be possible to test the models by comparing an alteration map with a fault map; the most intense K-metasomatism should be associated with fault zones if the first model is correct, whereas distribution should be more diffuse and widespread if the second model is correct. This problem is ideally suited for analysis using AVIRIS data.

4. THE SOCORRO POTASSIUM ANOMALY

The Datil-Mogollon volcanic field, southwestern New Mexico (Fig. 1) was part of a huge Oligo-Miocene volcanic province related to the Rio Grande Rift. Here, huge calderas were sources for sheets of silicic ignimbrites erupted prior to development of Basin and Range topography (Elston, 1978). Socorro, New Mexico, lies on a boundary between two domains of imbricate normal fault blocks that are tilted in opposite directions (Chapin, 1989).

The Socorro potassium anomaly is an L-shaped zone in which one arm trends northward along the axis of the early rift Popotosa basin (Fig. 1). The other arm extends southwest from Socorro across an overlapping series of late Oligocene calderas. Using only the volume of altered tuffs (900 km^3) and an average enrichment of 2.9% K_2O , a minimum of 6.4×10^{10} tons of potassium has been added within the anomaly (Chapin and Lindley, 1986). The Socorro area is ideal for the study of K-metasomatism because five regional ash-flow tuff

sheets extend across the potassium anomaly and well beyond it, allowing traverses from fresh rock into progressively more metasomatized rocks within the same stratigraphic unit. In addition, interbedding of basaltic andesite lavas between the ash-flow tuff sheets permits comparison of alteration effects on both mafic and silicic rocks (Chapin and Lindley, 1986).

5. ANALYSIS OF AVIRIS DATA

This study was initiated as a result of the observation that syn-extensional sedimentary and volcanic rocks within the Whipple detachment terrane, southeastern California-western Arizona, display a distinctive spectral signature in LANDSAT Thematic Mapper data (Beratan et al., 1990). We hypothesized that this signature is related to compositional changes resulting from syn-extensional K-metasomatism. Although the added potassium would not be apparent in the visible and near-IR spectral range, associated hematite should be. Therefore, AVIRIS data was acquired for the Whipple Mountains area and for Socorro, New Mexico. We focus on the Socorro data in this paper.

A 3-component RGB image was made with a channel within the Fe^{+3} absorption feature assigned to blue, a channel within the Fe^{+2} absorption feature assigned to green, and a channel containing a calcite absorption feature assigned to red (Fig. 2). These three channels produced an image that displays a remarkable degree of lithologic discriminability. Not only can basaltic andesites be distinguished from silicic tuffs, but different basaltic andesite and tuff units can be delineated (Fig. 2). Also identifiable are Precambrian crystalline units and younger metasedimentary units, most notably the Pennsylvanian Madera Limestone. In fact, comparison of detailed field mapping (Chamberlin, 1982) and Chapin's field work in the area suggests that the lithologic discrimination possible with the image is approximately equal to that observable in the field.

Intense K-metasomatism is indicated by a deep orange color in the 3-component RGB image. The alteration spectral signature is independent of initial rock type, occurring both in metasomatized silicic tuffs and basaltic andesite lavas, which is consistent with the tendency for K-metasomatism to homogenize rock compositions. The origin of this distinctive spectral signature is apparent in an image which displays the ratio of a channel within the Fe^{+3} absorption feature vs. a pure-reflectance channel. The energy return displayed by the pure-reflectance channel is a measure of the albedo of the rocks; in general, light-colored rocks are more silicic than dark-colored rocks, and so this channel provides a crude indication of rock type. The ratio image highlights areas in which the energy return displayed by the Fe^{+3} channel is significantly lower than expected, based on that from the pure-reflectance channel. The ratio image thus highlights rocks which contain significant amounts of Fe^{+3} -bearing minerals, probably hematite. These areas correspond to the deep orange areas on the 3-component RGB image.

6. CONCLUSIONS

Our preliminary results show that K-metasomatism can be mapped from AVIRIS data. This represents a significant advance since, due to the visual subtlety of the alteration, large numbers of chemical analyses have been

required previously to construct even a crude alteration map. We have begun systematic sample collection based on the image analysis. Chemical analysis of these samples will allow us to calibrate the AVIRIS spectral data in order to determine the corresponding degree of alteration. The alteration map produced from this data should allow testing of the two metasomatism models.

7. REFERENCES CITED

- Bartley, J. M., and Glazner, A. F., 1985, Hydrothermal systems and Tertiary low-angle normal faulting in the southwestern United States: *Geology*, v. 13, p. 562-564.
- Beratan, K. K., Blom, R. G., Nielson, J. E., and Crippen, R. E., 1990, Use of Landsat Thematic Mapper images in regional correlation of syntectonic strata, Colorado River extensional corridor, California and Arizona: *Jour. Geophys. Res.*, v. 95, no. B1, p. 615-624.
- Chamberlin, R. M., 1982, Geologic map, cross sections, and map units of the Lemitar Mountains, Socorro County, New Mexico: New Mexico Bureau of Mines and Mineral Resources, Open-file Report 169, 3 plates, scale 1:12,000.
- Chapin, C. E., 1989, Volcanism along the Socorro accommodation zone, Rio Grande rift, New Mexico, *in* Chapin, C. E., and Zidek, J. (eds.), *Field Excursions to Volcanic Terranes in the Western United States, Volume I: New Mexico Bureau of Mines and Mineral Resources, Memoir 46*, p. 46-119.
- Chapin, C. E., and Lindley, J. I., 1986, Potassium metasomatism of igneous and sedimentary rocks in detachment terranes and other sedimentary basins: Economic implications: *Arizona Geol. Soc. Digest*, v. 16.
- Elston, W. E., 1978, Mid-Tertiary cauldrons and their relationship to mineral resources, southwestern New Mexico: A brief review, *in* Chapin, C. E., and Elston, W. E. (eds.), *Field guide to selected cauldrons and mining districts of the Datil Mogollon volcanic field, New Mexico: New Mexico Geol. Soc. Special Pub. 7*, p. 107-113.

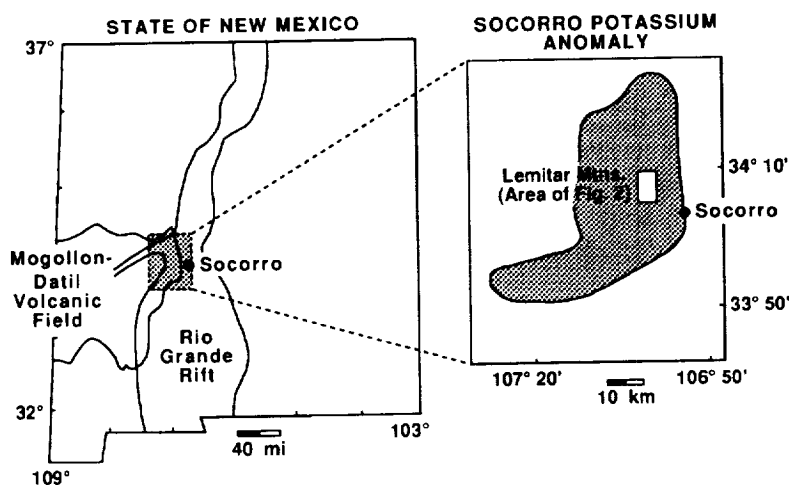


Figure 1. Map showing the location and approximate extent of the Socorro potassium anomaly. (Modified from Chapin and Lindley, 1986.)

Figure 2. (See Slide 1.) 3-component RGB image of the study area; AVIRIS data collected in August, 1990. Blue = AVIRIS band 12; green = band 48; red = band 213.

100-52
10004
1/4

**AUTOMATING SPECTRAL UNMIXING OF AVIRIS DATA
USING CONVEX GEOMETRY CONCEPTS**

Joseph W. Boardman

Center for the Study of Earth from Space
Cooperative Institute for Research in the Environmental Sciences
Campus Box 449 University of Colorado
Boulder, CO 80309-0449

1. INTRODUCTION

1.1. Spectral Mixture Analysis and Its Current Limitation

Spectral mixture analysis, or unmixing, has proven to be a useful tool in the semi-quantitative interpretation of AVIRIS data (Boardman and Goetz, 1991 and references therein). Using a linear mixing model and a set of hypothesized endmember spectra, unmixing seeks to estimate the fractional abundance patterns of the various materials occurring within the imaged area. However, the validity and accuracy of the unmixing rest heavily on the "user-supplied" set of endmember spectra. Current methods for endmember determination are the weak link in the unmixing chain.

1.2. Goals of Automated Unmixing and Its Promise

Automated unmixing seeks to estimate the number of endmembers, their spectral signatures and abundance patterns, using only the mixed data and a physical model. It should be an objective and repeatable process that uses no ground-based information. Such a method promises to take full advantage of the wealth of information currently "locked-up" in AVIRIS data sets. The method outlined here seeks to keep this promise by using spectral mixing inherent in AVIRIS data to its advantage. These ideas are an extension and follow-on to those first proposed by Craig (1990).

2. A GEOMETRIC VIEW OF SPECTRAL MIXING AND UNMIXING

2.1. Spectra are Points in an n -Dimensional Scatterplot

Spectra can be thought of as points in an n -dimensional scatterplot, where n is the number of bands. The coordinates of the points in n -space consist of n -tuples of values that are simply the spectral radiance or reflectance values in each band for a given pixel. An understanding of this concept of "spectral space" is crucial for the following discussion. The distribution of these points in n -space can be used to estimate the number of spectral endmembers and their pure spectral signatures. Although collected in 220 bands, the inherent dimensionality of AVIRIS data is typically much lower, in the range of 3 to 10. This degeneracy is illustrated by the high correlation among bands.

2.2. Convex Geometry : Facets; Faces; Vertices; Hulls; and Simplices in n -D

Convex geometry deals with the geometry of convex sets (Valentine, 1964) and, despite its richness and depth, is within the grasp of anyone with a vivid imagination and geometric intuition. Many useful applications have been developed (Lay, 1982). A convex set in n -dimensions is defined as a set of points that are linear combinations of some set of points, where the weights are all positive and sum to unity. This is also the exact definition of the linear spectral mixture model.

Some of the terminology used in convex geometry is illustrated in a 2-d case in Figure 1. All the points are interior to the triangle, since they are positive, unit-sum, linear combinations of the three corners. A body made up of $n+1$ points is the simplest

possible, that has some interior, and is called a **simplex**. In this 2-d case it is a triangle. Sub-elements of a convex body are its **faces**. The $(n-1)$ -d faces of a simplex are called **facets**. The 0-d faces are **vertices**. The exterior surface of a set of points, made up of adjacent facets, is its **convex hull**. It consists of the facets that would get "painted" if you "rolled" the point set on a $(n-1)$ -d "ink pad". In 3-d the simplex is a tetrahedron and it has four vertices and four triangle facets. These concepts and definitions generalize to n dimensions, despite being harder to visualize. In n -d the simplex has $n+1$ vertices and $n+1$ facets of dimension $n-1$.

2.3. Unmixing as a Convex Geometry Problem

Automated spectral unmixing is a convex geometry problem. We are given the scatterplot of points. Determining its inherent dimensionality tells us the number of mixing endmembers. There are $n+1$ endmembers if the data is inherently n -dimensional, assuming the endmembers are spectrally distinct in terms of the observing instrument. Estimating the spectral signatures of the mixing endmembers is done by finding the "best-fitting" simplex that contains the scatterplot. The vertices of this simplex represent the $n+1$ mixing endmembers. Estimation of the abundances of each endmember, at each pixel, corresponds to a simple transformation of the data to barycentric coordinates. Since the simplex contains all the data points, the derived fractions will be positive and sum to unity, as desired.

3. PRACTICAL METHODS FOR APPLICATION

Applying this endmember derivation approach to AVIRIS data is done in several steps. First the observed radiance data is reduced to apparent reflectance using an atmospheric and solar model, ATREM (Gao and Goetz, 1993). The next step is to determine the data dimensionality and to separate signal from noise. A modified version of the MNF-transform (Green et al., 1988) is used, in place of standard PC analysis, to address the noise properties of AVIRIS data. This involves: estimation of the noise covariance matrix; a rotation and scaling of the data to make the noise isotropic with unit variance in all bands; and a subsequent eigen-analysis of this transformed data. In this MNF-space the number of valid dimensions can be determined by joint inspection of the images and the final eigenvalues. Usually a small number of dimensions explain almost all the signal, with the complementary bands associated with salt-and-pepper noise images and unit eigenvalues. A basis for the signal subspace is calculated and the data are projected onto it, fixing its dimension. The output of this process is apparent reflectance data, projected onto a spanning subspace of minimum dimension, with most of the noise removed.

The estimates of the spectral endmembers are determined by finding the "best-fitting" simplex that contains the projected data. Craig (1990) proposes the "smallest" simplex containing the data as a proxy for the "best" simplex. Numerically, he seeks to maximize a determinant subject to inequality constraints. Geometrically, this shrinks the simplex but keeps all the data inside. Other methods for "best" simplex determination are the subject of current research. Orientations and positions of the $n+1$ facets of the "best" simplex may also be determined through analysis of the facets of the convex hull of the projected data. Sets of pixels that are void in one or more endmembers actually map the faces of the desired simplex. Recognizing these "flats" is one way to determine the "best" simplex". Once the best simplex is determined, the endmember estimates are given by its vertices. These endmembers must give positive fractions for abundances that sum to unity for every pixel, since the simplex contains the data. Finally, the data are unmixed by converting to barycentric coordinates and the endmember spectra are projected back to the original band-space to derive their full-resolution spectra.

The validity of the process can be assessed by its outputs. Automated unmixing delivers estimates of the endmembers and estimates of the spatial patterns of fractional abundance of these endmember materials. The endmember spectra should be reasonable and be identified with real Earth materials and "shade". The corresponding spatial abundance images, interpreted together with the spectra, provide another performance

check. The spatial information in the abundance images is useful in interpreting and naming the derived endmember spectra, capitalizing on the unique dual spectral/spatial nature of AVIRIS data. Ideally, each endmember spectrum and corresponding abundance image will be reconciled with a named material, perhaps through the use of a spectral library and expert system. The derived spectra have used all bands of all pixels and thus have a much higher signal-to-noise ratio than individual spectra. Furthermore, there are quite few of them by comparison to the raw spectra. Time-intensive procedures can be used to analyze this small set of low-noise, derived spectra, with the unmixing results allowing interpretation of the full set of observed spectra.

4. EXAMPLE APPLICATION TO AVIRIS DATA

Convex geometry unmixing has been applied to many AVIRIS scenes, yielding promising results in both vegetation and geological study areas. Two examples will be shown at the workshop, Jasper Ridge and North Grapevine Mountains.

4.1. Jasper Ridge Example

In this example, 172 bands of 1992 AVIRIS data yielded a 4-d convex data set. The five endmember spectra and their corresponding abundance images are shown in Slide 2. In this case the interpretation of the endmembers is clear. The five derived endmembers are : shade; water; soil; green vegetation; and dry vegetation. The shapes of the spectra are reasonable and seem to represent "pure" materials, even in cases like shade where no image pixel was nearly pure. This illustrates the ability of the method to project beyond the observed mixed data to estimate endmembers. Pure pixels are not required.

4.2. North Grapevine Mountains Example

In this example, 45 bands of the SWIR portion of 1989 AVIRIS data were used. These data were reduced to approximate apparent reflectance by the empirical line method (Kruse et al., 1993). Using this restricted set of bands, four endmembers were identified. The best-fit simplex and the data are shown in Figure 2, along with plots of two of the endmembers. The four endmembers identified are : shade; featureless materials; carbonate; and sericite. The maps of sericite and carbonate abundance agree well with previous studies (Kruse et al., 1993) and the derived spectra are easily identified.

5. DISCUSSION , CONCLUSIONS AND CAVEATS

Convex geometry can be used successfully to address the most important questions in spectral unmixing, the estimation of the number of the endmembers and their spectra. The method outlined here builds on the work of Craig (1990), treating shade as another unknown, obviating the need for a "dark-point" bias correction. Combining AVIRIS data, ATREM and the convex geometry method, one can derive the number of endmembers, estimates of their pure spectra and maps of their apparent abundance, using **absolutely no ground data.**

The method presented here has limitations and pitfalls. Some are inherent, some can be solved and removed with further research. It assumes a wide range of fractional abundances, so it cannot unmix a single pixel, or a homogeneous scene. The current computer programs are limited to scenes with no more than 8 or so endmembers, because of the "curse of dimensionality" (Craig, 1990). Any material that occurs in a fixed proportion in every pixel is essentially "invisible" to the method. This can cause the other derived endmembers to actually be spectra of mixtures, not pure materials.

6. ACKNOWLEDGMENTS

This work was supported by Alex Goetz at CSES, through NASA grant NAS5-31711. Fred Kruse donated AVIRIS data and helpful advice. The concepts of the method are a direct result of work done at CSIRO, DEG, Sydney, Australia. My

understanding and thoughts draw heavily on interaction with Australian colleagues: Jon Huntington; Maurice Craig; and Andy Green. Blame is mine, credit theirs.

7. REFERENCES

- Boardman, J. W. and A. F. H. Goetz, 1991, "Sedimentary Facies Analysis Using Imaging Spectrometry : a Geophysical Inverse Problem", in : *Proceedings of the Third AVIRIS Workshop*, JPL Publication 91-28, pp. 4-13.
- Craig, M., 1990, "Unsupervised Unmixing of Remotely Sensed Images", in: *Proceedings of the Fifth Australasian Remote Sensing Conference*, Perth, Australia, pp. 324-330.
- Gao, B-C, K. B. Heidebrecht and A. F. H. Goetz, 1993, Derivation of Scaled Surface Reflectances from AVIRIS Data, *Remote Sensing of Environment*, vol. 44, no. 2, pp. 165-178.
- Green, A. A., M. Berman, P. Switzer and M. D. Craig, 1988, "A Transformation for Ordering Multispectral Data in Terms of Image Quality with Implications for Noise Removal", *IEEE Transactions on Geoscience and Remote Sensing*, vol. 26, no. 1, pp. 65-74.
- Kruse, F., A. B. Lefkoff and J. B. Dietz, 1993, Expert System-Based Mineral Mapping in Northern Death Valley, California/Nevada, Using the Airborne Visible/Infrared Imaging Spectrometer (AVIRIS), *Remote Sensing of Environment*, vol. 44, no. 2, pp. 309-336.
- Lay, S. R., 1982, *Convex Sets and their Applications*, John Wiley and Sons, New York.
- Valentine, F. A., 1964, *Convex Sets*, McGraw-Hill Book Company, New York.

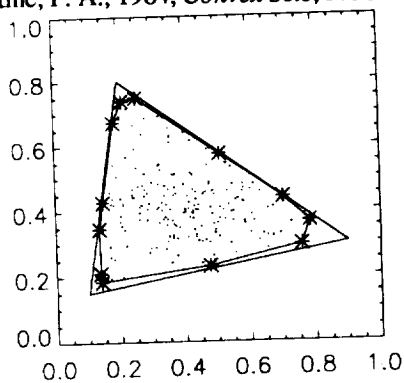


Figure 1. Two hundred points, interior to a triangle illustrate the concepts of convex geometry. The points are all positive, unit-sum combinations of the triangle vertices. Twelve of the points, marked with asterisks, are the vertices of the convex hull. The convex hull has facets that are line segments. All the data are surrounded by the triangle, a 2-d simplex, that has 3 1-d facets and 3 0-d vertices.

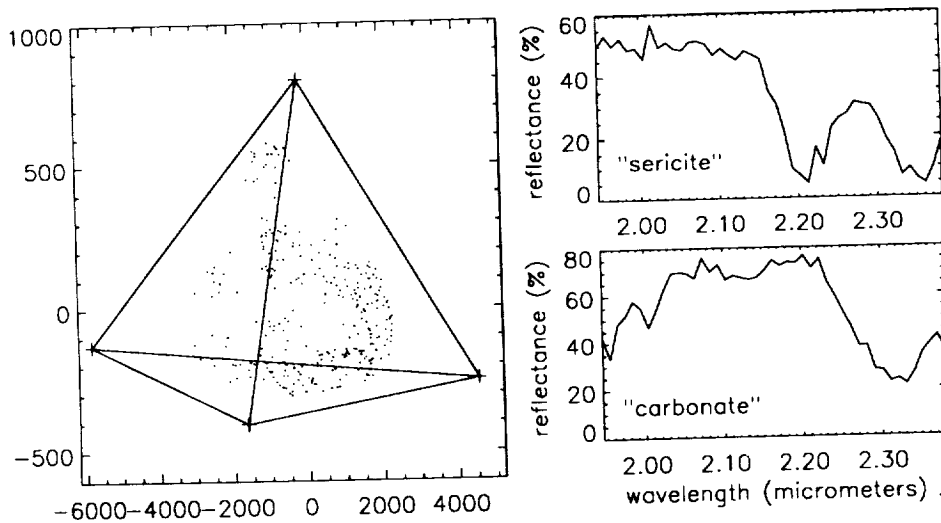


Figure 2. a) Best-fitting simplex surrounds the vertices of the convex hull of the data . Third axis is perpendicular to the paper. b) Two of the derived endmembers, identified as "sericite" and "carbonate". Sericite is the "top" vertex in 2a, carbonate is the "bottom" vertex, shade is to the "right".

15-82
4/1005
4

AVIRIS CALIBRATION USING THE CLOUD-SHADOW METHOD

K.L. Carder, P. Reinersman, R.F. Chen

University of South Florida St. Petersburg
Marine Science Department
140 Seventh Avenue South
St. Petersburg, FL 33701-5016

More than 90% of the signal at an ocean-viewing, satellite sensor is due to the atmosphere (Gordon, 1987), so a 5% sensor-calibration error when viewing a target that contributes but 10% of the signal received at the sensor may result in a target-reflectance error of more than 50%. Since prelaunch calibration accuracies of 5% are typical of space-sensor requirements, recalibration of the sensor using ground-based methods (e.g. Gordon, 1987; Carder et al. 1993) is required for low-signal targets. Known target reflectance or water-leaving radiance spectra and atmospheric-correction parameters are required.

In this article we describe an atmospheric-correction method that uses cloud-shadowed pixels in combination with pixels in a neighboring region of similar optical properties to remove atmospheric effects from ocean scenes. These neighboring pixels can then be used as known reflectance targets for validation of the sensor calibration and atmospheric correction. The method uses the difference between water-leaving radiance values for these two regions. This allows nearly identical optical contributions to the two signals (e.g. path radiance and Fresnel-reflected skylight) to be removed, leaving mostly solar photons backscattered from beneath the sea to dominate the residual signal. Normalization by incident solar irradiance reaching the sea surface provides the remote-sensing reflectance of the ocean at the location of the neighbor region.

Errors result from this method if corrections are not made for the following: 1) reduction of the path radiance over the shadowed pixels resulting from partial shadowing of the overlying atmospheric column; and 2) adjacency effects resulting from solar-derived photons leaving the water from the bright, surrounding waters that are scattered into the field of view for the shadowed pixels.

The initial application of the shadow-neighbor method was made assuming that the sensor calibration is correct. For illustrative purposes, assume that the solar zenith angle θ_0 is 45° , and that the angle from the pixel to the sensor θ is 0° . A small cumulus cloud (about 1 km diameter) at 1.2 km altitude removes direct solar photons and shades a region. The water-leaving radiance from this shady region directed toward the sensor is designated L_{ws} . The wavelength dependence of terms in this article have been left out for brevity. This radiance results from skylight photons which have been scattered from beneath the ocean surface.

Adjacent to the shadowed region is a neighboring patch of water with identical inherent optical properties to those of the shadowed region, differing only in the fact that direct, solar photons as well as skylight irradiate it. The water-leaving radiance from the neighbor region is designated L_{wn} . Since the cloud is quite small, it occludes a similar fraction of the sky for both shadow and neighbor patches, and

contributes a similar amount of diffusely scattered light to each. Furthermore, the atmospheric columns over each are considered to be identical. Therefore, both the path radiance contributed to the total signals and the diffuse attenuation t of the L_w signals are nearly equal. Later, we will investigate the differences induced by the fact that a short column of the atmosphere over the shadow is shaded from solar photons by the cloud.

To second order, the path radiance consists of a portion due to molecular or Rayleigh scattering, L_r , one due to aerosol scattering, L_a , and one due to multiple scattering, L_{ra} . Let the radiance measured at the sensor when viewing an area in unshadowed water be given by (Wang and Gordon, 1992).

$$1) \quad L_{1n} = L_a + L_r + L_{ra} + t L_{wn}$$

where

- L_{1n} = measured radiance when viewing an unshadowed (neighbor) pixel
- L_a = path radiance due to aerosol scattering
- L_r = path radiance due to Rayleigh scattering
- L_{ra} = path radiance due to Rayleigh-aerosol interaction
- t = diffuse transmittance of the atmosphere for water-leaving radiance
- L_{wn} = water-leaving radiance of neighbor pixel
- L_{ws} = water-leaving radiance of shadowed pixel.

The apparent path transmittance of the water-leaving radiance from the shadowed pixel may not be equivalent to the term used in Eq. 1. Use of the "diffuse transmittance" is justified when viewing a large homogeneous area where the radiance scattered out of the viewing path is balanced by the radiance scattered into it from adjacent areas of the scene. In the case of the shadowed pixel, the adjacent areas of the scene are generally brighter, and so the apparent transmittance may be increased.

If Δ terms express perturbations due to non-homogeneity in the scene illumination, the total radiance at the sensor when viewing a shadowed pixel may be written

$$(2) \quad L_{1s} = L_a - \Delta L_a + L_r - \Delta L_r + L_{ra} - \Delta L_{ra} + (t + \Delta t) L_{ws}$$

In general, the water-leaving radiance may be expressed as the sum of two parts: one part caused by backscattering of incident, diffuse skylight, and the other by backscattering of the direct solar beam by water and hydrosols. For the neighbor and shadowed pixels, respectively,

$$(3) \quad L_{wn} = sky L_{wn} + sol L_{wn}; \quad L_{ws} = sky L_{ws} + sol L_{ws}$$

Under the assumptions that the shadowed pixel receives no direct sun and that the incident sky light at both pixels is the same, that is

$$(4) \quad L_{ws} = sky L_{ws} = sky L_{wn},$$

$$(5) \quad L_{1n} - L_{1s} = \Delta L_a + \Delta L_r + \Delta L_{ra} + t_{sol} L_{wn} - \Delta t_{sky} L_{wn}$$

The first three terms on the right of Eq. 5 depend on the length of the shadowed portion of viewing path to the shadowed pixel. The height of the intersection of the viewing path and the upper edge of the cylinder of atmosphere shaded by the cloud can be determined from scene geometry. The layer of atmosphere below this intersection would normally be the source of less than 20% of the Rayleigh scattering, so we will assume that the Rayleigh-aerosol correction term, ΔL_{ra} , must be negligible. Then, following Gordon et al. (1987), for the aerosol and Rayleigh corrections we may write

$$(6) \quad \Delta L_x = \{\omega_x \tau'_x F_o^* P_x(\theta, \theta_o, \lambda)\} t' / 4\pi, \quad x = a, r$$

where

$$\begin{aligned} \tau'_x &= \text{optical thickness of shaded viewing path (vertical)} \\ \omega_x &= \text{single-scattering albedo} \\ F_o^* &= F_o e^{-(\tau-\tau')/\cos\theta_o} \\ F_o &= \text{extra-terrestrial solar irradiance} \\ P_x(\theta, \theta_o) &= \{P_x(\theta_-) + [\rho(\theta) + \rho(\theta_o)] P_x(\theta_+)\} / \cos\theta \\ \cos\theta_{\pm} &= \pm \cos\theta_o \cos\theta + \sin\theta_o \sin\theta \cos(\phi - \phi_o) \\ \rho(\theta) &= \text{Fresnel reflectance } (\theta) \\ P_x(\theta) &= \text{scattering phase function} \\ t' &= \text{diffuse transmittance from top of layer to top of atmosphere} \\ t &= \exp\{-(\tau_r/2 - \tau'_r/2 + \tau_{oz} - \tau'_{oz})/\cos\theta\}. \end{aligned}$$

The term involving Δt in equation (2) represents the apparent increase in diffuse transmittance of water-leaving radiance when viewing a shadowed pixel. The work of Tanre et al. (1979) indicates that this term is proportional to the difference in water-leaving radiances from the shadowed and neighbor pixels and is dependent on the geometry of the particular case. We will express Δt as

$$(7) \quad \Delta t = t * \sigma (L_{wn} - L_{ws}) / L_{ws} = t * \sigma (sol L_{wn} / sky L_{wn}).$$

Preliminary Monte Carlo simulations indicate that $\sigma(550 \text{ nm})$ is of the order of 0.1 for circular shadows of radius equal to 1 km for moderately turbid atmospheres ($\tau_a = 0.2$). Thorough investigation of the dependence of σ on wavelength and geometry is pending. Using equation (7) and equation (5) we obtain

$$(8) \quad sol L_{wn} = \{L_{tn} - L_{ts} - \Delta L_a - \Delta L_r\} / t(1-\sigma).$$

Now define (Gordon et al. 1987)

$$(9) \quad \epsilon(\lambda_i, \lambda_j) = \frac{\omega_a(\lambda_i) \tau'_a(\lambda_i) P_a(\theta, \theta_o, \lambda_i)}{\omega_a(\lambda_j) \tau'_a(\lambda_j) P_a(\theta, \theta_o, \lambda_j)}$$

then

$$(10) \quad \frac{\Delta L_a(\lambda_i)}{\Delta L_a(\lambda_j)} = \epsilon(\lambda_i, \lambda_j) \frac{F_o^*(\lambda_i) t'(\lambda_i)}{F_o^*(\lambda_j) t'(\lambda_j)} = S(\lambda_i, \lambda_j)$$

then

$$(11) \quad t(\lambda_i) [1-\sigma(\lambda_i)]_{sol} L_{wn}(\lambda_i) = L_{tn}(\lambda_i) - L_{ts}(\lambda_i) - \Delta L_r(\lambda_i) - S(\lambda_i, \lambda_j) \{L_{tn}(\lambda_j) - L_{ts}(\lambda_j) - \Delta L_r(\lambda_j) - t(\lambda_j) [1-\sigma(\lambda_j)]_{sol} L_{wn}(\lambda_j)\}$$

If λ_j is a wavelength such as 780 nm where the water-leaving radiance is essentially zero, then $sol L_{wn}(\lambda_j) = 0$, and

$$(12) \quad \Delta L_a(780) = L_{tn}(780) - L_{ts}(780) - \Delta L_r(780)$$

and

$$(13) \quad t(\lambda_i) (1-\sigma(\lambda_i))_{sol} L_{wn}(\lambda_i) = L_{tn}(\lambda_i) - L_{ts}(\lambda_i) - \Delta L_r(\lambda_i) - S(\lambda_i, 780) [L_{tn}(780) - L_{ts}(780) - \Delta L_r(780)].$$

From scene geometry, the cloud height H and height of the shadowed viewing path can be calculated. Then, $\Delta L_r(\lambda)$ can be determined for all λ by differencing Lowtran 7 results for the entire air column and the air column down to height H . The aerosol correction term, $\Delta L_a(780)$, is then determined by Eq. 12. Knowledge of wind speed allows estimation of $\epsilon(\lambda_i, 780)$ (Gregg and Carder, 1990), and thus $S(\lambda_i, 780)$. The $\sigma(\lambda_i)$ term involved in the transmissivity correction has been estimated by Monte Carlo simulations to be described later. Thus, Eq. 13 allows $sol(L_{wn}(\lambda_i))$ to be calculated.

The results for an AVIRIS scene, 19 November, 1992 seaward of Key Biscayne, Florida are shown in Figure 1, where terms from Eq. 5 are normalized by the incoming solar irradiance $_{\text{sol}}E_d$ (no skylight) to form remote-sensing reflectance spectra. Note that the spectrum resulting from the cloud-shadow method differs from that using conventional atmospheric correction methodology (see Carder et al., 1993) by only about 3.5%. This derived reflectance spectrum can in principle serve as a calibrated ground target to help with model parameterization for atmospheric correction of the entire scene, or in validation of the calibration of a sensor for scenes where conventional methods were unavailable.

REFERENCES

- Carder, K.L. et al., "AVIRIS calibration and application in coastal oceanic environments," *Remote Sens. Environ.*, vol. 44, pp. 205-216, 1993.
- Elterman, L., "UV, visible, and IR attenuation for altitudes to 50 km," Report AFCRL-68-0153, Air Force Cambridge Res. Lab, Bedford MA, 1968.
- Gordon, H.R., "Calibration requirements and methodology for remote sensors viewing the oceans in the visible," *Remote Sens. Environ.*, vol.22, pp.103-126, 1987.
- Watson, W. et al., "A simple spectral solar irradiance model for cloudless maritime atmosphere," *Limnol. Oceanogr.*, 35(8), pp. 1657-1675, 1990.
- Tanre, D. et al., "Atmosphere modeling for space measurements of ground reflectances, including bidirectional properties," *Appl. Opt.*, vol. 18, pp.3587-3594, 1979.
- Wang, M. et al., "Atmospheric correction of second generation ocean color sensors: a preliminary algorithm," *Appl. Opt.*, vol. 31, pp. 4247-4260, 1992.

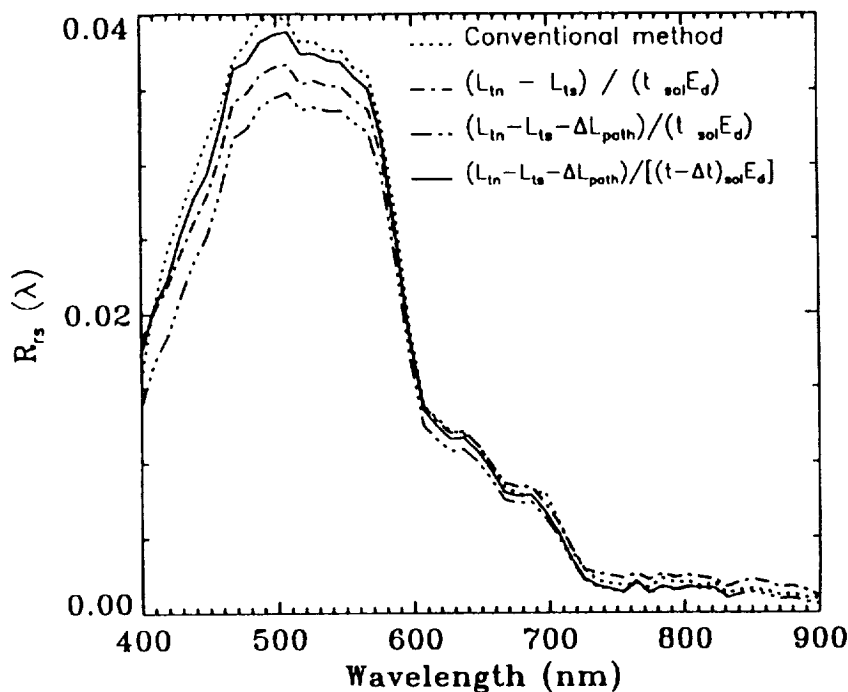


Fig. 1: Remote-sensing reflectance spectra using conventional atmospheric-correction methods and the cloud-shadow method where path-shadow and transmittance perturbations are sequentially removed.

26-43
1/9

FIELD OBSERVATIONS USING AN AOTF POLARIMETRIC IMAGING SPECTROMETER

Li-Jen Cheng, Mike Hamilton, Colin Mahoney, and George Reyes
Jet Propulsion Laboratory, California Institute of Technology
Pasadena, CA 91109

1. INTRODUCTION

This paper reports preliminary results of recent field observations using a prototype acousto-optic tunable filter (AOTF) polarimetric imaging spectrometer. The data illustrate application potentials for geoscience.

The operation principle of this instrument is different from that of current airborne multispectral imaging instruments, such as AVIRIS. The AOTF instrument takes two orthogonally polarized images at a desired wavelength at one time, whereas AVIRIS takes a spectrum over a predetermined wavelength range at one pixel at a time and the image is constructed later. AVIRIS does not have any polarization measuring capability. The AOTF instrument could be a complement tool to AVIRIS.

Polarization measurement is a desired capability for many applications in remote sensing. It is well known that natural light is often polarized due to various scattering phenomena in the atmosphere. Also, scattered light from canopies is reported to have a polarized component (Vanderbilt et al., 1988). To characterize objects of interest correctly requires a remote sensing imaging spectrometer capable of measuring object signal and background radiation in both intensity and polarization so that the characteristics of the object can be determined. The AOTF instrument has the capability to do so.

The AOTF instrument has other unique properties. For example, it can provide spectral images immediately after the observation. The instrument can also allow observations to be tailored in real time to perform the desired experiments and to collect only required data. Consequently, the performance in each mission can be increased with minimal resources.

The prototype instrument was completed in the beginning of this year. A number of outdoor field experiments were performed with the objective to evaluate the capability of this new technology for remote sensing applications and to determine issues for further improvements.

2. ACOUSTO-OPTIC TUNABLE FILTER

The AOTF consists of a birefringence crystal to which one or several piezoelectric transducers are bonded. When a RF signal is applied, the transducer generates acoustic waves launching into the crystal. The propagating acoustic waves produce a periodic modulation of the index of refraction. This provides a moving phase grating that diffracts portions of an incident light beam. For a fixed acoustic frequency, only a narrow band of optical frequencies can approximately satisfy the phase-matching condition and be collectively diffracted. As the RF changes, the center of optical bandpass changes accordingly. This creates a tunable bandpass filter.

In a birefringence crystal, there are two types of light waves, ordinary and extraordinary, with polarization orthogonal to each other. In an AOTF, the grating

diffracts an ordinary wave into an extraordinary wave and vice versa. If the incident beam is unpolarized, there will be two orthogonally polarized diffracted beams exiting at the opposite sides of the undiffracted beam, as illustrated in Figure 1. This provides opportunities to measure polarization of incident light.

3. PROTOTYPE SYSTEM

The system contains an optical subsystem, two integrating CCD cameras, a RF generator and a power amplifier, a 386 IBM-PC compatible computer for control and data acquisition and monitors. The unique part of the system is the optical configuration as illustrated in FIGURE 2. It contains a 3 inch aperture, zoom telelens set with variable focal length of 80-120 mm as the objective lens; an aperture located at the objective lens image plane for allowing only photons from the desired scene to pass through; a collimating lens ($f=40\text{mm}$) to create an intermediate pupil plane whose cross section is comparable with that of an AOTF; an AOTF located at the pupil plane, a field lens to create adequate beam diversion for imaging at the cameras; and two cameras for recording two polarized images separately. The operation wavelength of this instrument is 0.48-0.77 microns. A more detailed description of the system was published in a recent paper (Cheng et al., 1993).

4. EXPERIMENTAL RESULTS

Several outdoor observations were performed at JPL and Ft. Huachuca, AZ during sunny days. Figure 3 gives a picture of the scene in a raw country site of Ft. Huachuca. Many interesting features in the scene were observed. Because of the page limitation, many of them are reported here as an illustration. A reflection reference plate of BaSO_4 , observable as a small bright rectangular object in the upper left part of the picture, was put in the scene for intensity normalization among images taken at different wavelengths. The distance between the plate and the instrument was about 3.5 km.

After the observations, image data were transferred to a 33 MHz 486 computer for data normalization, image cube formation, and data analysis using the interactive data language (IDL) in the MS window environment.

The scene can be approximately divided into three areas: 1) a vegetation rich area covering the lower part of the picture, 2) a wide open area with reddish soil, dry grass, a dirt road, and a few bushes, located above the first area, and 3) a ridge, across the top of the picture, with a mixture of trees and dry grass.

In the left part of Area 1, there is a group of trees, possibly local oak trees. From their appearance, there are two types of trees in the group. One has a bright green color and is named Tree 1. The other has a grayish green color and is named Tree 2. Figures 4 and 5 give typical observed spectra of Tree 1 and Tree 2, respectively. In comparison, Tree 1 has high reflection in the near infrared wavelength region and high absorption around 0.68 micron, due to chlorophyll, whereas Tree 2 has low reflection in the infrared and low absorption around 0.68 micron. If Tree 1 and Tree 2 belong to same species, one could conclude that Tree 2 is not in a healthy state.

Figure 6 shows a pair of observed spectra at a distant tree on the ridge at the far upper left corner of Figure 3. In comparison with the spectra in Figure 4, one easily noted feature is that the measured intensities of the spectra become significantly higher as wavelength decreases. This observation and high background intensities in all measured spectra are consistent with the thought that a considerable amount of scattered

light due to dust and aerosols in air was added to the measured sign. The existence of haze in the air was also noticed in a color picture of the scene taken by an ordinary camera.

The map of vegetation is an important subject for earth sciences. The spectral derivative method is known to be an effective way of evaluating canopies (Wessman, 1990). One effective way to obtain a vegetation map is to make an image of spectral derivatives from the observed image cubes at a chlorophyll red edge wavelength. Figure 7 shows a spectral derivative image at 0.7 micron generated from the data. The image is a map of chlorophyll or the vegetation index. The bright parts correspond to canopies with sharp red edge absorption. These canopies also have higher measured reflection in the near-infrared wavelength region. Most parts of Area 2 are dark, as expected because the surface contains mostly bare soil and dry grass. There are several man-made objects, such as two cars and an antenna disk, which become invisible.

The spectral data in Figures 4-6 show considerable differences in signal intensity between two polarizations. The intensity minimum of the chlorophyll absorption at the vertical polarization shifts slightly toward longer wavelength with respect to that at horizontal polarization. The observation of this shift is consistent with the existence of high background light due to scattered light from dust and aerosols in the air. The polarization phenomena in the atmosphere near the surface are very complicated. The data observed so far do suggest that vegetation could have characteristic polarization spectra. This is a subject requiring more studies.

5. CONCLUSION

The preliminary results stated in this paper have illustrated the capability of the AOTF instrument in remote sensing by taking both intensity and polarization parameters. This new capability will create new opportunities for advancing geoscience as well as many other fields.

6. ACKNOWLEDGMENTS

The research described in this paper was performed by the Center for Space Microelectronics Technology, Jet Propulsion Laboratory, California Institute of Technology, under a contract with the National Aeronautics and Space Administration, and was jointly sponsored by the Army Space Technology and Research Office and the Planetary Instrument Definition and Development Program, National Aeronautics and Space Administration.

7. REFERENCES

- Cheng, L.J., T.H. Chao, M. Dowdy, C. Labaw, C. Mahoney, G. Reyes, K. Bergman, "Multispectral Imaging Systems Using Acousto-Optic Filter", SPIE Proceedings, Vol. 1874, p. 224-231 (1993).
- Vanderbilt, V.C. and K.J. De Venecia, 'Specular, Diffuse, and Polarized Imagery of an Oat Canopy', IEEE Trans. Geoscience and Remote Sensing, Vol. 26, p. 451-462 (1988).
- Wessman, C.A., 'Evaluation of Canopy Biochemistry' in 'Remote Sensing of Biosphere Functioning', edited by R.J. Hobbs and H.A. Moony (Springer-Verlag, New York, 1990), p. 135-156.

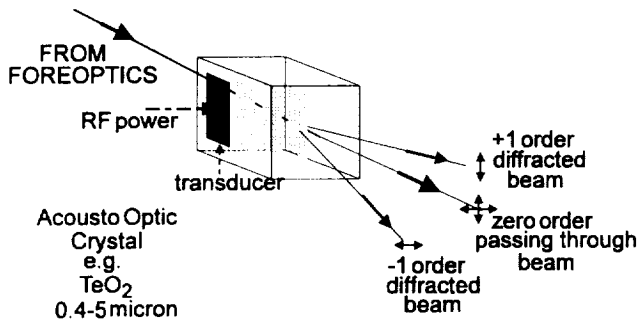


Figure 1. Schematic of a non-collinear AOTF.

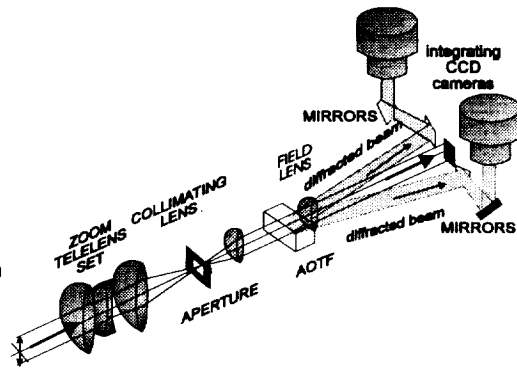


Figure 2. Schematic diagram of the ground system optical configuration.

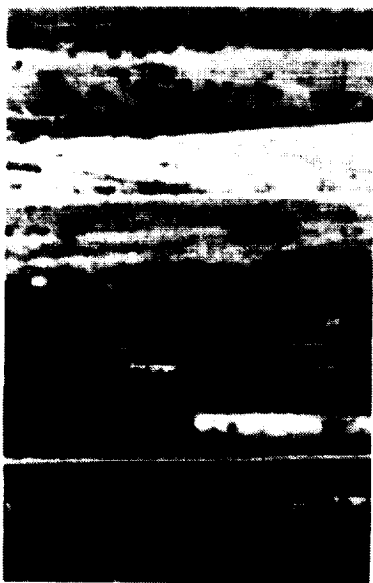


Figure 3. Picture of the scene studied.

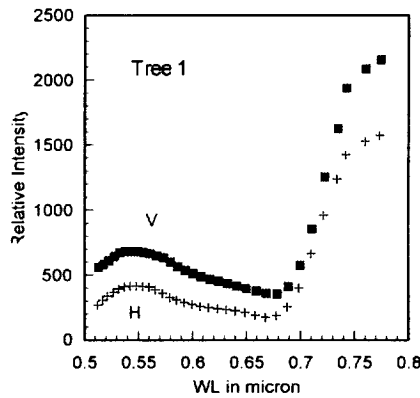


Figure 4. Spectra of Tree 1 with vertical and horizontal polarization

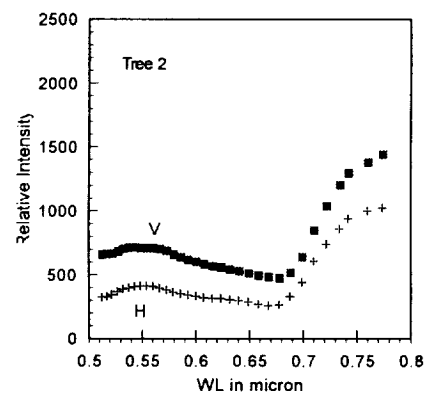


Figure 5. Spectra of Tree 2 with vertical and horizontal polarization

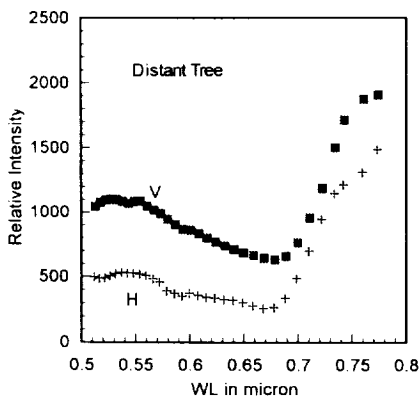


Figure 6. Spectra of distant tree with vertical and horizontal polarization



Figure 7. Derivative spectral image at 0.7 micron

57-43
41-07
11

Instantaneous Field of View and Spatial Sampling of the Airborne Visible/Infrared Imaging Spectrometer (AVIRIS)

Thomas G. Chrien and Robert O. Green

Jet Propulsion Laboratory, California Institute of Technology,
4800 Oak Grove Dr., Pasadena CA 91109 USA

Abstract

The Airborne Visible/Infrared Imaging Spectrometer (AVIRIS) measures the upwelling radiance in 224 spectral bands. These data are acquired as images of approximately 11 by up to 100 km in extent at nominally 20 by 20 meter spatial resolution. In this paper we describe the underlying spatial sampling and spatial response characteristics of AVIRIS.

1.0 AVIRIS Spatial Resolution and Sampling Interval

The spatial field stop of the AVIRIS optical system is defined by one of four 200 μm circular fibers for each of the spectrometers (Chrisp et al., 1987). The numerical aperture of the fibers tapers off smoothly at the edges. In other words, it is not a sharp pillbox function, but a circularly symmetric Gaussian-like function. By the time you add aberrations and scanner smear, a circularly symmetric Gaussian is an excellent approximation. This is shown in Figure 1 for data measured in the laboratory from a narrow beam (0.1 milliradians) of collimated light scanned across a portion of the AVIRIS field of view (FOV). The slightly jagged nature of the data represents line-to-line scan jitter.

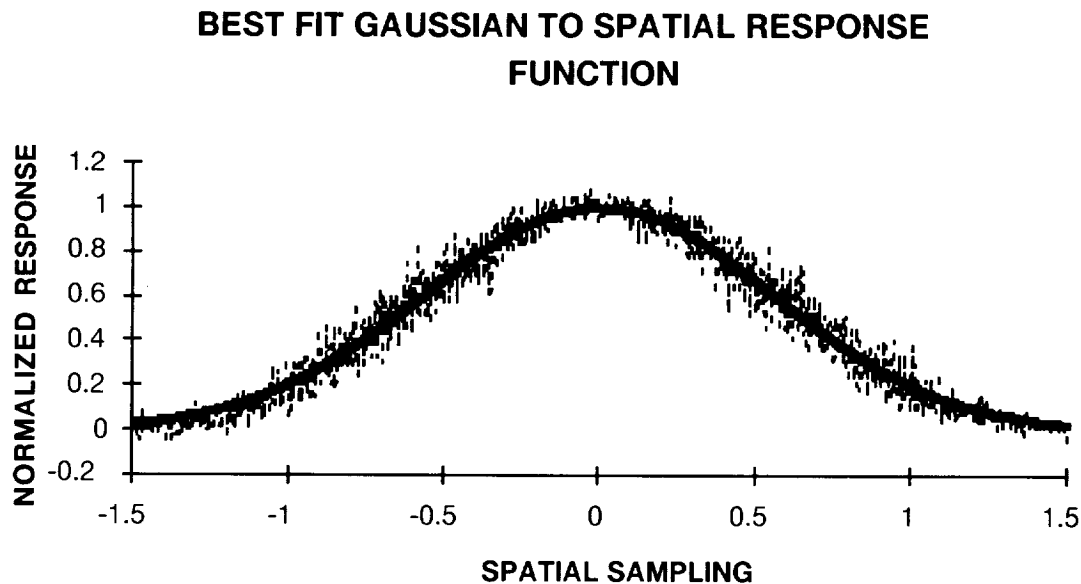


Figure 1. AVIRIS spatial response function.

The AVIRIS spatial response function or instantaneous field of view (IFOV), including scan smear, is a Gaussian function with a FWHM of 1.313 spatial samples and a line-to-line RMS jitter of 0.077 spatial samples. Adjacent pixel samples within a given line are separated by 0.85 milliradians (Miller, 1987). Using this factor to convert to milliradians, the IFOV is 1.12

milliradians and the line-to-line jitter is 0.066 milliradians. Cross-track, these figures are independent of altitude. Ground spot sizes are, of course, the product of IFOV (in radians) and the aircraft platform altitude (AGL). AVIRIS operates from a NASA ER-2 at nominally 20 ±1 km altitude above sea level. A diagram of these relationships is shown in Figure 2, where $s(n)$ refers to the n th cross-track sample.

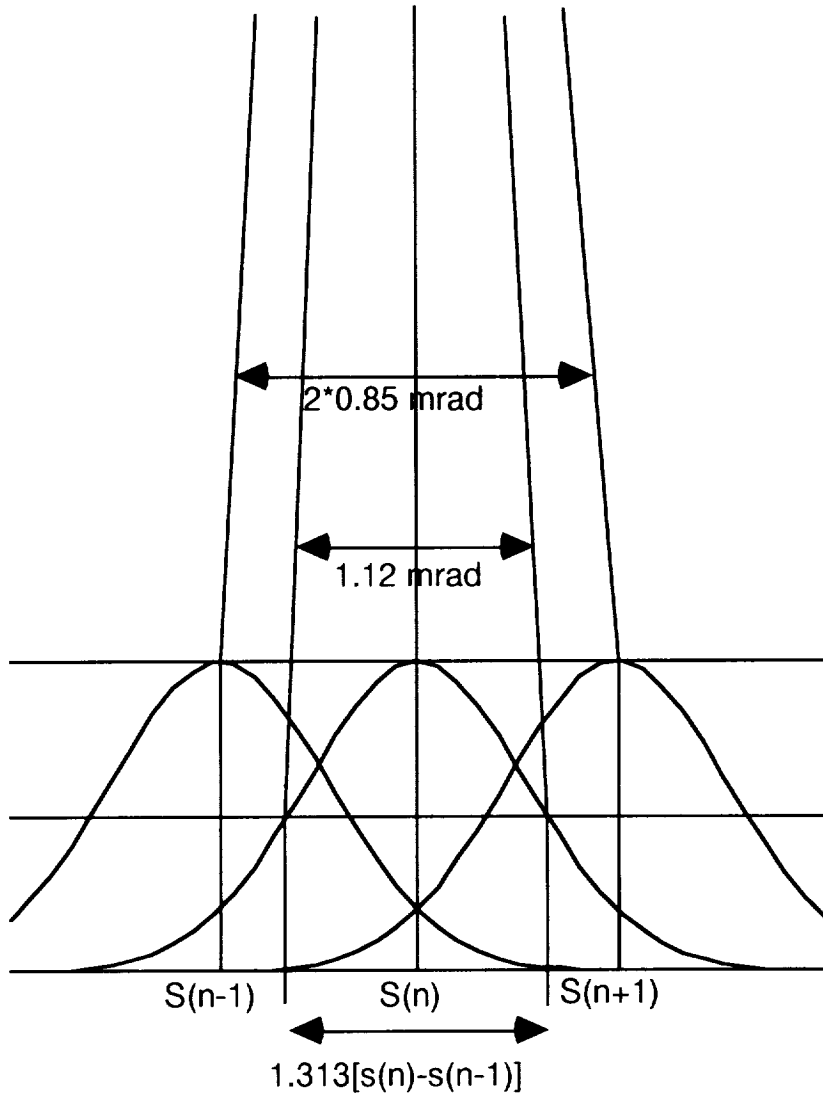


Figure 2. Cross-track sampling

The detector read-out delay will cause a $(n-1)/66$ sample shift, where n is the read-out position of the spectral channel with respect to each of the four spectrometers. Table 1 can be used to determine the appropriate value for the index n for a given spectral channel. This read-out delay is compensated in the radiometrically calibrated data distributed to investigators (Green et al., 1991).

Table 1. The index n for various spectral channels

Spectrometer	Channel	n
A	001	1
	032	32
B	033	1
	096	64
C	097	1
	160	64
D	161	1
	224	64

The down-track sampling distance is due entirely to the motion of the aircraft from line to line. This is determined by the product of the aircraft velocity and the line repeat period of 1/12 of a second. For the ER-2, this distance is nominally 17 meters. Figure 3 shows the sampling where $L(k)$ refers to the k th down-track line. In the down-track case, the GIFOV spot size can become less than the sampling interval for mountains above 4.8 km ASL when the aircraft is at 20 km ASL.

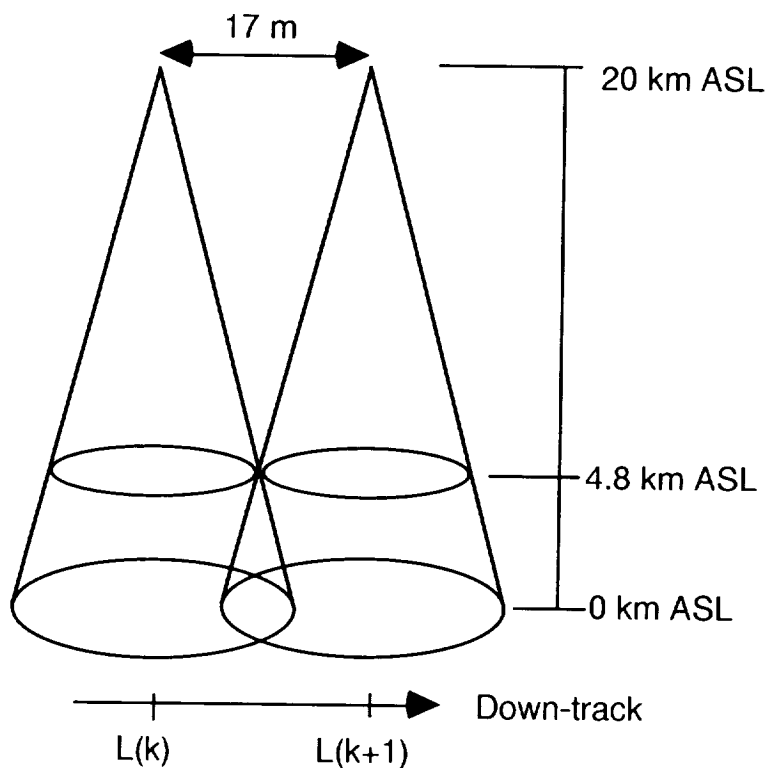


Figure 3. Down-track sampling.

2.0 Summary

The spatial sampling and spatial response function of the AVIRIS system in the cross and down track directions have been described. These characteristics should be taken into account when quantitatively measuring expressed spectral abundance of discrete objects of less than 20 by 20 m size.

3.0 Acknowledgements

This research was carried out at the Jet Propulsion Laboratory, California Institute of Technology, under contract with the National Aeronautics and Space Administration.

4.0 References

Chrip, M. P., T. G. Chrien and L. Stiemle, "AVIRIS Foreoptics, Fiber Optics and On-board Calibrator", SPIE, v 834, Imagins Spectroscopy II, 1987.

Green, R.O., Steve Larson and Ian Novack, "Calibration of AVIRIS digitized data," in Proceedings of the Third AVIRIS Workshop, R. O. Green , editor, JPL Publication 91-28, Jet Propulsion Laboratory, Pasadena, CA, pp. 109-118, 1991.

Miller, D. C., "AVIRIS Scan Drive Design and Performance", SPIE, vol. 834, Imagins Spectroscopy II, 1987.

**AIRBORNE VISIBLE/INFRARED IMAGING SPECTROMETER (AVIRIS):
RECENT IMPROVEMENTS TO THE SENSOR**

Thomas G. Chrien, Robert O. Green, Charles M. Sarture
Christopher Chovit, Michael L. Eastwood, and Bjorn T. Eng

Jet Propulsion Laboratory, California Institute of Technology, Pasadena, CA 91109

1.0 INTRODUCTION

AVIRIS is a NASA-sponsored Earth-looking imaging spectrometer designed, built and operated by the Jet Propulsion Laboratory. Spectral, radiometric and geometric characteristics of the data acquired by AVIRIS are given in Table 1. AVIRIS has been operational since 1989, however in each year since 1989 major improvements have been completed in most of the subsystems of the sensor. As a consequence of these efforts, the capabilities of AVIRIS to acquire and deliver calibrated imaging spectrometer data of high quality have improved significantly over those in 1989. Improvements to AVIRIS prior to 1992 have been described previously (Porter et al., 1990, Chrien et al., 1991, Chrien et al., 1992). In the following sections of this paper we describe recent and planned improvements to AVIRIS in the sensor task.

2.0 SENSOR IMPROVEMENTS**2.1 1992 Engineering and Maintenance Cycle**

A planned replacement of the 1985 vintage high density tape recorder (HDTR) was undertaken during this maintenance cycle. Following environmental testing a thermal control system was integrated into the new HDTR to allow operations at the ER-2 aircraft Q-bay temperatures. Incorporation of this recorder into the AVIRIS sensor expanded the data capacity from 6 to 10 gigabytes or from 600 to 1000 linear kilometers of airborne data acquisition per flight. This new recorder also provided an order of magnitude reduction in the per unit cost of recording media. A spare recorder was acquired to allow timely recovery upon HDTR malfunction.

To improve the signal-to-noise performance of AVIRIS, efforts were made to reduce the noise contribution of the pre-amplifier circuitry in each of the AVIRIS spectrometers. This activity resulted in a reduction in noise from approximately 1.8 to 1.1 digitized numbers. Fixed pattern noise was reduced in AVIRIS through increased shielding of the timing and signal chain cables.

To provide improved AVIRIS absolute radiometric calibration, several modifications were made to the onboard calibrator subsystem. Based on failures in 1991, the AVIRIS onboard calibrator bulb was replaced in 1992 with a bulb of longer life and improved stability. An improved color balancing filter was added to provide a more uniform signal across the four AVIRIS spectrometers. Data from the onboard calibrator are recorded with each AVIRIS flight line and provided with all AVIRIS data distributed to investigators.

During the 1992 maintenance cycle a number of the transmissive elements in the AVIRIS sensor were modified. Spectrometer spherical mirrors were recoated to repair accumulated corrosion damage. Anti-reflection coatings were added to the hatch window, the foreoptics window and the foreoptics termination of the fiber harness. These coatings provided incremental improvements in AVIRIS throughput. At this time, the foreoptics window was tilted to minimize the effects of unwanted internal reflections.

Prior to fiber harness installation in 1992, a failure was noted in the primary fiber connecting the C spectrometer to the foreoptics. The spare infrared fiber previously integrated into the fiber harness was installed. Use of the spare fiber introduced an integer shift of three spatial samples in the C spectrometer data. This shift was compensated in the calibrated AVIRIS data prior to distribution to the investigator. The spare infrared fiber performed nominally throughout the seven month flight season.

Following these modifications to the sensor a calibration experiment was held to characterize and validate the performance of AVIRIS. This inflight calibration experiment was held on the 30th of May 1992 at Rogers Dry Lake, California. Surface and atmosphere measurements were acquired at the time of the AVIRIS overflight. The MODTRAN2 (Berk et al., 1989) radiative transfer code was constrained by these in situ measurements to predict the radiance arriving at the AVIRIS aperture. Agreement between the AVIRIS-measured and MODTRAN2-predicted radiance was better than 7 percent. This close agreement demonstrates that AVIRIS performed as expected based on the sensor improvements achieved in this engineering period.

2.2 1993 Engineering and Maintenance Cycle

Optical elements in the AVIRIS sensor were modified and improved during this time period. A set of new fiber harnesses were procured and one of them installed in AVIRIS. The new fiber material was manufactured to have improved strength and resistance to humidity degradation. Problems with both breakage and humidity damage have been encountered with the previous 1986 vintage fiber material. Improvements were made to the spectrometer fiber optic connector to improve repeatability and stability of spectral alignment. The bi-conic surface in the fiber optic connector was found to be critical to the alignment stability of the spectrometers. A poorly machined connector was shown to account for the change in the spectral calibration of the B spectrometer during the 1992 flight season and has since been replaced.

To further improve energy throughput, new spectral order blocking filters were installed in the AVIRIS spectrometers. These filters provided both higher throughput in the band pass and improved blocking of unwanted energy. The improvement in spectrometer B ranges between 20 and 50 percent. In the C spectrometer a 5 to 30 percent increase in throughput was achieved. Better long wavelength energy blocking was achieved in spectrometer D. Reduction in this background energy decreased the noise in the D spectrometer by as much as 30 percent.

During calibration and characterization of AVIRIS in 1993, a nonlinearity in response was discovered for extremely bright targets. The problem was traced to a set of clamping diodes in the pre-amplifiers that are required to compensate for multiplexer switching transients. These diodes have been adjusted to effectively eliminate the nonlinear effects for the imaging of all terrestrial surfaces.

An additional improvement to the onboard calibrator was implemented in this period. In the past, the onboard calibrator signal was reflected into the optical system from one of two sides of a shutter. The side of the shutter measured was an unpredictable function of the flight line acquisition timing. A 3% difference in the reflectance of the two sides of the shutter was measured in 1992. A change was implemented in 1993 to measure both sides of the shutter at the beginning and end of each flight line. This eliminates any ambiguity in the measured onboard calibrator signal.

During this engineering cycle, a new automated spectral calibration capability was implemented for AVIRIS. This allows direct measurement of the spectral response function of each of the 224 AVIRIS channels. During previous years, typically 10 channels of each spectrometer were manually calibrated and the remainder calibrated through interpolation. With this new automated system, a complete set of spectral calibration data is acquired in about 8 hours.

The current inflight determined performance of AVIRIS is discussed in a companion paper (Green et al., 1993).

2.3 Future Engineering and Maintenance Plans

In order to improve reliability and improve AVIRIS performance, a new set of focal planes are planned to be integrated into AVIRIS prior to the 1995 flight season. These focal planes will be based on current detector and multiplexor technology. Improved reliability is expected as well as a significant decrease in focal plane noise with respect to the current 1986 technology focal planes. As a consequence of the decreased noise anticipated in the new focal planes, the AVIRIS digitization will be increased from 10 to 12 bits to fully encode this improved precision.

Improvements are planned for the onboard calibrator including the introduction of an inflight spectral reference that will be used to fully monitor the inflight spectral calibration of AVIRIS. Direct viewing of the downwelling solar irradiance by the AVIRIS spectrometers is also being considered as an additional inflight calibration source. Higher frequency updates of the navigation data via a direct link to the aircraft inertial navigation system and ground positioning system are also being explored.

3.0 CONCLUSION

Since AVIRIS first became operational in 1989 the AVIRIS system has been undergoing incremental improvements. A number of these improvements have occurred in the sensor component of AVIRIS project. In all cases, the driver for these modifications and upgrades has been the quality of data provided to the science investigators. The important modifications in 1992 and 1993 have been described.

Plans are to continue to improve AVIRIS performance in the future. For the AVIRIS sensor, significant improvements may be achieved in the focal planes, onboard calibrator and platform pointing and position telemetry. By pursuing these improvements and upgrades, AVIRIS will continue to have an important role in providing calibrated imaging spectrometer data to researchers across the earth science disciplines.

4.0 ACKNOWLEDGMENTS

This research was carried out at the Jet Propulsion Laboratory, California Institute of Technology, under contract with the National Aeronautics and Space Administration.

5.0 REFERENCES

- Berk, A, "MODTRAN: A moderate resolution model for LOWTRAN 7", GL-TR-0122, AFGL, Hanscomb AFB, MA, 42 pp., 1989
- Chrien, Thomas G. , "Current Instrument Status of the Airborne Visible/Infrared Imaging Spectrometer (AVIRIS)", Proc. Third AVIRIS Workshop, JPL Publication 91-28, Jet Propulsion Laboratory, Pasadena, CA, pp. 302-313, 1991.
- Chrien, Thomas G., "AVIRIS: Recent Instrument Maintenance, Modifications and 1992 Performance", Proc. Third Annual Airborne Geoscience Workshop, JPL Publication 92-14, Jet Propulsion Laboratory, Pasadena, CA, pp. 78-79, 1992.
- Green, Robert O., "Inflight Calibration of AVIRIS in 1992 and 1993", Proc. Fourth AVIRIS Workshop, JPL Pub. 93-26, Jet Propulsion Laboratory, Pasadena, CA, 1993.
- Porter, W. M., "Evolution of the Airborne Visible/Infrared Imaging Spectrometer (AVIRIS) Flight and Ground Data Processing System", Proceedings of SPIE, Vol. 1298, 1990.

6.0 TABLES

Table 1. AVIRIS Data Characteristics

SPECTRAL	Wavelength range	400 to 2500 nm
	Sampling	≤ 10 nm
	Spectral response (fwhm)	10 nm nominal
RADIOMETRIC	Calibration	≤ 1 nm
	Radiometric range	0 to maximum lambertian
	Sampling	~ 1 dn noise rms
	Absolute calibration	$\leq 7\%$
	Intraflight calibration	$\leq 2\%$
GEOMETRIC	Precision/noise	exceeding NEdL/SNR requirement
	Field of view (FOV)	30 degrees (11 km)
	Instantaneous FOV	1.0 mrad (20 m)
	Calibration	≤ 0.2 mrad
	Flight line length	Up to ten 100 km flight lines

Table 2. AVIRIS Operational Characteristics

SENSOR	Imager type	Whiskbroom scanner	
	Cross track samples	614 elements	
	Scan rate	12 scans/second	
	Dispersion	Four grating spectrometers (A,B,C,D)	
	Detectors	224 detectors (32,64,64,64) Si & InSb	
	Digitization	10 bits (planned 12 bits in 1994)	
	Data rate	17 mbits/second	
	Spectrum rate	7300 spectra/second	
	Data capacity	>10 gigabytes ($>10,000$ km ²)	
	Onboard calibration	Radiometric and spectral	
	Position & pointing	X, Y, Z and roll, pitch, yaw	
	Launches	~ 30 per year	
	DATA FACILITY	Performance monitoring	48 hours from acquisition
		Archiving	One week from acquisition
		Quick-look distribution	One week from acquisition
Calibration		Two weeks from request	
Quality monitoring		Prior to distribution	
Distribution	Two weeks from request		
Engineering analysis	High priority as required		

Table 3. AVIRIS Data Acquisitions	1991	1992	1993-projected
Months of operations	7	8	7
Aircraft bases	5	4	4
Principal investigators supported	52 (Europe)	32	35
Investigator sites flown	137	172	200
Launches	36	34	35
Inflight calibration experiments	3	3	3
Square kilometers flown	115,000	127,300	140,000
Flight scenes	1150	1273	1400
Gigabytes archived	161	178	196
Data scenes calibrated/distributed	498	847	1000
Approximate data turnaround (months)	5	2.5	1

**Comparison of Three Methods for Materials Identification and Mapping
with Imaging Spectroscopy**

Roger N. Clark¹, Gregg Swayze^{1, 3}, Joe Boardman²,
and Fred Kruse^{2, 3}

¹U.S. Geological Survey
MS 964 Box 25046 Federal Ctn., Denver, CO 80225

²Center for the Study of Earth from Space (CSES)
Cooperative Institute for Research in Environmental Sciences (CIRES)
University of Colorado, Boulder, CO 80309-0449

³Department of Geological Sciences, University of Colorado,
Boulder 80309

We are comparing three methods of mapping analysis tools for imaging spectroscopy data. The purpose of this comparison is to understand the advantages and disadvantages of each algorithm so others would be better able to choose the best algorithm or combinations of algorithms for a particular problem. The 3 algorithms are:

- 1) The spectral feature modified least squares mapping algorithm of Clark et al (1990, 1991): programs mbandmap and tricorder;
- 2) The Spectral Angle Mapper Algorithm (Boardman, 1993) found in the CU CSES SIPS package;
- 3) The Expert System of Kruse et al. (1993 and references therein).

The comparison uses a ground-calibrated 1990 AVIRIS scene of 400 by 410 pixels over Cuprite, Nevada. Along with the test data set is a spectral library of 38 minerals. Each algorithm is tested with the same AVIRIS data set and spectral library. The minerals tested are shown in Table 1. Field work has confirmed the presence of many of these minerals in the AVIRIS scene (Swayze et al. 1992).

The spectral feature modified least squares mapping algorithm removes a continuum from spectral features in reference library spectra as well as from each spectrum in an imaging spectrometer data set. The continuum-removed spectra are compared to the continuum-removed reference spectra and a modified least squares fit is performed. The correlation coefficients from the fits are compared and the best fitting material for that spectral feature (or group of features) is selected. The algorithm has an advantage in that the complete shape of a particular absorption band is tested. This tends to reduce the noise sensitivity. It is also insensitive to topographic effects or to errors in the derived reflectance level. The algorithm can also be used as a general shape algorithm (for example, an entire spectrum could be tested

for shape, as well as specific absorption bands). Multiple spectral features in a material are weighted in the proportions of the feature area (under its continuum) in the library reference spectrum.

The Spectral Angle Mapper (SAM) algorithm was designed to measure the spectral similarity between unknown and reference spectra. It is designed to be easy to use and sensitive to unknown illumination differences introduced by topographic effects. It assumes the data have been reduced to apparent reflectance, so the data origin corresponds with a "pure black" spectrum. SAM calculates the angle between the observed and reference spectra, treating them as vectors in n -dimensional space, where n is the number of bands used. This angle value is the arc-cosine of the dot product of the two spectra, after they have been normalized to unit length. Small angles indicate high similarity. By doing this on a pixel-by-pixel basis, with a series of reference spectra, maps of spectral similarity, nearly unaffected by topographic effects, are produced.

The Expert System algorithm has an advantage in that relationships between the features of a particular material can be included in the identification process. This can include a more sophisticated knowledge of spectral features than in the above systems. First a generalized algorithm for extraction of absorption features from digital spectral libraries automatically produces "fact tables" characterizing the individual absorption features. An "expert" (knowledgeable user) then interactively analyzes these library results to determine key absorption features for mineral identification. These key features are in turn used in simple rules to examine each picture element (pixel) in an imaging spectrometer data set. An information data cube is produced that contains measurements of the certainty of occurrence of specific materials in the library at each pixel. An image map is also produced showing the best mineral match for each pixel. The major drawback of this system is that it is particularly sensitive to low signal-to-noise data. It is primarily designed as a "first" cut analysis tool to help assign names to image spectra and map their general spatial distribution.

Results of the comparison will be presented at the workshop.

Table 1
Minerals used in Comparison

Ammonium Smectite	Halloysite
Alunite (K)	Hematite 2wt% + quartz
Natroalunite 65mol% Na	Illite
Natroalunite 80mol% Na	NH ₄ Illite/Smectite
Ammonioalunite	Jarosite
Ammoniojarosite	Kaolinite (wxl)
Analcime	Kaolinite (pxyl)
Buddingtonite	Lepidochrosite
Calcite	Mesolite
Carphosiderite (Na-Jarosite)	Montmorillonite (Ca)
Chlorite (Fe)	Montmorillonite (Na)
Chlorite (Mg)	Muscovite
Diaspore	Natrolite
Dickite	Nontronite
Dolomite	Paragonite
Epidote	Pyrophyllite
Ferrihydrite	Scolecite
Goethite	Silic Rhyolite Tuff
Gypsum	Zoisite

References

- Boardman, J.: Spectral Angle Mapper: A tool for measuring Spectral Similarity. In preparation.
- Clark, R.N., A.J. Gallagher, and G.A. Swayze: Material Absorption Band Depth Mapping of Imaging Spectrometer Data Using a Complete Band Shape Least-Squares Fit with Library Reference Spectra, .I Proceedings of the Second Airborne Visible/Infrared Imaging Spectrometer (AVIRIS) Workshop. JPL Publication 90-54, 176-186, 1990.
- Clark, R.N., G.A. Swayze, A. Gallagher, N. Gorelick, and F. Kruse: Mapping with Imaging Spectrometer Data Using the Complete Band Shape Least-Squares Algorithm Simultaneously Fit to Multiple Spectral Features from Multiple Materials, *Proceedings of the Third Airborne Visible/Infrared Imaging Spectrometer (AVIRIS) Workshop*, JPL Publication 91-28, 2-3, 1991.
- Kruse, F.A., Lefkoff, A.B., and Dietz, J. B., 1993: Expert System-Based Mineral Mapping in Northern Death Valley, California/Nevada using the Airborne Visible/Infrared Imaging Spectrometer (AVIRIS): *Remote Sensing of Environment* Special issue on AVIRIS, May-June, 309-336.
- Swayze, G.A. R.N. Clark, S. Sutley, and A Gallagher, Ground-Truthing AVIRIS Mineral Mapping at Cuprite, Nevada, *Summaries of the Third Annual JPL Airborne Geosciences Workshop, Volume 1: AVIRIS Workshop*. JPL Publication 92-14, 47-49, 1992.



95-32
41010
1 2

Comparison of Methods for Calibrating AVIRIS Data to Ground Reflectance

Roger N. Clark¹, Gregg Swayze¹, Kathy Heidebrecht²,
Alexander F. H. Goetz², and Robert O. Green³

¹U.S. Geological Survey
MS 964 Box 25046 Federal Ctn., Denver, CO 80225

²Center for the Study of Earth from Space (CSES)
Cooperative Institute for Research in Environmental Sciences (CIRES)
University of Colorado, Boulder, CO 80309-0449

³Jet Propulsion Laboratory, California Institute of Technology
Pasadena, California 91109-8099

We are comparing three basic methods of calibrating AVIRIS data to ground reflectance:

1) Atmospheric radiative transfer models with the solar flux can be used to calibrate AVIRIS radiance data. Specific methods include the University of Colorado CSES ARP and ATREM algorithms.

2) Robert Green's modified MODTRAN and AVIRIS radiance model. This method is similar to #1 but differs in that the solar radiance is bypassed (so any errors in the solar flux are canceled too).

3) Ground calibration using known sites in the AVIRIS scene.

We are using 1992 AVIRIS data over Cuprite, Nevada, and Blackhawk Island, Wisconsin, as our test scenes. Both these sites have extensive field measurements. The Cuprite site had a very clear atmosphere, thus path radiance was dominated by Rayleigh scattering with little or no flux beyond 1 μm . The Blackhawk site has more aerosols, with significant path radiance flux beyond 2 μm .

We found that models that rely on the solar flux tend to have serious errors. This led to a modification of the CSES ATREM algorithm in 1993 to correct empirically for such problems. To date, the published solar flux spectra have disagreements of greater than $\pm 7\%$ at AVIRIS 1992 resolution and sampling. Unfortunately, these disagreements can impart spectral features greater than 10% in calibrated spectra. Further, it is not clear which, if any, of the published solar flux measurements is correct. It is even possible that some of the spectral features in the solar spectrum are variable.

Green's method uses the AVIRIS radiance along with radiance measured over Roger's Dry Lake for each season, and thus cancels the solar radiance from the calibration. This calibration is dependent on an accurate reflectance of the Roger's Dry Lake surface, a problem limited by the field spectrometer technology available. For the 1993 calibration, we have tried to improve this step with laboratory measurements of Roger's Dry Lake samples measured at the USGS

Denver Spectroscopy Laboratory in conjunction with field measurements (results not yet available).

Ground calibrated AVIRIS data proved to be the best calibration locally. In this method, one or more large uniform calibration sites have their reflectance measured in the field and/or on a laboratory spectrometer, and the corresponding spectra in the AVIRIS scene over the site(s) are used to derive a set of path radiance offsets and multipliers. The disadvantages of this method are that it requires very careful field work to find scenes with large spectrally bland and uniform areas, and it applies to only one elevation level. Our experience is that this calibration requires about one person-month to complete. For elevations in the scene higher than the calibration site, there are residual positive atmospheric features and for elevations lower there are residual atmospheric absorption bands. Outside the main atmospheric bands (0.76- μm oxygen, 0.95- μm water, 1.15- μm water, 1.38- μm water, 1.9- μm water, and 2- μm CO₂ absorptions), the data are calibrated very well.

A remaining problem with the radiative transfer models is with the path radiance correction. Neither algorithm (#1, #2 above) correctly predicted the aerosol path radiance over Blackhawk Island. These models assume Rayleigh scattering with little or no aerosols and thus little or no path radiance flux at wavelengths beyond 1 μm .

It appears that the best possible AVIRIS calibration would be a combination of a radiative transfer correction followed by a ground calibration. This combined method would perform a basic correction of atmospheric absorptions at all elevations, and remove Rayleigh scattering. The ground calibration would correct for fine details, such as errors in solar flux or the AVIRIS radiance calibration, and could better correct for unusual path radiance due to aerosols.

The U. S. Geological Survey, Digital Spectral Reflectance Library:
Version 1: 0.2 to 3.0 μm

41011

Roger N. Clark, Gregg A. Swayze, Trude V.V. King, Andrea J. Gallagher,
and Wendy M. Calvin*

U.S. Geological Survey
MS 964 Box 25046 Federal Ctn., Denver, CO 80225

*U.S. Geological Survey, Branch of Astrogeology
2255 N. Gemini Dr., Flagstaff, AZ 86001

We have developed a digital reflectance spectral library, with management and spectral analysis software. The library includes 500 spectra of 447 samples (some samples include a series of grain sizes) measured from approximately 0.2 to 3.0 μm . The spectral resolution (Full Width Half Maximum) of the reflectance data is ≤ 4 nm in the visible (0.2-0.8 μm) and ≤ 10 nm in the NIR (0.8-2.35 μm). All spectra were corrected to absolute reflectance using an NBS Halon standard. Library management software lets users search on parameters (e.g. chemical formulae, chemical analyses, purity of samples, mineral groups, etc.) as well as spectral features.

Minerals from sulfide, oxide, hydroxide, halide, carbonate, nitrate, borate, phosphate, and silicate groups are represented. X-Ray and chemical analyses are tabulated for many of the entries, and all samples have been evaluated for spectral purity. The library also contains end and intermediate members for the olivine, garnet, scapolite, montmorillonite, muscovite, jarosite, and alunite solid-solution series. We have included representative spectra of H_2O ice, kerogen, ammonium-bearing minerals, rare-earth oxides, desert varnish coatings, kaolinite crystallinity series, kaolinite-smectite series, zeolite series, and an extensive evaporite series. Because of the importance of vegetation to climate-change studies we have include 17 spectra of tree leaves, bushes, and grasses.

The library and software will be available as a U.S.G.S. open file report. PC user software is available to convert the binary data to ascii files (a separate U.S.G.S. open file report). Additionally, an ftp binary file will be on line at the U.S.G.S. in Denver. Users may build customized libraries for their own instruments using the library software. We are currently extending spectral coverage to 150 μm and will make this library available on CD-ROM.



10-40
4/10/12

APPLICATION OF A TWO-STREAM RADIATIVE TRANSFER MODEL
FOR LEAF LIGNIN AND CELLULOSE CONCENTRATIONS
FROM SPECTRAL REFLECTANCE MEASUREMENTS (PART 1)

James E. Conel, Jeannette van den Bosch, and Cindy I. Grove

Jet Propulsion Laboratory, California Institute of Technology
Pasadena, California

1. Introduction. Lignin and nitrogen contents of leaves constitute the primary rate-limiting parameters for the decomposition of forest litter, and are determinants of nutrient- and carbon-cycling rates in forest ecosystems (Melillo et al., 1982). Wessman et al. (1988a) developed empirical multivariate relationships between forest canopy lignin amount and the (first-difference) AIS spectral response in three bands spread over the wavelength interval 1256-1555 nm. Wessman et al. (1988b) and McLellan et al. (1991) developed similar regression relationships from laboratory reflectance measurements on dried samples prepared in a standard fashion. They used four to six infrared bands for analysis of nitrogen, lignin and cellulose content of foliage in forest and prairie species. In the present article (Parts 1 and 2) the feasibility of compositional determinations is explored using positions of composite absorption bands that originate from mixtures of lignin, cellulose, and possibly other chemical constituents in the spectral reflectance of green leaves. To carry out this program, we employ full-spectral-resolution single-leaf diffuse reflectance measurements made with a laboratory spectrometer and integrating sphere. The leaf and other chemical reflectance data compiled by Elvidge (1990) have also been utilized extensively.

2. Model. The spectra of fresh leaves contain strong liquid water absorptions that may mask nearly completely the spectral signatures of other leaf chemical constituents (e.g., Elvidge, 1990). A background liquid leaf water reflectance spectrum is required to remove the effects of liquid water. Previously, such a background spectrum was estimated using mixtures of glass beads and liquid water (Goetz et al. 1990). In the present work on the other hand, the so-called Kubelka-Munk (KM) theory of radiative transfer (Wendlandt and Hecht, 1966) was used to estimate the liquid water spectrum from the leaf diffuse spectral reflectance itself. In a first approximation single leaves are assumed to consist of distinct but well-mixed liquid water and dry components each characterized by intrinsic absorption (k_w , k_d) and scattering (s_w , s_d) functions (hereafter simply intrinsic functions). The dry components are in turn assumed to consist of well-mixed lignin, cellulose, starch, protein, and other organic compounds (see Elvidge, 1990, for representative visible and near-infrared spectra). In the KM theory, which was originally developed to calculate the reflectance of paint films, independent as well as purely backward scattering (van de Hulst, 1980) are assumed by all constituents. These assumptions are almost certainly violated to one extent or another in leaves. Comparing the k- and s-functions of KM theory with parameters of two-stream atmospheric models (see, for example, Coakley and Chylek, 1975), shows k is identified with particle absorption, given by $1 - \omega_0$, where ω_0 is the single scattering albedo, and s with the scattered fraction $\omega_0\beta$, where β is the average forward scatter for isotopically incident radiation (Wiscombe and Grams, 1976).

3. Calculation of k- and s-functions. We develop mixing laws that comprise relationships between bulk leaf scattering (S) and absorption (K) functions

and the intrinsic functions of assumed individual components; the bulk functions are simple linear sums of the intrinsic functions weighted by constituent concentrations (c_w , c_d). For a simple two-component system, the intrinsic functions are isolated individually by use of reflectance (R) and transmittance (T) measurements on single leaves, both wet and desiccated, together with theoretical relationships for R and T for single uniform layers from KM theory (Wendlandt and Hecht, 1966, p. 60). Allen and Richardson (1968) first used single leaf R and T data to calculate k- and s-coefficients for cotton leaves. The intrinsic functions derived in this way for *Liquidambar styraciflua* (sweetgum) are given in Figure 1.

4. Leaf water reflectance. Given k_w and s_w of Figure 1, the reflectance $R_{w\infty}$ of a semi-infinite body of "pure" liquid leaf water was calculated from the so-called KM remission function (Kortum, 1969, p.180, discusses the remission function). A light path through a stack of 5 or 6 leaves approximates an infinite thickness condition at all wavelengths between 400-2500 nm, since no change in reflectance occurs with addition of further layers. The resulting $R_{w\infty}$ is shown in Figure 2. The function represented has been smoothed once by a three-point "hanning" filter (Blackman and Tukey, 1958) to suppress fluctuations in the calculated k- and s-functions from noise in the reflectance data themselves. The curve of Figure 2 has been taken arbitrarily to represent a generic background water reflectance for derivation of dry constituent spectral residuals from the optically infinite thickness green leaf diffuse reflectance. An example comparing $R_{w\infty}$ with the equivalent semi-infinite reflectance for sweetgum, calculated from K and S via the remission function, is shown in Figure 3. Both curves have been translated to zero reflectance at 1452 nm, and the water reflectance was adjusted by a single scale factor to achieve the match shown. Similar adjustments of origin and scale in $R_{w\infty}$ were required in calculation of residuals for foliage of other species, as described next.

5. Reflectance residuals. We calculated fractional residual reflectances for sweetgum, sycamore (*Platanus racemosa*), pinyon pine (*Pinus monophylla*) and bigberry manzanita (*Arctostaphylos glauca*) using the generic water reflectance curve. These results are given in Figure 4 for the spectral region 1400-1900 nm. The fractional residual reflectance is defined as $1 - (R_{w\infty} - R_{i\infty})/R_{w\infty}$ where $R_{i\infty}$ is the measured (or calculated) reflectance for infinite thickness of species i. The diffuse reflectance data for sycamore, pinyon pine, and manzanita were taken from Elvidge (1990). These examples are distinguished from one another by apparent systematic displacements of reflectance minima from one species to the next and by the presence of both major and minor structures in the pinyon and manzanita residuals that are not shared by the other examples. The noise-equivalent reflectance variation ($ne\Delta R$) in these data was estimated numerically by calculating residuals from a second-degree polynomial fit to a smooth piece of the raw sweetgum reflectance (1500-1600 nm, 24 points) with a resulting rss error of 0.0000016 in reflectance units and an average fractional uncertainty of 0.000001.

6. Comparison of desiccated leaf and residual spectra. From the derived k_d and s_d values given in Figure 1 we also calculated the expected reflectance $R_{d\infty}$ for desiccated sweetgum via the remission function, and compared structures in that reflectance with structures present in the (presumed liquid water-free) residual spectrum for sweetgum in Figure 3. This comparison is made in Figure 5. Apart from positions of minor features these curves do not resemble one another; the presence of important (lignin + cellulose + other) absorptions remains masked in the extracted residual spectrum. Features in the calculated sweetgum spectrum $R_{d\infty}$ are, on the other hand, present in the pinyon and manzanita residuals in Figure 4.

7. **Acknowledgments.** We thank Chris Elvidge of Desert Research Institute, Reno, Nevada, for use of his reflectance data. Conversations with Dr. Barry Prigge, Botany Dept., UCLA, are also gratefully acknowledged. This article presents results of research at Jet Propulsion Laboratory, California Institute of Technology, under contract with NASA.

8. References.

- Blackman R.B. and J.W. Tukey, 1958, *The Measurement of Power Spectra*, Dover Publications, Inc., New York, 190 pp.
- Coakley, J. and P. Chylek, 1975, "The Two-Stream Approximation in Radiative Transfer: Including the Angle of the Incident Radiation," *J. Atmos. Sci.*, **32**, pp. 409-418.
- McLellan, T.M., J.D. Aber, M.E. Martin, J.M. Melillo and K.J. Nadelhoffer, 1991, "Determination of Nitrogen, Lignin, and Cellulose Content of Decomposing Leaf Material by Near Infrared Reflectance Spectroscopy," *Can. J. For. Res.*, **21**(11), pp. 1684-1688.
- Melillo, J.M., J.D. Aber and J.F. Muratore, 1982, "Nitrogen and Lignin Control of Hardwood Leaf Litter Decomposition Dynamics," *Ecology*, **63**, pp. 621-626.
- van de Hulst, H.C., 1980, *Multiple Light Scattering*, vol. 2, Academic Press, New York, pp. 700-703.
- Wendlandt, W.W. and H.G. Hecht, 1966, *Reflectance Spectroscopy*, Wiley-Interscience, New York, 298 pp.
- Wessman, C.A., J.D. Aber, D.L. Peterson and J.M. Melillo, 1988a, "Remote Sensing of Canopy Chemistry and Nitrogen Cycling in Temperate Forest Ecosystems," *Nature*, **335**, pp. 154-156.
- Wessman, C.A., J.D. Aber, D.L. Peterson and J.M. Melillo, 1988b, "Foliar Analysis Using Near Infrared Reflectance Spectroscopy," *Can. J. For. Res.*, **18**, pp. 6-11.
- Wiscombe, W.J. and G.W. Grams, 1976, "The Backscattered Fraction in Two-Stream Approximations," *J. Atmos. Sci.*, **33**, pp. 2440-2451.

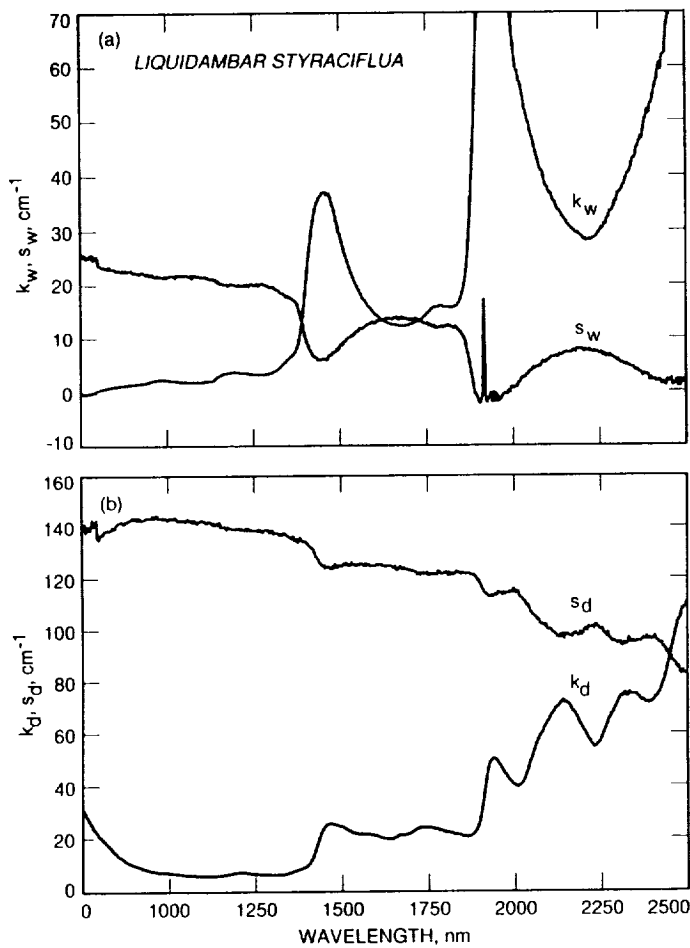


Figure 1. *L. styraciflua*. (a) intrinsic functions for leaf liquid water component. (b) intrinsic functions for bulk desiccated leaf components.

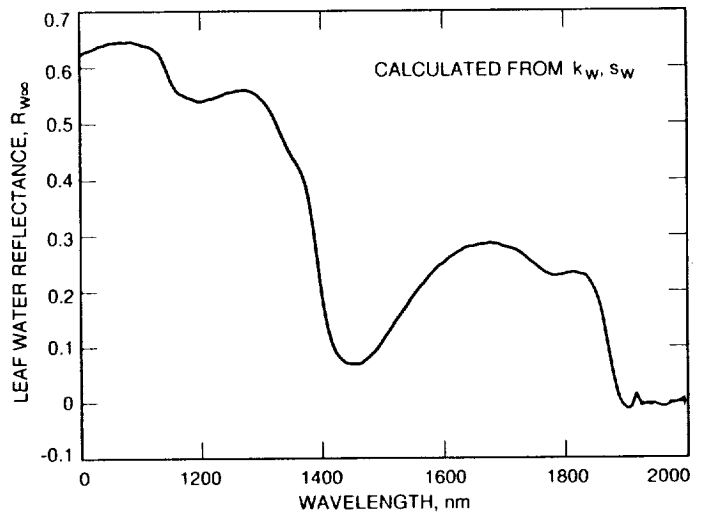


Figure 2. *L. styraciflua* leaf liquid water reflectance calculated from k_w and s_w .

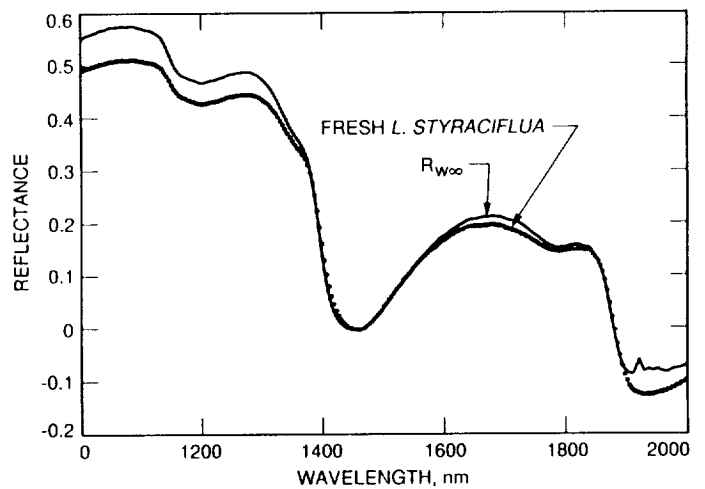


Figure 3. Liquid water reflectance $R_{w\infty}$ compared to the infinite thickness reflectance of *L. Styraciflua*.

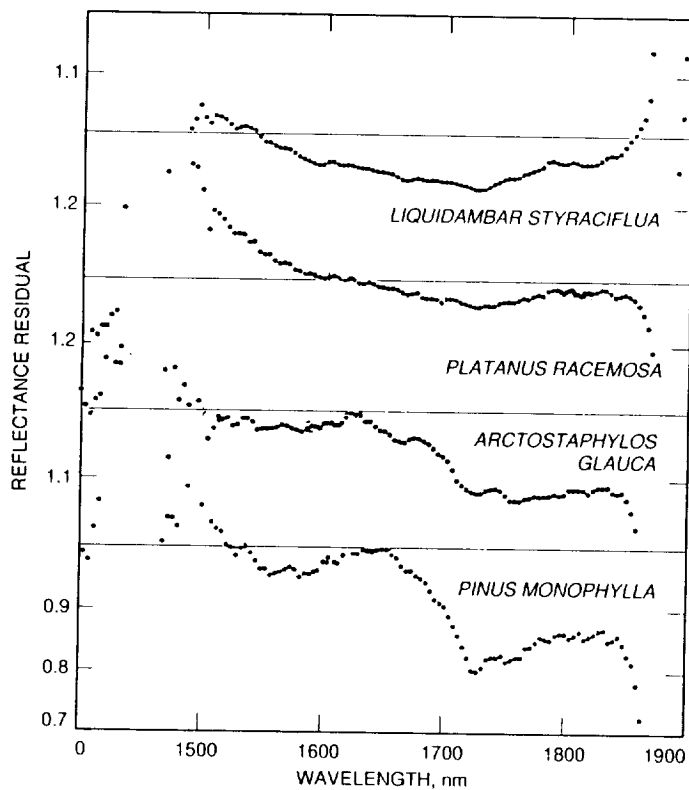


Figure 4. Reflectance residuals for fresh leaves and needles of four plant species.

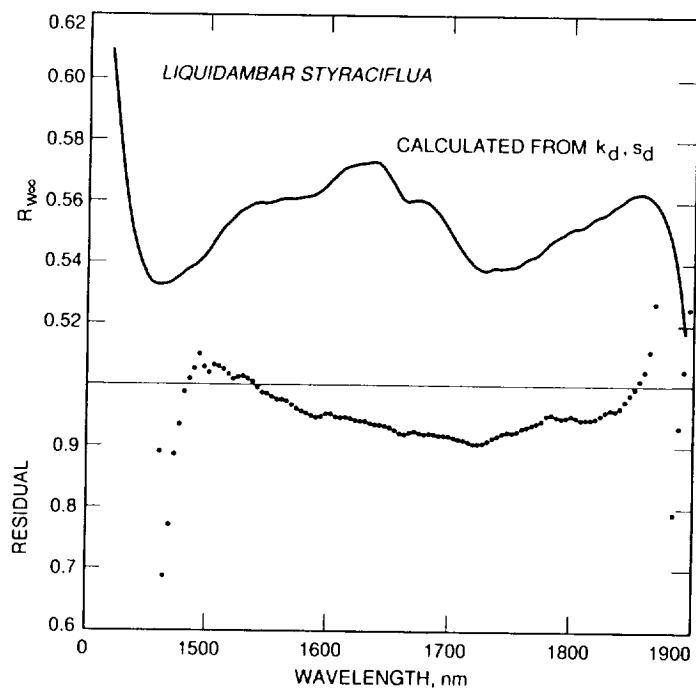


Figure 5. Comparison of the calculated desiccated leaf reflectance for *L. styraciflua* with its fresh leaf reflectance residual.



93-13
41013
11

**APPLICATION OF A TWO-STREAM RADIATIVE TRANSFER MODEL FOR
LEAF LIGNIN AND CELLULOSE CONCENTRATIONS FROM SPECTRAL
REFLECTANCE MEASUREMENTS (PART 2)**

James E. Conel, Jeannette van den Bosch, and Cindy I. Grove

Jet Propulsion Laboratory, California Institute of Technology
Pasadena, California

1. Interpretation of desiccated leaf spectra. Continuing the work described in Part 1, we next sought to understand structures in the dry extracted and derived spectra using calculated reflectances of hypothetical simple two-component mixtures. The reflectances and mixing models used, including the model employed to derive $R_{w\infty}$, ultimately require validation; this has not yet been possible beyond certain qualitative comparisons described here.

In Figure 1 the calculated spectrum $R_{d\infty}$ is compared with lignin and cellulose reflectances (from Elvidge, 1990). A simple interpretation of band position in the desiccated leaf spectrum appears possible in terms of these two end members. We examined this more closely by calculating reflectances of cellulose-lignin and other mixtures and comparing band positions between the hypothetical mixes and $R_{d\infty}$.

Bulk reflectance relationships based on composite scattering and absorption functions were developed from the KM theory for artificial mixtures of dry constituents (and liquid water with dry constituents described here). Many idealized configurations of constituents in single leaves, each individually described by the KM reflectance and transmittance formulae, seem possible. Each has its own macroscopic mixing formula. Some simple possibilities are: (1) single layers comprised of well-mixed pure components, (2) multiple stacked uniform layers of pure end members, and (3) side-by-side compartments of pure end members arranged in single layers. Here we confine attention to (1), lacking a definite basis to pursue another option. Since intrinsic functions of representative major (or minor) pure chemical end members of leaves have not yet been obtained, the development of mixing relations must proceed approximately, in the present case as follows. For two components {1,2} the ratio K_{12}/S_{12}

$$\frac{K_{12}}{S_{12}} = \frac{c_1 \frac{k_1}{s_1} + c_2 \frac{k_2}{s_2} \frac{s_2}{s_1}}{c_1 + c_2 \frac{s_2}{s_1}} \quad (1)$$

of a mixture is $c_1 + c_2 = 1$. Except for the ratio s_2/s_1 , the values of the component k/s -ratios are known from the remission function if the spectral diffuse reflectance $R_{j\infty}$ for each component j is known. We will calculate an approximate effective composite ratio K_{12}/S_{12} for the {1,2} mixture by setting $s_2/s_1 = 1$ for all wavelengths, and take the diffuse reflectances of leaf chemical constituents, a number of which have been measured by Elvidge (1990), to estimate k/s -ratios of end-members. In so doing effects of possible impurities, nonuniformity in packing, particle size, and finite sample thickness on reflectances of assumed end members are ignored. The reflectance $R_{12\infty}$ of a two-component mix is calculated from Figure 2 and illustrates application of the model represented by Equation (2) to a mixture of lignin and cellulose, parameterized as the fraction of cellulose (gm/gm) in the mix. Determination of composition in this

$$R_{12\infty} = \frac{1 - \sqrt{K_{12}/(K_{12} + 2S_{12})}}{1 + \sqrt{K_{12}/(K_{12} + 2S_{12})}} \quad (2)$$

simple dry system might be made from measurement of band position; best resolved and clearest to interpret (although unobservable in the residual spectra from green leaves) is that between 1444 and 1484 nm. This band (reflectance minimum) position is a non-linear function of cellulose fraction f_c , given accurately by $\lambda(f_c) = 1456 + 97.9f_c - 119f_c^2 + 54f_c^3 - 4.5f_c^4$, and is very insensitive to changes in lignin concentration for $.5 \leq f_c \leq 1.0$. For example, suppose the spectral sampling interval $\Delta\lambda$ is that of AVIRIS, 10 nm, and that three perfect spectral band determinations are possible at 1484 and 1474 and 1464 nm. The minimum resolvable difference in lignin concentration Δf_c is approximately 0.75 between the first pair of these and about 0.10 between the second pair. A similar relationship, spectrally less well defined, prevails for the complex of bands between 1650 and 1850 nm.

We return now to interpretation of band positions of $R_{d\infty}$ in Figure 1. From the regression formula for $\lambda(f_c)$ a reflectance minimum at 1460 nm implies a lignin concentration in the two-component dry mix of 94%, and a similar abundance from the band near 1775 nm. This exceeds by far the expected lignin abundance in plant materials of 10 - 35% dry weight (Crawford, 1981).

Other chemical constituents in addition to lignin and cellulose make spectral contributions to the desiccated foliar reflectance, and will alter by dilution the relative abundances of lignin and cellulose present. The nature of the spectral contributions so introduced will be described qualitatively using hypothetical two-component systems, cellulose-starch and cellulose-protein (D-ribulose 1-5-diphosphate carboxylase), illustrated in Figures 3 and 4. Combinations with other plant chemical constituents might be worked out from spectral data given by Elvidge (1990). The admixing of starch with cellulose displaces the 1485-nm cellulose band to shorter wavelengths, similar to lignin. The 1775-nm band position is largely unaffected. The admixing of protein with cellulose produces displacements opposite (but of comparatively small magnitude) to those of both starch and lignin at 1485 nm and to shorter wavelengths at 1775 nm, also similar to that of lignin. Thus both protein and starch mimic spectrally the presence of lignin in mixes with cellulose, especially at 1775 nm. The isolation of lignin concentration from band position alone without knowledge of other end member concentrations thus seems problematical.

2. Mixing of desiccated and liquid water components. Mixing relationships employed in the present application of KM theory together with spectral reflectances of mixtures based thereon have been worked out to isolate signatures of supposed desiccated leaf components and to aid interpretation of spectral signatures of derived reflectance residuals. The theory applied to leaf reflectance awaits detailed experimental validation but offers another set of relationships that suggests its usefulness. We used the intrinsic k- and s-functions of Figure 1 in Part 1 of this article together with Equations (1) and (2) to calculate for sweetgum the spectral reflectance of intermediate mixtures of wet and dry components. These calculations are illustrated in Figure 5. A comparison with single leaf reflectance data as a function of relative water content given by Hunt and Rock (1989) is suggestive.

3. Reflectance retrieval from AVIRIS. The previous analysis leading to plots of residuals given in Figure 4 in Part 1 was based on diffuse spectral reflectance

measurements made under idealized conditions with a laboratory spectrometer. The largest spectral variations in these residuals amount to approximately 2 % in the 1700-nm region. Reflectance variations are also present below this level. Under field conditions, using measurements of the upwelling radiance at AVIRIS, an atmospheric model is ordinarily required to retrieve an effective surface (Lambertian) reflectance, unless ground targets can be used (Elvidge, 1988). Noise arising from spatial fluctuations or uncertainties in atmospheric properties and from AVIRIS will contribute uncertainty to the reflectance values so derived. We carried out numerical experiments with the LOWTRAN 7 (Kneizys et al., 1983) radiative transfer model to estimate uncertainties due to atmospheric variations. It proves advantageous to recalibrate AVIRIS in-flight using local surface targets to eliminate channel-to-channel variations in radiance that are thought to originate from changes in the radiometric calibration coefficients between laboratory and in-flight conditions.

For homogeneous, plane-parallel atmospheric conditions over uniform ground of Lambertian surface reflectance ρ_s , the radiance at AVIRIS is represented approximately as

$$L(\mu, \mu_0, \tau) = \frac{F_{\odot}}{4\mu} \left[S(\mu, \mu_0, \tau) + \frac{4\rho_s}{1 - \rho_s \bar{s}} \mu \mu_0 T(\mu, \mu_0, \tau) \right] \quad (3)$$

In Equation (3) πF_{\odot} is the solar irradiance, $S(\mu, \mu_0, \tau)$ is the atmospheric scattering function, $T(\mu, \mu_0, \tau)$ is the two-way diffuse plus direct atmospheric transmittance, \bar{s} is the hemispherical backscatter function, μ and μ_0 are cosines of the zenith angles of viewing and solar incidence directions respectively, and τ is optical depth. Spectral dependence of the atmospheric and surface quantities is implied. An in-flight calibration experiment redefines the radiometric calibration in terms of in-flight coefficients Φ^* given by

$$\Phi^* = \frac{(L_m)_c}{(DN - DN_0)_c} \quad (4)$$

where DN and DN_0 represent instrument and dark current response for the conditions of calibration, and $(L_m)_c$ is the radiance at AVIRIS obtained from a radiative transfer model (LOWTRAN and/or MODTRAN) using measured atmospheric conditions. $(L_m)_c$ is given approximately by

$$(L_m)_c = \left[\frac{S_c}{4\mu_c} + (\mu_0)_c T_c R_c + (\mu_0)_c T_c \bar{s}_c R_c^2 \right] F_{\odot} \quad (5)$$

With the in-flight calibration factors, the ground reflectance R_g is

$$R_g = -\frac{A}{B} - \bar{s} \left(\frac{A}{B} \right)^2 + \left[1 + 2\bar{s} \left(\frac{A}{B} \right) \right] \frac{\Phi^*}{B} (DN - DN_0) - \bar{s} \frac{\Phi^{*2}}{B^2} (DN - DN_0)^2 \quad (6)$$

where $(DN - DN_0)$ represents the dark-current corrected in-flight instrument response, and

$$A = \frac{S F_{\odot}}{4\mu}, \quad B = \mu_0 T F_{\odot}$$

The expression for R_g , Equation (6), is independent of the solar irradiance, but use of the in-flight calibration coefficients Φ^* has introduced additional variables pertaining to atmospheric conditions during calibration and also the calibration target reflectance R_c . We applied standard error propagation formulas to Equation (6) to evaluate a fractional uncertainty σ_{R_g}/R_g from fluctuations in all the atmospheric parameters (taken equal for both calibration and observation experiments) and from the AVIRIS response parameterized as the signal/noise ratio. The LOWTRAN model evaluated was midlatitude summer, rural aerosols, surface meteorological range 25 km, surface reflectance 0.50, and solar zenith angle $22^\circ.179$. The calculated uncertainty as a function of AVIRIS signal/noise ratio at 1700 nm with prescribed atmospheric uncertainties, written collectively as σ_a/a to represent σ_S/S , etc., is shown in Figure 6. Values of σ_{R_g}/R_g less than a few percent are achieved only for uniform atmospheric conditions ($\sigma_a/a < .01$) and high signal/noise ratios (> 100).

4. Summary. We used the Kubelka-Munk theory of diffuse spectral reflectance in layers to analyze influences of multiple chemical components in leaves. As opposed to empirical approaches to estimation of plant chemistry, the full spectral resolution of laboratory reflectance data was retained in an attempt to estimate lignin or other constituent concentrations from spectral band positions. A leaf water reflectance spectrum was devised from theoretical mixing rules, reflectance observations, and calculations from theory of intrinsic k- and s-functions. Residual reflectance bands were then isolated from spectra of fresh green leaves. These proved hard to interpret for composition in terms of simple two component mixtures such as lignin and cellulose. We next investigated spectral and dilution influences of other possible components (starch, protein). These components, among others, added to cellulose in hypothetical mixtures, produce band displacements similar to lignin, but will disguise by dilution the actual abundance of lignin present in a multicomponent system. This renders interpretation of band positions problematical. Knowledge of end-members and their spectra, and a more elaborate mixture analysis procedure may be called for (see, for example, Kortum, 1969, p. 303). Good observational atmospheric and instrumental conditions and knowledge thereof are required for retrieval of expected subtle reflectance variations present in spectra of green vegetation.

5. Acknowledgments. We thank Chris Elvidge of Desert Research Institute, Reno, Nevada, for use of his reflectance data. Conversations with Dr. Barry Prigge, Botany Dept., UCLA, are also gratefully acknowledged. This article presents results of research at Jet Propulsion Laboratory, California Institute of Technology, under contract with NASA.

6. References.

- Allen, W.A. and A.J. Richardson, 1968, "Interaction of Light with a Plant Canopy," *J. Opt. Soc. Am.*, **58**(8), pp. 1023-1028.
- Blackman R.B. and J.W. Tukey, 1958, *The Measurement of Power Spectra*, Dover Publications, Inc., New York, 190 pp.
- Coakley, J. and P. Chylek, 1975, "The Two-Stream Approximation in Radiative Transfer: Including the Angle of the Incident Radiation," *J. Atmos. Sci.*, **32**, pp. 409-418.
- Crawford, R.L., 1981, *Lignin Biodegradation and Transformation*, Wiley-Interscience, New York.
- Elvidge, C.A., 1988, "Vegetation Reflectance Features in AVIRIS Data," *Proceedings of the International Symposium on Remote Sensing of Environment, Ann Arbor*,

- Michigan, 26-30 October*, Environmental Research Institute of Michigan, pp. 721-733.
- Elvidge, C.A., 1990, "Visible and Near Infrared Reflectance Characteristics of Dry Plant Materials," *Int. J. Remote Sensing*, **11**(10), pp. 1775-1795.
- Goetz, A.F.H., B.C. Gao, C.A. Wessman, and W.D. Bowman, 1990, "Estimation of Biochemical Constituents from Fresh, Green Leaves by Spectrum Matching Techniques," *IGARSS 1990*, May 20-24, University of Maryland.
- Hunt, E.R., Jr. and B.N. Rock, 1989, "Detection of Changes in Leaf Water Content Using Near- and Middle-Infrared Reflectances," *Remote Sens. Environ.*, **30**, pp. 43-54.
- Kortum, G., 1969, *Reflectance Spectroscopy*, Springer-Verlag New York Inc., New York, 366 pp.
- Kneizys, F.X., E.P. Shettle, L.W. Abrew, J.H. Chetwynd, G.P. Anderson, W.O. Gallery, J.E.A. Selby, and S.A. Clough, 1988, "Users Guide to LOWTRAN 7," Environmental Research Paper No. 1010, **AFGL-TR-88-0177**, Air Force Geophysics Laboratory, Hanscomb AFB, MA, 137 pp.
- McLellan, T.M., J.D. Aber, M.E. Martin, J.M. Melillo and K.J. Nadelhoffer, 1991, "Determination of Nitrogen, Lignin, and Cellulose Content of Decomposing Leaf Material by Near Infrared Reflectance Spectroscopy," *Can. J. For. Res.*, **21**(11), pp. 1684-1688.
- Melillo, J.M., J.D. Aber and J.F. Muratore, 1982, "Nitrogen and Lignin Control of Hardwood Leaf Litter Decomposition Dynamics," *Ecology*, **63**, pp. 621-626.
- van de Hulst, H.C., 1980, *Multiple Light Scattering*, vol. 2, Academic Press, New York, pp 700-703.
- Wendlandt, W.W. and H.G. Hecht, 1966, *Reflectance Spectroscopy*, Wiley-Interscience, New York, 298 pp.
- Wessman, C.A., J.D. Aber, D.L. Peterson and J.M. Melillo, 1988a, "Remote Sensing of Canopy Chemistry and Nitrogen Cycling in Temperate Forest Ecosystems," *Nature*, **335**, pp. 154-156.
- Wessman, C.A., J.D. Aber, D.L. Peterson and J.M. Melillo, 1988b, "Foliar Analysis Using Near Infrared Reflectance Spectroscopy," *Can. J. For. Res.*, **18**, pp. 6-11.
- Wiscombe, W.J. and G.W. Grams, 1976, "The Backscattered Fraction in Two-Stream Approximations," *J. Atmos. Sci.*, **33**, pp. 2440-2451.

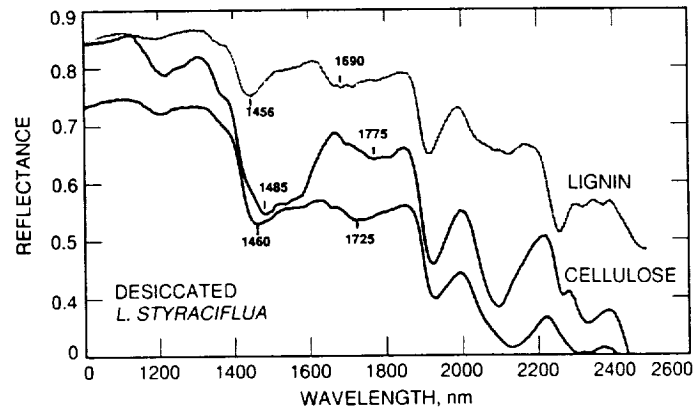


Figure 1. Reflectances of lignin, cellulose, and desiccated *L. styraciflua*.

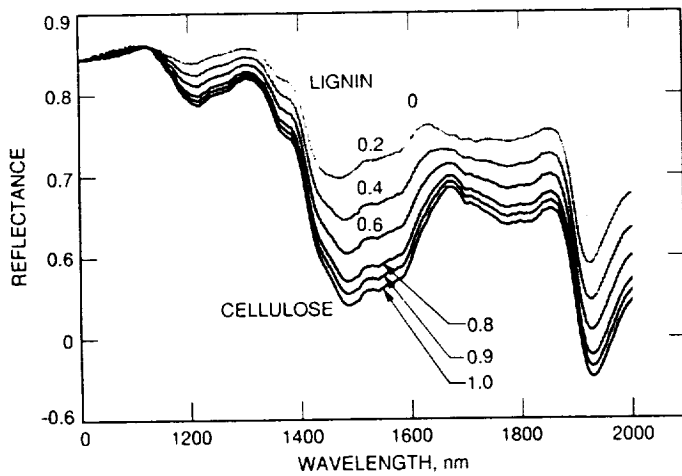


Figure 2. Reflectances of hypothetical mixes of cellulose and lignin. Curves are for cellulose fractions of 1.0 (pure cellulose), 0.9, 0.8, 0.6, 0.4, 0.2, and 0.0 (pure lignin).

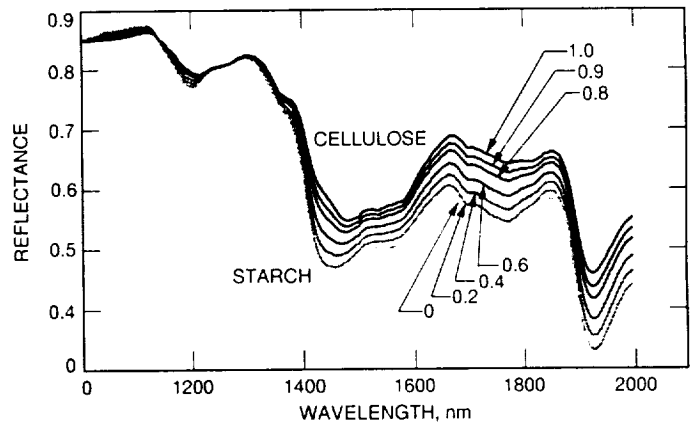


Figure 3. Reflectances of hypothetical mixes of cellulose and starch. See caption Figure 2 for curve assignments.

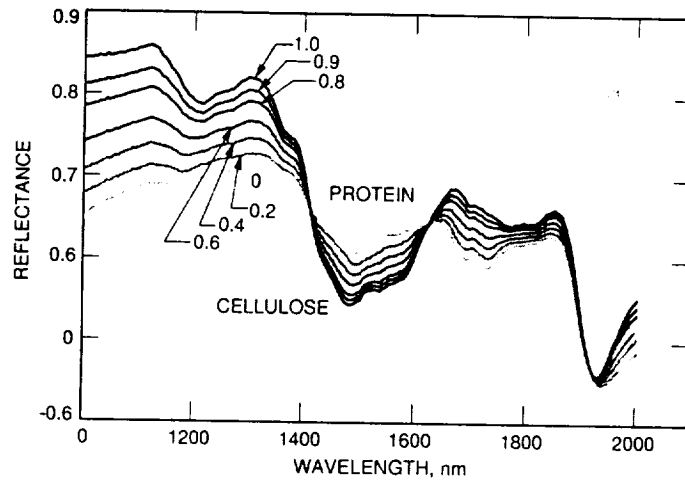


Figure 4. Reflectances of hypothetical mixes of cellulose and protein. See caption Figure 2 for curve assignments.

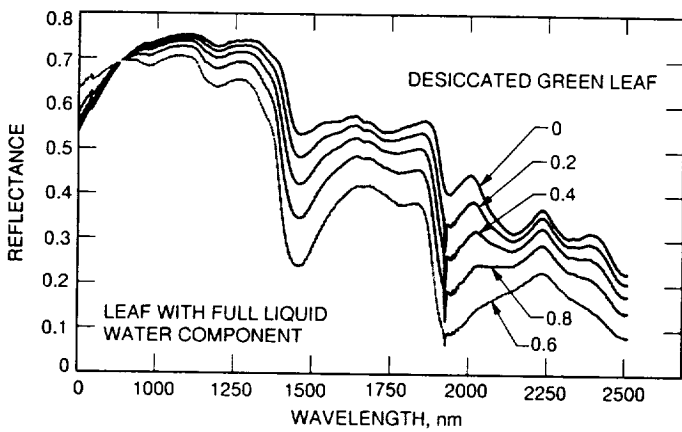


Figure 5. Reflectances of hypothetical combinations of desiccated *L. styraciflua* and leaf liquid water components.

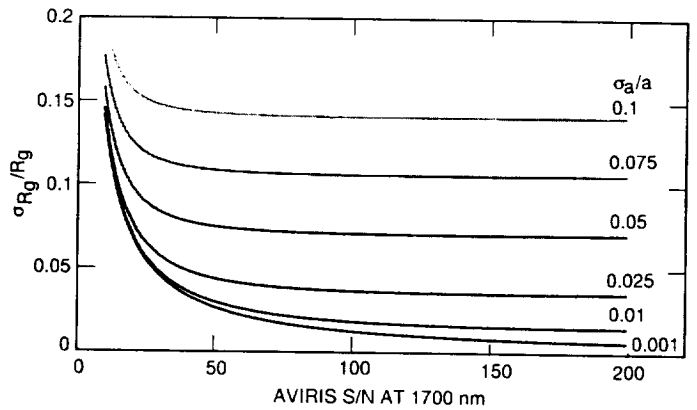


Figure 6. Calculated uncertainties in retrieved surface reflectance for AVIRIS S/N and atmospheric variability.



274-52
111014
11

DISCRIMINATION OF POORLY EXPOSED LITHOLOGIES IN AVIRIS DATA

William H. Farrand and Joseph C. Harsanyi

HYDICE Project Office
Naval Research Laboratory, Code 9120
Washington, DC 20375

1. INTRODUCTION

One of the advantages afforded by imaging spectrometers such as AVIRIS is the capability to detect target materials at a sub-pixel scale. This paper presents several examples of the identification of poorly exposed geologic materials- materials which are either subpixel in scale or which, while having some surface expression over several pixels, are partially covered by vegetation or other materials.

Sabol et al. (1992) noted that a primary factor in the ability to distinguish sub-pixel targets is the spectral contrast between the target and its surroundings. In most cases, this contrast is best expressed as an absorption feature or features present in the target but absent in the surroundings. Under such circumstances, techniques such as band depth mapping (Clark et al., 1992) are feasible. However, the only difference between a target material and its surroundings is often expressed solely in the continuum. We define the "continuum" as the reflectance or radiance spanning spectral space between spectral features. Differences in continuum slope and shape can only be determined by reduction techniques which consider the entire spectral range; i.e., techniques such as spectral mixture analysis (Adams et al., 1989) and recently developed techniques which utilize an orthogonal subspace projection operator (Harsanyi, 1993). Two of the three examples considered herein deal with cases where the target material differs from its surroundings only by such a subtle continuum change.

2. LOW PROBABILITY DETECTION BASED ON ORTHOGONAL SUBSPACE PROJECTION

The goal of the investigations discussed herein is to discriminate a given lithology of spectral signature, d . Ideally, this goal could be accomplished by suppressing the spectra of background materials and maximizing the SNR of the signature of interest. Recent work by Harsanyi and Chang (1993) and Harsanyi et al. (1993) has outlined a method for achieving this goal through the technique of orthogonal subspace projection.

For greater detail, the reader is referred to the above references; however in brief, the equation for a mixed pixel composed of desired and undesired spectral signatures can be written as:

$$L = da + Ug + n \quad (1)$$

where d is the desired spectral signature of the lithology of interest, a is the desired signature abundance, U is a matrix whose columns are the undesired spectral signatures, and g is a vector containing the abundances of the undesired signatures. The vector n is assumed to be Gaussian noise which is independent and identically distributed.

In the case where the columns of U are known, an orthogonal subspace projection operator, P can be constructed:

$$P = (I - UU^{\#}) \quad (2)$$

where $U^\# = (U^T U)^{-1} U^T$ is the pseudoinverse of U . Multiplying this operator against every term in equation (1) has the effect of eliminating the Ug term thereby leaving only a transform of the desired target signature.

When the columns of U are not known, an estimate of their contribution can still be gleaned from the data. In this case, an estimate of the projection operator in equation 2 can be obtained from the first and second order statistics of the scene or scene subsection being processed. It is shown in Harsanyi (1993) and Harsanyi et al. (1993), that an operator:

$$w^T = d^T \tilde{P} \quad (3)$$

can be formed which will not only act to null the unknown, undesired background signatures, but also will maximize the SNR of the desired low probability target spectrum.

A drawback of the low probability detection algorithm is that the target material does, in fact, have to be a minor component in the scene. That is to say not present in enough pixels to be used as an endmember.

3. STUDY AREAS AND PRELIMINARY RESULTS

Three areas were examined in this study from three separate AVIRIS collections. These areas are: the Lunar Crater Volcanic Field (LCVF) of northern Nye County, Nevada; an area south of Mono Lake in Mono County, California; and a section along the Couer d'Alene river valley in Kootenai County, Idaho. The LCVF data were acquired on October 9, 1992, the Mono Lake data were acquired on August 20, 1992 and the Couer d'Alene data on May 24, 1993. All three data sets were acquired within an hour of solar noon.

The lithology being sought in the LCVF was a palagonite tuff exposed within the walls of the Easy Chair Crater tuff and cinder cone. Significant exposures of the palagonite tuff are restricted to two outcrops on the western rim of the crater. The exposures of tuff extend along the crater wall for as much as 100 m, with notable vertical exposure, but from an overhead perspective, the latitudinal extent of the tuff outcrop is only on the order of 5 to 8 m. The crest of the crater rim is covered by thinly bedded tuffs, cinders, grasses and scrub brush. In the area surrounding the crater are alluvial deposits derived from rhyolitic tuffs. Spectra of the palagonite tuff and several background materials are shown in Figure 1. Figure 2 compares a reflectance spectrum extracted from the AVIRIS data (the data were converted to reflectance via the empirical line method) over a tuff rich pixel with an average of several sample spectra measured on the RELAB laboratory spectroradiometer. The fact that the AVIRIS-derived spectrum is different from that of samples measured in the laboratory demonstrates that the tuff is present only at a subpixel scale.

In the area examined that was south of Mono Lake, the lithology of interest was the Bishop Tuff. South of the study area the Bishop Tuff becomes the dominant lithology; however, in the area of interest outcrops of Bishop Tuff are small and sporadic and occur generally on a subpixel scale although isolated exposures can fill the pixel. The Bishop Tuff reflectance spectrum closely resembles that of Quaternary aeolian and alluvial materials in the area; thereby complicating the detection problem.

Ferric oxide rich mine tailings spread along the Couer d'Alene river valley are the target of the third investigation. Downriver detection of these tailings becomes extremely difficult, because while the material is spectrally distinct from its surroundings, it is very poorly exposed due to the abundant vegetation in the area.

A routine written in IDL (RSI, 1992) that implements the low probability detection algorithm was applied to subsections of the aforementioned scenes including the LCVF subsection shown in Fig. 3. The low probability detection output image in Fig. 4, demonstrates an excellent discrimination of the palagonite tuff outcrops in the wall of Easy Chair Crater. Examples from the Mono Lake and Couer d'Alene scenes will also be shown.

4. ACKNOWLEDGMENTS

The authors are grateful to R.O. Green of JPL for providing the LCVF and Couer d'Alene AVIRIS data and to Chris Elvidge of DRI for the Mono Lake data. Thanks also to Steve Pratt of Brown University for the RELAB spectra.

5. REFERENCES

- Adams, J.B., M.O. Smith, and A.R. Gillespie, 1989, "Simple models for complex natural surfaces: A strategy for the hyperspectral era of remote sensing". *Proc. IEEE Int. Geosci. Rem. Sens. Symp. '89*, I, 16-21.
- Clark, R.N., G.A. Swayze, and A. Gallagher, 1992, "Mapping the mineralogy and lithology of Canyonlands, Utah with imaging spectrometer data and the multiple spectral feature mapping algorithm". *Summaries of the 3rd JPL Airborne Geoscience Workshop*. (R.O. Green, ed.) JPL publ.92-14, vol. 1, 11-13.
- Harsanyi, J.C., 1993, *Detection and Classification of Subpixel Spectral Signatures in Hyperspectral Image Sequences*, Ph.D. Dissertation, University of Maryland, Baltimore County, 112 pp.
- Harsanyi, J.C. and C.Chang, 1993, "Hyperspectral image classification and dimensionality reduction: An orthogonal subspace projection approach". (submitted to) *IEEE Trans. Geosci. Rem. Sens.*
- Harsanyi, J.C., W.H. Farrand, and C.Chang, 1993, "Detection of low probability, subpixel targets in hyperspectral images with unknown backgrounds". (in preparation for) *IEEE Trans. Geosci. Rem. Sens.*
- Research Systems, Inc., 1993, *IDL User's Guide Version 3.0*, Boulder, CO.
- Sabol, D.E., J.B. Adams, and M.O. Smith, 1992, "Quantitative subpixel spectral detection of targets in multispectral images". *J. Geophys. Res.*, 97, 2659-2672.

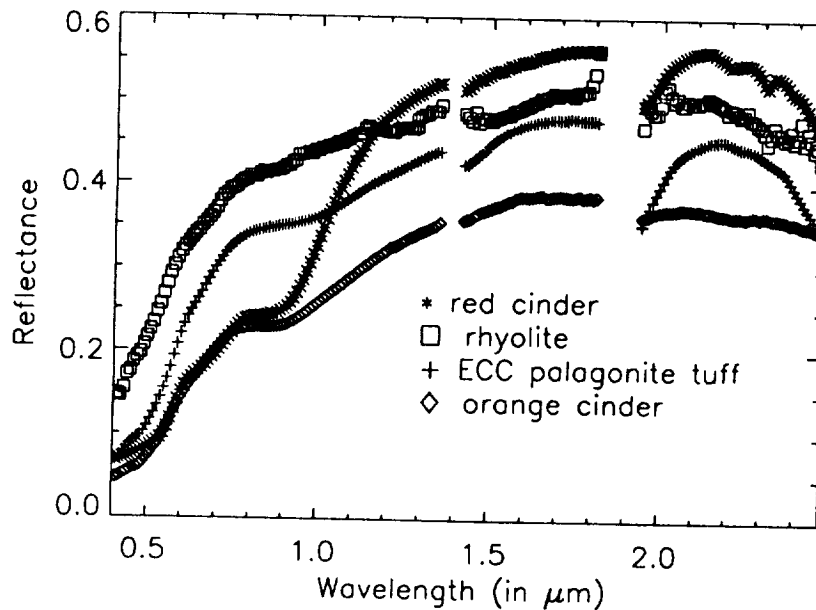


Figure 1. Reflectance spectra of geologic units at or near Easy Chair Crater. The greatest potential for confusion is between the tuff, rhyolite and orange cinder.

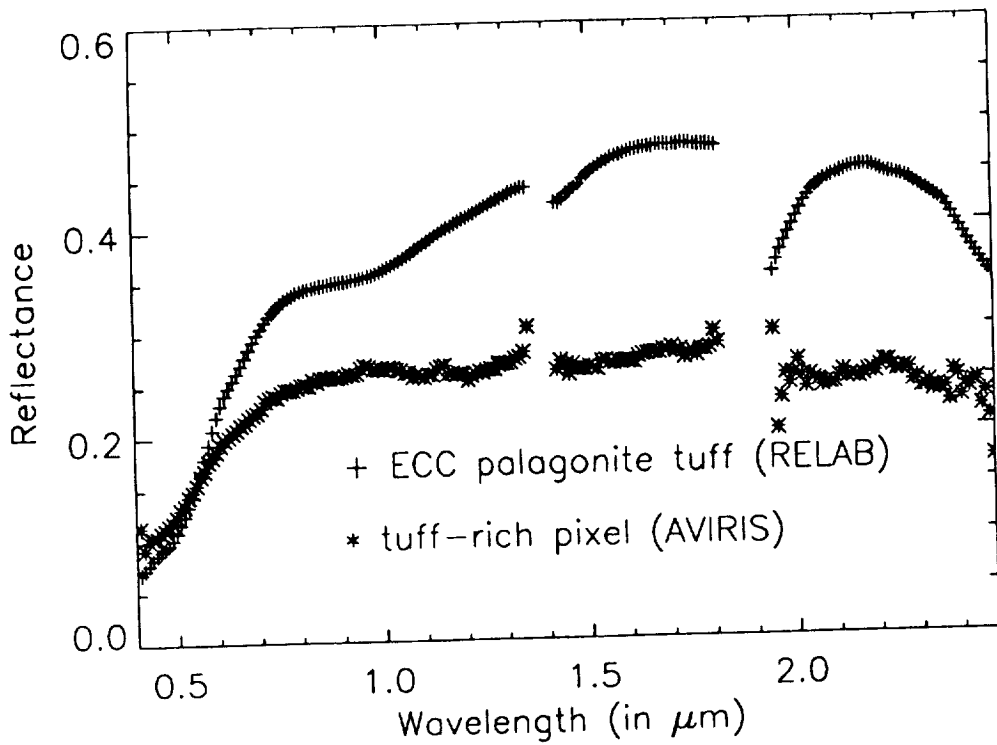


Figure 2. Average of 5 tuff sample spectra measured at RELAB compared with tuff-rich pixel spectrum extracted from AVIRIS data. The disparity demonstrates that the tuff is present at a subpixel scale.



Figure 3. 1.611 μm AVIRIS channel subsection containing Easy Chair Crater. Oxidized basaltic cinders are bright as are dry wash deposits. Arrows indicate subpixel scale tuff outcrops in crater walls.

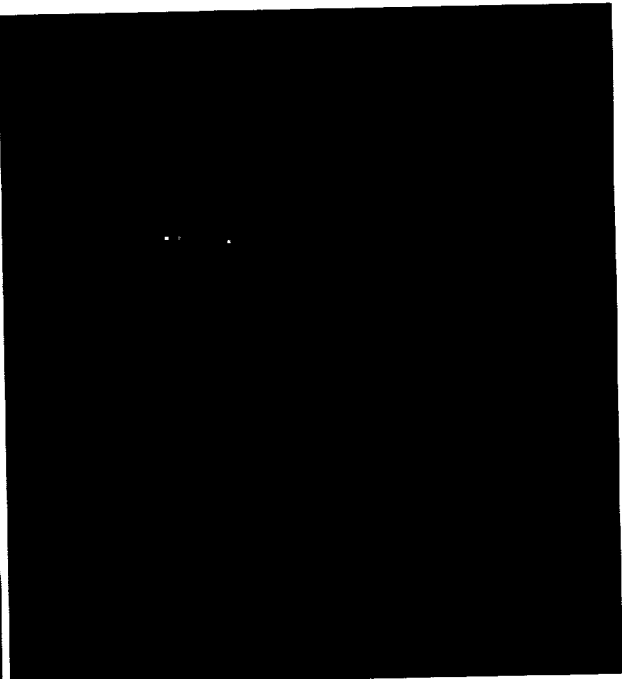


Figure 4. Low probability detection algorithm output image. The two tuff outcrops are accurately discriminated. The small playa at the crater's center is also highlighted since it contains a lesser fraction of palagonite.

5/15/88
41015
P 4

SPECTRAL DECOMPOSITION OF AVIRIS DATA

Lisa Gaddis, Laurence Soderblom, Hugh Kieffer, Kris Becker, Jim Torson,
and Kevin Mullins

U.S. Geological Survey
2255 N. Gemini Drive
Flagstaff, AZ 86001

1. INTRODUCTION

A set of techniques is presented that uses only information contained within a raw Airborne Visible/Infrared Imaging Spectrometer (AVIRIS) scene to estimate and to remove additive components such as multiple scattering and instrument dark current. Multiplicative components (instrument gain, topographic modulation of brightness, atmospheric transmission) can then be normalized, permitting enhancement, extraction, and identification of relative reflectance information related to surface composition and mineralogy. An expanded discussion of these analyses is now in review for submission to the Journal of Geophysical Research. The technique for derivation of additive-component spectra from a raw AVIRIS scene is an adaptation of the "regression intersection method" of Crippen (1987). This method uses two surface units that are spectrally homogeneous, spatially extensive, and located in rugged terrain. For a given wavelength pair, subtraction of the derived additive component from individual band values will remove topography in both regions in a band/band ratio image. Normalization of all spectra in the scene to the average scene spectrum (e.g., Kruse, 1988) then results in cancellation of multiplicative components and production of a relative-reflectance scene. The resulting AVIRIS product contains relative-reflectance features due to mineral absorptions that depart from the average spectrum. These features commonly are extremely weak and difficult to recognize, but they can be enhanced by using two simple 3-D image-processing tools. The validity of these techniques will be demonstrated by comparisons between relative-reflectance AVIRIS spectra and those derived by using JPL standard calibrations. The AVIRIS data used in this analysis were acquired over the Kelso Dunes area (34°55'N, 115°43'W) of the eastern Mojave Desert, Calif. (in 1987) and the Upheaval Dome area (38°27'N, 109°55'W) of the Canyonlands National Park, Utah (in 1991).

2. FUNDAMENTAL CONCEPTS

In simple terms, there are six major, wavelength-dependent components of a typical spectrum that must be dealt with to derive surface reflectance from measured DN values at visible and near-infrared wavelengths. They include solar flux (F); atmospheric transmission (T); surface reflectance (R); atmospheric scattering ($A\uparrow$ and $A\downarrow$, irradiance at the top and bottom of the atmosphere, respectively); and the instrument gain (G) and dark current (D). Solar flux is well known; atmospheric transmission has characteristic "windows" through which spectral observations can be made, but they vary in "clarity" with atmospheric gas and/or water vapor content. Surface reflectance (as related to mineral composition) is the quantity we seek; it is influenced by a variety of parameters, including terrain roughness and particle size, texture, composition, and moisture content of surface materials. Atmospheric scattering varies with the amounts and types of particulates and gas molecules in the atmosphere; its influence decreases with increasing wavelength. Instrument gain and dark-current values characterize the sensor response; here the gain is assumed to be linear and both the dark current and the gain are assumed to be constant over the imaging field. These components combine in additive and multiplicative ways to form a measured spectrum.

The largest portion of energy in a measured raw spectrum is the direct-reflected component, which is essentially the product of solar flux, two-way atmospheric transmission, surface reflectance, surface photometric function (P), and instrument gain. In rugged terrain, surface reflectance includes the effects of topography as it modulates incident and reflected sunlight. The photometric properties of the surface define its light-scattering behavior; they are a function of viewing phase (α), incidence (i), and emission (ϵ) angles. The direct-reflected component, written $FT^2RP(\alpha, i, \epsilon)G$, contains the surface reflectance information that we seek.

A second major component in a measured raw spectrum is surface-reflected skylight, or the diffuse light scattered to the surface through multiple interactions with the atmosphere and surface and reflected directly back to the sensor. Surface-reflected skylight includes upward atmospheric transmission, downwelling scattered radiation at the bottom of the atmosphere ($A\downarrow$, which incorporates the solar flux and downward atmospheric transmission), surface reflectance, and instrument gain, and it can be written $TA\downarrow RG$. The other major additive component in a measured raw spectrum is upwelling diffuse skylight ($A\uparrow G$, where $A\uparrow$ incorporates the solar flux and two-way atmospheric transmission), is also called path radiance or haze. This diffuse skylight is mostly due to atmospheric scattering, although the surface is weakly involved where it contributes to multiple scattering at the base of the atmosphere. Together these two components compose the atmospheric scattering component, and they are not separable. The last major additive component of a spectrum is the instrument dark current (D), a measure of instrument background noise that serves to elevate the spectrum by a roughly constant amount. These relationships can be expressed as

$$(1) \quad \text{Raw spectrum} = (FT^2RPG) + [(TA\downarrow RG) + (A\uparrow G)] + D$$

where the first is the multiplicative term we seek and the last three are additive terms.

3. ADDITIVE COMPONENTS

Our technique for derivation of additive-component spectra (an adaptation of the "regression intersection method" of Crippen, 1987) relies on selection of two units in a multispectral image that are spectrally homogeneous, spatially extensive, and located in rugged terrain. More explicitly, each selected unit must have a contrasting, dominant reflectance, must be larger than $\sim 10^2$ pixels, and must have a strong brightness modulation due to topography. We start with two spectral bands substantially separated in wavelength, and we produce 2-D cluster plots of pixel DN values for the two areas. Regression lines are fitted to these histograms for each area; their intersection point represents all additive terms for those wavelengths. In this manner intersection values are derived for all bands and are subtracted to remove additive components at all wavelengths. To correct for the effects of total additive components in an entire multispectral scene, we assumed that the atmosphere over the scene was homogeneous and that variation in surface reflectance as it affects the surface-reflected skylight can be neglected. Using ISIS software developed for spectral analyses of 3-D imaging spectrometer "cubes" (Torson, 1989), we applied these techniques to two units from an AVIRIS scene of the Mojave Desert, including parts of the Granite Mountains and the Kelso Dunes (Gaddis et al., 1992).

The initial step in our derivation of the total additive spectrum for each wavelength in the AVIRIS Mojave Desert scene was to select a single reference band (e.g., band #177, $\lambda = 1.98 \mu\text{m}$) and to derive corresponding intersections with every other band. We found the solution for band 177 to be consistent (e.g., DN=75) only when paired with bands at longer wavelengths ($> 1.4 \mu\text{m}$). Using this solution and calculating an additive-component spectrum for each of the two selected units, we found the two spectra to be similar at longer wavelengths and different at shorter wavelengths. These differences at smaller wavelengths are attributable to differences in atmospheric column height between the two sites; the Granite Mountains site (elev. = $\sim 6700'$) shows less atmospheric scattering than the Kelso Dunes site (elev. = $\sim 2600'$). The calculated additive spectrum for each of the two units in the Mojave AVIRIS scene clearly shows features of

the atmospheric scattering spectrum and the detailed structure of an instrument dark-current spectrum. For validation of these techniques, the derived total additive spectra was deconvolved into Rayleigh, Mie, and instrument dark-current components.

4. MULTIPLICATIVE COMPONENTS

Subtracting the calculated total additive component from raw AVIRIS data removes the additive effects of atmospheric scattering and the instrument dark current, and the total direct-reflected component remains. In addition to the surface-reflectance information we seek, the direct-reflected component (FT²RPG) contains the multiplicative influences of topography (including the effects of terrain roughness and of the geometry of instrument viewing and solar illumination), atmospheric transmission, and instrument gain. These influences can be removed through two normalization procedures to arrive at relative reflectance (c.f. "internal average relative" reflectance of Kruse, 1988). We applied these techniques to derivation of relative reflectance from a raw AVIRIS scene from Upheaval Dome and compared the derived relative-reflectance spectra to calibrated spectra from the same units. Here we summarize briefly those results.

Most differences in brightness among units in a direct-reflected component multispectral image are due to differences in unit albedo and in illumination due to topography. We used an equal-area normalization to scale the sum of all of the DNs in each spectrum to a constant, arbitrary value. Such an operation scales the variation in broadband albedo among the units in a scene to a common value of overall brightness, and thereby it mutes the influence of topography on the relative brightnesses of the units. To remove the remaining multiplicative terms (atmospheric transmission and instrument gain), we normalized the data again, dividing each spectrum by an average scene spectrum; the FT²G term will cancel out, resulting in the reflectance of the surface relative to a scene-average spectrum.

To identify possible mineral-absorption features in the relative-reflectance spectra in this analysis, we first used a 3x3x3-pixel low-pass filter to suppress small-scale (high-frequency) "noise" and then a 1x1x15-pixel high-pass filter to enhance the strength of the relatively weak absorption features by removing long-wavelength variations. After features are visually identified with the enhanced filtered data, however, unfiltered data are then compared with laboratory spectra and can be used to derive images that are interpretable in terms of relative absorption-band strengths and positions, and thus serve as indicators of surface mineralogy.

These procedures for derivation of relative-reflectance information were applied to AVIRIS data for the Upheaval Dome. The dome (diameter~5 km), on the Colorado Plateau in Utah, consists of a series of complexly faulted sedimentary formations that have been uplifted in the center and surrounded by a structurally depressed ring of rocks (e.g., Shoemaker, 1956). Representative spectra from each of the five major geologic formations of the dome were extracted from the raw relative-reflectance (low-pass filtered) and calibrated (scaled intensity/solar flux, or I/F) AVIRIS data. The relative-reflectance spectra show a variety of absorption bands at wavelengths of 0.45-0.65 and 2.0-2.3 μm . In general, calibrated spectra show more complex, stronger absorption features in these wavelength ranges, but in all cases the spectra are comparable directly with features observed in the relative-reflectance spectra.

To identify mineral components, spectrum-matching was applied to spectra from major geologic formations at Upheaval Dome and used to search through the JPL SPAM spectral library (Grove et al., 1992) at wavelengths of 0.45-0.65 and 2.0-2.3 μm . Spectral band-depth analysis (e.g., Clark et al., 1990) was used to compute the band depth of an observed absorption feature relative to its continuum and to calculate a goodness-of-fit parameter for a given similarity threshold. We find mineral matches for the Upheaval Dome units that are broadly consistent both with the results of Clark et al. (1992) and with the major unit lithologies (Huntoon et al., 1982). An iron-bearing, carbonate-type

composition for the Kayenta and Chinle Formations is consistent with the marine sandstones, limestones, and siltstones of these units, and a clay-bearing mineralogy is consistent with the compositions of the ripple-marked, cross-bedded shales and siltstones of the Moenkopi, White Rim, and Organ Rock Formations.

5. SUMMARY

These preliminary results demonstrate our success in extracting reasonable mineral signatures from complex AVIRIS data. Use of these techniques for derivation of additive-component spectra not only allows decoupling of atmospheric scattering from surface reflectance, but it also provides an independent check on the behavior of the instrument through analyses of instrument dark-current behavior. If the atmospheric-scattering component of the total additive spectrum can be decomposed into instrument dark-current and Rayleigh and Mie scattering components, then the instrument dark current can be studied. In addition, treatment of the multiplicative components of the measured AVIRIS spectra has allowed extraction of surface-reflectance data that can be interpreted in terms of surface mineralogy.

REFERENCES CITED

- Clark, R.N., A.J. Gallagher and G.A. Swayze, 1990, Material absorption band depth mapping of imaging spectrometer data using a complete band shape least-squares fit with library reference spectra, *Proc. 2nd AVIRIS Workshop, JPL Pub. 90-54*, 176-186.
- Clark, R.N., G.A. Swayze and A. Gallagher, 1992, Mapping the mineralogy and lithology of Canyonlands, Utah, with imaging spectrometer data and the multiple spectral feature mapping algorithm, *3rd Ann. Air. Geosci. Workshop, JPL Pub. 92-14*, 11-13.
- Crippen, R.E., 1987, The regression intersection method of adjusting image data for band ratioing, *Int. Jour. Rem. Sens.*, 8, 137-155.
- Gaddis, L.R., Soderblom, L.A., Kieffer, H.K., and Mullins, K.F., 1992, Separation of AVIRIS data into atmospheric, instrumental, and surface reflectance components through forced internal consistency, *Eos Trans., Am. Geophys. Union*, v. 73, 184-185.
- Grove, C., S. Hook and E. Paylor, 1992, Laboratory reflectance spectra of 160 minerals (0.4 to 2.5 micrometers), *JPL Pub. 92-2*, 208 pp.
- Huntoon, P.W., G.H. Billingsley, and W.J. Breed, 1982, *Geologic map of Canyonlands National Park and vicinity, Utah*, Canyonlands Nat. Hist. Assn.
- Kruse, F.A., 1988, Use of airborne imaging spectrometer data to map minerals associated with hydrothermally altered rocks in the northern Grapevine Mountains, Nevada and California, *Rem. Sens. Env.*, 24, 31-51.
- Shoemaker, E.M., 1956, Structural features of the central Colorado Plateau and their relation to uranium deposits, *U.S. Geol. Surv. Prof. Pap. 300*, 155-170.
- Torson, J.M., 1989, Interactive image cube visualization and analysis, *Proc., Chapel Hill [North Carolina] Workshop on Volume Visualization*, 33-38.

516-43
41016

REMOTE SENSING OF SMOKE, CLOUDS, AND FIRE USING AVIRIS DATA

Bo-Cai Gao^{1,2}, Yoram J. Kaufman², and Robert O. Green³

¹University Space Research Association, Code 913, NASA Goddard Space Flight Center, Greenbelt, MD 20771

²Climate and Radiation Branch, Code 913, NASA Goddard Space Flight Center, Greenbelt, MD 20771

³Jet Propulsion Laboratory, California Institute of Technology, Pasadena, California, 91109-8099

1. INTRODUCTION

Clouds remain the greatest element of uncertainty in predicting global climate change (Houghton et al., 1990). During deforestation and biomass burning processes, a variety of atmospheric gases, including CO₂ and SO₂, and smoke particles are released into the atmosphere. The smoke particles can have important effects on the formation of clouds because of the increased concentration of cloud condensation nuclei. They can also affect cloud albedo through changes in cloud microphysical properties (King et al., 1993). Recently, great interest has arisen in understanding the interaction between smoke particles and clouds (Kaufman et al., 1992).

In this paper, we describe our studies of smoke, clouds, and fire using the high spatial and spectral resolution data acquired with the NASA/JPL Airborne Visible/Infrared Imaging Spectrometer (AVIRIS) (Vane, 1987; Vane et al., 1993).

2. THE AVIRIS DATA

AVIRIS collects spectral imaging data in the 0.4–2.5- μm wavelength range in 224 10-nm channels with a spatial resolution of 20 m from an ER-2 aircraft at 20-km altitude. An interesting data set was acquired on August 20, 1992, over an area near Stockton in northern California. The scene contains areas covered by active fire, burn scars, smoke, clouds, vegetation, and a small water pond. The data set offers an excellent opportunity to study the radiative properties of smoke, clouds, and fire. Our preliminary results are described in this paper.

3. RESULTS

3.1 Smoke

We have found that smoke is readily observable in images between 0.4 and 0.75 μm . The effects of smoke decrease with increasing wavelength. It is difficult to observe smoke from images beyond 1 μm . Figure 1(a) shows a 0.47- μm AVIRIS image. Smoke in the lower part of the image is clearly seen. The areas with active fires are located near the center (slightly upper) portion of the image. Most parts of the white areas in the image are clouds. Figure 1(b) shows a 2.13- μm image. Smoke disappears completely in this image.

(a)

AVIRIS IMAGE OVER LINDEN, CA (8/92)
(0.47 μm , FIRE, CLOUD, & SMOKE)



(PROCESSED ON IMAGECUBE, NASA/GSFC)

(b)

AVIRIS IMAGE OVER LINDEN, CA (8/92)
(2.13 μm , FIRE, CLOUD, & SMOKE)



(PROCESSED ON IMAGECUBE, NASA/GSFC)

Fig. 1. A 0.47- μm AVIRIS image (a) and a 2.13- μm AVIRIS image (b). Smoke is clearly seen in the lower part of (a), but disappears completely in (b).

Using radiative transfer modeling techniques, we have retrieved optical depths and the mean particle radius of smoke particles. The derived optical depths vary with spatial locations. The derived mean particle radius is approximately 0.5 μm . As wavelength increases, the ratio of wavelength to the mean particle radius increases, and the scattering of solar radiation by smoke particles decreases. This is the reason that smoke is difficult to detect in images beyond 1 μm .

3.2 Clouds

The active fire produced hot air and smoke. As a result, strong convection was induced. As the lower air that contained a lot of water vapor was lifted to upper levels, the air was cooled down and clouds were formed. We have examined in detail the cloud spectra from the AVIRIS data. The shapes of the spectra around 1.6 and 2.2 μm show that the clouds are water clouds, not ice clouds. The reflectances of the clouds in the 0.8–1.6 μm region are greater than theoretical predictions, contrary to the belief of anomalous water cloud absorption in the near-IR spectral region (Stephens and Tsay, 1990).

We have also found that the depths of the oxygen band near 0.76 μm in cloud spectra are sensitive to cloud height variations. It may be possible to derive “effective” cloud heights using the oxygen band. The “true” cloud heights are difficult to obtain because of the complicated absorption and scattering processes inside the clouds (Wu, 1985).

3.3 Fires and Hot Surfaces

The temperatures of active fire-burning areas are several hundred degrees higher than non-burning areas. The emitted radiation from the fire-burning area is easily observable in images between 2.0 and 2.5 μm . The emission effect is also detectable in images around 1.6 μm . Below 1.2 μm , the emission effect is difficult to detect. The hot smoldering surface areas can be identified in images between 2.0 and 2.5 μm if appropriate stretches are applied to the images. Figure 2 shows such an example. The bright areas in this figure are hot surfaces.

4. Summary

Using AVIRIS data, we have discovered important radiative properties of smoke, clouds, and fire, as described in Section 3.

5. References

- Houghton, J. T., G. J. Jenkins, and J. J. Ephraums (Eds.), *Climate Change, the IPCC Scientific Assessment*, Cambridge Univ. Press, New York, 1990.
- Kaufman, Y. J., A. Setzer, D. Ward, D. Tanre, B. N. Holben, P. Menzel, M. C. Pereira, and R. Rasmussen, “Biomass burning airborne and spaceborne experiment in the Amazonas (BASE-A),” *J. Geophys. Res.*, 97, 14,581–14,599, 1992.
- King, M. D., L. F. Radke, and P. V. Hobbs, “Optical properties of marine stratocumulus clouds modified by ships,” *J. Geophys. Res.*, 98, 2729–2739, 1993.

- Stephens, G. L., and S.-C. Tsay, "On the cloud absorption anomaly," *Q. J. R. Meteorol. Soc.*, 671-704, 1990.
- Vane, G. (ed.), *Airborne visible/infrared imaging spectrometer (AVIRIS)*, JPL Publication 87-38, Jet Propulsion Laboratory, Pasadena, California, 1987.
- Vane, G., R. O. Green, T. G. Chrien, H. T. Enmark, E. G. Hansen, and W. M. Porter, "The Airborne Visible/Infrared Imaging Spectrometer (AVIRIS)," *Remote Sens. Environ.*, 44, no. 2, 127-143, 1993.
- Wu, M.-L. C., "Remote sensing of cloud-top pressure using reflected solar radiation in the oxygen A-band," *J. Clim. Appl. Meteorol.*, 24, 539-546, 1985.

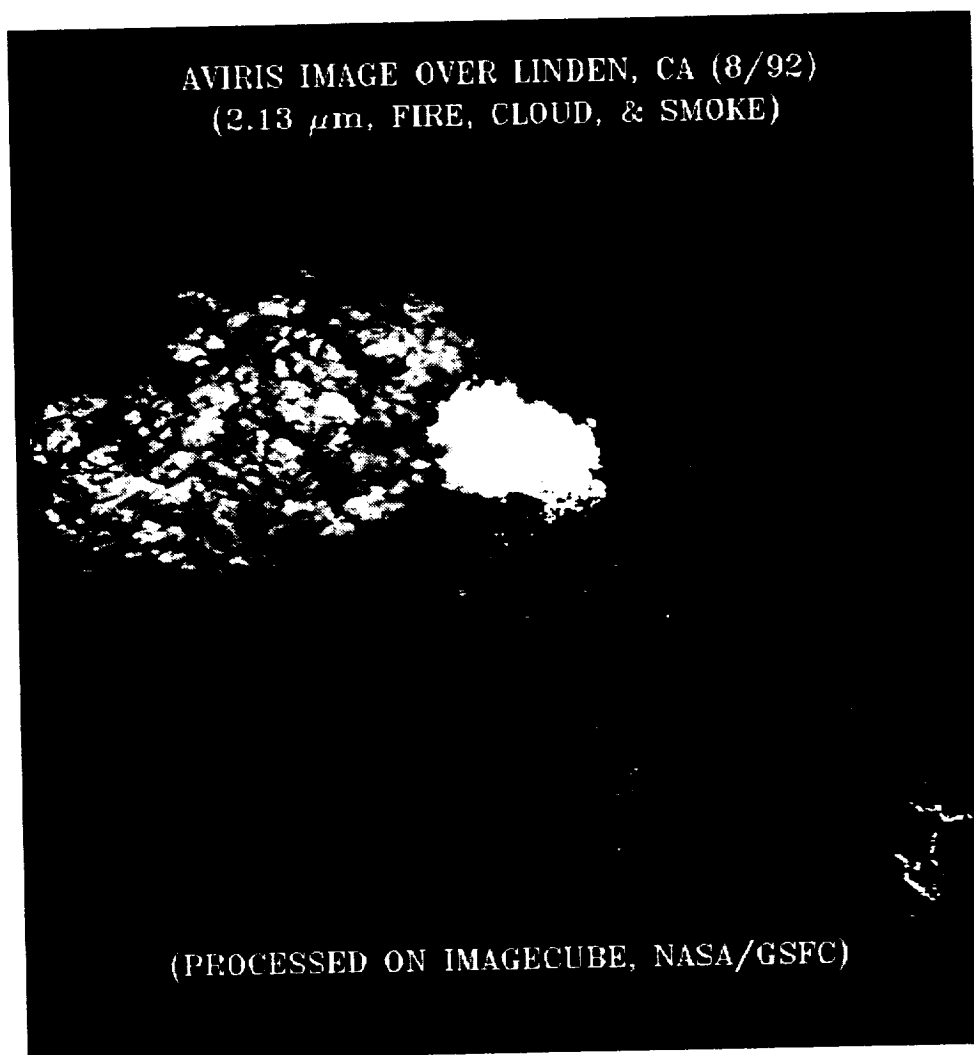


Fig. 2. A 2.13- μm AVIRIS image stretched to show hot surfaces (bright areas).

Use of Data from the AVIRIS Onboard Calibrator

Robert O. Green

Jet Propulsion Laboratory, 4800 Oak Grove Dr., Pasadena, CA 91109 USA

97-32
11017
1/1

ABSTRACT

The AVIRIS onboard calibrator became operational in 1992. This subsystem on the AVIRIS sensor has operated nominally throughout the 1992 and 1993 flight season. This paper describes the data measured by the onboard calibration and the two primary uses of these data.

1.0 INTRODUCTION

The AVIRIS onboard calibrator subsystem measures the intensity on a current stabilized lamp (Chrien et al., 1991) at the beginning and end of each flight line. This signal is measured through three filters and from the surface of a closed shutter. These four measurements are referred to as the high, spectral, low and dark onboard calibration data. Onboard calibrator measurements are delivered with all AVIRIS data as a four line AVIRIS image file. Each line has 614 samples and corresponds to one of the onboard calibrator positions. In this paper only the high intensity and dark data from the onboard calibrator are used.

Data from the onboard calibrator have two primary uses. First, the data may be used to optimize the tractability of the calibration of the delivered AVIRIS data to the laboratory radiometric calibration standard. Second, these data may be used to monitor and normalize the inflight radiometric performance of AVIRIS through the flight season (Green et al., 1992). These uses are described and an example presented in the following sections of the paper.

2.0 TRACTABILITY TO THE LABORATORY RADIOMETRIC CALIBRATION

A set of measurements from the onboard calibrator is acquired in conjunction with the radiometric calibration of AVIRIS in the laboratory. These data are acquired as AVIRIS data are measured from the radiometrically calibrated integrating sphere. From analysis of the AVIRIS digitized numbers (DN) and the integrating sphere radiance the radiometric calibration coefficients are calculated for AVIRIS (Chrien, et al., 1990). At the same time, a set of data is analyzed from the AVIRIS onboard calibrator. This data set consists of the average high minus dark onboard calibrator signal for the period of laboratory radiometric calibration. A plot of the high minus dark data at the time of laboratory calibration in 1992 is given in Figure 1. These data measure AVIRIS radiometric performance in terms of the onboard calibrator signal and are provided with all delivered AVIRIS data in 1992 and 1993.

With each AVIRIS, airborne flight line data from the onboard calibrator are measured. A plot of the high minus dark data for the AVIRIS inflight calibration experiment held on the 30th of May 1992 is given in Figure 2. These data measure AVIRIS inflight radiometric performance in terms of the onboard calibrator signal. If the onboard calibrator is stable, then a ratio of the laboratory signal over the inflight signal will show any change in AVIRIS performance. Some change is expected given that the operational environment inside the Q-bay of the ER-2 at 20 km altitude, 4 psi, and less than 10 degrees C differs considerably from the environment in the AVIRIS laboratory. A plot of the ratio of the laboratory signal over inflight signal for the onboard calibrator is given in Figure 3. A ratio of 1.0 indicates no onboard calibrator measured change in radiometric performance. This plot shows AVIRIS to be remarkably stable between the laboratory and flight over Rogers Dry Lake. The small disagreement at 410 nm is likely related to a quantization error due to the low signal from the onboard calibrator. At 1400, 1900, and 2500, the error may be attributed to a difference in water vapor in the AVIRIS sensor between the laboratory and the 20 km altitude. Though the agreement is quite good, multiplying this ratio by the delivered AVIRIS radiance will incrementally improve the tractability of the inflight radiance to the laboratory standard. A plot of the onboard calibrator corrected radiance for Rogers Dry Lake is given in Figure 4. Analysis of the stability of the onboard calibrator in the laboratory as well as the current supplied to the lamp indicates the onboard calibrator should be stable to better than the 3 percent level.

3.0 FLIGHT SEASON PERFORMANCE NORMALIZATION AND MONITORING

The second primary use of the onboard calibrator is for monitoring and normalizing the radiometric performance of AVIRIS from flight to flight during the flight season. When comparing AVIRIS data acquired at multiple sites in the flight season a ratio of the inflight high minus dark signal

between flights may be used to bring those AVIRIS data sets into agreement. This method is currently being used with the inversion of AVIRIS measured radiance to apparent surface reflectance (Green, 1990, and Green et al., 1993a) using an inflight calibration experiment (Conel et al., 1988, and Green et al., 1993b) as the absolute radiometric calibration.

4.0 FUTURE PLANS

As the performance of the onboard calibrator is further validated the correction described may become an option available directly from the AVIRIS data facility. In 1994, it is planned that the onboard calibrator will be improved to increase the radiometric stability to better than 3%. In addition, spectral and geometric calibration standards may be incorporated into the AVIRIS onboard calibrator.

5.0 CONCLUSION

The onboard calibrator may be used to improve the tractability of the inflight radiometric calibration of AVIRIS and to normalize the radiometric characteristics of the data set acquired at different times in the flight season. In 1992 and 1993, it is left to the science investigator to perform the simple calculations required to utilize these data.

6.0 ACKNOWLEDGMENTS

This research was carried out at the Jet Propulsion Laboratory, California Institute of Technology, under contract with the National Aeronautics and Space Administration.

7.0 REFERENCES

- Chrien, T. G., R. O. Green, and M. L. Eastwood, "Accuracy of the Spectral and Radiometric Laboratory Calibration of the Airborne Visible/Infrared Imaging Spectrometer", Proc. SPIE Conference on Aerospace Sensing, Imaging Spectroscopy of the Terrestrial Environment, Orlando, Florida, 16-20 April, 1990.
- Chrien, Thomas G., Michael L. Eastwood, Charles M. Sarture, Robert O. Green, and Wallace M. Porter, "Current Instrument Status of the Airborne Visible/Infrared Imaging Spectrometer (AVIRIS)", Proc. Third AVIRIS Workshop, JPL Publication 91-28, Jet Propulsion Laboratory, Pasadena, CA, pp. 302-313, 1991.
- Conel, J. E., R. O. Green, R. E. Alley, C. J. Bruegge, V. Carrere, J. S. Margolis, G. Vane, T. G. Chrien, P. N. Slater, S. F. Biggar, P. M. Teillet, R. D. Jackson, and M. S. Moran, "In-flight radiometric calibration of the Airborne Visible/Infrared Imaging Spectrometer (AVIRIS)", SPIE Vol. 924, Recent Advance in sensors, radiometry and data processing for remote sensing, 1988.
- Green, Robert O., "Retrieval of Reflectance from Calibrated Radiance Imagery Measured by the Airborne Visible/Infrared Imaging Spectrometer (AVIRIS) for Lithological Mapping of the Clark Mountains, California", Proc. Second AVIRIS Workshop, JPL Publication 90-54, Jet Propulsion Laboratory, Pasadena, CA, pp. 167-175, 1990.
- Green, Robert O., James E. Conel and Thomas G. Chrien, "Airborne Visible-Infrared Imaging Spectrometer (AVIRIS): Sensor System, Inflight Calibration and Reflectance Calculation", International Symposium on Spectral Sensing Research, pp. 22, in press, 1992.
- Green, Robert O., James E. Conel and Dar A. Roberts, "Estimation of Aerosol Optical Depth and Calculation of Apparent Surface Reflectance from Radiance Measured by the Airborne Visible-Infrared Imaging Spectrometer (AVIRIS) Using MODTRAN2", SPIE Conf. 1937, Imaging Spectrometry of the Terrestrial Environment, in press, 12 p. 1993a.
- Green, Robert O., James E. Conel, Mark Helmlinger, Jeannette van den Bosch, Chris Chovit and Tom Chrien, "Inflight Calibration of AVIRIS in 1992 and 1993", Proc. Fourth JPL Airborne Geoscience Workshop, JPL Publication 93-26, Jet Propulsion Laboratory, Pasadena, CA, 1993b.

8.0 FIGURES

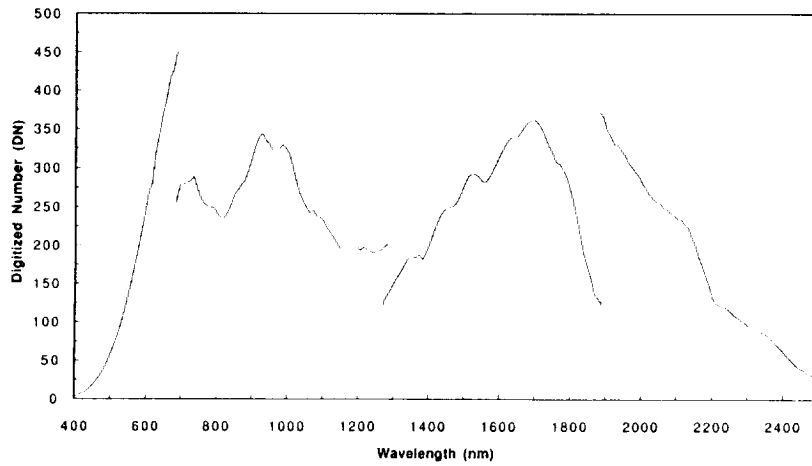


Figure 1. High minus dark shutter intensity signal measured by the onboard calibrator at the time of AVIRIS sensor calibration in the laboratory.

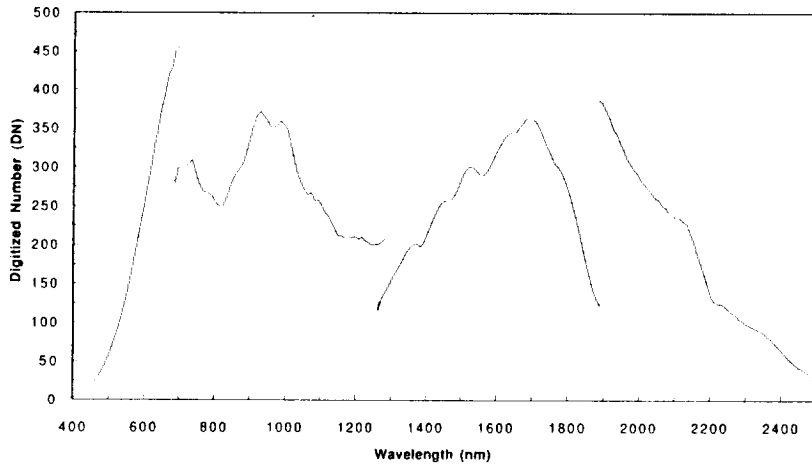


Figure 2. High minus dark signal for the AVIRIS onboard calibrator measured inflight over Rogers Dry Lake, California on the 30th of May 1992.

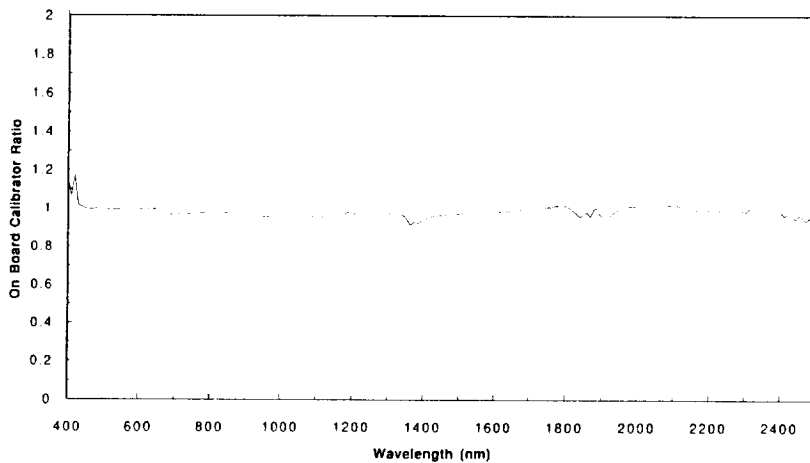


Figure 3. Ratio of the onboard calibrator signal measured in the laboratory divided by the signal inflight.

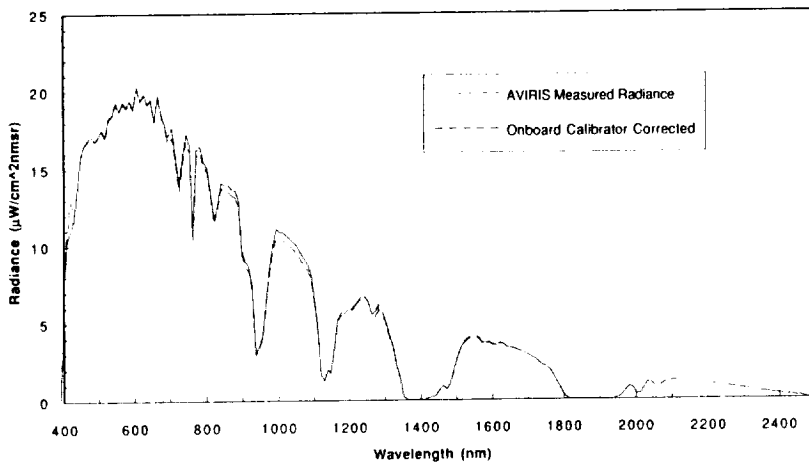


Figure 4. Comparison of the delivered spectral radiance from AVIRIS and the onboard calibrator modified radiance.

Inflight Calibration of AVIRIS in 1992 and 1993

Robert O. Green, James E. Conel, Mark Helmlinger, Jeannette van den Bosch, Chris Chovit, and Tom Chrien

Jet Propulsion Laboratory, 4800 Oak Grove Dr., Pasadena CA 91109 USA

Abstract

In order to pursue the quantitative research objective of AVIRIS, the spectral, radiometric characteristic of the sensor must be known at the time of flight data acquisition. AVIRIS is rigorously calibrated in the laboratory. In addition, three times each year these characteristics of AVIRIS are validated through an inflight calibration experiment. Absolute radiometric calibration and signal-to-noise results are present for the inflight calibration experiment orchestrated in 1992 and 1993.

1.0 Introduction

AVIRIS was developed to pursue quantitative research of the Earth's terrestrial surface and atmosphere from calibrated geometrically coherent spectroradiometric measurements. In contrast to a broadband sensor, an imaging spectrometer resolves the molecular absorption and particle scattering signatures of surface and atmospheric constituents. From imaging spectrometer measurements, constituents are unambiguously identified and the abundance is determined. As an example of AVIRIS data, the combined spectral and spatial characteristics of AVIRIS are shown in Slide 10 with an image acquired over Moffett Field including the southern part of the San Francisco Bay, California.

To achieve the quantitative research objectives of the AVIRIS sensor, the calibration of AVIRIS must be valid while AVIRIS is acquiring data from the NASA ER-2 aircraft. The operational environment inside the Q-bay of the ER-2 at 20 km altitude differs from that in the AVIRIS laboratory in temperature, pressure, vibration and high frequency electromagnetic fields. AVIRIS is calibrated in the laboratory prior to each flight season (Chrien, 1990). To validate, characterize and monitor the calibration and performance of AVIRIS in the flight environment, inflight reflectance-based calibration experiments using ground targets are routinely carried out at the beginning, middle and end of each flight season (Conel et al., 1988; Green et al., 1988; Green et al., 1990; Green et al., 1992). The AVIRIS results for inflight calibration experiments in 1992 and 1993 are presented in this paper.

2.0 AVIRIS Inflight Calibration Experiment

At the beginning of the 1992 and 1993 operational periods, inflight calibration experiments were held at Rogers Dry Lake, California. At the time of the AVIRIS overflight the surface reflectance and atmosphere properties were measured with field instruments for a calibration target on the homogeneous dry lake bed. The surface reflectance of this target was characterized with 20 measurements of a specific 200 m by 40 m area on the lake bed. The resulting standard deviation of the mean of these measurements for the calibration target is less than 0.5 percent reflectance across this spectral interval. The reflectance of the calibration target measured in 1992 is given in Figure 1.

To characterize the atmosphere, solar irradiance measurements were acquired with a stable solar radiometer (Bruegge et al., 1990) from sunrise through local solar noon in ten discrete spectral channels in the range from 370 to 1050 nm. Data from nine of these channels were used to estimate the atmospheric optical depth by the Langley technique at the time of the AVIRIS overflight. Data from the channel centered at 940 nm of this radiometer were used to estimate the total column water vapor during the AVIRIS data acquisition (Reagan et al., 1987; Bruegge et al., 1990).

The surface reflectance, optical depth and water vapor determination were used to constrain the MODTRAN radiative transfer code (Berk et al., 1989). The MODTRAN code predicted radiance spectrum at the AVIRIS aperture is compared with AVIRIS sensor reported radiance. This sensor reported radiance is traced to the laboratory irradiance lamp and onboard calibrator (Green, 1993).

MODTRAN has been modified to allow: 1) inclusion of the measured surface reflectance, 2) constraint of the MODTRAN atmospheric models with the measured optical depths, and 3) direct constraint of MODTRAN with the measured water vapor amount. In addition, an updated high spectral resolution solar irradiance spectrum (Green and Gao, 1993) has been incorporated in the modified MODTRAN code.

3.0 Radiometric Calibration

The MODTRAN predicted radiance and AVIRIS measured radiance spectra for the experiment held on the 30th of May 1992 is given in Figure 2. The mean absolute agreement excluding the regions of

strong atmospheric absorption is 6.9 percent. Results for the experiment held on the 18th of May 1993 are given in Figure 3. An agreement of 5.2 percent was achieved.

This disagreement at the 5 to 7 percent level between the predicted and measured radiance may be attributable to at least three sources of error. First, systematic error in the field measurements and their reduction may be present. Second, the MODTRAN calculation of upwelling radiance may contain some error. Third, some change in performance of AVIRIS is likely from the laboratory to flight environment, and finally, the laboratory irradiance and model solar irradiance standard may disagree at some level.

4.0 Spectral Calibration

Through analysis of the atmospheric absorption bands measured in the AVIRIS spectrum, the inflight spectral calibration of AVIRIS may be determined (Green et al., 1988; Green et al., 1990). This analysis has been carried out for the calibration experiments on 30th of May and 9th of October 1992. For the 30th of May, the four AVIRIS spectrometers showed a better than 1 nm agreement between the laboratory spectral calibration and the inflight determination. On the 9th of October however, a -2.4 nm shift in the B spectrometer spectral calibration was measured. This shift is likely related to the fiber to spectrometer connection. In 1993 an improved connector was installed for all AVIRIS spectrometers. It is recommended that the spectral calibration of the B spectrometer be shifted -2.4 nm if required for the proposed data analysis. It is worth noting that AVIRIS was originally designed to a spectral accuracy of 5 nm.

For the 18 May 1993 inflight calibration experiment the spectral calibration in all four spectrometers was determined to agree with the laboratory measurements at better than 0.5 nm.

5.0 AVIRIS Data Precision

For these experiments in 1992 and 1993 the inflight precision was determined based on variation in the signal from a homogeneous portion of Rogers Dry Lake. This precision is presented as signal-to-noise in Figure 4. These signal-to-noise plots have been scaled to the AVIRIS reference radiance (Green et al., 1988) to allow direct comparison. In Figure 5 the precision is presented for 1992 and 1993 as noise equivalent delta radiance. In each of these years AVIRIS vastly exceeded the original signal-to-noise requirement for the sensor.

6.0 Conclusion

In 1992 and 1993 the calibration of AVIRIS was validated for the sensor inflight through a series of field experiments. Based on these experiments, the absolute radiometric calibration of AVIRIS is shown to be approaching 5 percent. In 1992 a spectral shift of -2.4 nm has been identified and is easily corrected by shifting the B spectrometer spectral calibration. In 1993 the inflight spectral calibration is found to correspond to the laboratory determination. Plans are under development to push the radiometric calibration of AVIRIS to 2 percent and spectral calibration to 0.1 nm. The current and planned quality of radiometric and spectral calibration is required for the quantitative algorithms being proposed and tested with AVIRIS data.

7.0 ACKNOWLEDGMENTS

This research was carried out at the Jet Propulsion Laboratory, California Institute of Technology, under contract with the National Aeronautics and Space Administration.

8.0 REFERENCES

- Berk, A., L. S. Bernstein, and D. C. Robertson, "MODTRAN: A moderate resolution model for LOWTRAN 7", Final report, GL-TR-0122, AFGL, Hanscomb AFB, MA, 42 pp., 1989.
- Bruegge, C. J., J. E. Conel, J. S. Margolis, R. O. Green, G. Toon, V. Carrere, R. G. Holm, and G. Hoover, "In-situ atmospheric water-vapor retrieval in support of AVIRIS validation", SPIE Vol. 1298, Imaging spectroscopy of the terrestrial environment, 1990.
- Chrien, T. G., R. O. Green, and M. Eastwood, "Laboratory spectral and radiometric calibration of the Airborne Visible/Infrared Imaging Spectrometer (AVIRIS)", SPIE Vol. 1298, Imaging spectroscopy of the terrestrial environment, 1990.
- Conel, J. E., R. O. Green, R. E. Alley, C. J. Bruegge, V. Carrere, J. S. Margolis, G. Vane, T. G. Chrien, P. N. Slater, S. F. Biggar, P. M. Teillet, R. D. Jackson, and M. S. Moran, "In-flight radiometric calibration of the Airborne Visible/Infrared Imaging Spectrometer (AVIRIS)", SPIE Vol. 924, Recent Advance in sensors, radiometry and data processing for remote sensing, 1988.

Green, R. O., G. Vane, and J. E. Conel, "Determination of aspects of the in-flight spectral, radiometric, spatial and signal-to-noise performance of the Airborne Visible/Infrared Imaging Spectrometer over Mountain Pass, Ca.", Proceeding of the Airborne Visible/Infrared Imaging Spectrometer (AVIRIS) Performance Evaluation Workshop, JPL Pub. 88-38, Jet Propulsion Laboratory, Pasadena, CA, pp. 162-184, 1988.

Green, R. O., J. E. Conel, V. Carrere, C. J. Bruegge, J. S. Margolis, M. Rast, and G. Hoover, "Inflight validation and Calibration of the Spectral and Radiometric Characteristics of the airborne visible/infrared imaging spectrometer (AVIRIS)", Proc. SPIE Conference on Aerospace Sensing, Imaging Spectroscopy of the Terrestrial Environment, Orlando, Florida, 16-20 April 1990.

Green, R. O., J. E. Conel, C. J. Bruegge, J. S. Margolis, V. Carrere, G. Vane and G. Hoover, "In-flight Calibration of the Spectral and Radiometric Characteristics of AVIRIS in 1991", Proc. Third Annual Airborne Geoscience Workshop, JPL Publication 92-14, Jet Propulsion Laboratory, Pasadena, CA, 1992.

Green, Robert O., "Use of Data from the AVIRIS Onboard Calibrator", Proc. Fourth JPL Airborne Geoscience Workshop, JPL Pub. 93-26, Jet Propulsion Laboratory, Pasadena, CA, 1993.

Green, Robert O. and Bo-Cai Gao, "A Proposed Update to the Solar Irradiance Spectrum Used in LOWTRAN and MODTRAN", Proc. Fourth JPL Airborne Geoscience Workshop, JPL Pub. 93-26, Jet Propulsion Laboratory, Pasadena, CA, 1993.

Reagan, J. A., K. Thome, B. Herman, and R. Gall, "Water vapor measurements in the 0.94 micron absorption band: calibration, measurements and data applications", Proc. IGARSS, Ann Arbor, 18-21 May 1987.

9.0 FIGURES

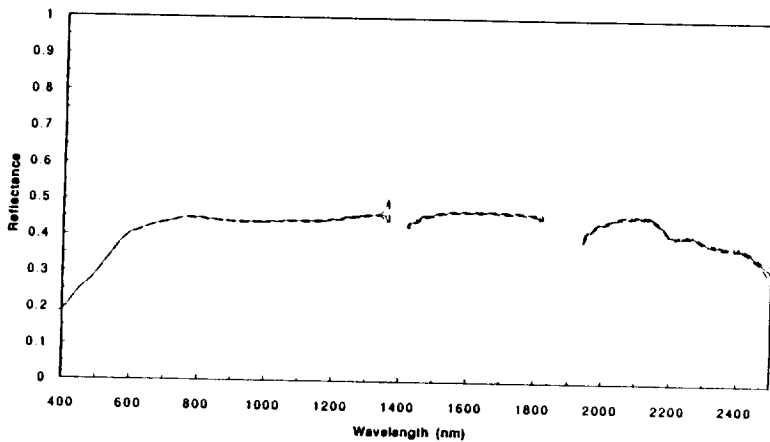


Figure 1. Field measured reflectance and uncertainty for the calibration target on Rogers Dry Lake, California on May 30 1992.

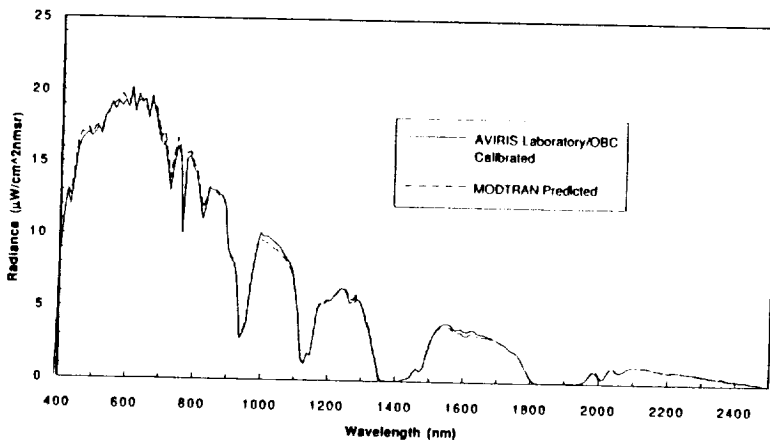


Figure 2. Comparison of the MODTRAN-predicted and AVIRIS-measured radiance for the inflight calibration experiment held on the 30th of May 1992.

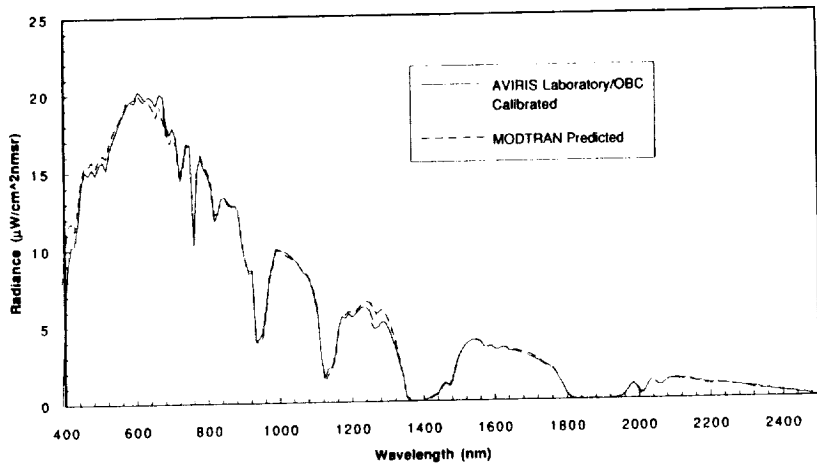


Figure 3. AVIRIS-measured and MODTRAN-predicted radiance for the Rogers Dry Lake inflight calibration experiment of the 18th of May 1993.

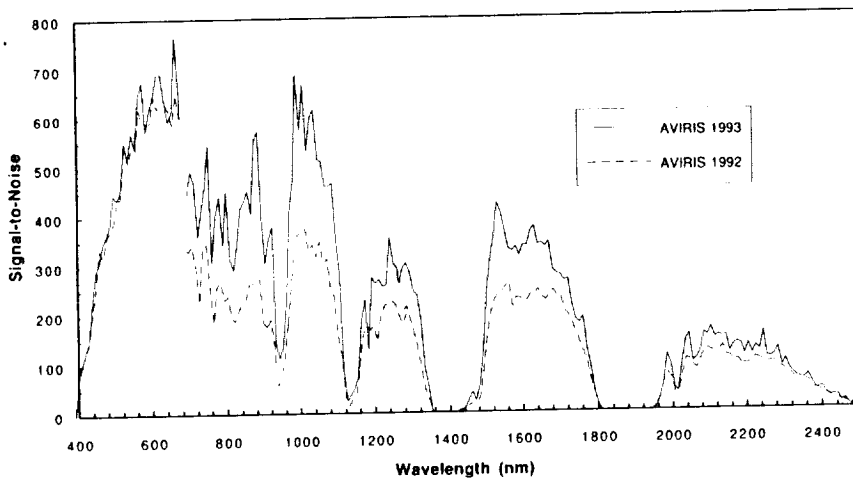


Figure 4. Inflight signal-to-noise for 1992 and 1993.

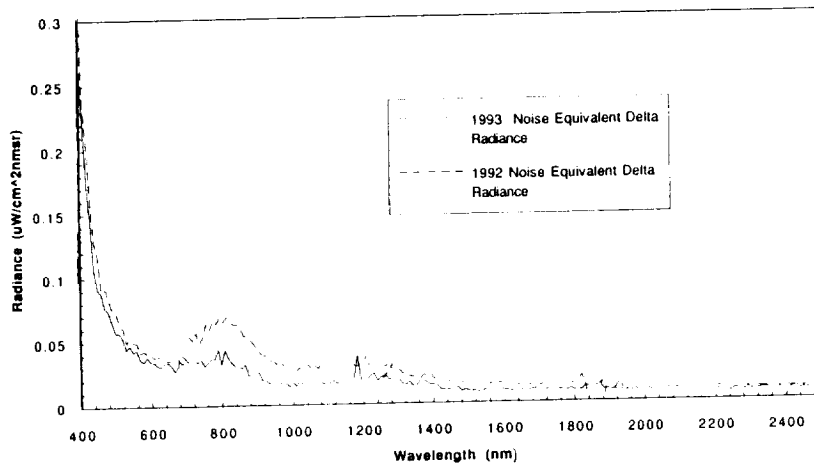


Figure 5. 1992 and 1993 inflight noise equivalent delta radiance.

10.0 SLIDE

Slide 10. AVIRIS color image cube of Moffett Field, California. The top panel is a color composite of three of the 224 AVIRIS spectral channels. The side panels portray the 224 spectral measurements of three of the 224 spatial samples.

Estimation of Aerosol Optical Depth and Additional Atmospheric Parameters for the Calculation of Apparent Reflectance from Radiance Measured by the Airborne Visible/Infrared Imaging Spectrometer

Robert O. Green¹, James E. Conel¹ and Dar A. Roberts²

¹Jet Propulsion Laboratory, California Institute of Technology, Pasadena CA 91109 USA

²University of Washington, Seattle, WA 98195

ABSTRACT

The Airborne Visible/Infrared Imaging Spectrometer measures spatial images of the total upwelling spectral radiance from 400 to 2500 nm through 10 nm spectral channels. Quantitative research and application objectives for surface investigations require inversion of the measured radiance to surface reflectance or surface leaving radiance. To calculate apparent surface reflectance, estimates of atmospheric water vapor abundance, cirrus cloud effects, surface pressure elevation and aerosol optical depth are required. Algorithms for the estimation of these atmospheric parameters from the AVIRIS data themselves are described. From these atmospheric parameters we show an example of the calculation of apparent surface reflectance from the AVIRIS-measured radiance using a radiative transfer code.

1.0 INTRODUCTION

Airborne Visible/Infrared Imaging Spectrometer (AVIRIS) data are acquired as 11 by up to 100 km images with 20 by 20 m spatial resolution. For each spatial element, 224 spectral channels are measured covering the region from 400 to 2500 nm. AVIRIS data are calibrated with respect to their spectral, radiometric and geometric characteristics in the laboratory (Chrien et al., 1990, Chrien et al., 1993); these calibrations are validated in-flight (Conel et al., 1988, Green et al., 1990a, Green et al., 1993). A valid calibration of AVIRIS is required for the radiative transfer based algorithms described.

In this paper, an AVIRIS data set acquired on the 2nd of June 1992 over a portion of the San Francisco peninsula that included the Jasper Ridge ecological preserve is examined. This AVIRIS scene covers 10 by 11 km and includes a variety of vegetated and unvegetated surface cover types. Figure 1 shows an AVIRIS measured radiance spectrum for a green grass area in this scene. The shape of this spectrum results from the solar irradiance, molecular and aerosol scattering of the atmosphere, gas absorption of the atmosphere, illumination geometry and the reflectance of the surface. The algorithms presented to estimate the atmospheric characteristics and to calculate apparent surface reflectance use the MODTRAN2 (Berk et al., 1989) radiative transfer code in conjunction with a non linear least squares spectral fitting (NLLSSF) procedure.

2.0 WATER VAPOR

Over most of the 400 to 2500 nm spectral range the strongest atmospheric absorber is water vapor (Green et al., 1989). In addition to absorbing strongly in this spectral range, the abundance of water vapor in the terrestrial atmosphere varies significantly both spatially and temporally. For example, greater than 20 percent variation in the spatial and temporal distribution of water vapor has been described for four AVIRIS data sets acquired at 12 minute intervals over the same site (Green et al., 1991a).

To compensate for water vapor absorption in AVIRIS spectra, a determination of total path water vapor is required for each spatial element. Water vapor algorithms for AVIRIS have been developed (Conel et al 1988, Green et al 1989, Green, et al. 1991a) based initially on the LOWTRAN7 (Kneizys et al., 1987) and currently on the MODTRAN2 (Berk et al., 1989) radiative transfer code. The latest water vapor algorithm fits the AVIRIS measured radiance for the 940 nm water band to a radiance spectrum generated by the radiative transfer code. A NLLSSF procedure is used with parameters allowing the atmospheric water vapor amount, the reflectance magnitude, the reflectance slope and a scaled surface leaf liquid water absorption spectrum to vary. Figure 2 shows the fit between the AVIRIS measured and the NLLSSF spectrum for the 940 water vapor absorption over the green grass target in the Jasper Ridge AVIRIS data. Over vegetated targets, leaf water absorption in this spectral region must be compensated in the algorithm to avoid incorrect estimation of the atmospheric water vapor. When applied to the entire AVIRIS Jasper Ridge data set a range in atmospheric water vapor from 9 to 22 precipitable millimeters of atmospheric water vapor was mapped.

3.0 CIRRUS CLOUDS

The presence of cirrus clouds will affect the radiance arriving at AVIRIS, and yet such cloud influence may be difficult to detect. The spectral bands in the strong atmospheric water vapor absorption region return signal only when high albedo targets such as cirrus clouds are present in the upper atmosphere. Based on this hypothesis, a cirrus cloud detection algorithm has been tested using the 1380 nm spectral channel of AVIRIS (Gao et al., 1991). On extremely low humidity days or at high altitudes some surface reflected signal may be measured at 1380 nm. Therefore, the AVIRIS channels located in the stronger water vapor absorption regions at 1880 or 2500 nm may provide more unambiguous cirrus cloud detection.

4.0 PRESSURE ELEVATION

In order to compensate for atmospheric absorption due to well mixed atmospheric gases and the effect of atmospheric molecular scattering, an estimate of the surface pressure elevation is required. An algorithm has been developed to estimate the surface pressure elevation (Green et al, 1991b and Green et al., 1993) from the AVIRIS measured radiance. This algorithm assesses the strength of the 760 nm oxygen absorption band measured in the AVIRIS data. The oxygen band strength is calibrated to surface pressure elevation using the oxygen band model in the MODTRAN2 radiative transfer code. Parameters constraining the pressure elevation, the reflectance magnitude and the reflectance slope in the 760 nm spectral region are allowed to vary in the fit. When applied to the entire Jasper Ridge AVIRIS data set, pressure elevations were calculated that ranged from 0 m towards the San Francisco Bay to 800 m in the mountains on the peninsula. These estimates are consistent with the topography of the region.

5.0 AEROSOL OPTICAL DEPTH

Under low visibility conditions the radiance scattered from atmospheric aerosols may comprise a significant proportion of the total radiance reaching AVIRIS. A NLLSSF algorithm has been developed to estimate the aerosol optical depth directly from the measured radiance. This algorithm optimizes the fit between the AVIRIS measured radiance and a MODTRAN2 modeled radiance with the aerosol optical depth as the primary fitting parameter. Parameters modeling the reflectance magnitude, the reflectance slope and leaf chlorophyll absorption are also included in the fitting algorithm. For the Jasper Ridge data an assumption of aerosol type was required. The MODTRAN2 rural aerosol model was used. Aerosol optical depths at 500 nm were calculated for the entire Jasper Ridge AVIRIS data set that ranged from 0.27 in the peninsula mountains to 0.53 near the San Francisco bay. An example of the fit achieved is given in Figure 3.

6.0 REFLECTANCE CALCULATION

Calculation of surface spectral reflectance from the total upwelling radiance measured by AVIRIS using a radiative transfer code has been pursued since the flights of AVIRIS in 1989 (Green, et al. 1990b, Green, et al. 1991b, Green et al. 1993). Using the water vapor, pressure elevation and aerosol optical depth estimates derived in the previous algorithms, the two way transmitted radiance and atmospheric path radiance spectrum are calculated for each spatial element with MODTRAN2. Computer lookup tables are used to accelerate these calculations. With these determined parameters the surface reflectance is calculated directly. Figure 4 shows the calculated reflectance spectra for the green vegetation target. The AVIRIS measured radiance for this target is shown in Figure 1. Inspection of this calculated reflectance spectrum shows compensation for the solar irradiance, atmospheric absorption and atmospherically scattered radiance.

7.0 CONCLUSION

Algorithms are described that allow estimation of the absorption and scattering characteristics of the atmosphere from sensor measured radiance. With estimation of these atmospheric parameters, apparent surface reflectance may be calculated from the measured radiance. The algorithms described use the MODTRAN2 radiative transfer code for modeling the absorption and scattering properties of the atmosphere. To analyze these sensor measured data with a radiative transfer code such as MODTRAN2, an accurate spectral, radiometric and geometric calibration of the data is required. As these algorithms are further validated, they will offer an approach to provide apparent surface reflectance data directly to the users of the AVIRIS data.

8.0 ACKNOWLEDGMENTS

This research was carried out at the Jet Propulsion Laboratory, California Institute of technology, under contract with the National Aeronautics and Space Administration.

9.0 REFERENCES

- Berk, A., L.S. Bernstein, and D.C. Robertson, "MODTRAN: A moderate resolution model for LOWTRAN 7", Final report, GL-TR-0122, AFGL, Hanscomb AFB, MA, 42 pp., 1989
- Chrien, T. G., R. O. Green, and M. L. Eastwood, "Accuracy of the Spectral and Radiometric Laboratory Calibration of the Airborne Visible/Infrared Imaging Spectrometer", Proc. SPIE Conference on Aerospace Sensing, Imaging Spectroscopy of the Terrestrial Environment, Orlando, Florida, 16-20 April, 1990.
- Chrien, Thomas G. and Robert O. Green, "Instantaneous Field of View and Spatial Sampling of the Airborne Visible/Infrared Imaging Spectrometer (AVIRIS)", Fourth JPL Airborne Geoscience Workshop, JPL Publication 93-26, Jet Propulsion Laboratory, Pasadena, CA, 1993.
- Conel, J. E., R. O. Green, R. E. Alley, C. J. Bruegge, V. Carrere, J. S. Margolis, G. Vane, T. G. Chrien, P. N. Slater, S. F. Biggar, P. M. Teillet, R. D. Jackson and M. S. Moran, "In-flight radiometric calibration of the Airborne Visible/Infrared Imaging Spectrometer (AVIRIS)", SPIE Vol. 924, Recent Advance in sensors, radiometry and data processing for remote sensing, 1988.
- Gao, B.-C., A. F. H. Goetz and W. J. Wiscomb, "Cirrus Cloud Detection from Airborne Imaging Spectrometer Data Using the 1.38 μ m Water Vapor Band", Geophys. Res. Lett, Vol. 20 no. 4 p. 301-304, 1991.
- Green, R. O., V. Carrere and J. E. Conel, "Measurement of atmospheric water vapor using the Airborne Visible/Infrared Imaging Spectrometer", Proc. ASPRS conference on Image Processing '89, Reno, Nevada, 23-26 April 1989.
- Green, R.O., J.E. Conel, V. Carrere, C.J. Bruegge, J.S. Margolis, M.Rast, and G. Hoover, "Determination of the in-flight spectral and radiometric characteristics of the airborne visible/infrared imaging spectrometer (AVIRIS)", Proceedings of the Second Airborne Visible/Infrared Imaging Spectrometer (AVIRIS) Workshop, JPL Pub. 90-54, Jet Propulsion Laboratory, Pasadena, CA, pp. 15-34, 1990a.
- Green, Robert O., "Retrieval of Reflectance from Calibrated Radiance Imagery Measured by the Airborne Visible/Infrared Imaging Spectrometer (AVIRIS) for Lithological Mapping of the Clark Mountains, California", Proc. Second AVIRIS Workshop, JPL Publication 90-54, Jet Propulsion Laboratory, Pasadena, CA, pp. 167-175, 1990b.
- Green, Robert O., James E. Conel, Jack S. Margolis, Carol J. Bruegge, and Gordon L. Hoover, "An Inversion Algorithm for Retrieval of Atmospheric and leaf Water Absorption From AVIRIS Radiance With Compensation for Atmospheric Scattering", Proc. Third AVIRIS Workshop, JPL Publication 91-28, Jet Propulsion Laboratory, Pasadena, CA, pp. 51-61, 1991a.
- Green, Robert O., "Retrieval of Reflectance From AVIRIS-Measured Radiance Using a Radiative Transfer Code", Proc. Third AVIRIS Workshop, JPL Publication 91-28, Jet Propulsion Laboratory, Pasadena, CA, pp. 200-210, 1991b.
- Green, Robert O., James E. Conel, Mark Helmlinger, Jeannette van den Bosch, Chris Chovit, "Inflight Calibration of AVIRIS in 1992 and 1993", Fourth JPL Airborne Geoscience Workshop, JPL Publication 93-26, Jet Propulsion Laboratory, Pasadena, CA, 1993.
- Green, Robert O., James E. Conel and Dar A. Roberts, "Estimation of Aerosol Optical Depth and Calculation of Apparent Surface Reflectance from Radiance Measured by the Airborne Visible-Infrared Imaging Spectrometer (AVIRIS) Using MODTRAN2", SPIE Conf. 1937, Imaging Spectrometry of the Terrestrial Environment, in press, 12 p. 1993.
- Kneizys, F.X., E.P. Shettle, G.P. Anderson, L.W. Abrew, J.H. Chetwynd, J.E.A. Shelby, and W.O. Gallery, Atmospheric Transmittance/Radiance; computer Code LOWTRAN 7, AFGL Hanscomb AFB, MA., 1987.

10.0 FIGURES

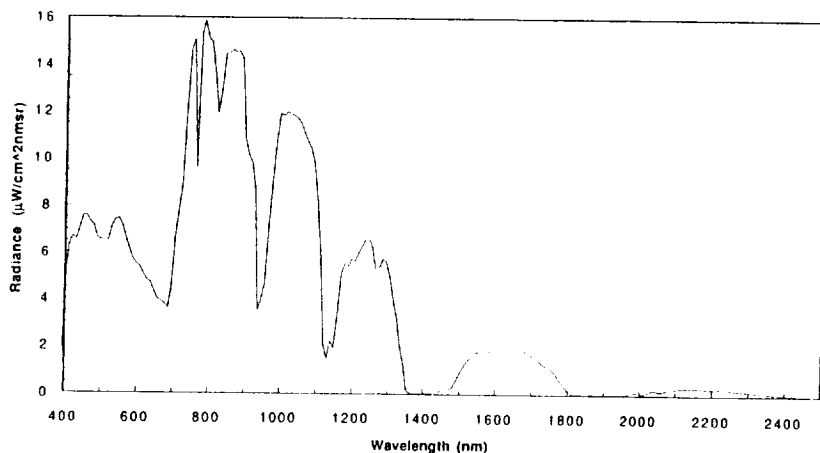


Figure 1. AVIRIS measured upwelling radiance spectrum of a green grass target at Jasper Ridge, CA.

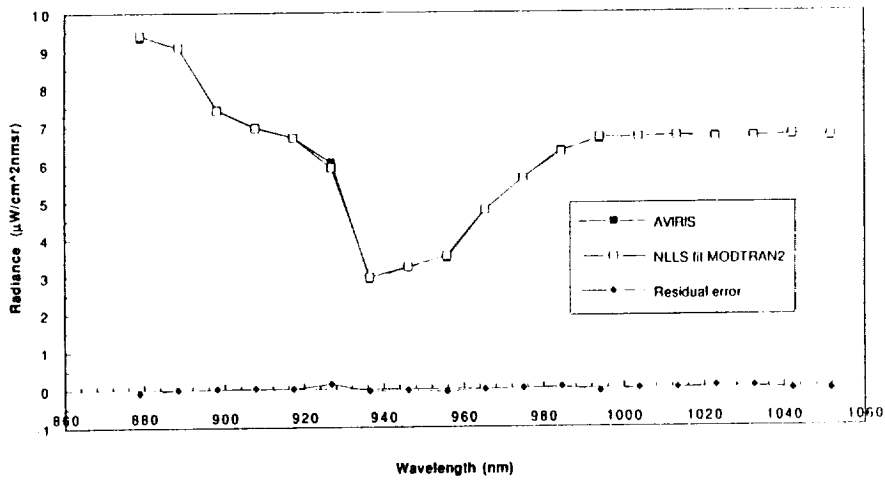


Figure 2. Fit and residual between an AVIRIS measured radiance spectrum and a NLLSF spectrum for estimation of total path atmospheric water vapor.

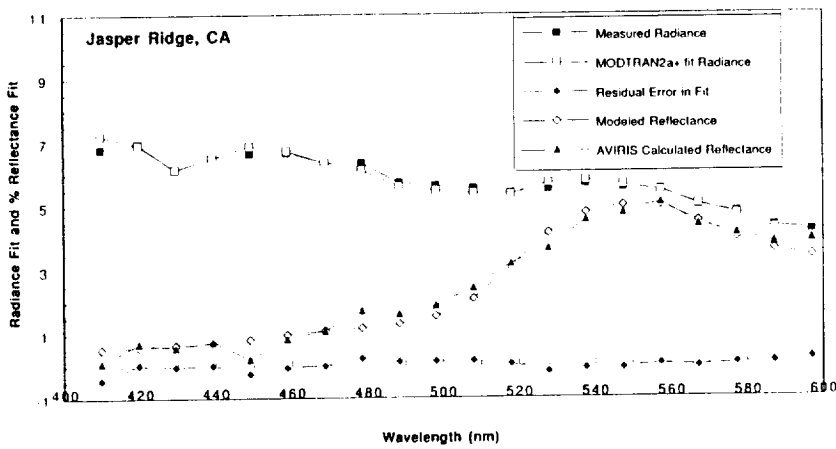


Figure 3. The nonlinear least squares fit between the AVIRIS measured radiance and the MODTRAN2 modeled radiance for estimation of aerosol optical depth. The modeled reflectance required for this fit in the 400 to 600 nm spectral region is also shown as is the resulting AVIRIS calculated reflectance.

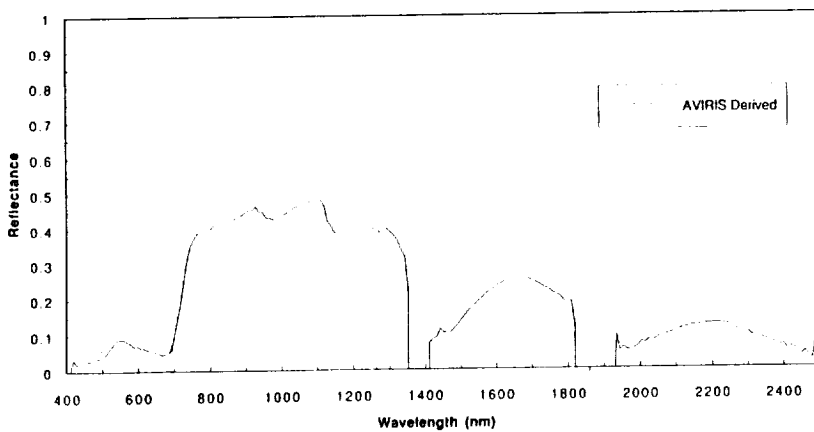


Figure 4. Calculated apparent surface reflectance for the green grass target.

Use of the Airborne Visible/Infrared Imaging Spectrometer to Calibrate the Optical Sensor on board the Japanese Earth Resources Satellite-1

Robert O. Green¹, James E. Conel¹, Jeannette van den Bosch,¹ and Masanobu Shimada²

¹Jet Propulsion Laboratory, California Institute of Technology, Pasadena CA 91109 USA

²Earth Observing Center/NASDA, 1401 Ohashi, Hatoyama-Machi, Hiki-Gun, Saitama-Ken, JAPAN

ABSTRACT

In this paper, we describe an experiment to calibrate the Optical Sensor on board the Japanese Earth Resources Satellite-1 with data acquired by the Airborne Visible/Infrared Imaging Spectrometer (AVIRIS).

On the 27th of August 1992 both the OPS and AVIRIS acquired data concurrently over a calibration target on the surface of Rogers Dry Lake, California. The high spectral resolution measurements of AVIRIS have been convolved to the spectral response curves of the OPS. These data in conjunction with the corresponding OPS digitized numbers have been used to generate the radiometric calibration coefficients for the eight OPS bands. This experiment establishes the suitability of AVIRIS for the calibration of spaceborne sensors in the 400 to 2500 nm spectral region.

1.0 INTRODUCTION

Calibration of remote sensing instruments is required: 1) to derive quantitative parameters of the Earth's surface, 2) to measure changes from region to region and from time to time, 3) to compare data between different sensors, and 4) to analyze measured data with computer model predictions.

The Japanese Earth Resources Satellite-1 (JERS-1) was launched in early 1992 with an Optical Sensor (OPS). OPS has eight bands in spectral region from 400 to 2500 nm. These bands range in width from 60 to 130 nm and are described in Table 1. OPS has approximately 20 m spatial resolution with a 75 km cross-track swath.

AVIRIS operates on a platform at 20 km altitude and measures the total upwelling spectral radiance from 400 to 2500 nm in the spectrum at 10 nm spectral intervals. Data are acquired as 11 km by up to 100 km images with 20 m spatial resolution. AVIRIS is calibrated in the laboratory before and after each flight season (Chrien et al., 1990). The laboratory calibration is validated inflight at the beginning, middle and end of each flight season (Conel et al., 1988, Green et al., 1990, and Green et al., 1992). This work has shown AVIRIS to have a radiometric calibration of better than 7 percent inflight.

The high spectral resolution and validated calibration of AVIRIS provide the basis for this experiment to calibrate OPS on-orbit (Green et al., 1993). Figure 1 shows a plot of the AVIRIS spectral coverage with the JERS-1 OPS spectral response curves and a transmission spectrum of the atmosphere.

2.0 JERS1/AVIRIS CALIBRATION EXPERIMENT

On August 27th a calibration experiment was carried out under clear sky conditions at Rogers Dry Lake. This site is located approximately 100 km north of Los Angeles in the State of California. Both JERS-1 OPS and AVIRIS imaged a calibration target on the dry lake bed on the 27th of August (see Slide 9). The calibration target was a homogeneous 40 by 200 meter area of the lake bed with blue tarps placed at each end. The spectral signature of these tarps allows unambiguous location of the lake bed calibration target in the AVIRIS imagery. Once located in the AVIRIS imagery, data from the corresponding region in the OPS imagery are extracted. For this experiment, the flight path of AVIRIS was oriented orthogonal to the JERS-1 ground track and extended to cover the entire OPS swath. To limit the effects from time-variable atmospheric transmittance, the AVIRIS overpass was synchronized with that of the JERS-1 OPS data acquisition.

3.0 AVIRIS DATA ANALYSIS

Total upwelling radiance spectra of the calibration target were extracted from the AVIRIS data. These data were calibrated based on the AVIRIS calibration files and calibration algorithms

250-19
41020
J. 4

(Green et al., 1991). The average AVIRIS spectrum of the 40 m by 200 m calibration target at Rogers Dry Lake is shown in Figure 2. To estimate the upwelling radiance at the top of the atmosphere, a transmittance spectrum from 20 km to 100 km calculated by the MODTRAN2a radiative transfer code (Berk et al., 1989) was used. Less than 2 percent absorption due to stratospheric ozone was calculated for the visible portion of the spectrum. At 760 nm absorption due to oxygen and at 2050 nm absorption due to carbon dioxide were also calculated. This transmittance spectrum was multiplied by the AVIRIS radiance spectra to correct the AVIRIS spectrum to the top of the atmosphere.

4.0 CALIBRATION OF JERS-1 OPS

Spectral response curves of the OPS bands were measured prior to launch of the JERS-1 satellite. These measured OPS curves were spline fit to the AVIRIS spectral channel positions. The resulting spline fit spectral response curves are shown in Figure 3. The high spectral resolution of AVIRIS allows accurate modeling of the eight OPS bands. Spectral weighting functions were developed from these spectral response curves to convolve the AVIRIS upwelling radiance to the eight bands of the JERS-1 OPS. AVIRIS derived upwelling radiance's for OPS bands are shown in Figure 4 in conjunction with the top of the atmospheric corrected AVIRIS spectrum.

From the uncalibrated JERS-1 OPS image of Rogers Dry Lake the digitized numbers (DN) of the calibration target were extracted. The dark signal of each OPS band was estimated based on a scene acquired at night and found to be 0.0 except for band 6 which had a value of 0.4 DN. OPS radiometric calibration coefficients (RCCs) are calculated from the OPS DN and the AVIRIS measured radiance convolved to OPS channels. For the 27th of August 1992 the RCCs for OPS are given in Table 2 in units of microwatts per square-centimeter nanometer steradian digitized-number ($\mu\text{W}/\text{cm}^2 \text{ nm sr DN}$). The nominal prelaunch RCCs are given in Table 2 as well.

5.0 FUTURE WORK

Work is planned to use the 100 km AVIRIS flight line to evaluate the variation in the calibration across the OPS swath derived from the 4096 different cross-track detectors for each OPS band.

During October 1992 and June 1993, JERS-1 OPS and AVIRIS acquired additional calibration data sets. These data will be analyzed to determine changes in the calibration of OPS through time.

Analysis of JERS-1 OPS onboard calibrator data and concurrent AVIRIS data will be used to establish the calibration for the OPS onboard radiometric source.

Finally, we will investigate the possibility of solving for the spectral band shape of JERS-1 OPS using concurrently acquired AVIRIS and OPS data over spectrally diverse targets.

6.0 CONCLUSION

JERS-1 OPS has been calibrated on orbit with the high altitude radiance spectra measured by the AVIRIS sensor. This experiment establishes the use of AVIRIS as a calibrated spectroradiometer at 20 km altitude for the calibration of current and future spaceborne sensors in this spectral region.

7.0 ACKNOWLEDGMENTS

This research was carried out at the Jet Propulsion Laboratory, California Institute of Technology, under contract with the National Aeronautics and Space Administration. Support for this experiment was provided by the National Space Development Agency of Japan.

8.0 REFERENCES

- Berk, A., L. S. Bernstein, and D. C. Robertson, "MODTRAN: A moderate resolution model for LOWTRAN 7", Final report, GL-TR-0122, AFGL, Hanscomb AFB, MA, 42 pp., 1989.
- Chrien, T. G., et al., "Laboratory spectral and radiometric calibration of the Airborne Visible/Infrared Imaging Spectrometer (AVIRIS)," SPIE Vol. 1298, Imaging spectroscopy of the terrestrial environment 1990.

Conel, J. E., et al., "In-flight radiometric calibration of the Airborne Visible/Infrared Imaging Spectrometer (AVIRIS)," SPIE Vol. 924, Recent Advance in sensors, radiometry and data processing for remote sensing, 1988.

Green, R. O., et al., "Determination of the In-Flight Spectral and Radiometric Characteristics of the Airborne Visible/Infrared Imaging Spectrometer (AVIRIS)", Proc. Second AVIRIS Workshop, JPL Publication 90-54, Jet Propulsion Laboratory, Pasadena, CA, pp. 15-22, 1990.

Green, R. O. et al., "Calibration of AVIRIS Digitized Data", Proc. Third AVIRIS Workshop, JPL Publication 91-28, Jet Propulsion Laboratory, Pasadena, CA, pp. 109-118, 1991.

Green, R. O. et al., "In-flight Calibration of the Spectral and Radiometric Characteristics of AVIRIS in 1991", Proc. Third Annual Airborne Geoscience Workshop, JPL Publication 92-14, Jet Propulsion Laboratory, Pasadena, CA, 1992.

Green, Robert O., James E. Conel, Jeannette van den Bosch, Masanobu Shimada and Masao Nakai, "On-orbit Calibration of the Japanese Earth Resources Satellite-1 Optical Sensor Using the Airborne Visible-Infrared Imaging Spectrometer", IGARSS'93, Tokyo Japan, Optical Sensor and Calibration, in press, 1993.

9.0 Tables

Table 1. JERS-1 OPS data characteristics

SPECTRAL		
Band	Center nm	Width nm
1	560	80
2	660	60
3	810	100
4	810	100*
5	1655	110
6	2065	110
7	2190	120
8	2335	130
GEOMETRIC		
Field of view	75 km	
Instantaneous field of view	18.3*24.2 m	
*Stereo angle (881 nm)	15.3 degrees	

Table 2. OPS Radiometric Calibration Coefficients from the JERS-1/AVIRIS Calibration Experiment

Band	Radiance	DN	Dark	AVIRIS RCC*	Prelaunch RCC*
1	16.26	25.58	0.00	0.6356	0.5400
2	16.49	33.78	0.00	0.4882	0.4098
3	12.36	26.93	0.00	0.4589	0.4133
4	12.30	27.06	0.00	0.4545	0.3983
5	02.83	40.23	0.00	0.0704	0.0653
6	00.91	23.59	0.40	0.0393	0.0336
7	00.97	29.84	0.00	0.0325	0.0269
8	00.57	23.21	0.00	0.0245	0.0200

*($\mu\text{W} / \text{cm}^2 \text{ nm sr DN}$)

10.0 Slide

Slide 9, which shows the AVIRIS image of Rogers Dry Lake calibration site, is located in the back pocket of the book. In this slide the vertical panels portray the 224 spectral measurements underlying each 20 m spatial element. A portion of the homogeneous playa surface was used as the calibration target for the AVIRIS/OPS calibration experiment.

11.0 Figures

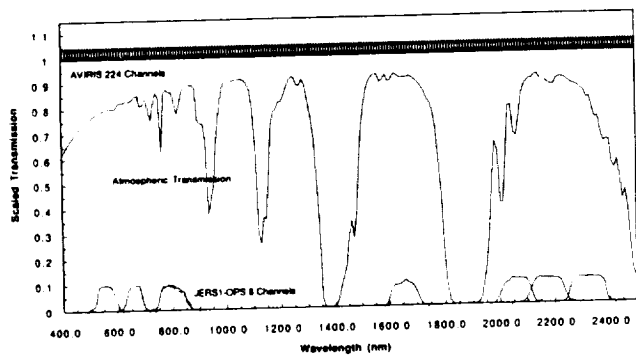


Figure 1. Depiction of the 8 JERS-1 OPS bands, typical atmospheric transmission and the 224 AVIRIS spectral channels.

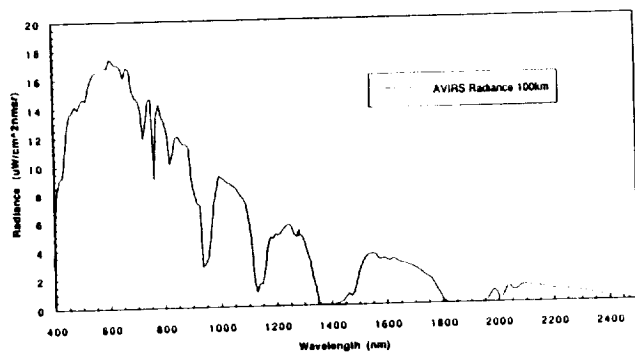


Figure 2. AVIRIS spectrum of upwelling radiance from calibration target.

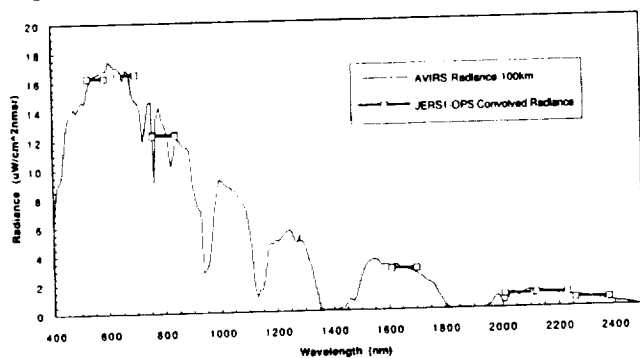


Figure 3. JERS-1 OPS spectral response curves spline fit to AVIRIS spectral channel positions.

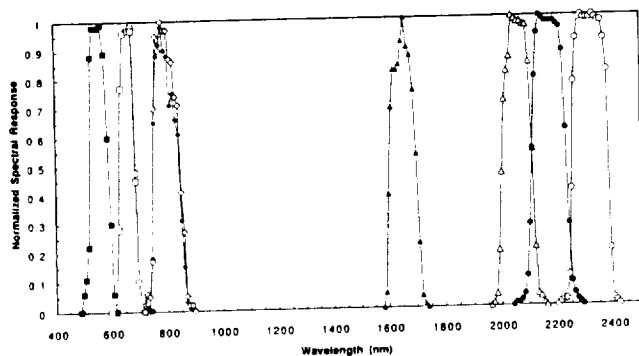


Figure 4. AVIRIS measured radiance in JERS-1 OPS spectral bands and AVIRIS spectrum corrected to top of the atmosphere.

A Proposed Update to the Solar Irradiance Spectrum Used in LOWTRAN and MODTRAN

Robert O. Green¹ and Bo-Cai Gao²

¹Jet Propulsion Laboratory, California Institute of Technology, Pasadena, CA 91109

²Goddard Space Flight Center, Greenbelt, MD

201-12
41021
p. 4

ABSTRACT

The calibrated upwelling radiance spectra measured by AVIRIS are increasingly being analyzed with radiative transfer codes. Analysis of AVIRIS data with the LOWTRAN and MODTRAN radiative transfer codes has led to indications of an error in the solar irradiance spectra used by these codes. This paper presents evidence for the error and a proposed update to the solar irradiance spectra used by LOWTRAN&MODTRAN.

1.0 INTRODUCTION

AVIRIS measures the total upwelling radiance at 20 km altitude through 224 spectral channels from 400 to 2500 nm. The upwelling radiance measured results from solar energy being transmitted, scattered and reflected from the atmosphere and surface. Quantitative analysis of calibrated AVIRIS radiance with radiative transfer codes requires accurate knowledge of the solar irradiance spectrum from 400 to 2500 nm at AVIRIS spectral resolution. The LOWTRAN (Kneizys et al., 1987) and MODTRAN (Berk et al., 1989) radiative transfer codes are increasingly used in the analysis of AVIRIS measured radiance. In this paper we describe the evidence for spectrally distinct errors in the solar irradiance spectrum shared by the codes. We present a proposed update to the LOWTRAN&MODTRAN solar irradiance.

2.0 LOWTRAN&MODTRAN SOLAR IRRADIANCE ERROR

A common radiative transfer based analysis of AVIRIS data is the inversion of AVIRIS measured radiance to apparent surface reflectance (Green et al., 1990; Green et al., 1993; Gao et al., 1992). When the MODTRAN radiative transfer code is used for this calculation, systematic and spectrally distinct discrepancies have been encountered (Green et al., 1992). This problem has been mitigated by using a MODTRAN based inflight calibration as the radiometric calibration for AVIRIS in the calculation of apparent reflectance. This approach effectively cancels any errors in the MODTRAN solar irradiance spectrum. An example of this discrepancy caused by using the LOWTRAN&MODTRAN solar irradiance is shown in Figure 1. In this figure the MODTRAN calculated reflectance and concurrently field measured field reflectance for the Rogers Dry Lake calibration target is given for the 2000 to 2500 nm spectral region. Also in this figure, the percent difference between the LOWTRAN&MODTRAN solar irradiance and proposed solar irradiance update is given. The erroneous features in the reflectance and irradiance difference correspond closely.

3.0 PROPOSED UPDATE SOLAR IRRADIANCE

The proposed update solar irradiance is based on the Neckels and Labs continuum spectrum (Neckels et al., 1984). The spectrum has been modified to include transmission of the solar atmosphere as measured by the ATMOS sensor on board the Space Shuttle. A plot of the LOWTRAN&MODTRAN solar irradiance spectrum and proposed update is given in Figure 2. In addition to the disagreement in the 2000 nm region a significant departure is evident near the 940 nm region. This is a region of strong water vapor absorption in the Earth's atmosphere and is consistent with the aircraft sensor platform source of the LOWTRAN&MODTRAN irradiance spectra.

A percent difference plot between the LOWTRAN&MODTRAN solar irradiance spectrum and proposed update is given in Figure 3. The spectrally distinct differences in the 2000 nm region approach 20 percent in magnitude. Discrepancies of 5 percent are seen between 900 and 2500 nm.

As a validation of the proposed update to the solar irradiance, the surface reflectance of the calibration target at Rogers Dry Lake was recalculated. A comparison of the calculated reflectance and field measured reflectance using the update irradiance is given in Figure 4. This improvement

in agreement between the measured and calculated reflectance shows the importance of the solar irradiance in calculating parameters from measured upwelling spectral radiance.

It is planned to provide this update to the solar irradiance spectrum to the developers of LOWTRAN&MODTRAN (Anderson, pers. comm.)

4.0 CONCLUSION

In the region from 900 to 2500 nm spectrally distinct errors in the solar irradiance spectrum are shown. These discrepancies are largely compensated for with use of the proposed update to the solar irradiance. Continued improvement of knowledge of the solar irradiance spectrum is required as quantitative algorithms are applied to measurement of radiance in this spectral region.

5.0 ACKNOWLEDGMENTS

This research was carried out at the Jet Propulsion Laboratory, California Institute of Technology, under contract with the National Aeronautics and Space Administration.

6.0 REFERENCES

- Anderson, G. P., Personal Communication, AFGL, Hanscomb AFB, MA, 1993.
- Berk, A., L. S. Bernstein, and D. C. Robertson, "MODTRAN: A moderate resolution model for LOWTRAN 7", Final report, GL-TR-0122, AFGL, Hanscomb AFB, MA, 42 pp., 1989.
- Gao, Bo-Cai, Dathleen Heidebrecht, and Alexander Goetz, "Software for the Derivation of Scaled Surface Reflectances From AVIRIS Data", Proc. of the Third JPL Airborne Geoscience Workshop, JPL Pub. 92-14, Jet Propulsion Laboratory, Pasadena, CA, 1992.
- Green, Robert O., "Retrieval of Reflectance from Calibrated Radiance Imagery Measured by the Airborne Visible/Infrared Imaging Spectrometer (AVIRIS) for Lithological Mapping of the Clark Mountains, California", Proc. Second AVIRIS Workshop, JPL Publication 90-54, Jet Propulsion Laboratory, Pasadena, CA, pp. 167-175, 1990.
- Green, Robert O., James E. Conel and Thomas G. Chrien, "Airborne Visible-Infrared Imaging Spectrometer (AVIRIS): Sensor System, Inflight Calibration and Reflectance Calculation", International Symposium on Spectral Sensing Research, pp. 22, in press, 1992.
- Green, Robert O., James E. Conel and Dar A. Roberts, "Estimation of Aerosol Optical Depth and Calculation of Apparent Surface Reflectance from Radiance Measured by the Airborne Visible-Infrared Imaging Spectrometer (AVIRIS) Using MODTRAN2", SPIE Conf. 1937, Imaging Spectrometry of the Terrestrial Environment, in press, 1993.
- Kneizys, F. X., E. P. Shettle, G. P. Anderson, L. W. Abrew, J. H. Chetwynd, J. E. A. Shelby, and W. O. Gallery, "Atmospheric Transmittance/Radiance; computer Code LOWTRAN 7", AFGL, Hanscom AFB, MA, 1987.
- Neckels, Heinz, and Dietrich Labs, "The Solar Radiation Between 3300 and 12500 A.", Sol. Phys, 90, pp. 205-258, 1984.

7.0 FIGURES

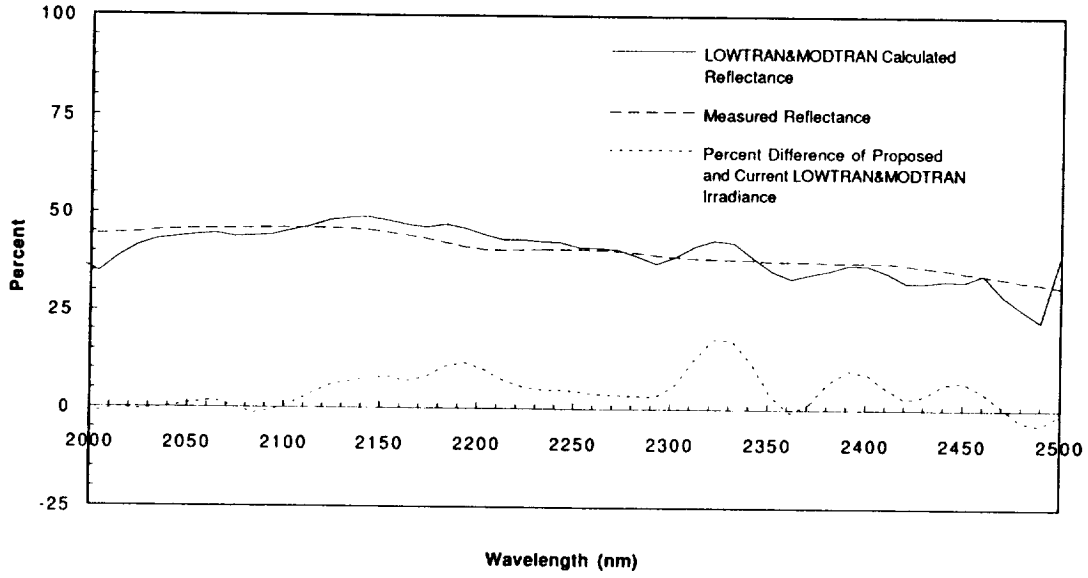


Figure 1. Comparison of LOWTRAN&MODTRAN calculated reflectance and field measured reflectance with the percent difference between the LOWTRAN&MODTRAN and the proposed update to the solar irradiance.

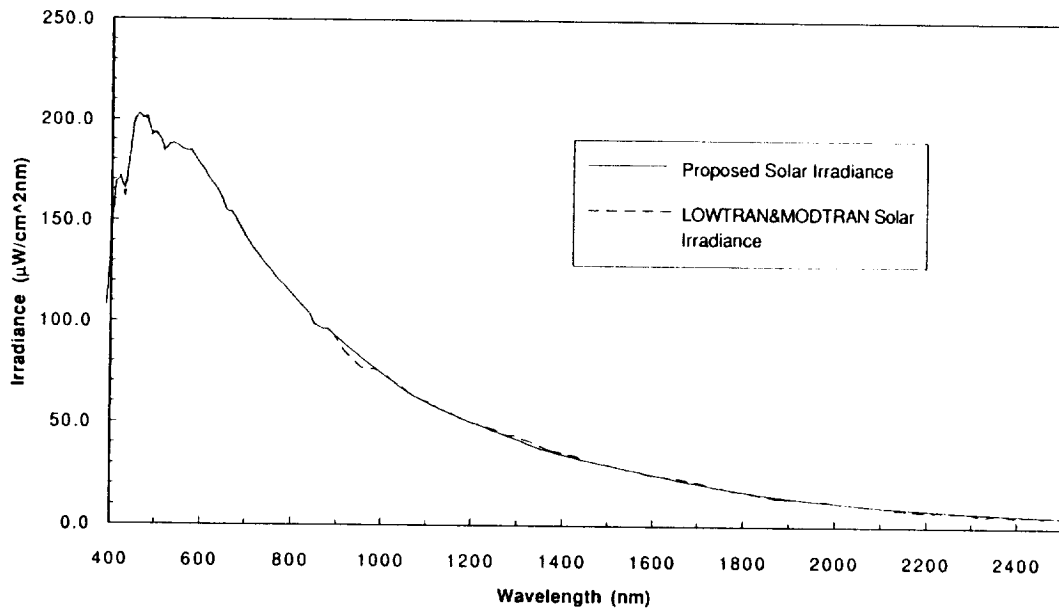


Figure 2. LOWTRAN&MODTRAN solar irradiance spectrum and proposed update.

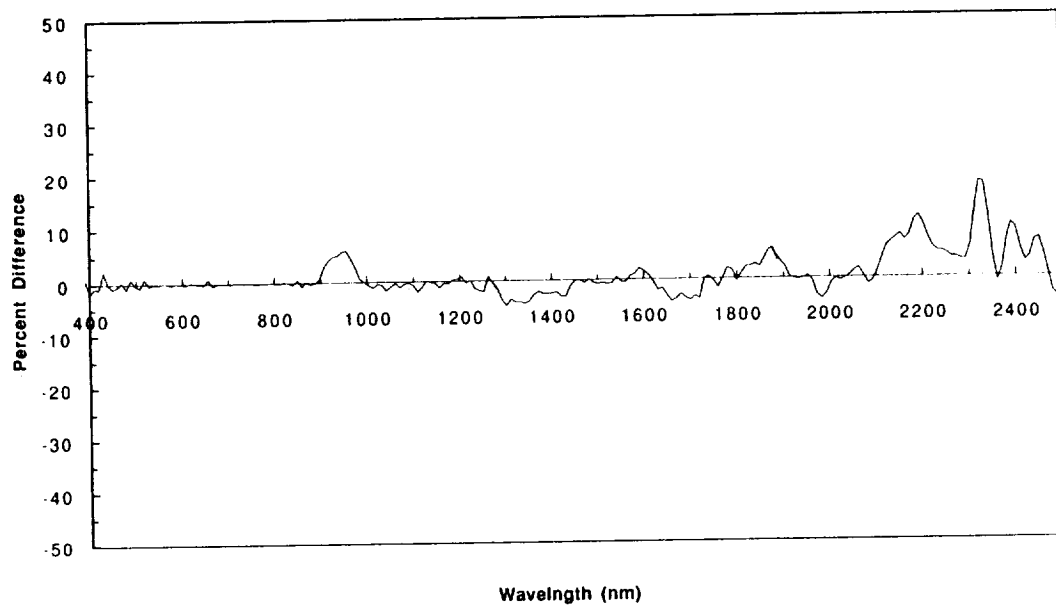


Figure 3. Percent difference between LOWTRAN&MODTRAN and the proposed update to the solar irradiance.

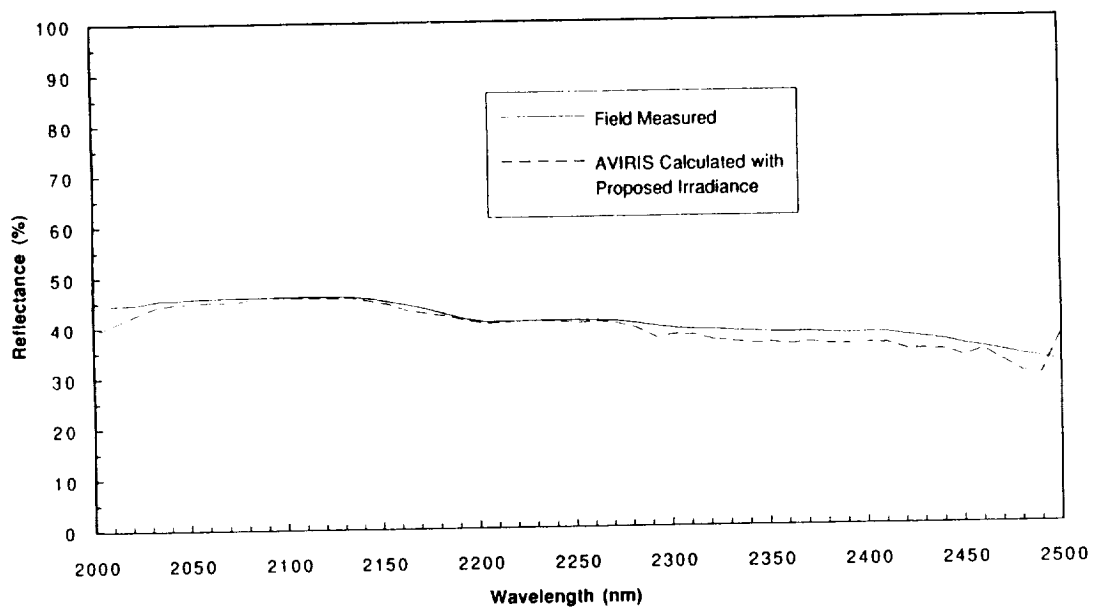


Figure 4. Comparison of radiative transfer calculated reflectance using proposed solar irradiance with field measured reflectance.

22-43
111022
p. 4

A Role for AVIRIS in the Landsat and Advanced Land Remote Sensing System Program

Robert O. Green and John J. Simmonds

Jet Propulsion Laboratory, California Institute of Technology, Pasadena, CA 91109

ABSTRACT

As a calibrated imaging spectrometer flying at a 20 km altitude, AVIRIS may contribute to the Landsat and the Advanced Land Remote Sensing System efforts. These contributions come in the areas of: 1) on-orbit calibration, 2) specification of new spectral bands, 3) validation of algorithms and 4) investigation of an imaging spectrometer for the Advanced Land Remote Sensing System.

1.0 INTRODUCTION

AVIRIS is a NASA-sponsored Earth-looking imaging spectrometer that measures the total upwelling radiance from 400 to 2500 nm through 224 imaging channels. A plot showing the 224 channels of AVIRIS and the six bands of the Landsat Thematic Mapper is shown in Figure 1. For AVIRIS, typically up to 10 images of 11 by up to 100 km at 20 m spatial resolution are acquired on a single flight. AVIRIS data are rigorously calibrated in the laboratory (Chrien et al., 1990) and validated in flight with respect to their spectral and radiometric characteristics. These characteristics are summarized in Table 1.

Currently Landsat has 6 bands in the 400 to 2500 nm spectral region. There is an increasing requirement that Landsat data be well calibrated to fulfill the measurement and monitoring roles of the Landsat data. Under the Advanced Land Remote Sensing System (ALRSS) there are options to add to the spectral coverage of sensors beyond Landsat 7. In this paper we describe potential contributions by AVIRIS in the areas of calibration and measurement augmentation to Landsat and ALRSS program.

2.0 RADIOMETRIC AND SPECTRAL CALIBRATION

Valid radiometric calibration is essential for many of the current and proposed algorithms and monitoring activities of Landsat. Because AVIRIS is a calibrated imaging spectrometer operating at 20 km altitude, underflights of Landsat by AVIRIS may be used to validate and/or establish the on orbit spectral and radiometric characteristics.

Spectral calibration algorithms are being developed to use concurrently acquired AVIRIS and Landsat-type data. These algorithms use a concurrently acquired AVIRIS and spaceborne sensor data to solve directly for the spectral band shapes. Concurrently acquired data over spectrally varying surface and atmospheric targets are required. From these data, a least squared error fitting algorithm is used to calculate the spectral band shape of the spaceborne sensor.

The radiometric calibration of Landsat may be established through underflight of Landsat by AVIRIS. Because AVIRIS is calibrated in flight (Green et al., 1993a) and AVIRIS measures data at a 20 km altitude, a Landsat calibration may occur in a nonclear sky or even cloudy conditions. This is a significant operational advantage over ground based calibrations.

AVIRIS is currently being used in this mode to calibrate the Optical Sensor (OPS) on board the Japanese Environmental Satellite JERS-1 (Green et al., 1993b). A plot showing the accurate convolution of the AVIRIS channels to the JERS-1 OPS bands is given in Figure 2. In Figure 3 the upwelling OPS radiance derived from AVIRIS is given. In the Landsat program, AVIRIS could be used in this mode beginning with Landsat 6.

3.0 SPECIFICATION OF FUTURE ALRSS BANDS

Analysis of AVIRIS data sets may be used to specify future bands for measuring and monitoring the Earth's surface as well as collecting information for the atmospheric correction of ALRSS data. Based on research with AVIRIS data there is evidence that additional spectral bands would improve measurements of: soils and rocks; manmade objects; vegetation; snow and ice; as well as coastal and inland waters.

In addition, based on analysis of AVIRIS data sets, ALRSS bands might be specified to measure: water vapor, aerosols, surface pressure, cirrus clouds, etc. for atmospheric correction (Green et al., 1993c; Goetz et al., 1993).

AVIRIS data may be used to investigate the optimal spatial resolution of ALRSS bands. For example, bands devoted to atmospheric characterization may not require the same high spatial resolution required for the measurement of surface features.

4.0 TESTING AND VALIDATION OF ALGORITHMS

Once a set of bands have been designated for the ALRSS sensor, AVIRIS data may be acquired and spectrally convolved to the exact band shapes. These simulated ALRSS images may be used to test proposed algorithms for the surface and atmosphere under a range of conditions. With this preparation, validated algorithms will be in place in advance of the spaceborne sensor launch.

5.0 AN IMAGING SPECTROMETER ON BOARD THE ALRSS

AVIRIS data are currently used for investigations spanning the disciplines of: terrestrial ecology; geology and soils oceanography and limnology; hydrology; atmospheric gas and aerosol investigations; snow hydrology; general spectral signature detection and evaluation; calibration; and algorithm development. It has been proposed to support these investigations and applications globally that an imaging spectrometer be included on an ALRSS. AVIRIS data may be used to evaluate requirements and tradeoffs between the spectral and spatial coverage for such a sensor on the ALRSS.

6.0 CONCLUSION

AVIRIS currently measures data for NASA investigators from the 20 km altitude of the ER-2 aircraft platform. Work is ongoing to maintain and improve the performance characteristics of the AVIRIS sensor. The current spectral, radiometric, geometric and calibration characteristics of AVIRIS allow it to fulfill an important role in the calibration of Landsat sensors. In addition, AVIRIS may be used to specify new bands and new capabilities on the ALRSS.

7.0 ACKNOWLEDGMENTS

This research was carried out at the Jet Propulsion Laboratory, California Institute of Technology, under contract with the National Aeronautics and Space Administration.

8.0 REFERENCES

- Chrien, T. G., R. O. Green, and M. Eastwood, "Laboratory spectral and radiometric calibration of the Airborne Visible/Infrared Imaging Spectrometer (AVIRIS)", SPIE Vol. 1298, Imaging spectroscopy of the terrestrial environment, 1990.
- Goetz, A. H. F., "Effects of Water Vapor and Cirrus Clouds on TM-Derived Apparent Reflectance Based on AVIRIS Experience", Workshop on Atmospheric Correction of Landsat Imagery, 29 June to 1 July, Torrance, CA, 1993.
- Green, Robert O. and Bo-Cai Gao, "Inflight Calibration of AVIRIS in 1992 and 1993", Proc. Fourth JPL Airborne Geoscience Workshop, JPL Pub. 93-26, Jet Propulsion Laboratory, Pasadena, CA, 1993a.
- Green, Robert O., James E. Conel, Jeannette van den Bosch, Masanobu Shimada and Masao Nakai, "On-orbit Calibration of the Japanese Earth Resources Satellite-1 Optical Sensor Using the Airborne Visible-Infrared Imaging Spectrometer", IGARSS'93, Tokyo Japan, Optical Sensor and Calibration, in press, 1993b.
- Green, Robert O. and James E. Conel, "Atmospheric Correction of Data collected by Airborne Visible-Infrared Imaging Spectrometer (AVIRIS) and Application to the Advanced Land Remote Sensing Systems", Workshop on Atmospheric Correction of Landsat Imagery, 29 June to 1 July, Torrance, CA, 1993c.

9.0 TABLE

Table 1. AVIRIS Data Characteristics

<u>SPECTRAL</u>	
Wavelength range	400 to 2500 nm
Sampling	< 10 nm
Spectral response (fwhm)	10 nm nominal
Calibration	<= 1 nm
<u>RADIOMETRIC</u>	
Radiometric range	0 to maximum lambertian
Sampling	~1 dn noise rms
Absolute calibration	<= 7 %
Intraflight calibration	<= 2 %
Precision/noise	exceeding NE Δ L/SNR requirement
<u>GEOMETRIC</u>	
Field of view (FOV)	30 degrees
Instantaneous FOV	1.0 mrad
Calibration	<= 0.2 mrad
Flight line length	Up to ten 100 km flight lines

10.0 FIGURES

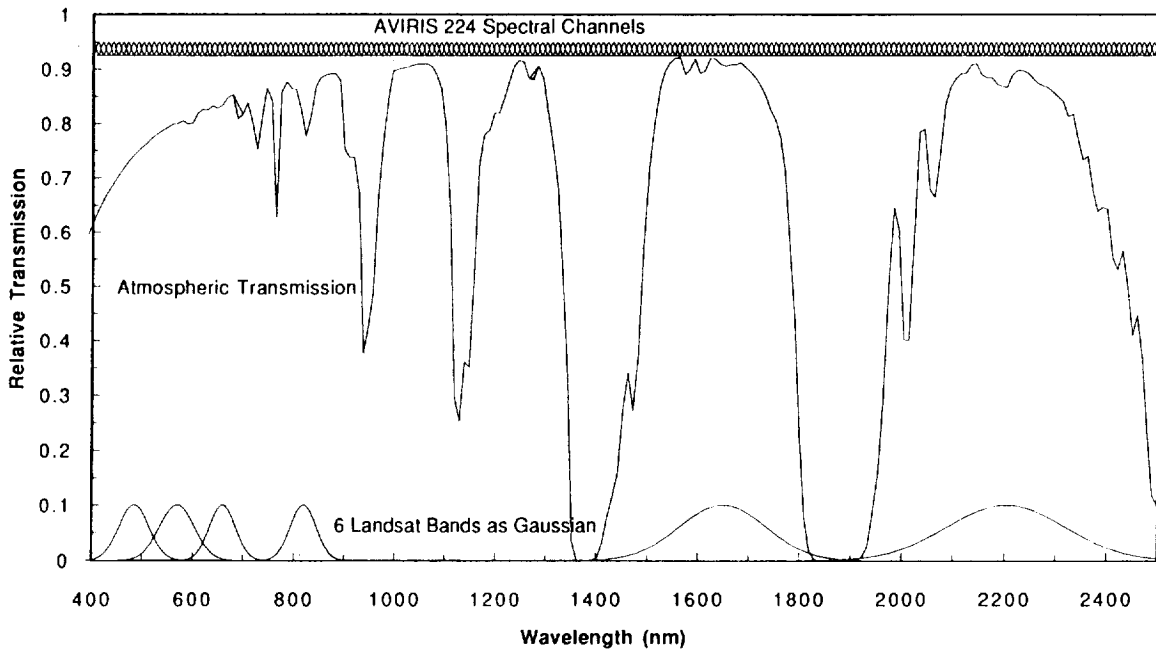


Figure 1. 224 AVIRIS channel plotted with the 6 visible to short wavelength infrared bands of the Landsat Thematic Mapper modeled as gaussian functions. A terrestrial transmission spectrum is shown as well.

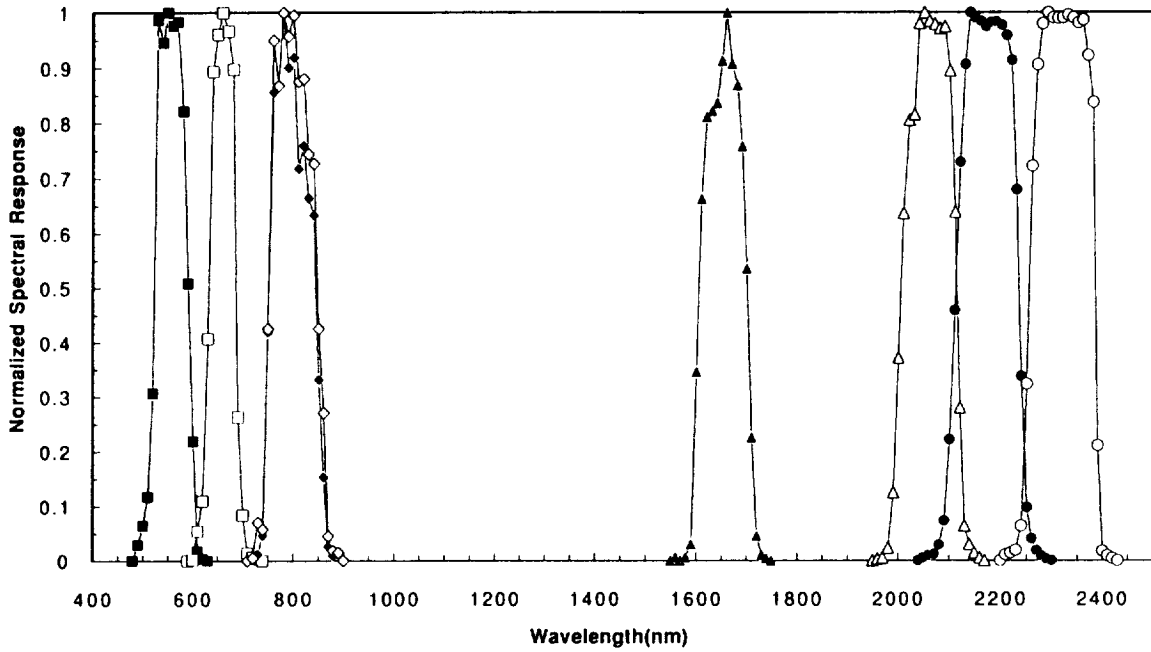


Figure 2. Weighted convolution filters mapping AVIRIS spectral channels to JERS-1 OPS bands.

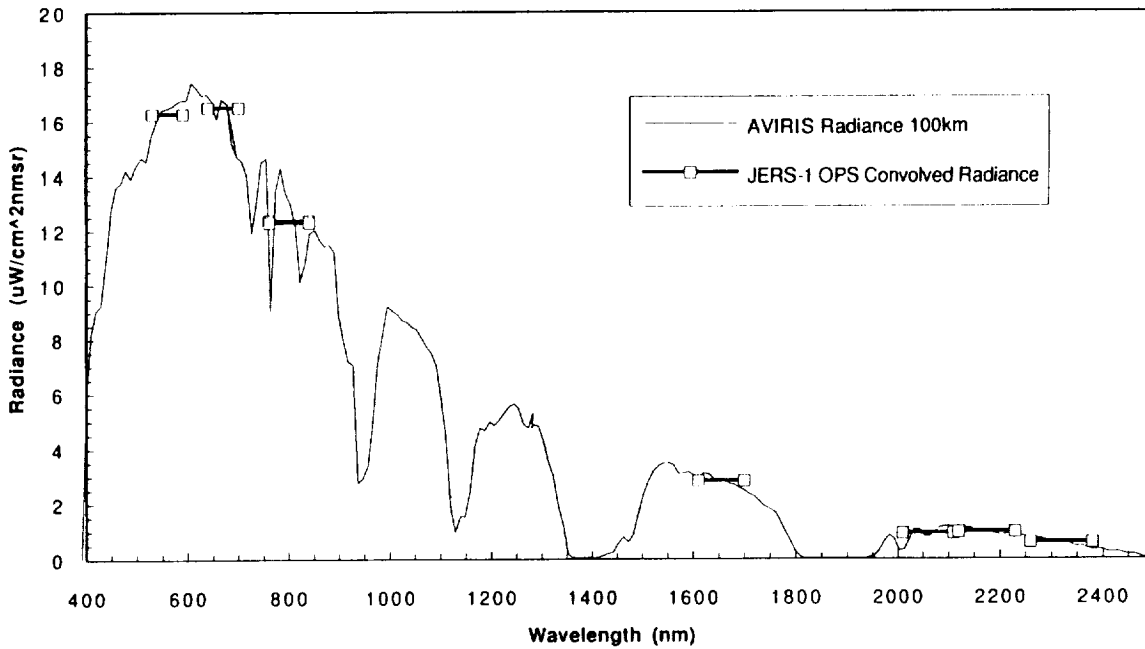


Figure 3. Measured upwelling radiance convolved to the JERS-1 OPS bands and AVIRIS radiance spectrum.

53-43
41023
16

Estimating Dry Grass Residues Using Landscape Integration Analysis
by

Quinn J. Hart, Susan L. Ustin, Lian Duan, and George Scheer

Department of Land, Air and Water Resources, University of California, Davis, 95616 USA

Introduction

The acreage of grassland and grassland-savannah is extensive in California, making direct measurement and assessment logistically impossible. Grasslands cover the entire Central Valley up to about 1200 m elevation in the Coast Range and Sierra Nevada Range. Kuchler's (1964) map shows 5.35 M ha grassland with an additional 3.87 M ha in Oak savannah. The goal of this study was to examine the use of high spectral resolution sensors to distinguish between dry grass and soil in remotely sensed images. Spectral features that distinguish soils and dry plant material in

Figure 1a

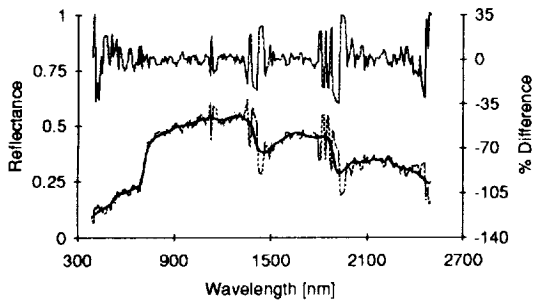


Figure 1b

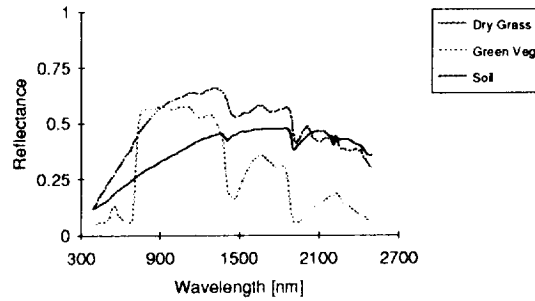


Figure 1c

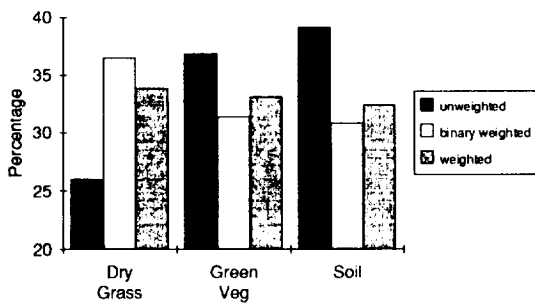


Figure 1d

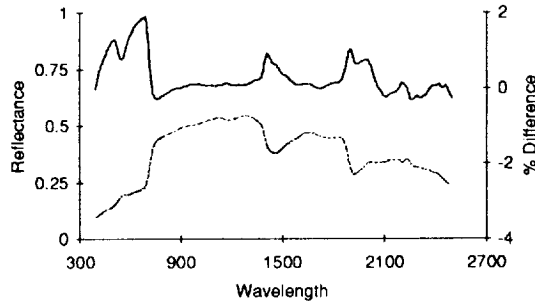


Figure 1: SMA performed on a weighted synthetic spectrum. Figure 1a shows the composite spectrum to be unmixed (with a noise term inversely proportional to the atmospheric transmission, above). Figure 1b shows the 3 endmember spectra used for unmixing. Figure 1c shows the results of SMA. Figure 1d shows the predicted spectrum from the unmixing and a ratio comparison (above) between the original and the signature predicted from the SMA.

the shortwave infrared (SWIR) region (Fig. 1b) are thought to be primarily caused by cellulose and lignin, biochemicals which are absent from soils or occur as breakdown products in humid substances that lack the narrow-band features. We have used spectral mixing analysis (SMA) combined with Geographic Information Systems (GIS) analysis to characterize plant communities and dry grass biomass. The GIS was used to overlay elevation maps, and vegetation maps with

the SMA results. The advantage of non-image data is that it provides an independent source of information for the community classification.

Test Site

The study area used for this research is located in the Central Coast Range just east of Lake Berryessa, CA. The area of approximately 80 km² includes the University of California's Stebbins Cold Canyon Preserve (SCCP). The complexity of the terrain results in a mosaic of grazed and ungrazed grasslands, oak woodlands, chaparral, riparian woodlands, agricultural cultivation, and other vegetation types. AVIRIS imagery was acquired on August 20, 1991 and August 20, 1992.

Spectral Mixture Analysis

We have assumed that the grasslands represent a reasonable approximation of linear spectral mixing up to a point of saturation at high biomass amounts. Results from an unconstrained SMA model using images calibrated to surface reflectance produced better fraction estimates than constrained reflectance models or unconstrained radiance models (Fig. 1c). Atmospheric bands were included in the SMA by using a weighting factor related to the transmission and scattering of a typical mid-latitude atmosphere MODTRAN prediction (Air Force Geophysical Laboratory), Figure 2.

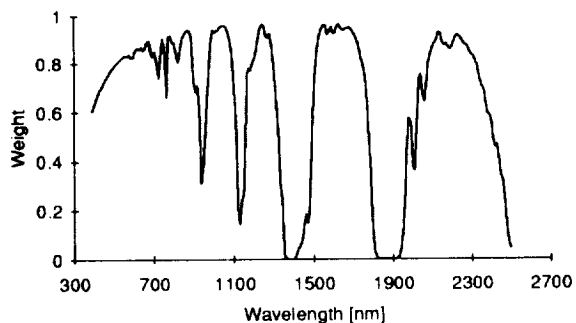


Figure 2: Weighting factor used for the SMA as a function of wavelength

The spectral library endmembers were measured in a Varian Cary 5E spectrometer of soil, dry grass, and other plant samples (leaves, bark) collected within the Berryessa study area. The GPS locations of these materials were included in our GIS data base. Specifically we used a *Heteromeles arbutifolia* (Toyon) leaf as the green foliar endmember, a Sehorn Clay Series soil, and a mixture of dry annual grass leaves for the dry grass endmember. Bark from *Quercus agrifolia* was used as a "woody" endmember.

We used the ARP and lignin/cellulose analysis program by Gao and Goetz (1990) to compare against the dry grass endmember fraction. We assumed that the cellulose/lignin estimate was a reasonable approximation of the biochemistry of dry leaf residues in this study. This analysis produced images having a more speckled appearance and larger variability between adjacent pixels than did the SMA results.

Landscape Integration

Topography data were used to predict "potential vegetation" types based on the landscape of the area and the physiographic dependence of the vegetation. These types of potential vegetation maps were combined with the SMA results to classify "actual vegetation" distribution. Digital Elevation Maps were produced for two USGS 7.5 min transparent overlays (Mt. Vaca and Monticello Dam). Because we were not able to perform all parts of this study in one package, we performed various parts of the work in Map and Image Processing System (MIPS), GRASS, and Arc/Info using both PC's and UNIX workstations. Elevation, aspect, slope, and accumulated runoff (R.watershed module in GRASS) were used to define potential vegetation types using a

Maximum Likelihood Separator (MLS). The SCCP vegetation map (based on ground surveys) was used for training sites of six vegetation types.

The topographically developed classification scheme does well at separating the grassland from the oak woodlands, due to their aspect dependance, and also identifies riparian zones using the accumulation and elevation layers. Rock outcroppings are over-estimated and chaparral, the most abundant community in the region, is under-represented. This resulted because the initial chaparral classification was relegated to the areas unoccupied by the more topographically distinct grasslands and oak woodlands.

The SMA fractions were also used as data layers in the GIS for classification of the SCCP. The SMA-based MLS classification does a better job separating the dry grasslands from the other communities. This is not surprising since one of the endmembers selected for the SMA was of dry grass. Even so, the accuracy of the prediction is striking. The SMA method was less successful discriminating oak woodlands and riparian woodlands which have similar endmember fractions. This effect might be improved if a multiple endmember approach like that of Roberts et al., (1992) were adopted. The rock outcroppings were over-predicted and the chaparral regions were under-predicted. The lower specificity of chaparral may be due to a varying spectral signature.

Finally, the DEM layers and the SMA fraction layers were combined to determine a final "actual vegetation" map. The resulting map is a remarkably good representation of the vegetation type distributions based on comparisons against the SCCP vegetation map and against aerial photographs. In fact, the combined map is better at defining the vegetation type distributions than the more simplified ground-based vegetation map. The grassland predictions suffered slightly, due to topographic variables driving some predictions toward other vegetation types even when the dry grass fraction identifies grasslands. However, the chaparral distribution improves in this map compared to the previous maps. Also, the rock outcrops show closer agreement with the field-based map. The riparian and oak woodlands are also well separated and accurately located when compared with the field-based map.

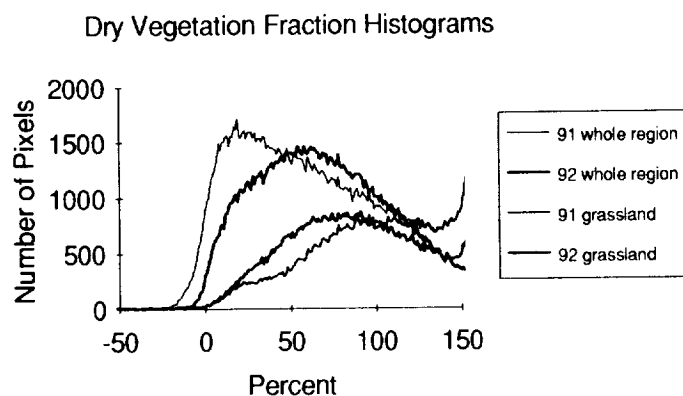


Figure 3: Dry grass fractions for the larger Berryessa region (upper curves) and for the grasslands area only (lower curves).

for the whole area and for the areas classified as grassland are shown in Fig. 3. Both the 1991

The landscape parameter maps developed for the SCCP subset were then created for the larger area covered by the two AVIRIS overflights and the same classifications were performed for the entire region. A significant portion of the total image was classified as grassland (Table 1). However, we still require a map of the spatial variation in dry biomass to monitor dry grass residues. To determine biomass distribution in the dry grasslands, non-grasslands and areas where grazing is unlikely were masked.

The histogram of dry vegetation fractions

and 1992 AVIRIS overflights show close agreement. As seen from the figure, most pixels having low dry vegetation fractions were classified as other vegetation types. To quantify the ranges of dry grass biomass, endmember fractions were divided into five frequency classes. These biomass classifications are consistent with spatial patterns in grassland biomass variation predicted. Predicted area coverage for all vegetation types is shown in Table 1.

Table 1. Distribution of areal coverage by vegetation class for the Berryessa Region.

Vegetation Class	Area Coverage (ha)
Oak Woodland	1262
Chaparral	2076
Riparian	990
Rock Outcrops	228
Grassland/no biomass	7
Grassland/low biomass	422
Grassland/medium biomass	1282
Grassland/high biomass	1516
Grassland/very high biomass	939
TOTAL	8722

Conclusion Summary

1. Spectral unmixing provides a good estimation of the spatial distribution of dry grass.
2. Spatial variation in endmember fractions represent varying proportions of these endmembers supporting conclusions of other authors (e.g., Gamon et al., 1993).
3. Masking non-grassland areas improves the ability to evaluate spatial variations in dry grass abundance.
4. Spectral measures alone are insufficient to separating and mapping all vegetation types in these communities.
5. Combined SMA and DEM data in a GIS produced vegetation maps as good or better than those based on field surveys.

BIBLIOGRAPHY:

- Card, D. H., D. L. Peterson, P. A. Matson, J. D. Aber, 1988, Prediction of Leaf Chemistry by the Use of Visible and Near Infrared Reflectance Spectroscopy. *Remote Sens. Environ.* 26:123-147.
- Gamon, J.A., C.B. Field, D.A. Roberts, S.L. Ustin and V. Riccardo, 1993, Functional patterns in an annual grassland during an AVIRIS overflight, *Remote Sens. Environ.* 44:1-15.
- Gao, C., and A. F. H. Goetz, 1990. Column atmospheric water vapor and vegetation liquid water retrievals from airborne imaging spectrometer data, *J. Geophys. Res.* 95: 3549-3564.
- Kuchler, A.W., 1964, Potential Natural Vegetation of the Conterminous United States. *Am. Geog. Soc. Spec. Pub.* 36.
- Roberts, D., M.O. Smith, D.E. Sabol, J.B. Adams, and S. Ustin, 1992, Mapping the spectral variability in photosynthetic and non-photosynthetic vegetation, soils, and shade using AVIRIS, in: R.Green (ed.) *Proc. 4th Airborne Sci. Workshop: AVIRIS, JPL92-14:* 38-40.
- Ustin, S.L., M.O. Smith, J.B. Adams, 1993, *Remote Sens. of Ecological Processes: A strategy for developing and testing ecological models using spectral mixture analysis*, in: J. Ehrlinger and C. Field (eds.) *Scaling Physiological Processes: Leaf to Globe.* Acad. Press, New York, pp.339-357.
- Wessman, C.A., 1990. Evaluation of canopy biochemistry. In: R.J. Hobbs and H.A. Mooney (eds.), *Remote Sensing of Biosphere Functioning*, Springer-Verlag, New York, pp. 135-156.

2/2/92
41024
1/1

Classification of High Dimensional Multispectral Image Data*

Joseph P. Hoffbeck and David A. Landgrebe

School of Electrical Engineering
Purdue University
West Lafayette, IN 47907

1. Introduction

A method for classifying high dimensional remote sensing data is described in this paper. The technique uses a radiometric adjustment to allow a human operator to identify and label training pixels by visually comparing the remotely sensed spectra to laboratory reflectance spectra. Training pixels for materials without obvious spectral features are identified by traditional means. Features which are effective for discriminating between the classes are then derived from the original radiance data and used to classify the scene. This technique is applied to Airborne Visible/Infrared Imaging Spectrometer (AVIRIS) data taken over Cuprite, Nevada in 1992, and the results are compared to an existing geologic map. This technique performed well even with noisy data and the fact that some of the materials in the scene lack absorption features. No adjustment for the atmosphere or other scene variables was made to the data classified. While the experimental results compare favorably with an existing geologic map, the primary purpose of this research was to demonstrate the classification method, as compared to the geology of the Cuprite scene.

2. The Scene

The data set used to demonstrate the technique is from the 1992 AVIRIS flight over the Cuprite Mining District in southwestern Nevada. The raw data consist of 220 spectral bands covering the range 0.4 to 2.5 μm . The site, which lies on the east side of U.S. Highway 95, has very little vegetation and several exposed minerals including alunite, buddingtonite, kaolinite, and quartz.

3. Identifying Training Pixels using Absorption Features

The reflectance spectra of four minerals as measured in the laboratory are shown in Figure 1 (Goetz et al., 1985). While the absorption features can be easily seen in the reflectance spectra measured in the laboratory, they can be quite difficult to see in the remotely sensed radiance spectra; therefore, the log residue method (Green et al., 1985) was used to adjust the shape of the radiance spectra to be more similar to the laboratory reflectance spectra. The log residue spectra were visually compared to the laboratory spectra, and 730 pixels of alunite, 71 pixels of buddingtonite, 232 pixels of kaolinite, and 385 pixels of quartz were identified in the Cuprite scene. Figure 2 shows the log residue spectrum of the average of each class.

Some pixels in the scene were mixtures of alunite and kaolinite. Since these pixels were not selected as training pixels, the final classification represented the dominant mineral in each pixel. If one were interested in mapping mixed pixels, training pixels for mixed alunite and kaolinite could be used to define an additional class.

* Work leading to this paper was funded in part by NASA Grant NAGW-925.

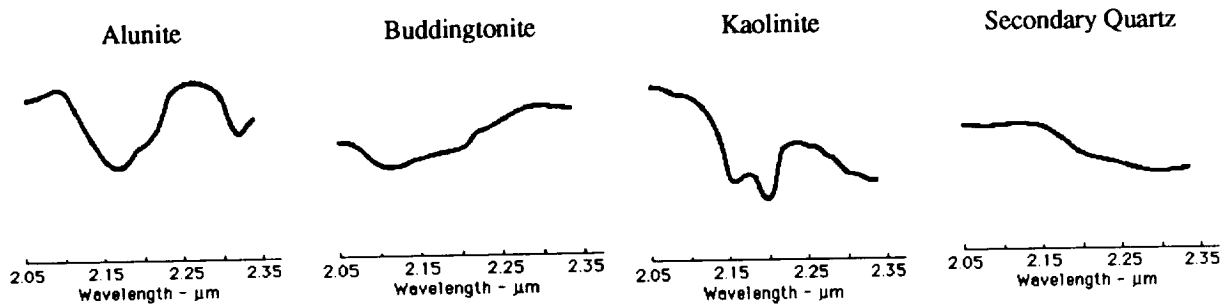


Figure 1. Laboratory Reflectance Spectra of four minerals (Goetz et al., 1985).

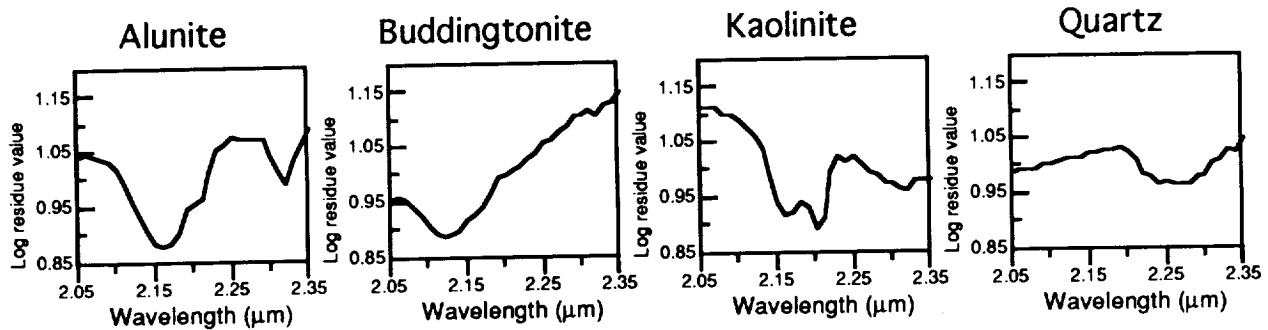


Figure 2. Log Residue of the Average of Each Class.

4. Initial Classification to Identify Other Classes

For materials that lack strong absorption features or whose reflectance spectra is unknown, it may be impossible to directly identify training pixels by comparison to laboratory reflectance spectra. Training pixels for these classes were identified as follows. Discriminant analysis (Fukunaga, 1990) was run on the raw radiance data using the four classes with known absorption features and using all 220 AVIRIS bands (0.4 to 2.5 μm). A maximum likelihood classifier was used to classify the first eight features and a probability map was produced. Areas of low likelihood suggested the location of further classes. Training pixels for argillized, tuff, and alluvium were then located in these areas.

Note that since classes like argillized, tuff, and alluvium do not have known absorption features, additional information was required to determine their identity. In this case the names of the classes argillized, tuff, and alluvium were determined by comparison with the geologic map in Figure 4 (Abrams et al., 1977). Had this information not been available, the training samples still could have been located and the classes mapped, but the names of the classes would not be known.

5. Feature Extraction and Classification

Discriminant analysis was run using all 8 classes and all 220 bands of the raw radiance data. Using the first seven discriminant features, the thematic map in Figure 3 was produced with a maximum likelihood classifier. A threshold was used classify pixels that were very unlikely to belong to any of the training classes as background. The classes background, alluvium, and tuff were all displayed as white in Figure 3.

The result can be compared to the geologic map in Figure 4* (Abrams et al., 1977). This map divides the Cuprite region into a silicified zone which contains abundant

* No attempt was made to adjust the geometry of the AVIRIS data to any geographic coordinate system, thus the geometry of Figures 8, 9, and 10 may not coincide.

quartz, an opalized zone which contains opal, alunite, and kaolinite, and an argillized zone. Comparing Figure 3 to the geologic map shown in Figure 4, note first that the region classified as quartz corresponds to the silicified zone in the geologic map. Note in addition to the central quartz zone, there two small quartz zones to the upper left and the lower left of the central zone that are similar in both maps. Next note that the regions classified as alunite and kaolinite lie in the opalized zone in the geologic map. The region classified as argillized corresponds to the region in the geologic map with the same name. Buddingtonite is not shown in the geologic map. Other researchers have classified this scene (Kierein-Young et al., 1989, Hook et al., 1990, Kruse et al., 1990).

The classification accuracy is difficult to assess quantitatively without knowledge of the actual dominant mineralogy for each pixel in the scene. Two indirect methods to estimate the accuracy of a maximum likelihood classification are the resubstitution method which is optimistically biased, and the leave-one-out method which provides a lower bound on the accuracy (Fukunaga, 1990). If the training pixels were representative of the classes in the scene, the true accuracy for the pixel classification would lie somewhere between these two values. Both the resubstitution accuracy and the leave-one-out accuracy for the classification in Figure 3 were 99.6%.

The fact that this method of classifying high dimensional remote sensing data is relatively insensitive to noise is demonstrated by noting that the final classification changed very little regardless of whether or not the water absorption bands were included in the analysis. The reflected radiation in these bands (1.36 - 1.41 μm and 1.82 - 1.93 μm) is completely absorbed by the atmosphere, and so the data in these bands contains only noise. When the water absorption bands were included the resubstitution accuracy and the leave-one-out accuracy were both 99.6% as mentioned above. When the water absorption bands were not included the resubstitution accuracy was 99.7% and the leave-one-out accuracy was 99.6%.

6. Conclusion

In this paper, a method has been demonstrated for analyzing a data set of high spectral dimensionality. Such high dimensional data not only makes possible the use of narrow spectroscopic features where they are known to exist, but is also able to make available the inherently higher information content of such data as predicted by signal theory principles. Training pixels for materials with strong absorption features were located in the data using the log residue method to adjust the radiance spectra to resemble the reflectance spectra. Training pixels for materials without strong absorption features or known reflectance spectra were located using other knowledge such as photo interpretation, ground observations, etc. Features maximally effective in discriminating between the classes so defined were then computed from the raw radiance data using the discriminant analysis method, and these features were classified using the maximum likelihood classifier.

This method generated good results even with noisy data and with classes that lacked strong absorption features. This method effectively combined the human operator's knowledge of chemical spectroscopy with the power and robustness of the statistical classifier to perform the classification, greatly reducing the dependence of the analysis process on both reflectance and wavelength calibration and on high signal-to-noise-ratio. It also does not require ground truth in the sense of observations taken from the ground, and thus can be applied to the analysis of data gathered from remote areas.

Bibliography

Abrams, M.J., R.P. Ashley, L.C. Rowan, A.F.H. Goetz, and A.B. Kahle, 1977, "Mapping of Hydrothermal Alteration in the Cuprite Mining District, Nevada, Using Aircraft Scanner Images for the Spectral Region 0.46 to 2.36 μm ," *Geology*, vol. 5, no. 12, pp. 713-718.

Fukunaga, K., 1990, *Introduction to Statistical Pattern Recognition*, Second Edition, Academic Press, New York, pp. 220-228, 445-455.

Goetz, A.F.H. and V. Srivastava, 1985, "Mineralogical Mapping in the Cuprite Mining District, Nevada," *Proceedings of the Airborne Imaging Spectrometer Workshop*, JPL Publication 85-41, pp. 22-31.

Green, A.A. and M.D. Craig, 1985, "Analysis of Aircraft Spectrometer Data With Logarithmic Residuals." *Proceedings of the Airborne Imaging Spectrometer Workshop*, JPL Publication 85-41, pp. 111-119.

Hook, S.J. and M. Rast, 1990, "Mineralogic Mapping Using Airborne Visible Infrared Imaging Spectrometer (AVIRIS) Shortwave Infrared (SWIR) Data Acquired Over Cuprite, Nevada", *Proceedings of the Second AVIRIS Workshop*, JPL Publication 90-54, pp. 199-207.

Kierein-Young, K.S. and F.A. Kruse, 1989, "Comparison of Landsat Thematic Mapper and Geophysical and Environmental Research Imaging Spectrometer Data for the Cuprite Mining District, Esmeralda and Nye Counties, Nevada", *Digest - International Geoscience and Remote Sensing Symposium (IGARSS)*, vol. 2, pp 961-964.

Kruse, F.A., K.S. Kierein-Young, and J.W. Boardman, 1990, "Mineral Mapping at Cuprite, Nevada With A 63-Channel Imaging Spectrometer," *Photogrammetric Engineering and Remote Sensing*, vol. 56, no. 1, pp 83-92.



Figure 3. Classification of AVIRIS data.

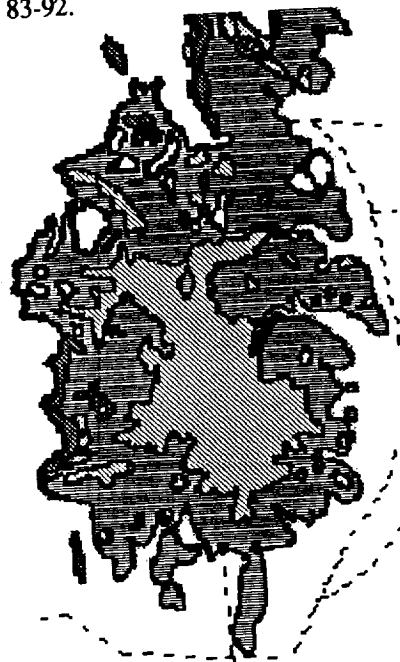


Figure 4. Geological map redrawn from Abrams et al., 1977.

235-82
41025
3/4

SIMULATION OF LANDSAT THEMATIC MAPPER IMAGERY USING AVIRIS HYPERSPECTRAL IMAGERY

Linda S. Kalman and Gerard R. Peltzer

The Aerospace Corporation
P.O. Box 92957
Los Angeles, CA 90009-2957

1. INTRODUCTION

In this paper we present a methodology for simulating multispectral imagery (MSI) using hyperspectral imagery (HSI), and present a validation of the technique using one nearly coincident Landsat TM and AVIRIS data set. Generation of MSI from HSI supports several investigations including selection of multispectral sensor band edges, and engineering trade studies related to on-board or ground-based aggregation of HSI to simulate MSI. In addition, the utility of this technique as a potential procedure for monitoring calibration changes in spaceborne instruments is also addressed.

2. SIMULATION METHODOLOGY

The signal, S_e , (in electrons) in a selected waveband of a multispectral sensor is given by :

$$S_e = K \int R(\lambda) F(\lambda) \lambda / hc d \lambda \quad (1)$$

where $R(\lambda)$ represents the spectral radiance distribution at the sensor aperture, $F(\lambda)$ is the combined spectral responsivity of the sensor (including spectral filter response, detector spectral responsivity, etc.), and K represents an assortment of wavelength independent components including sensor aperture solid angle, integration time, detector size, etc. The conversion between photons and electrons is represented by the term λ/hc . The integration is performed over the spectral bandpass of the band in question.

The process of inverting equation (1), eg. the estimation of $R(\lambda)$ from a measured signal does not have a unique solution. Instead, one may estimate the equivalent radiance, R_e , ie. the spectrally flat radiance distribution which when used in equation (1) would produce the same measured signal:

$$S_e = K \int R_e F(\lambda) \lambda / hc d \lambda \equiv K R_e \int F(\lambda) \lambda / hc d \lambda \quad (2)$$

Equating (1) and (2) we have a definition of this equivalent radiance:

$$R_e = \int R(\lambda) F(\lambda) \lambda d \lambda / \int F(\lambda) \lambda d \lambda \quad (3)$$

The equivalent radiance, R_e , when multiplied by the nominal sensor bandpass, $\Delta\lambda$, is commonly referred to as the "inband" radiance. The relationship between this inband radiance and Landsat digital values, D_n , is defined through the calibration information supplied with Landsat data :

$$R_e \Delta\lambda = \text{Gain} * D_n + \text{Offset} \quad (4)$$

Simulation of Landsat digital data can therefore be accomplished through computation of the inband radiance, $R_e \Delta\lambda$, followed by application of the appropriate band calibration coefficients.

Calibrated imagery, such as that produced by the AVIRIS sensor is an ideal

candidate for estimation of $R(\lambda)$. Given n hyperspectral bands spanning the bandpass of the multispectral sensor band being simulated, equation (3) can be approximated as :

$$Re = \frac{\sum_{i=1}^n R_A(i) F(\lambda_i) \lambda_i \Delta\lambda_i}{\sum F(\lambda_i) \lambda_i \Delta\lambda_i} \quad (5)$$

where $R_A(i)$ is the calibrated spectral radiance measured in AVIRIS band i , λ_i is the center wavelength of band i , $\Delta\lambda_i$ is the bandpass of band i , and $F(\lambda_i)$ is the spectral response value of the sensor being simulated at wavelength λ_i . The fidelity with which Re can be generated depends on the calibration accuracy of the hyperspectral imagery and also improves as the number and spectral resolution of the hyperspectral bands covering the bandpass in question increases.

3. EXPERIMENT AND RESULTS

We have investigated the merits of this simulation technique using an AVIRIS scene collected nearly coincident with a Landsat TM scene. The AVIRIS scene obtained on 10/08/90 at 1041 Z, and covers the area surrounding Corvallis Oregon. A Landsat 5 TM scene (geometrically corrected, P type data) was collected on the same day at approximately 1745 Z. Weather reports generated at Eugene (50 miles away) as well as the general appearance of both images indicate a relatively clear, cloud free atmosphere during the acquisitions. The FWHM and center wavelength files accompanying the calibrated AVIRIS imagery were used in equation (3). Preflight measurements of the Landsat sensor spectral response function (Engel, 1990) were used as a source for $F(\lambda_i)$.

The six reflective bands of the Landsat 5 TM instrument were simulated using equations (3) and (5) along with calibration data found in the TM data header file. (A multiplicative sun angle correction based on the change in solar zenith angle between the two collections was applied to the simulated TM radiances prior to conversion to digital counts.)

3.1 Evaluation of Results

A portion of the TM scene was geometrically warped to overlay the AVIRIS data. A common sub area of the two images was then extracted for statistical analysis. Color composites of the simulated and actual TM scenes are provided in Slide 3. Histograms of the simulated and actual TM bands were computed for the spatially registered areas. A few of the histograms are displayed in Figure 1 and a summary of the scene statistics presented in Table 1. The agreement between simulated and actual scene statistics and histograms is exceptionally good. Both band 4 and band 5 histogram comparisons show the simulated image histograms to be slightly compressed. To investigate the source of this effect we computed statistics for several homogeneous sub areas in the simulated TM imagery and corresponding areas in the unwarped, original TM image. Samples of these results are plotted in Figure 2. Linear relationships between simulated Dn and actual TM Dn were found to exist for each band. The linear regression data are shown in Table 2. Several investigators (including Thome et al, 1993) have observed a decrease in TM response in each band over the course of the years. Since EOSAT has not changed calibration coefficients since 1986, we would expect that use of those coefficients to compute Dn from the radiance derived using the AVIRIS data would yield higher values than the actual digital values observed in the TM scene. Unfortunately, this is not what we observed. This discrepancy suggests that perhaps the AVIRIS calibration for this data set is erroneously low. With only one data set it is difficult to draw decisive conclusions regarding the source of these discrepancies.

In this analysis we have focussed upon the radiometric fidelity of the simulation procedure. A rigorous simulation of multispectral imagery would include an accurate

modeling of electronic and signal dependent noise in the image, as well as modification of the MTF characteristics as appropriate. The spectral band aggregation generally produces the desirable effect of decreasing the noise level in the simulated image. The user is then free to add back in the desired amount of noise expected in the sensor product so long as the individual spectrometer band noise levels are comparable to those of the sensor to be simulated. Furthermore, the aggregation procedure increases the effective bit-resolution of the simulated data, allowing the user to explore design tradeoffs related to bit allocation and digitization schemes. Finally, the accuracy of the simulation is dependent upon the spectral resolution of the HSI. The number of bands actually required will most likely depend on the shape and complexity of the sensor response function being simulated.

3.2 Potential applications of the simulation technique.

Discrepancies between the simulated TM data and the actual TM data can be attributed to calibration errors in either instrument, as well as to the coarseness arising from the limited number of AVIRIS spectral bands covering any given TM band, particularly in the shorter wavelengths. Changes in responsivity for the TM instrument throughout the years have been observed by investigators including Thome et al. (1993). We performed an experiment in which we shifted the long wavelength edge of the TM2 spectral response curve; in effect, changing the effective filter passband. The long edge was shifted from -10 nm to +10 nm from its nominal position. The statistics derived from these experiments are shown in Table 3. It is clear that a change in filter response similar to this could be detected and quantified using imagery simulated from underflights with a hyperspectral sensor such as AVIRIS. We are currently performing analyses to determine if this procedure can be used to identify the exact nature of the change in filter response : eg. to distinguish between shifts at the low or high wavelength end, or both, as well as changes in transmittance due to contamination of the optical surfaces or changes in detector responsivity over time.

4.0 SUMMARY

We have presented a procedure for simulating multispectral imagery using hyperspectral data. The simulation technique is straightforward and has been shown to produce encouraging results in the one case studied, although with only one data set it is impossible to distinguish errors in the AVIRIS calibration or the TM calibration. We are currently in the process of obtaining additional data sets to use in further validation of the procedure. It is clear however, that reasonable simulations of multispectral imagery can be produced using this technique. A simulation technique such as this provides the capability to perform engineering design trades for future multispectral sensors related to determination of spectral band placement. In addition, the analysis technique may be useful as a tool for monitoring changes in calibration of space sensors using aircraft underflights. The sensitivity of this technique for detecting changes in sensor characteristics is currently under study.

5.0 ACKNOWLEDGEMENTS

The authors wish to thank Dr. P. Slater (Univ. of Arizona, Tucson) for his helpful comments and suggestions regarding the course of this work. This work was supported by the Aerospace Sponsored Research program.

6.0 REFERENCES

- Engel, J., SBRC (Private Communication).
- Thome, K.J., D. I. Gellman, R.J. Parada, S. F. Biggar, P.N. Slater, and M.S. Moran, 1993. "In-flight Radiometric Calibration of Landsat-5 Thematic Mapper from 1984 to Present", Vol. 1938-14, Proc. SPIE, Orlando, Fla. April, 1993.

Table 1. Comparison of Simulated Scene Statistics with Actual Scene Statistics		
Band	Simulated Mean Dn	Actual Mean Dn
1	54.3	54.0
2	22.2	22.0
3	24.1	24.0
4	40.3	41.0
5	55.3	57.9
7	24.5	25.8

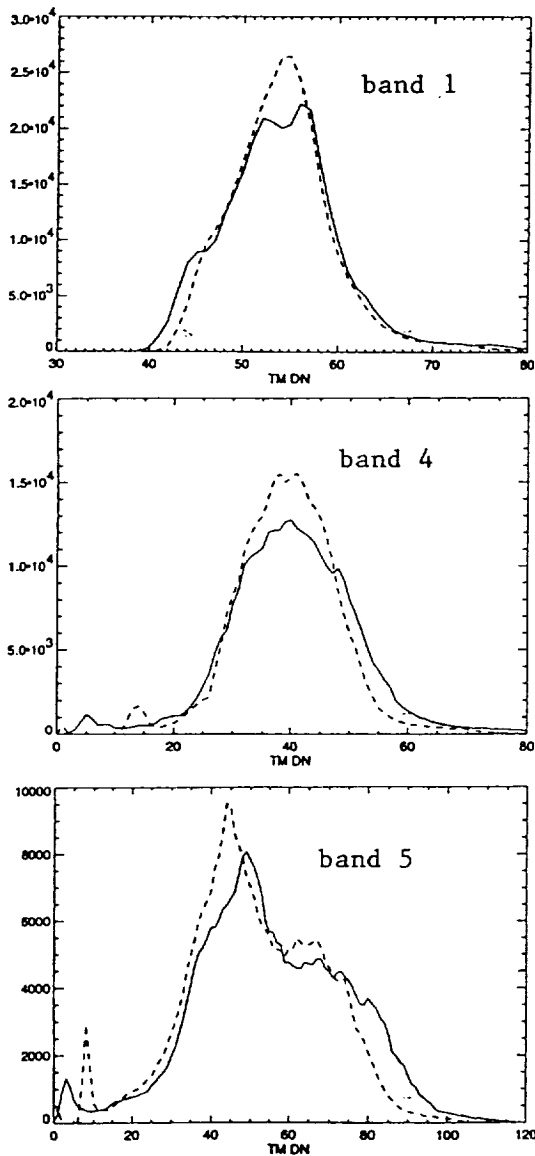


Figure 1. Histogram Plots of Simulated (dotted line) and actual (solid line) TM scenes.

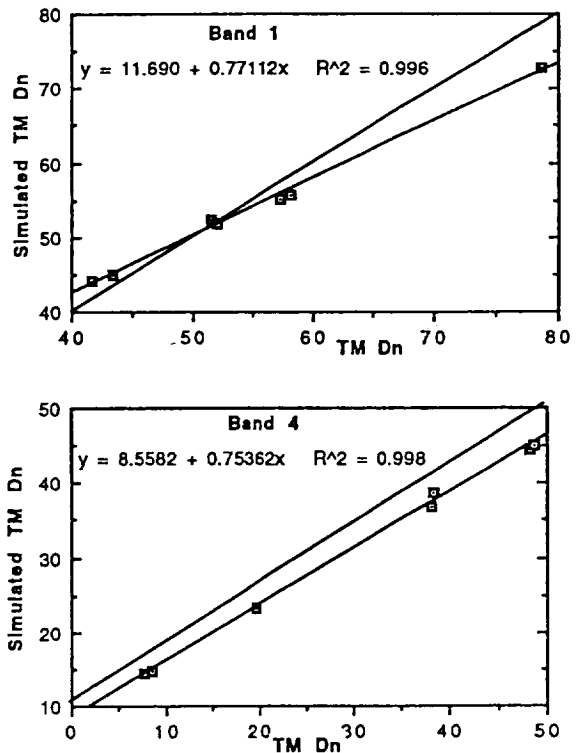


Figure 2. Simulated Dn plotted against actual Dn for corresponding subareas (bands 1 and 4).

Table 2. Equation coefficients describing the relationship between simulated and actual TM values. Simulated (Y) = Gain * Actual (X) + Offset		
Band	Gain	Offset
1	.77	1.69
2	.83	4.58
3	.81	4.94
4	.75	8.56
5	.82	5.65
7	.91	2.31

Table 3. Statistics Derived from Shifting Upper Edge of TM Band 2 response function.		
Band	Shift (nm)	Simulated Scene Mean Dn
2	-10	20.5
	- 4	21.9
	0	22.9
	+ 4	23.8
	+10	25.3

226-43
 470.26
 4

**THE EFFECTS OF AVIRIS ATMOSPHERIC CALIBRATION METHODOLOGY
 ON IDENTIFICATION AND QUANTITATIVE MAPPING OF SURFACE
 MINERALOGY, DRUM MTNS., UTAH**

Fred A. Kruse^{1, 2} and John L. Dwyer^{2, 3}

¹Center for the Study of Earth from Space (CES), Cooperative Institute for Research in
 Environmental Sciences (CIRES), University of Colorado, Boulder
 Campus Box 449, Boulder Colorado 80309-0449

²Department of Geological Sciences, University of Colorado, Boulder

³Hughs STX Corporation, Sioux Falls, South Dakota

1. INTRODUCTION

The Airborne Visible/Infrared Imaging Spectrometer (AVIRIS) measures reflected light in 224 contiguous spectral bands in the 0.4 to 2.45 μm region of the electromagnetic spectrum (Porter and Enmark, 1987). Numerous studies have used these data for mineralogic identification and mapping based on the presence of diagnostic spectral features. Quantitative mapping requires conversion of the AVIRIS data to physical units (usually reflectance) so that analysis results can be compared and validated with field and laboratory measurements. This study evaluated two different AVIRIS calibration techniques to ground reflectance; an empirically-based method and an atmospheric model based method to determine their effects on quantitative scientific analyses. Expert system analysis and linear spectral unmixing were applied to both calibrated data sets to determine the effect of the calibration on the mineral identification and quantitative mapping results. Comparison of the image-map results and image reflectance spectra indicate that the model-based calibrated data can be used with automated mapping techniques to produce accurate maps showing the spatial distribution and abundance of surface mineralogy. This has positive implications for future operational mapping using AVIRIS or similar imaging spectrometer data sets without requiring *a priori* knowledge.

2. The Drum Mountains Site

The Drum Mountains, located in the semi-arid terrain of west-central Utah were selected for study because of the good exposure of diverse rock types and alteration mineralogy. The detailed geology of the area is well documented (Baily, 1974; Lindsey, 1979). Extensive amounts of remotely sensed imagery and ground-based data including ground spectral measurements have been collected from all rock units and alteration types, and many rock and soil samples have been analyzed in the laboratory. Rocks exposed in the study area include limestones, dolomites, and shales which overlie a heterogeneous sequence of quartzite and argillite. Volcanic rocks, hydrothermally altered in places, occur in fault contact and overlying the sedimentary units and some carbonate rocks adjacent to the volcanics have been bleached and recrystallized. Contact metamorphism has resulted in development of calcsilicate mineralization in the central part of the study area.

3. Calibration of AVIRIS data

3.1 Empirical Line Method Calibration

The Drum Mountains AVIRIS data were calibrated to apparent reflectance using the empirical line method (Roberts et al., 1985). AVIRIS radiance spectra for ground targets were used in a linear regression to calculate coefficients to linearly transform the aircraft spectra to match the ground spectra. This method requires *a priori* knowledge in the form of field measurements, which were acquired for both light and dark ground targets. Gains and offsets were calculated to force the AVIRIS spectra to match the field spectra. These gains and offsets were then used to calibrate the Drum Mountains AVIRIS data to apparent reflectance.

3.2 Atmospheric Model-based Calibration

The other calibration technique applied to the Drum Mountains AVIRIS data involved the use of a radiative transfer model-based technique (Gao and Goetz, 1990). Apparent reflectance spectra were first obtained by dividing each AVIRIS spectrum by the solar irradiance curve above the atmosphere. A number of theoretical water vapor transmittance spectra for the 0.94 and 1.1 μm water vapor bands were calculated for varying amounts of atmospheric water vapor using an approximate radiative transfer code called "Simulation of the Satellite Signal in the Solar Spectrum (5S)" (Tanre et al., 1986) and the Malkmus (1967) narrow band spectral model. The modeled spectra are run through the three-channel ratioing method to generate a lookup table of water vapor concentrations that can be used to convert the AVIRIS apparent reflectance measurements to total column water vapor. The output of this procedure is an image showing the spatial distribution of various water vapor concentrations as derived for each pixel of the AVIRIS data. The water vapor image is then used along with transmittance spectra derived for each of the atmospheric gases CO_2 , O_3 , N_2O , CO , CH_4 , and O_2 using the Malkmus narrow band model and 5S model to produce scaled surface reflectance (Gao and Goetz, 1990). This model-based technique produces total water vapor column images and reflectance calibrated AVIRIS data without *a priori* knowledge.

4. Comparison of Calibration Results and Scientific Validation

4.1 Reflectance Spectra

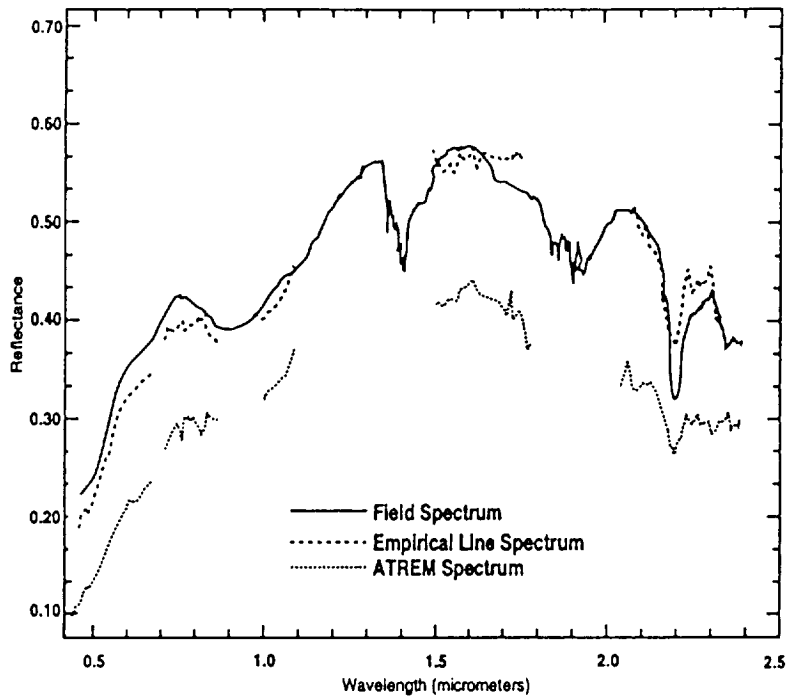
The results of the two calibration techniques described above were compared by extracting reflectance spectra from calibrated AVIRIS images and comparing with field and laboratory spectra. Figure 1 shows a field spectrum compared to AVIRIS spectra extracted from both the empirical line (EL) calibrated and atmospheric model (AM) calibrated data. Note that the EL AVIRIS spectrum matches the position and shape of the laboratory spectrum (particularly at 2.2 μm) more closely than the AM AVIRIS spectrum. The EL spectra, also were consistently brighter than the AM spectra and absorption features near 0.9 and 2.2 μm in the AM spectrum were consistently suppressed as compared to the EL spectrum. These general characteristics were observed for several different areas using the two AVIRIS calibration methods. Initially, the suppression of the 0.9 μm feature was attributed to model-based calibration error caused by the assumption made in the AM method that most materials are spectrally flat in the 0.9 region. Subsequently, the AVIRIS data were recalibrated using only the 1.14 μm water band and the resulting spectra were virtually indistinguishable. Thus, the suppression of the 0.94 μm band must be attributed to some other cause. In fact, it appears that perhaps it is the EL method that is enhancing the absorption bands rather than the AM method suppressing them.

4.2 Automated Feature Extraction and Expert System Analysis

Thematic image products were generated showing the distribution of major mineral constituents for the Drum Mountains site using an expert system approach. The expert system is an absorption feature based technique that uses rules built from a spectral library to identify unknown minerals in imaging spectrometer data (Kruse et al., 1993). The success of this approach depends on having high-quality, well calibrated spectral data. Once the data are properly calibrated, the procedure is to treat each pixel individually and sequentially to remove a continuum (normalize), extract the features, and to compare the features found in the AVIRIS data to the feature rules. The result of these analyses is a new data cube consisting of a single image for each endmember showing the degree of match to the rules (Kruse et al., 1993).

Image maps derived from both the EL and AM calibrated AVIRIS data using the expert system techniques were compared to conventional geologic maps for the Drum Mountains site (Bailey, 1974, Lindsey, 1979). In general, these images showed good correspondence to known mineralogy for distinct lithologic units. For example, areas of dolomite could be easily distinguished from the Prospect Mountain Quartzite, which contains primarily clay minerals. In addition, previously unmapped mineralogical variation was mapped within the different units. While the details of these image maps has not been verified in the field, samples from selected units (Tremper, 1991) indicate that to the first order the mineralogy being mapped using the imaging spectrometers is accurate. Limitations are likely related to the relatively low signal-to-noise-ratios of the 1990 AVIRIS data. Very similar mineralogical results were obtained using both the EL and the AM calibrated data. The expert system results from the AM data were

Figure 1. Comparison of an EL calibrated and AM calibrated spectrum for the same pixel to a field spectrum. Portions of the AVIRIS spectra in the atmospheric water bands have been masked.



noticeably noisier, however, as would be expected based on the previous descriptions of how this calibration suppresses absorption features.

4.3 Linear Spectral Unmixing

Spectral mixing is a consequence of the mixing of materials having different spectral properties within the ground field-of-view (GFOV) of a single image pixel. Boardman (1992) addressed the mixing problem using singular value matrix decomposition (SVD) to linearly unmix AVIRIS data. This technique assumes that most mixing is on the macroscopic scale, and thus linear. To the first order, this model appears to adequately represent the surface geologic conditions.

Linear spectral unmixing was applied to each of the calibrated Drum Mountains AVIRIS data sets using endmember spectral libraries derived from the two calibrated data sets using the expert system. The output of the unmixing process was an image data cube of endmember abundances, an abundance sum image, and a root-mean-square (rms) error image. Interactive analysis of these images showed that each library explained most of the spectral variation in the Drum Mountains AVIRIS data in its respective calibrated data set. In general, similar results were obtained using both the EL and the AM calibrations. The locations and relative abundances of specific minerals were very similar (see Slide 4). There were some obvious differences between the images. For example, the two "illite" images show differences in absolute abundances. The EL image shows a crescent shaped area of high concentrations (yellow) along the right edge of the image. The AM image shows a similar shaped area, however, the concentrations are somewhat lower (purple and blue). These differences are attributable to degeneracy of the AM spectral endmember library caused by increased similarity of spectra by suppression of spectral features.

5. DISCUSSION AND SIGNIFICANCE OF THE RESULTS

Comparison of reflectance spectra and derived thematic maps from the empirical- vs model-based calibrations demonstrated that both data sets contained basically the same mineralogical information about the ground surface. The empirical line method, however, emphasized mineral absorption features, thus it was better suited to analysis using absorption-feature-based techniques. In particular, more consistent results were obtained when this reflectance data was analyzed using an expert-system approach. While similar endmember spectra were

identified using the atmospheric model, suppression of the absorption bands in the AM calibrated data (relative to the EL data) caused less effective mapping of spectral variation. Once unique endmember spectra were identified, however, linear spectral unmixing worked equally well on both calibrated data sets, producing very similar results.

The significance of this research is that it demonstrates that a model-based calibration method for imaging spectrometer data requiring no *a priori* knowledge can be used to produce reflectance data for quantitative scientific analysis. This achieves the goal of being able to extend analysis techniques developed for analysis of one area to analysis of a second, unknown area. With the advent of imaging spectrometers, model-based calibration methods, and the quantitative techniques outlined here, imaging spectrometers can be used to extract ground surface characteristics without having to first conduct a field survey.

6. ACKNOWLEDGMENTS

This research was funded by U. S. Geological Survey Cooperative Agreement 14-08-0001-A0746.

7. REFERENCES

- Bailey, G. B., 1974, The occurrence, origin, and economic significance of gold-bearing jasperoids in the central Drum Mountains, Utah: Unpublished Ph. D. Dissertation, Stanford University, 300 p.
- Boardman, J. W., 1992, Sedimentary Facies Analysis Using Imaging Spectrometry: A Geophysical Inverse problem: Unpublished Ph. D. Dissertation, University of Colorado, Boulder, 212 p.
- Gao B. and Goetz, A. F. H., 1990, Column atmospheric water vapor and vegetation liquid water retrievals from airborne imaging spectrometer data: Journal of Geophysical Research, v. 95, no. D4, p. 3549-3564.
- Kruse, F. A., Lefkoff, A. B., and Dietz, J. B., 1993, Expert System-Based Mineral Mapping in northern Death Valley, California/Nevada using the Airborne Visible/Infrared Imaging Spectrometer (AVIRIS): Remote Sensing of Environment, Special issue on AVIRIS, May-June 1993, p. 309 - 336.
- Lindsey, D. L., 1979, Geologic map and cross-sections of Tertiary rocks in the Thomas Range and northern Drum Mountains, Juab County, Utah: U. S. Geological Survey Map I-1176, Washington, D.C.
- Malkmus, W., 1967, Random Lorentz band model with exponential-tailed S line intensity distribution function: J. Opt. Soc. Am., v 57, p. 323-329.
- Porter, W. M., and Enmark, H. T., 1987, A system overview of the Airborne Visible/Infrared Imaging Spectrometer (AVIRIS): in Proceedings, 31st Annual International Technical Symposium, Society of Photo-Optical Instrumentation Engineers, v. 834, p. 22-31.
- Roberts, D. A., Yamaguchi, Y., and Lyon, R. J. P., 1985, Calibration of Airborne Imaging Spectrometer Data to percent reflectance using field spectral measurements: in Proceedings, Nineteenth International Symposium on Remote Sensing of Environment, Ann Arbor, Michigan, October 21-25, 1985.
- Tanre, D., Deroo, C., Duhaut, P., Herman, M., Morchrette, J. J., Perbos, J., and Deschamps, P. Y., 1986, Simulation of the Satellite Signal in the Solar Spectrum (5S), Users's Guide (U. S. T. de Lille, 59655 Villeneuve d'ascq, France: Laboratoire d'Optique Atmospherique).
- Tremper, C. W., 1991, The mineralogy and chemistry of rocks from the Drum Mountains, west-central Utah: Internal report to the U. S. Geological Survey (P.O # 2451234), Department of Geology, Northern Illinois University, DeKalb, Illinois, 76 p.

207-4/3
11/027
4

AVIRIS SPECTRA CORRELATED WITH THE CHLOROPHYLL CONCENTRATION OF A FOREST CANOPY

John Kupiec
Geoffrey M. Smith

Department of Geography, University College of Swansea,
Singleton Park, Swansea SA2 8PP, United Kingdom.

and

Paul J. Curran

Department of Geography, University of Southampton,
Highfield, Southampton SO9 5NH, United Kingdom.

1. INTRODUCTION

Imaging spectrometers have many potential applications in the environmental sciences. One of the more promising applications is that of estimating the biochemical concentrations of key foliar biochemicals in forest canopies (Peterson *et al.*, 1988; Wessman *et al.*, 1989; Johnson and Peterson, 1991). These estimates are based on spectroscopic theory developed in agriculture (Curran, 1989) and could be used to provide the spatial inputs necessary for the modelling of forest ecosystem dynamics and productivity (Committee on Earth Sciences, 1989). Several foliar biochemicals are currently under investigation ranging from those with primary absorption features in visible to middle infrared wavelengths (e.g., water, chlorophyll) to those with secondary to tertiary absorption features in this part of the spectrum (e.g., nitrogen, lignin). The foliar chemical of interest in this paper is chlorophyll; this is a photoreceptor and catalyst for the conversion of sunlight into chemical energy and as such plays a vital rôle in the photochemical synthesis of carbohydrates in plants.

The aim of the research reported here was to determine if the chlorophyll concentration of a forest canopy could be correlated with the reflectance spectra recorded by the Airborne Visible/Infrared Imaging Spectrometer (AVIRIS).

2. DATA COLLECTION AND METHODS

The study site is located 35 km NE of Gainesville, Florida. Fourteen plots (50 X 50 m) had been established in a mature stand of slash pine. Half of these plots had been fertilised and the other half were controls (Gholz *et al.*, 1991). Each plot had a uniform canopy structure and similar background.

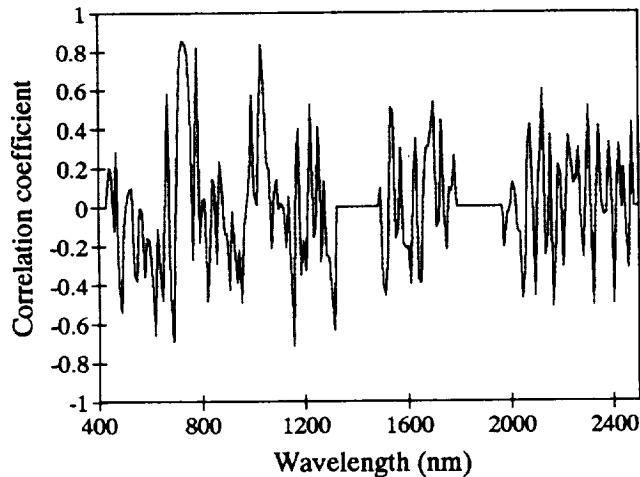
In July 1992 twenty needle samples were collected from the upper canopy of each of the 14 plots. Chlorophyll concentration was determined in the laboratory using standard spectrophotometry of tissue extracts in a 90% acetone solution (Mackinney, 1941). The mean chlorophyll concentrations were 2.10 mg g⁻¹ (σ 0.82 mg g⁻¹) and 1.33 mg g⁻¹ (σ 0.40 mg g⁻¹) for the fertilised and control plots respectively.

Four images of the study site were recorded by the AVIRIS within a 50 minute period on the 8th July 1992. These images were atmospherically corrected to 'scaled surface reflectance' by The Centre for the Study of the Earth from Space (CSES) at the University of Colorado in Boulder using the 'Atmospheric Removal Program' (ATREM) (Gao *et al.*, 1992). The 14 plots were located within each image using an affine transformation calculated from ground control points. Two check points indicated an average error of less than one pixel. A reflectance spectrum for each plot was extracted from each of the four images. These spectra were averaged by plot and transformed to a first derivative of the reflectance values.

3. THE CORRELATION BETWEEN FIRST DERIVATIVE REFLECTANCE AND CHLOROPHYLL CONCENTRATION

Correlation coefficients between first derivative reflectance and chlorophyll concentration were calculated for each AVIRIS waveband (Figure 1).

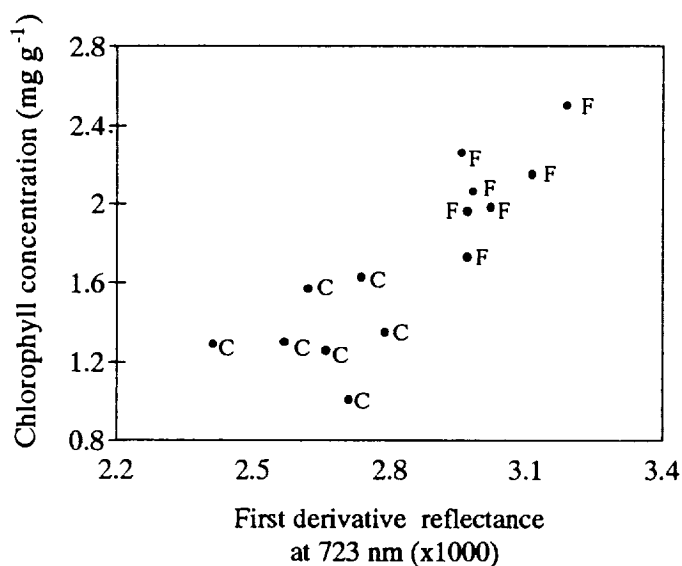
Figure 1. Correlation coefficients between first derivative reflectance and chlorophyll concentration for 14 plots. Note that the very low signals in the water absorption bands have been rescaled to zero.



The maximum correlation coefficient is 0.85 and occurs at a wavelength of 723 nm. This is located on the edge of the chlorophyll absorption feature in a spectral region used by others for the spectral estimation of chlorophyll concentration (Gates 1980; Baret *et al.*, 1987; Curran *et al.*, 1990).

First derivative reflectance data at 723 nm were extracted from the first derivative spectra and plotted against chlorophyll concentration (Figure 2). The relationship between these two variables is not only near linear it is also functionally direct. An *increase* in chlorophyll concentration will result in *increases* in the depth of the absorption feature, the steepness of its long wavelength edge and thereby the first derivative of reflectance.

Figure 2. First derivative reflectance at 723 nm plotted against chlorophyll concentration for 14 plots, of which 7 are (C)ontrol and 7 are (F)ertilised.



Stepwise regression was used to explore further the relationship between first derivative reflectance and chlorophyll concentration (Table).

Table. The results of a stepwise regression analysis between first derivative reflectance and chlorophyll concentration.

Step No.	Waveband (nm)	R ²	Change in R ²
1	723	0.73	0.73
2	2371	0.87	0.14
3	1552	0.96	0.09

The first step of the regression analysis selected the wavelength in which there was the largest correlation between first derivative of reflectance and chlorophyll concentration (723 nm); this accounted for 73% of the variation in chlorophyll concentration. Subsequent selections were for wavelengths reported to be associated with other foliar biochemical constituents (Williams and Norris, 1987). Research is in progress to explain these subsequent wavelength selections.

4. CONCLUSION

This is the first study to report a correlation between the AVIRIS spectra and chlorophyll concentration. The challenge ahead is to correlate the AVIRIS spectra with other foliar biochemicals (e.g., water, nitrogen, lignin, cellulose) and then to use this experience as a basis for the design of methodologies for the *estimation* of foliar biochemical concentrations.

ACKNOWLEDGEMENTS

We wish to thank Professor H. Gholz (University of Florida, Gainesville) who established the study site with funding from the NSF and provided support and advice throughout this research. The research was funded by the NERC (UK) by means of a research grant to PJC and a studentship to GMS and the NASA Earth System Science Division by means of a research grant and AVIRIS flight time to PJC.

REFERENCES

- Baret, F., Champion, L., Guyot, G., Podaire, L. 1987. Monitoring wheat canopies with a high spectral resolution radiometer. *Remote Sensing of Environment*, 22:367-378.
- Committee on Earth Sciences. 1989. *Our Changing Planet: The FY90 Research Plan (The U.S. Global Change Research Program)*, U.S. Department of Interior, Reston, VA.
- Curran, P.J. 1989. Remote sensing of foliar chemistry. *Remote Sensing of Environment*, 30:271-278.
- Curran, P.J., Dungan, J.L., Gholz, H.L. 1990. Exploring the relationship between reflectance red edge and chlorophyll content in slash pine. *Tree Physiology*, 7:33-48.
- Gao, B-C, Heidebrecht, K.B. and Goetz, A.F.H., 1992, *Atmospheric removal program (ATREM) users guide*. Centre for the Study of the Earth from Space, Cooperative Institute for Research in Environmental Sciences, University of Colorado, Boulder.
- Gates, D.M. 1980. *Biophysical Ecology*. Springer-Verlag, New York.
- Gholz, H.L., Vogel, S.A., Cropper, W.P. Jr., McKelvey, K., Ewel, K.C., Teskey, R.O., Curran P.J. 1991. Dynamics of canopy structure and light interception in *Pinus elliottii* stands, North Florida. *Ecological Monographs*, 61, 33-51.
- Johnson, L.F., Peterson, D.L. 1991. AVIRIS observations of forest ecosystems along the Oregon transect. *Proceedings of the Third Airborne Visible/Infrared Imaging Spectrometer (AVIRIS) Workshop*. Ed. R.O. Green. May 20-21 1991. JPL publication 91-28, Pasadena, CA, 190-199.
- Mackinney, G. 1941. Absorption of light by chlorophyll solutions. *Journal of Biological Chemistry*, 140:315-322.
- Peterson, D.L., Aber, J.D., Matson, P.A., Card, D.H., Swanberg, N.A., Wessman, C.A., Spanner, M.A. 1988. Remote sensing of forest canopy and leaf biochemical contents. *Remote Sensing of Environment*, 24:85-108.
- Wessman, C.A., Aber, J.D., Peterson, D.L. 1989. An evaluation of imaging spectrometry for estimating forest canopy chemistry. *International Journal of Remote Sensing*, 10:1293-1316.
- Williams, P. and Norris, K. 1987. *Near infrared technology in the agricultural and food industries*. American Association of Cereal Chemists Inc., St. Paul, MN.

**AVIRIS AND TIMS DATA PROCESSING AND DISTRIBUTION
AT THE
LAND PROCESSES DISTRIBUTED ACTIVE ARCHIVE CENTER**

G. R. Mah
EROS Data Center
Sioux Falls, SD 57198

J. Myers
Aircraft Data Facility, NASA-Ames Research Center
Moffett Field, CA 94035-1000

1. INTRODUCTION

The U. S. Government has initiated the Global Change Research Program, a systematic study of the Earth as a complete system. NASA's contribution to the Global Change Research Program is the Earth Observing System (EOS), a series of orbital sensor platforms and an associated data processing and distribution system. The EOS Data and Information System (EOSDIS) is the archiving, production, and distribution system for data collected by the EOS space segment and uses a multilayer architecture for processing, archiving, and distributing EOS data. The first layer consists of the spacecraft ground stations and processing facilities that receive the raw data from the orbiting platforms and then separate the data by individual sensors. The second layer consists of Distributed Active Archive Centers (DAAC) that process, distribute, and archive the sensor data. The third layer consists of a user science processing network. The EOSDIS is being developed in a phased implementation. The initial phase, Version 0, is a prototype of the operational system. Version 0 activities are based upon existing systems and are designed to provide an EOSDIS-like capability for information management and distribution. An important science support task is the creation of simulated data sets for EOS instruments from precursor aircraft or satellite data.

The Land Processes DAAC, at the EROS Data Center (EDC), is responsible for archiving and processing EOS precursor data from airborne instruments such as the Thermal Infrared Multispectral Scanner (TIMS), the Thematic Mapper Simulator (TMS), and the Airborne Visible and Infrared Imaging Spectrometer (AVIRIS). AVIRIS, TIMS, and TMS are flown by the NASA-Ames Research Center (ARC) on an ER-2. The ER-2 flies at 65000 feet and can carry up to three sensors simultaneously. Most jointly collected data sets are somewhat boresighted and roughly registered.

The instrument data are being used to construct data sets that simulate the spectral and spatial characteristics of the Advanced Spaceborne Thermal Emission and Reflection Radiometer (ASTER) instrument scheduled to be flown on the first EOS-AM spacecraft. The ASTER is designed to acquire 14 channels of land science data in the visible and near-IR (VNIR), shortwave-IR (SWIR), and thermal-IR (TIR) regions from .52 μm to 11.65 μm at high spatial resolutions of 15 m to 90 m. Stereo data will also be acquired in the VNIR region in a single band. The AVIRIS and TMS cover the ASTER VNIR and SWIR bands, and the TIMS covers the TIR bands. Simulated ASTER data sets have been generated over Death Valley, California, Cuprite, Nevada, and the Drum Mountains, Utah using a combination of AVIRIS, TIMS, and TMS data, and existing digital elevation models (DEM) for the topographic information.

2. TIMS ARCHIVE TRANSCRIPTION

The ARC and the DAAC have instituted a program to transcribe the existing ARC aircraft data holdings into an enhanced DAAC-compatible format with associated metadata and browse images. The new data format is shown in figure 1. It is similar to the old ARC format except that a new mission header that contains much of the flight summary report information has been added, as well as navigation data on a scanline-by-scanline basis as an additional band [channel] of data. Data from the aircraft's navigation system are matched to the appropriate scanline data, with interpolated data used between navigation data samples.

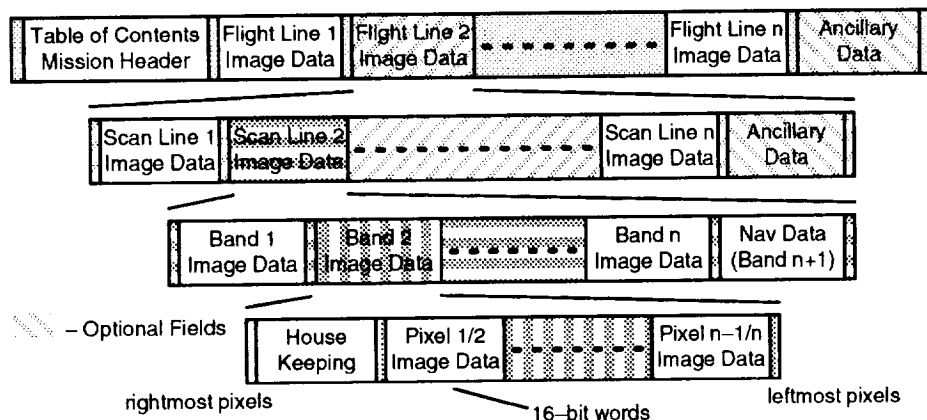


Figure 1. Aircraft Data Archive Format

The browse images for the TIMS are generated during the transcription process by subsampling and decorrelation-stretch (D-stretch) processing data from channels 5, 3, and 1 (red, green, and blue, respectively). The browse image is basically an online version of the Jet Propulsion Laboratory (JPL) hardcopy TIMS browse (quick-look) product. Browse images and metadata are used to populate the Version 0 Information Management System (IMS).

The DAAC is making arrangements to transcribe the TIMS holdings at Stennis Space Center (SSC). The TIMS data at the SSC will be transcribed using a modified version of the system used to transcribe the data at the ARC. The transcription activity is scheduled to run through 1994. The primary 1993 activity is the cataloging of SSC holdings, with actual data transcription and ingest into the DAAC occurring in 1994.

3. AVIRIS ACTIVITIES

The DAAC and the JPL have agreed to have the DAAC process and distribute historical AVIRIS data. Plans call for a phased implementation of these capabilities. The first phase will be the implementation of distributed order processing for 1992 data. An online catalog of metadata and browse images will be available through the Version 0 IMS at the DAAC with order processing and product generation [retrievals] at the JPL. The second phase will be the transcription of historical AVIRIS data into a DAAC-compatible format and the generation of associated browse images and metadata for IMS population. The AVIRIS retrieval processing system is being modified to support both JPL and DAAC requirements and will be installed in both locations. When the data has been transcribed, the DAAC will assume responsibility for handling orders for historical data, and the JPL will only process current-season data. Once a flight season has ended, that season's data will be available from the DAAC as historical data.

The historical data sets available at the DAAC will be limited to the 1991 European campaign data, all standard product data sets, and full season data from 1992 onward. It was decided by both the DAAC science advisory panel and the AVIRIS project that, given the increased performance of the AVIRIS in 1992, the expected volume of pre-1992 data orders would not justify transcription of all pre-1992 data. All other pre-1992 data will still be available through special request from the AVIRIS Data Facility at the JPL.

4. DATA AVAILABILITY

Metadata and browse images for ARC and SSC aircraft data and AVIRIS data are entered into the Version 0 IMS. The IMS serves as an online catalog to access the DAAC holdings and to accept order requests. Orders for ARC or SSC data will be processed directly by the DAAC and orders for AVIRIS data will be passed to the JPL initially, and later processed at the DAAC.

Users will be able to form a database query using geographic location and other criteria. Geographic coordinates can be entered numerically or graphically using the mouse to select a region of interest. When a search is completed, the metadata for the flightlines or scenes meeting the search criteria can be displayed. Browse images can also be displayed interactively or transferred over Internet using anonymous FTP.

5. EOS SENSOR SIMULATIONS

An ASTER data set has been simulated by using TMS data for the VNIR and SWIR channels, TIMS data for the TIR channels, and a DEM for the stereo product. The ASTER stereo VNIR data will be used to generate a DEM, so it was felt that going directly to a DEM would be more appropriate than attempting to simulate the nadir- and backwards-looking images that would be acquired to create a DEM. The four VNIR bands were simulated exactly, but the TMS bandpasses only covered the first SWIR band exactly, straddled the next four SWIR bands, and provided no coverage of the last SWIR band. The TIMS provided coverage in all five of the TIR bands. The band matching between the ASTER, AVIRIS, TIMS, and TMS is shown in table 1.

The original data set was acquired by the ARC over Death Valley, CA on 22 November 1991. The TIMS and TMS were optically adjusted so they would be boresighted and have a ground resolution of 50 m. A 512 pixel by 512 scanline subset of the flightline was used for the simulation.

The first step in the simulation process was to correct for the aspect ratio distortion of the scanning process used to acquire the data. A version of the C130RECT program written by scientists at the JPL was used for correction. The corrected data were then registered to the DEM using an image-warping algorithm in the Land Analysis System (LAS) Tie-Points function. The DEM had a cell size of 90 m, so it was upsampled in resolution to 50 m cells for the registration process. Ten control points were selected in the TIMS image to register it to the DEM. Tie-Points was again used to register the TMS image to the TIMS image using 12 control points.

After the registration processes, the full-resolution image was rearranged to have the same band structure as the ASTER (see table 1). It was assumed that the aircraft image was acquired in the center of an ASTER swath as shown in figure 2. ASTER VNIR data will be acquired at 15 m resolution, so the TMS data were upsampled using the LAS cubic convolution function. The SWIR data are acquired at 30 m resolu-

tion and also required upsampling. The TIR data are acquired at 90 m resolution and were downsampled. The VNIR data registered to the DEM are shown in figure 3.

The simulated data set was presented at the joint ASTER science team meeting in February 1993 for review. At the meeting it was suggested that AVIRIS data could generate a high-fidelity simulation of the VNIR and SWIR bands using the ASTER filter functions, and that ground-truth data be provided to facilitate algorithm development.

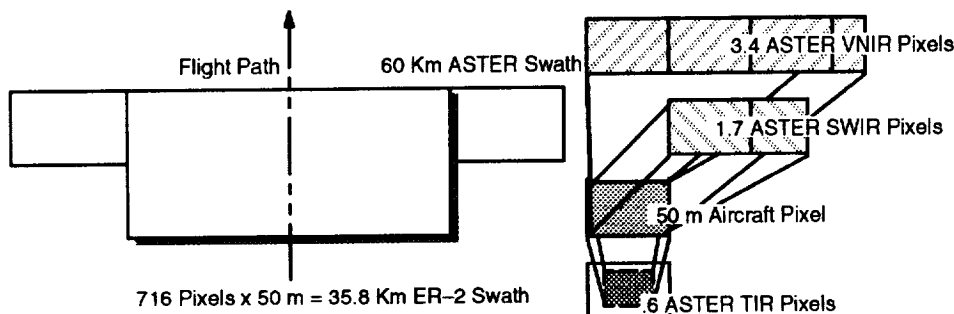


Figure 2. Spatial Mapping of Aircraft Data to ASTER

Table 1. ASTER Channel Mappings

ASTER	Band	TIMS		AVIRIS		TMS	
		Range (um)	Ch	Range (um)	Ch	Range (um)	Ch
VNIR	1	.52 - .6		13 - 21	3	.52 - .60	
	2	.63 - .69		25 - 30	5	.63 - .69	
	3N/3B	.76 - .86		41 - 51	7	.76 - .86	
SWIR	4	1.6 - 1.7		133 - 143	9	1.55 - 1.75	
	5	2.14 - 2.18		191 - 194	10	2.08 - 2.35	
	6	2.16 - 2.22		195 - 199	10	2.06 - 2.35	
	7	2.23 - 2.29		200 - 205	10	2.06 - 2.35	
	8	2.29 - 2.36		207 - 213	10	2.06 - 2.35	
	9	2.36 - 2.43		214 - 220	10	2.06 - 2.35	
TIR	10	8.12 - 8.47	1	8.2 - 8.6			
	11	8.47 - 8.82	2	8.6 - 9.0			
	12	8.92 - 9.27	3	9.0 - 9.4			
	13	10.25 - 10.95	5	10.2 - 11.2			
	14	10.95 - 11.85	6	11.2 - 12.2			



Figure 3. ASTER VNIR composite and DEM

ASTER simulations over test sites at Lake Tahoe, CA; Cuprite, NV; and the Drum Mountains, UT have also been generated. AVIRIS data are being used to simulate the VNIR and SWIR bands, while TIMS data are used for the TIR bands. The Cuprite data set will have a DEM derived from aerial photography, while the Drum Mountains data set uses a DEM derived from SPOT stereo data. Some atmospheric corrections may also be performed using prototype ASTER algorithms to obtain radiances at the ground. Further work may involve the use of other prototype algorithms to generate simulated higher level products.

6. CONCLUSIONS

Airborne scanner data are very useful in the simulation of EOS instruments and will be archived at the DAAC for use in both the EOS and general scientific research. As part of the archival process, the DAAC has populated the IMS with detailed metadata and browse images to aid user access to the data.

41029

MEASUREMENTS OF CANOPY CHEMISTRY WITH 1992 AVIRIS DATA AT BLACKHAWK ISLAND AND HARVARD FOREST

Mary E. Martin and John D. Aber

Complex Systems Research Center
Morse Hall
University of New Hampshire
Durham, NH 03824

1 Introduction

The research described in this paper was designed to determine if high spectral resolution imaging spectrometer data can be used to measure the chemical composition of forest foliage, specifically nitrogen and lignin concentration. Information about the chemical composition of forest canopies can be used to determine nutrient cycling rates and carbon balances in forest ecosystems (Melillo et al. 1982, Aber et al. 1992). This paper will describe the results relating data from the Airborne Visible/Infrared Imaging Spectrometer (AVIRIS) to field measured canopy chemistry at Blackhawk Island, WI and Harvard Forest, MA.

2 Methods

A total of forty plots were sampled at Harvard Forest, Petersham, MA and Blackhawk Island, Wisconsin Dells, WI. Plots were characterized by the collection of green leaf samples at the time of the AVIRIS overflight and by litterfall collections to determine the species composition of the canopy. Fresh leaf samples collected within 10 days of the overflight were used to determine the concentrations of nitrogen, lignin, cellulose, and water for each species. Water content was determined by measuring fresh and oven dry sample weights. Lignin and cellulose concentrations were determined by sulfuric acid digestion, and CHN combustion method determined carbon, hydrogen and nitrogen concentrations.

Atmospheric corrections of the AVIRIS data were done by the ATREM program (Gao et al. 1992). Following the ATREM correction, a secondary correction was made based on field spectra measured at Blackhawk Island. The first derivative of the mean of four spectra for each plot was used in the analysis. Two to three wavelengths were chosen in a multiple linear regression of reflectance data vs field measured chemistry. Specific wavelengths were chosen due to their

statistical fit to the data and their relationship to known absorption features of molecular bonds present in the samples.

3 Results

AVIRIS reflectance data at .946 and 2.29 μm were used to predict nitrogen concentration at Blackhawk Island, corresponding to absorption features in C-H and N-H bonds, respectively. All references to molecular bond absorption features are from Osborne et al. 1986. Reflectance data at .79 and 1.7 μm were used to predict lignin concentrations, corresponding to absorption by aromatic molecular structures. The relationships between measured and predicted nitrogen and lignin concentrations are shown in Figure 1. This relationship, based on field sampling at Blackhawk Island, was then applied to the entire image, yielding chemical concentration estimates for the entire island (Figure 2).

In the analysis of Harvard Forest data, the equations developed at Blackhawk Island were applied to the AVIRIS data. This resulted in an overestimation of both nitrogen and lignin concentration. However, when the same wavelengths were used in a regression equation relating reflectance data to *Harvard Forest* field data, a much better prediction was obtained. The equations which best predicted nitrogen and lignin at Harvard Forest used different wavelengths than the Blackhawk Island equations (Figure 3). Differences in atmospheric corrections between the two scenes, i.e. both scenes were normalized to Blackhawk Island field spectra, may explain the selection of different wavelengths for the best predictive equation. Nitrogen was best predicted with .773 and 2.15 μm , corresponding to N-H and NH₂ bonds, respectively. Lignin was predicted best with 1.54, 2.11 μm . An estimation of foliar nitrogen and lignin concentration is shown in Figure 4.

Predictions from AVIRIS data at Harvard Forest are currently being used to drive an ecosystem model predicting ecosystem carbon balance. A critical input parameter in this model is foliar nitrogen concentration which is used to determine the maximum rate of photosynthesis (Aber et al 1992).

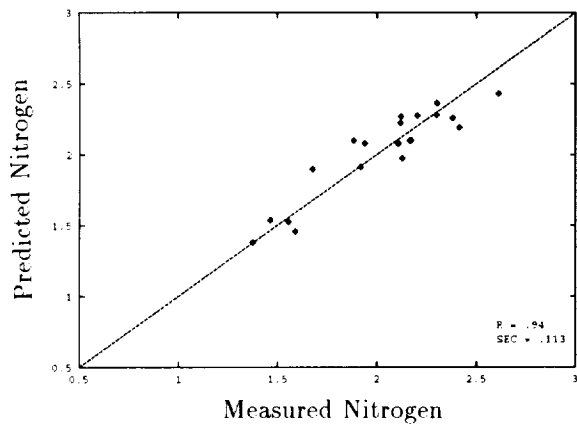
4 References

Aber, J.D. and C.A. Federer, 1992, "A generalized, lumped-parameter model of photosynthesis, evapotranspiration and net primary production in temperate and boreal forest ecosystems," *Oecologia*, vol. 92, pp463-474.

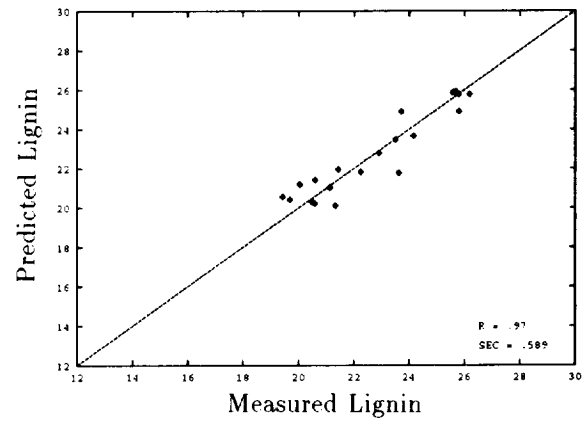
Gao, B.-C, H.B. Heidebrecht, and A.F.H. Goetz, 1992, *Atmospheric Removal Program (ATREM) User's Guide*, Center for the Study of Earth from Space/CIRES, University of Colorado, Boulder, CO.

Melillo, J.M., J.D. Aber, and J.F. Muratore, 1982, Nitrogen and lignin control of hardwood leaf litter decomposition in relation to soil nitrogen dynamics and litter quality, *Ecology*, vol. 66, pp266-275.

Osborne, B.G. and T.Fearn, 1986, *Near Infrared Spectroscopy in Food Analysis*, Longman Scientific and Technical Publishing Co.



a.

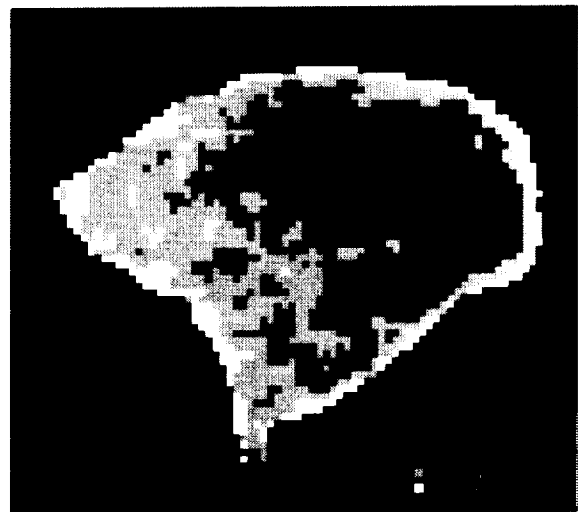


b.

Figure 1. Blackhawk Island canopy nitrogen(a) and lignin(b) concentrations predicted from 1992 AVIRIS data vs field measured nitrogen and lignin. R = correlation coefficient, SEC = standard error of calibration.

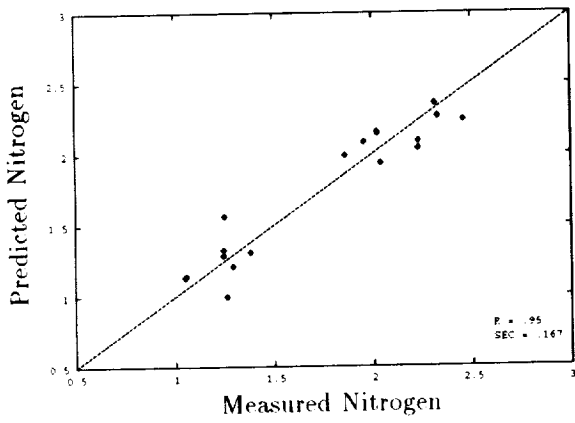


a.

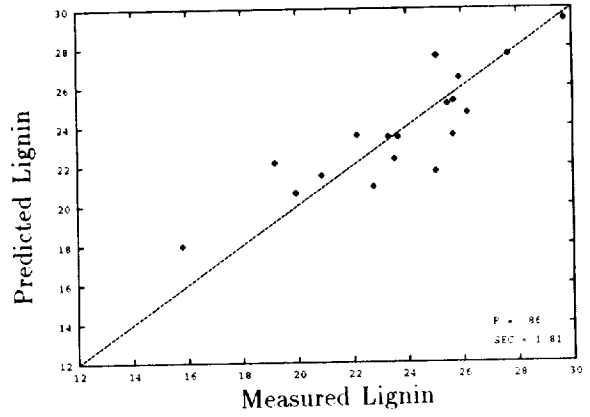


b.

Figure 2. Blackhawk Island canopy nitrogen(a) and lignin(b) concentrations predicted from 1992 AVIRIS data.

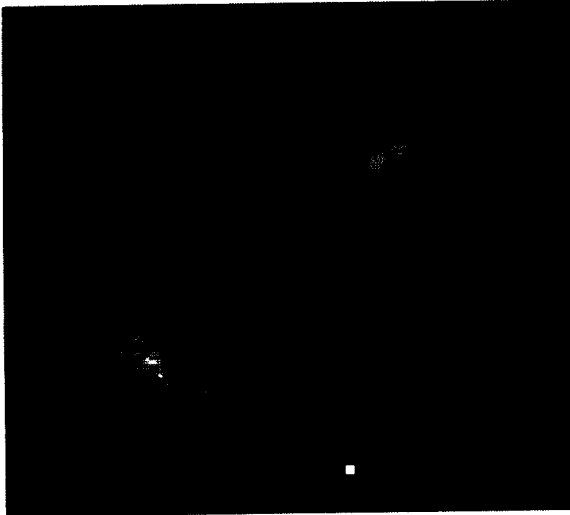


a.

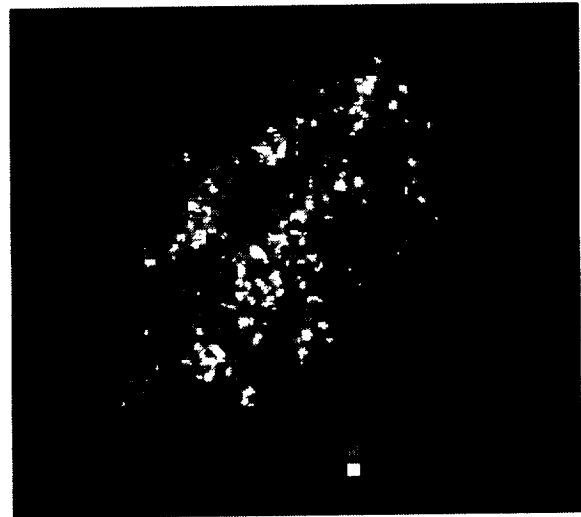


b.

Figure 3. Harvard Forest canopy nitrogen(a) and lignin(b) concentrations predicted from 1992 AVIRIS data vs field measured nitrogen and lignin.



a.



b.

Figure 4. Harvard Forest canopy nitrogen(a) and lignin(b) concentrations predicted from 1992 AVIRIS data.

41030

CLASSIFICATION OF THE LCVF AVIRIS TEST SITE WITH A KOHONEN ARTIFICIAL NEURAL NETWORK

Erzsébet Merényi¹, Robert B. Singer¹ and William H. Farrand²

¹University of Arizona, LPL, PIRL, Tucson, AZ 85721

²SAIC, 803 W Broad Street, Suite 100, Falls Church, VA 22046

1. BACKGROUND AND DATA

We are presenting a classification of an AVIRIS spectral image of the Lunar Crater Volcanic Field (LCVF) (Fig. 1.a). Geologic mapping from such data is made possible by distinctive mineral signatures: absorption features and the shape of the spectral continuum. The subtle spectral shape differences between some of the geological units in this scene along with the high dimensionality of the spectra presents a challenging pattern recognition task (Fig. 2.). We found an artificial neural network powerful in separating 13 geological units based on the full spectral resolution.

The LCVF, in northern Nye County, Nevada, was the primary focus of the NASA-sponsored Geologic Remote Sensing Field Experiment in the summer of 1989. It consists of over 100 square miles of Quaternary basaltic pyroclastic and flow deposits (Scott and Trask, 1971). These deposits lie atop ignimbrites and silicic lava flows of Tertiary age and in turn are overlain by Quaternary alluvial and playa deposits. This AVIRIS image was collected on September 29, 1989 at 11:44 PDT. The 256-by-256 pixel subsection in this study contains oxidized basaltic cinder deposits, the southern half of the Lunar Lake playa, and outcrops of the Rhyolite of Big Sand Spring Valley (mapped by Ekren et al., 1972). Vegetation in LCVF is sparse, but locally abundant within washes and near springs (Fig. 1.a).

2. CLASSIFICATION TECHNIQUE AND RESULTS

Artificial neural networks (ANN's) are parallel distributed computing architectures that learn to solve problems from examples. An introduction and overview can be found, for example, in (Pao, 1991). ANN's have proved powerful for the classification of complicated, noisy, real-life data (e. g., Huang and Lippman, 1987; Benediktsson *et al.* 1990; Hepner *et al.* 1990; Merényi *et al.* 1992). Many varieties of ANN's have been devised for different types of tasks. The most widely used paradigm is the Backpropagation, owing to its general applicability. Backpropagation, however, can be difficult to train, especially with large input vectors. Good training for the separation of classes with subtle differences may require a very high number of training samples. This could be problematic in remote sensing applications, because of limited field knowledge.

We used here a Kohonen-type Self-Organizing ANN combined with a categorization learning output layer (by NeuralWare, Inc., 1991). This first establishes a topological map of the cluster structure of the data in its 2-D hidden Kohonen layer (Kohonen, 1988), in an unsupervised regime. Then it is trained, in supervised mode, to assign class labels to the training patterns. The preformed clusters help keep the ANN from learning contradicting class labels by merely memorizing each case instead of deriving class properties. This can easily happen with a Backpropagation network when the number of training samples is small. Another advantage over Backpropagation is

that the training is easier and much shorter. More details on how this ANN configuration works is given in Howell *et al.* (1993).

Approximately 30 training samples were selected for each of 13 spectral types (Fig. 2. left box) on the basis of spectral pattern differences and geological field knowledge. The data set consisted of 158 channels after the exclusion of spectrometer overlap, atmospheric water bands and excessively noisy channels. As explained on Fig. 2., the ANN produces reliable classification for all 13 classes, based on training with 0.6% of the image data. Corresponding geological maps (e. g., Scott and Trask, 1971) and field experiences confirm that each class is an identifiable geological unit in the test site. The 3 units that were mapped by earlier linear mixture modeling (Farrand and Singer, 1991), cinder, rhyolite and playa, are well matched and further broken down according to more subtle compositional differences which are in turn indicative of geologic processes (Fig. 1.b).

As little as 0.6% of the image data was sufficient for training to produce the presented geological details with this ANN. An important advantage of the Self-Organizing neural network over the most commonly used Back-propagation is that it achieves higher classification accuracy on test data based on a small amount of training data (e. g., Benediktsson *et al.* 1990). This enables very cost-effective sampling of remote sensing sites.

Acknowledgements: The computing facilities of the Lunar and Planetary Laboratory and the Planetary Image Research Laboratory, of the University of Arizona, software support by James Winburn and contributions by NASA Space Grant Intern Trevor Laing are cheerfully acknowledged.

REFERENCES

- Benediktsson, J. A., P. H. Swain, O. K. Ersoy and D. Hong, 1990, "Classification of Very High Dimensional Data Using Neural Networks", *IGARSS'90 10th Annual International Geoscience and Remote Sensing Symp.* Vol. 2. p. 1269,
- Ekren, E.B., E.N. Hinrichs and G.L. Dixon, 1973, "Geologic map of the Wall quadrangle, Nye County, Nevada", USGS Misc. Geol. Inv. Map I-719, scale 1:48,000.
- Farrand, W.H. and R.B. Singer, 1991, "Analysis of altered volcanic pyroclasts using AVIRIS data", *Proc. Third AVIRIS Workshop, JPL Publication 91-28*, Jet Propulsion Laboratory, Pasadena, Ca.
- Hepner, G. F., T. Logan, N. Ritter, N. Bryant, 1990, "Artificial Neural Network Classification Using a Minimal Training Set: Comparison to Conventional Supervised Classification", *Photogrammetric Eng. & Remote Sensing*, Vol. 56, No. 4, pp. 469-473
- Howell, E. S., E. Merényi, L. A. Lebofsky, 1993, "Using Neural Networks to Classify Asteroid Spectra", forthcoming, *JGR Planets*
- Huang, W. and R. Lippman, 1987, "Comparisons Between Neural Net and Conventional Classifiers", *IEEE First International Conference on Neural Networks*, Vol. IV, San Diego, pp. 485-494.
- Kohonen, T., 1988, *Self-Organization and Associative Memory*, Springer-Verlag, New York
- Merényi, E., R. B. Singer, J. S. Miller, 1992, "Spectral Analysis of the Surface of Mars: Neural Network Classification of High Spectral Resolution Images", *Bull. A.A.S.*, 24 No. 3, p. 979
- NeuralWare, Inc., 1991, *NeuralWorks Professional II Manual*
- Pao, Y. H., 1989, *Adaptive Pattern Recognition and Neural Networks*, Addison-Wesley
- Scott, D.H. and N.J. Trask, 1971, "Geology of the Lunar Crater Volcanic Field, Nye County, Nevada", USGS Prof. Paper 599-I.

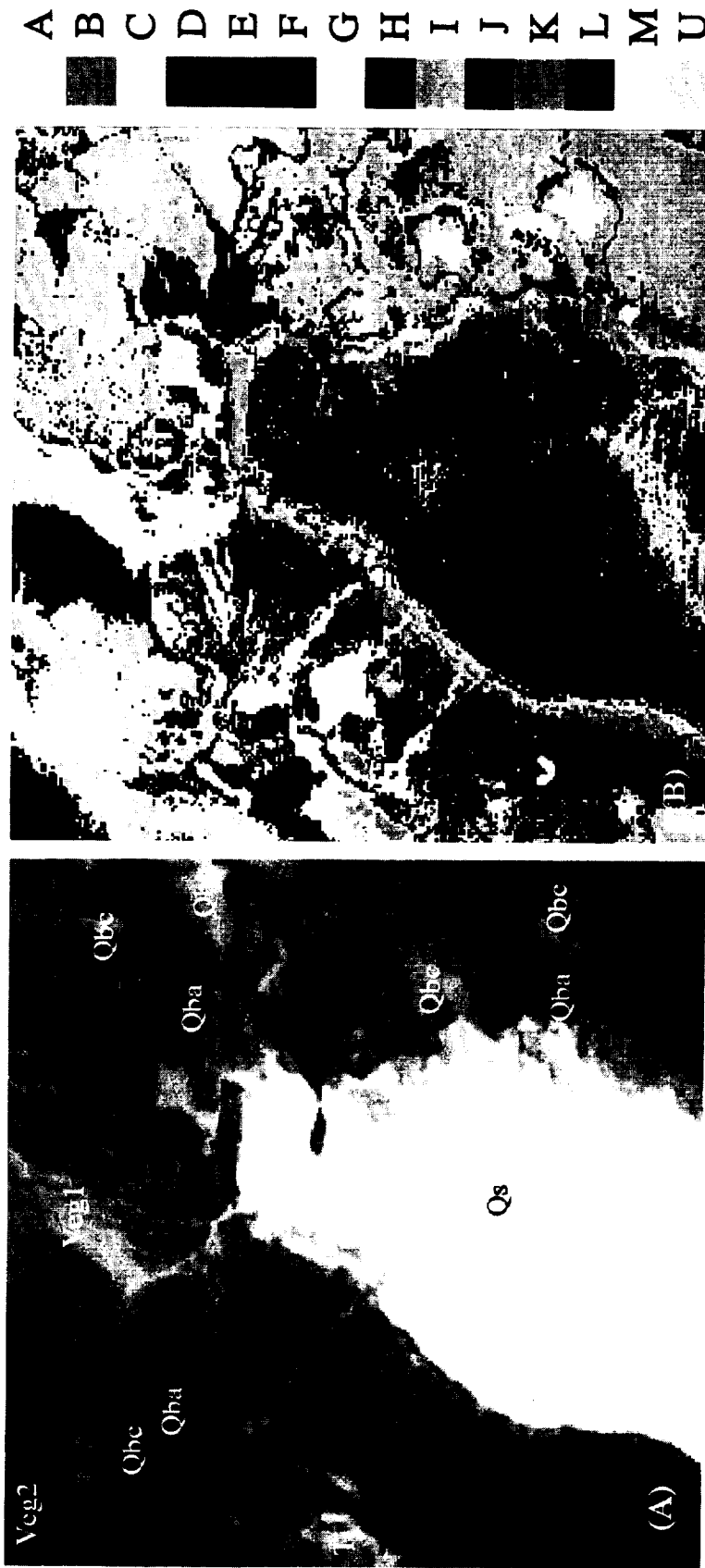
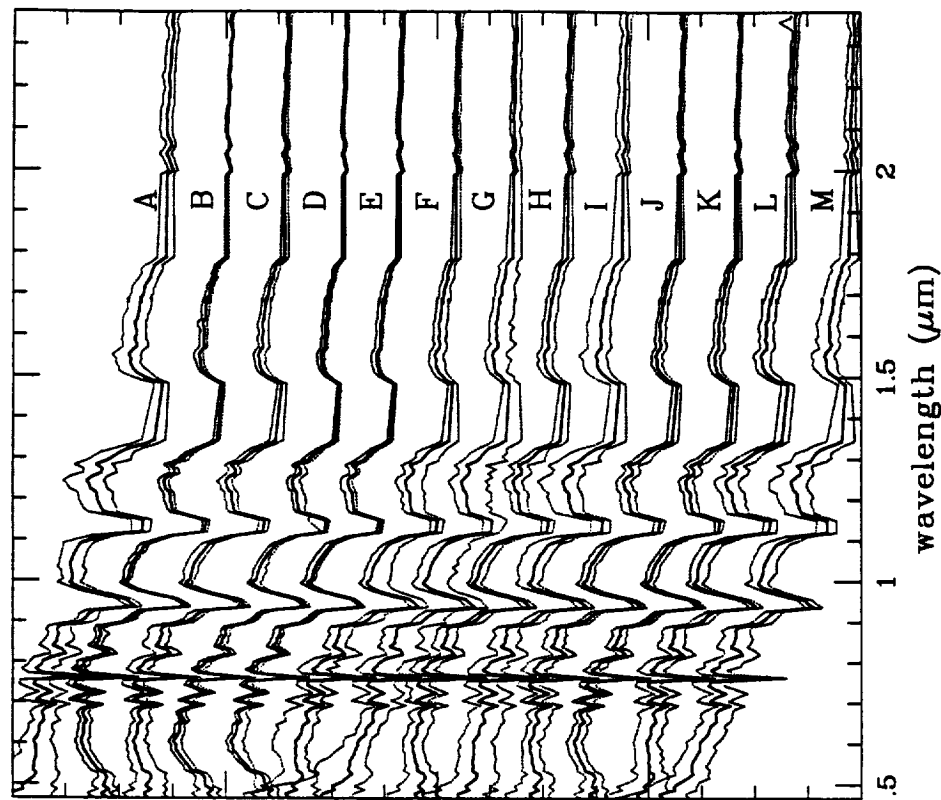


Figure 1. a) The LCVF study area. Labels mark some of the major geologic units based on the map by Scott and Trask (1971) and on our field knowledge. Qba - Basaltic ejecta aprons; Qb2 - Intermediate, black to gray weathered basalt; Qbc - Cinder cones; Qs - Sedimentary deposits; Ti - Ignimbrite and rhyolite flows, rhyolitic to andesitic; sequence. Veg1 - grass; Veg2 - scrub brush; b) Classification map, produced by a self-organizing ANN. (See also Slide 5, in color, for better distinction between classes.) A - highly oxidized cinders; B - rhyolite of Big Sand Springs Valley; C - vegetation type 1, probably grass; D - southern playa; E - northern playa (clay-rich); F - young basalt flows; G - Shingle Pass Tuff; H - Quaternary alluvium derived from silic volcanics;

I - old basalt flow; J - vegetation type 2, probably scrub brush; K - basalt cobbles on playa surface; L - ferric oxide rich soil; M - poorly oxidized dark cinders; U - unclassified (~10% of the pixels). Geologic maps confirm that these 13 classes correspond to known geologic units. The 3 endmember features mapped by earlier linear mixing modeling, cinder, rhyolite and playa, are covered and further refined by our 3 different cinder units (A, L and M), rhyolite (B), and southern and northern playa units (D and E), respectively. In addition, the ANN can separate two different vegetation types (C, J) from each other and from class B (rhyolite). These spectra are similar enough (see Fig. 2.) to cause singularity problems for linear inversion methods.



Right: Mean spectrum and the envelope of the extremes for each of the spectral classes A - M on Figure 1.a, produced by the neural network after it was trained on the samples shown in the left box. As seen, the mean spectra of these classes very closely match the mean spectra of the training sample sets. Quantitative evaluation shows that the relative difference between class and sample means is within 1% for classes B, D and E, between 5 - 10% for classes C and F - M, and between 5 - 20% for class A.

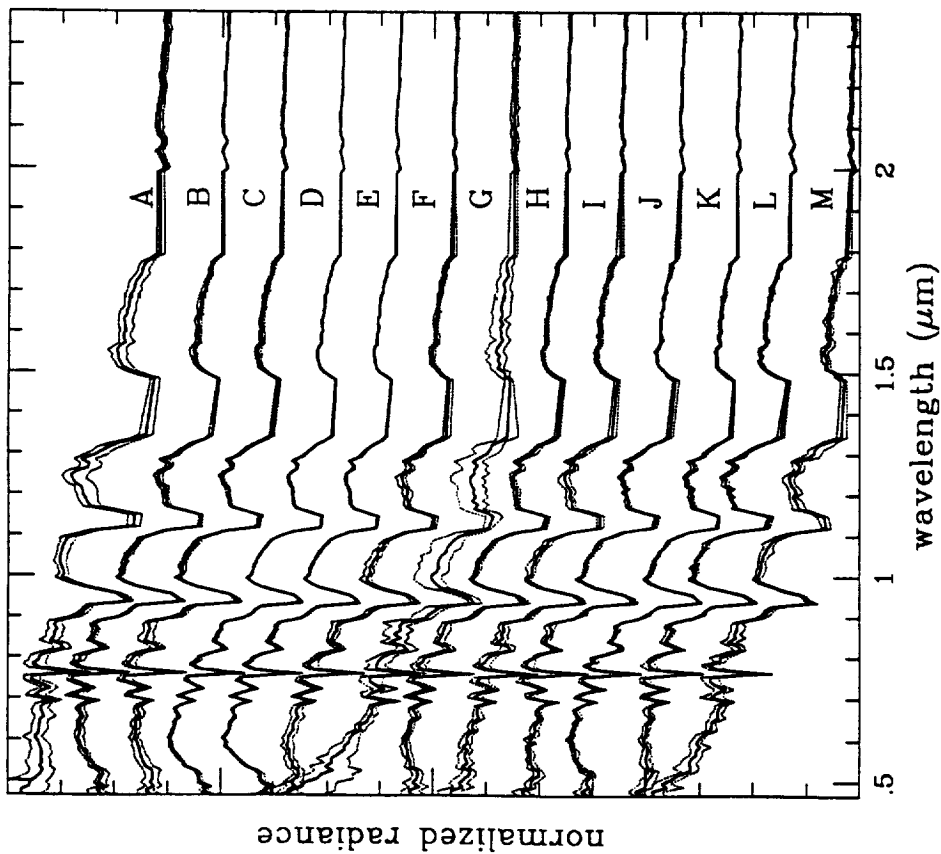


Figure 2. Comparison of the training spectra with the classification results. Left: Mean spectrum and the envelope of the training spectra for each class. The samples were taken from the radiance image, which was previously brightness normalized to cancel illumination geometry and albedo effects and thus retain only the spectral characteristics. Each training set contains only about 30 spectra. The water absorption bands were excluded from the analysis.

531-32

41031

5

Extraction of Auxiliary Data from AVIRIS Distribution Tape for Spectral, Radiometric, and Geometric Quality Assessment

Peter Meyer*, Robert O. Green, and Thomas G. Chrien

Jet Propulsion Laboratory (JPL), California Institute of Technology
4800 Oak Grove Drive, Pasadena, CA 91109, pmeyer@rsl.geogr.unizh.ch

1. INTRODUCTION

Remotely sensed data are affected by system (sensor and platform), and scene related effects. For quantitative investigations the spectral, radiometric and geometric characteristics of the system and scene have to be known.

The relevant effects and their possible influence on an image have to be specifically determined for every remote sensing system and adequate description parameters need to be updated and reported on a regular basis (Teillet, 1992) as they are carried out, e.g., for the AVIRIS system (Vane et al., 1988, Chrien et al., 1990, Chrien et al., 1991, and Chrien, 1992). It is evident that the strength of the influence of similar effects is very dependent on the accessibility of auxiliary information about such sensor systems. Degradation in a spaceborne system can normally be just reported and cannot be corrected. In contrast, an airborne sensor can be evaluated, maintained and improved periodically. Such maintenance efforts are particularly important because airborne systems are exposed to extreme and changing environments. These include tens of takeoffs and landings each year as well as extreme changes in temperature and humidity on the tarmac and in flight.

For the AVIRIS system there are environmental stresses such as changes in temperature, air pressure, humidity, vibration of the platform or scene-related reasons like atmospheric conditions, and topography. The information contained in the auxiliary files included with the AVIRIS data can be used to assess these effects and compensate for them. In addition, the spectral, radiometric and geometric calibration data contained in the auxiliary file are required for quantitative analysis of the data.

The paper describes tools to access the auxiliary information that characterizes the AVIRIS system. These tools allow the examination of parameters that may impact the quality of the measured AVIRIS image. An example of the use of this auxiliary data was carried out with regard to a parametric geocoding approach as reported by Meyer (1993). Emphasis is placed on the reported auxiliary information that describes the geometric character of the AVIRIS data in 1991. Results are presented using data from the AVIRIS flight #910705, run 6 and 7 of the NASA MAC Europe '91 campaign in a test site in Central Switzerland.

*now at University of Zurich-Irchel, Remote Sensing Laboratories (RSL), Winterthurerstrasse 190, CH-8057 Zurich

2. THE IPSRS TOOLS

The tools are part of the quality assessment module of the Information Processing System for Remote Sensing Data (IPSRS) as initially reported by Meyer (1992) and Meyer and Itten (1992). The IPSRS approach proposes two parts, information extraction and information management, to complete processing of remotely sensed data. The first part consists of the modules' data quality assessment and preprocessing and the latter of the modules' classification and presentation.

Table 1 shows the currently available tools. These are implemented with IDL (Interactive Data Language, a proprietary language of Research System Inc. (1993)). All programs run in the foreground and have a user-friendly interface. There is the possibility to select the tools out of an overview using pop-up menus (tools.pro) or let the tasks run as a single function. All results are presented with plots (black and white and some of them in color) that can be printed to a Postscript laser printer. Additional parameters can be derived from the auxiliary data set such as pre-calibration, post-calibration (1992, 1993), dark current, offset, noise equivalent radiation (1990, 1991), noise spike replace list, spike threshold (1992, 1993), dropped line list, and geometric calibration (1992, 1993).

3. RESULTS FOR THE CURRENT DATA SET

Some plots out of the examination of the data set are presented in Figures 1-4.

Figure 1: Spectral response function full width at half maximum (FWHM) of the corresponding Gaussian function. These response functions are required to compare other spectral data with AVIRIS measurements.

Figure 2: Altitude measurements of the 1991 navigation data, based on barometric measurements, compared with the values of the ADOUR system for run 6. The ADOUR is a high-precision, dual-antenna, dual-frequency, ground-based conical radar tracking system operated by the Swiss Army (Meyer, 1993). The systematic error for the ADOUR system for elevation and azimuth is ± 0.2 mrad and for distance ± 7 m. These requirements could be confirmed for the current data set (Meyer, 1993). Accepting the ADOUR measurements to be a good representation of the reality, the plot proves that the deviation of the altitude for the navigation data is within the expected range, which is for an unaided LTN90-116 Inertial Navigation System (INS) 0.9 nmi/h (Perrin, 1993).

Figure 3 and Figure 4: Comparison of navigation roll and the instrument roll for run 6 and run 7: When the pilot begins recording AVIRIS data the sensor gyros are initialized as horizontal. Occasionally, due to aeronautical reasons, the ER-2 aircraft is not fully leveled at this time. This offset affects the quality of roll correction for the entire flight line. Figure 3 shows that the aircraft was almost levelled and that during the whole flight the possible range of $\pm 1.5^\circ$ was never exceeded. For run 7, a large offset was present at the initialization time and caused a saturation of the roll gyro after line number 451 (Figure 4). For this flight, the saturation of the roll gyro rendered investigation of the aircraft roll at high precision impossible. Fortunately, saturation of the roll gyro occurs only rarely.

4. OUTLOOK

Beginning in the 1992 flight season, the ER-2 INS was using a GPS-based system. Test results of a similar configuration show excellent results with an accuracy of 7.05 ± 21.34 m (Perrin, 1993). These changes will make it

possible to define the flight line and reconstruct the observation geometry of AVIRIS as a basic requirement for a parametric geocoding approach.

5. ACKNOWLEDGMENTS

The first author would like to thank the Swiss Research Foundation and NASA for supporting the project and K.I. Itten (RSL), G. Vane, R. O. Green, and E. G. Hansen (JPL) for providing special assistance. The support of the NASA Ames Research Center, the Swiss Air Force, and Litton, Aero Products, Woodlands, CA is gratefully acknowledged. Thanks for technical assistance go to H. I. Novack, M. Solis, P. J. Nielsen, J. J. Genofsky, C. Chovit, R. E. Steinkraus, and H. O. Gundersen (JPL).

The research described in this paper was carried out at the Jet Propulsion Laboratory, California Institute of Technology, and was sponsored by the Swiss Research Foundation, Project No. 8220-33290.

Table 1: Available ISPRS tools for quality assessment for AVIRIS data.

Data characteristics	ISPRS tool name	Description and remarks
Spectral		
Central band position	CentBandPos.pro	Band center wavelength [nm].
Spectral response function FWHM	Bandwith.pro	The full width at half maximum of the spectral response function (assumed to be Gaussian) [nm].
Radiometric		
Radiometric calibration	RadCor.pro	Multipliers determined in the laboratory for converting DN values to units of radiance.
Vignetting	CTVignetting.pro	Factors to correct for differences in the instrument's cross-track sensitivity.
On-board calibration	Onboardcal.pro	Numbers that are the on-board calibration high-intensity position response in DN.
Geometric		
Velocity	NavRead1.pro	N-S, E-W velocity, true air speed, vertical velocity, and ground speed reported by the aircraft inertial navigation system (INS) [m/s].
Location (INS)	NavRead2.pro	Longitude, latitude, altitude of the aircraft, reported by the aircraft INS system [degree].
Attitude (INS)	NavRead3.pro	Navigation roll, pitch, and true heading, reported by the aircraft INS [degrees].
Instrument's roll compensation	EngRead2.pro	Instrument roll with 11 symmetrically distributed readings per scanline reported by the AVIRIS instrument's rate gyro; values need to be within range of $\pm 1.5^\circ$.
Instrument's pitch	EngRead3.pro	Instrument pitch value with 11 symmetrically distributed readings per scanline reported by the AVIRIS instrument's rate gyro [degree].
Instrument's mirror rotation	EngRead4.pro	Linearity count for the mirror rotation with 11 symmetrically distributed readings per scanline.
Quality assessment of the auxiliary data		
Roll	NavAnal4A.pro	Comparison between the navigation roll with a selected reading of the instrument roll.
Pitch	NavAnal4B.pro	Comparison between the navigation pitch with a selected reading of the instrument roll.
Altitude	NavAnal3A.pro	Comparison between the navigation altitude and the corresponding information of the high-precision, dual-antenna, dual-frequency, ground-based conical radar tracking system ADOUR (Meyer, 1993).
Ground speed	NavAnal3B.pro	Comparison between the navigation ground speed and the corresponding information of the ADOUR.
True heading, yaw, central mass direction	NavAnal5A.pro	Calculation of the yaw and central mass direction using the N-S, E-W velocity, and the true heading of the navigation data.

6. REFERENCES

- Chrien, T. G., R. O. Green, and M. L. Eastwood (1990), Accuracy of the Spectral and Radiometric Laboratory Calibration of the Airborne Visible/Infrared Imaging Spectrometer (AVIRIS), in *Proc. of the Second Airborne Visible/Infrared Imaging Spectrometer (AVIRIS) Workshop*, JPL Publ. 90-54, pp. 15-34.
- Chrien, T. G., M. L. Eastwood, C. M. Sarture, R. O. Green, and W. M. Porter (1991), Current Instrument Status of the Airborne Visible/Infrared Imaging Spectrometer (AVIRIS), in *Proc. of the Third Airborne Visible/Infrared Imaging Spectrometer (AVIRIS) Workshop*, JPL Publ. 91-28, pp. 302-313.
- Chrien, T. G. (1992), AVIRIS: Recent Instrument Maintenance, Modifications and 1992 Performance, in *Proc. of the Third Annual JPL Airborne Geoscience Workshop*, JPL Publ. 92-14, Vol. 1, Pasadena, CA, pp. 78-79.
- Meyer, P. (1992), Segmentation and symbolic description for a classification of agricultural areas with multispectral scanner data, *IEEE Transaction on Geoscience and Remote Sensing*, Vol. 30, 5: 673-679.
- Meyer, P., and Itten, K. I. (1992), Datenbankbasierte Klassifikation eines Multispektralscanner-Datensatz, *Zeitschrift für Photogrammetrie und Fernerkundung*, 5/92:149-158.
- Meyer, P. (1993), A Parametric Approach for the Geocoding of Airborne Visible/Infrared Imaging Spectrometer (AVIRIS) Data in Rugged Terrain, *Remote Sensing of Environment* (submitted).
- Perrin, D. (1993), Personal communication (fax Jan 28, 1993).
- Research Systems, Inc.®(1993), IDL User's Guide, Version 3.0, Boulder, CO.
- Teillet, P. M. (1992), An Algorithm for the Radiometric and Atmospheric Correction of AVHRR Data in the Solar Reflective Channels, *Remote Sens. of Environ.*:41:185-195
- Vane, G., W. M. Porter, J. H. Reimer, T. G. Chrien, and R. O. Green (1988), AVIRIS Performance during the 1987 Flight season: An AVIRIS Project Assessment and Summary of the NASA-Sponsored Performance Evaluation, in *Proc. of the AVIRIS Performance Evaluation*, JPL Publ. 88-38, Pasadena, pp. 1-20.

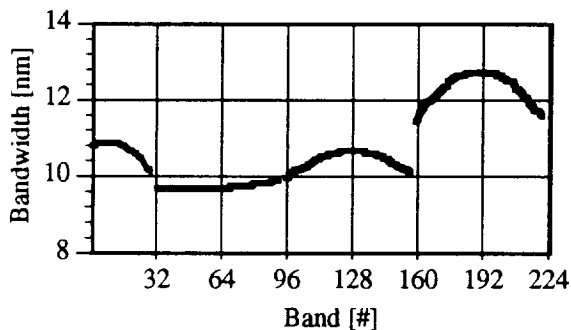


Figure 1: Spectral response function FWHM

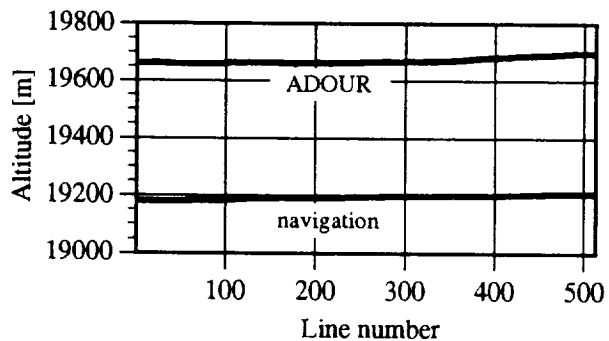


Figure 2: Altitude comparison between navigation data and ADOUR data.

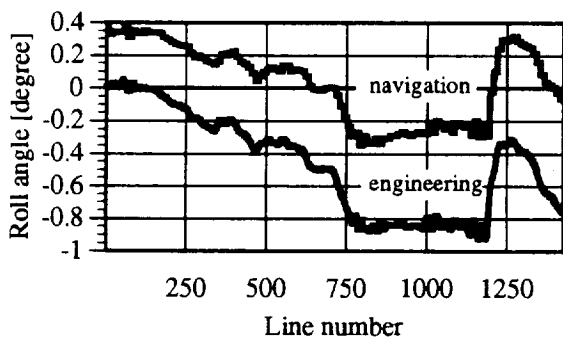


Figure 3: Comparison of navigation roll and instrument roll for run 6.

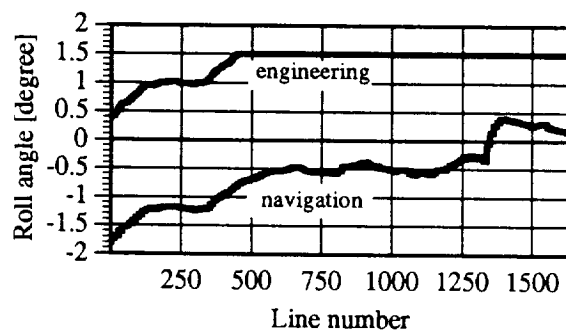


Figure 4: Comparison of navigation roll (thin line) and instrument roll (thick line) for run 7.

Preprocessing: Geocoding of AVIRIS Data using Navigation, Engineering, DEM, and Radar Tracking System Data

Peter Meyer*, Steven A. Larson, Earl G. Hansen, and Klaus I. Itten¹

Jet Propulsion Laboratory (JPL), California Institute of Technology
4800 Oak Grove Drive Pasadena, CA 91109, pmeyer@rsl.geogr.unizh.ch

¹ University of Zurich, Remote Sensing Laboratories (RSL), CH-8057 Zurich

1. INTRODUCTION

Remotely sensed data have geometric characteristics and representation which depend on the type of the acquisition system used. To correlate such data over large regions with other real world representation tools like conventional maps or Geographic Information Systems (GIS) for verification purposes, or for further treatment within different data sets, a coregistration has to be performed. In addition to the geometric characteristics of the sensor there are two other dominating factors which affect the geometry: the stability of the platform and the topography. There are two basic approaches for a geometric correction on a pixel-by-pixel basis: (a) A parametric approach using the location of the airplane and inertial navigation system data to simulate the observation geometry and (b) a non-parametric approach using tie points or ground control points (Itten and Meyer, 1993). It is well known that the non-parametric approach is not reliable enough for the unstable flight conditions of airborne systems, and is not satisfying in areas with significant topography, e.g. mountains and hills. The present work describes a parametric preprocessing procedure which corrects effects of flight line and attitude variation as well as topographic influences and is described in more detail by Meyer (1993c).

2. BASIS OF THE STUDY

Test site and image data: The area "Zug-Buochserhorn" is the standard test site of the Remote Sensing Laboratories, University of Zurich-Irchel in Central Switzerland. The region was covered by the AVIRIS flight #910705, run 6 of the NASA MAC Europe'91 campaign providing a data swath with an average nominal pixel size of about 18m. The first scene, Zug, represents a hilly area with highest elevation differences of about 600m and slopes with typical angles between 15° and 60°. The second scene, Rigi, is an example of mountainous terrain with elevation differences of about 1400m and maximum slope angles up to 90°.

AVIRIS auxiliary data: The quality assessment for the actual data set is described in detail in Meyer et al. (1993b). The current work uses the navigation data roll, pitch, and true heading (generated through the ER-2 Inertial Navigation System) and the roll and pitch of the AVIRIS instrument's precision gyros.

Digital elevation model (DEM): The test area is covered by the two digital models (DHM-25) Zug and Rigi generated by the Swiss Federal Office of Topography**. They have a resolution of 25m in i and j direction and of 0.10 m in elevation e with an average error in elevation of $2.2m \pm 1.0m$ for model Zug, and $4.4m \pm 1.8m$ for Rigi.

ADOUR conical radar tracking system: The ground-based immobile tracking radar system ADOUR is a dual antenna, dual frequency radar with a conical scan tracking system operated by the Swiss Air Force (Thomson-CSF, 1987). For the

* now at: University of Zurich-Irchel, Remote Sensing Laboratories, Winterthurerstrasse 190, CH-8057 Zurich

**DEM data courtesy: Swiss Federal Office of Topography, July 05, 1993

current approach the three parameters latitude x , longitude y , and altitude z are used. The systematic error for elevation and azimuth is $\pm 0.2\text{mrad}$ and $\pm 7\text{m}$ for distance with an update interval of 0.2 second.

Ground reference information: A forest map was generated by scanning the green (forest) plate of the Swiss Topographic Map, scale 1:25,000, edition 1987 at $50\ \mu\text{m}$ with an Optronics 5040 Scanner. The average cartographic accuracy is about 5.0 m. A shoreline map was produced by digitizing the same map in an ARC/Info using a digitizing tablet. The average (theoretical) accuracy is $\pm 8.0\text{m}$.

3. METHOD

Figure 1 gives an overview of the core task for the new method for geocoding AVIRIS data. The basic goal is to reconstruct for every pixel the geometric situation at the time it was acquired with AVIRIS. This includes three major aspects. The first considers the flight line and attitude of the ER-2 aircraft, the second reconstructs the current observation geometry and the third treats the situation on the surface. This approach includes the three different coordinate systems (c,r) for the raw file, longitude x , latitude y , and altitude z together with roll ω , pitch ϕ , and true heading χ for the observation geometry and $(i,j, e_{i,j})$ for the DEM.

Flight line and attitude of the ER-2 aircraft: The x, y , and z of the aircraft need to be known as a first step. For the 1991 European flight the information results from an unaided LTN90-116 INS navigation system with a position accuracy of 0.9 nmi/h (Perrin, 1993). These data are not accurate enough for the current approach. Therefore, ADOUR data are used as an alternative. The description of the attitude of the aircraft is based on the χ from the navigation data and the ω and ϕ from the instrument data.

Current observation geometry: The basic idea is shown in Figure 2 and described in more detail by Larson et al. (1994). The effort is to obtain the underlying surface out of the well-known location (=flight line) and the current attitude of the aircraft. The position vector $X_{c,r}$ represents the location of pixel (c,r) in the aircraft coordinate system (x,y,z) at the instant the pixel was acquired by the instrument and for the ideal case where $\omega = \phi = \chi = 0^\circ$:

$$X_{c,r} = \left(\left[\tan \left[\left(c - \frac{\max P - 1}{2} \right) \frac{FOV}{\max P} \right] Z_{x,y} \right] \right), \quad (1)$$

where c = pixel number of pixel (c,r) within line r of the raw image, $\max P$ = maximum number of pixels per line (614), FOV = Field of View (in rad), and $Z_{x,y}$ = altitude of ER-2 for the current x and y . The pixelwise calculation of the actual pointing direction includes correction of the panoramic distortion. The vector $X_{c,r}$ is modified by rotations about the ω , ϕ , and χ axis (vector $X_{c,r}''$, Figure 2). The transformed position vector $X_{c,r}'''$ is computed as follows:

$$X_{c,r}''' = \begin{pmatrix} 1 & -\chi & -\phi \\ \chi & 1 & -\omega \\ \phi & \omega & 1 \end{pmatrix} X_{c,r}. \quad (2)$$

Situation on surface: The topography causes a shift in the apparent pixel location, and affects the pixel size. The goal is now to find the intersection between the pixel location vector $X_{i,j}'''$ and the surface of the DEM. Within the neighborhood

around the transformed pixel location vector $X''_{i,j}$, a test vector $X^*_{i,j}$ is searched for, which converges to $X''_{i,j}$.

$$X^*_{i,j} = \begin{pmatrix} i - i_{Nadir} \\ j - j_{Nadir} \\ \frac{(Z_{x,y} - e_{i,j})}{v} \end{pmatrix}, \quad (3)$$

where i_{Nadir} = i-coordinate of the true nadir point, j_{Nadir} = j-coordinate of the true nadir point, $e_{i,j}$ = elevation of the test point at position (i,j), and $Z_{x,y}$ = altitude of ER-2 for the current x and y. To allow for a more precise selection of the corresponding surface point, the DEM oversampled to a grid size of 6m is used. To define the intersection point on the surface, the normalized dot product of $X^*_{i,j}$ and $X''_{i,j}$ is calculated. The vector $X^*_{i,j}$ best representing $X''_{i,j}$ is that for which the dot product DP has the smallest difference from 1. To represent the pixel size dependent on the topography, the four corner points (6m grid size) of every pixel are separately calculated. To prevent changes to the radiometric characteristics, the original value is selected by an improved extraction algorithm during the resampling to an 18m grid size, thereby eliminating the need to interpolate the values.

4. DISCUSSION AND OUTLOOK

There are currently no well-established methods of quantitatively assessing the success of a geocoding process. Visual inspection provides useful information, but cannot be used to intercompare methods. Statistical results based on residual calculation of single ground control points allow only a local error assessment.

For the discussion, the Rigi scene is selected because of the more challenging topography. Figure 3 shows bands 13, 18, and 28 of the geocoded image overlaid by the scanned forested areas (green line) and digitized shoreline (blue line). The enlarged areas are selected dependent on their aspect and slope angle. In general, the results show a good correspondence between the geocoded image and the map for all existing topographical locations. A few locations show minor miscorrespondence. These problems are almost always restricted to single pixels and no general tendency can be recognized. The errors may result from changes in reality between the time the aerial photographs (which are the basis for the topographic maps) were acquired (1987) and the AVIRIS data acquisition, and on the fact that maps are the result of a generalization while AVIRIS displays every occurrence within its resolution characteristics. Figure 3B demonstrates another problem of the ground reference information. While the lower regions of the forested slope correspond perfectly, the AVIRIS image extends significantly the forest area on the upper limits. This "misregistration" is based on the problem of the determination of the forest border along the timber line and its representation in the forest map through symbolic point signatures which are suppressed through the scanning process. Figure 3D and Figure 3E portray areas with rapidly changing slope angles. The blue shoreline proves for subarea (D) and the green forest line for subarea (E) the good correspondence. The additional verification calculates the average deviation of the geocoded image compared with the forest and lake map for checkpoints. Lines 1 and 2 of Table 1 indicate the results of this test and confirm the visual validation. No systematic deviation was found. To double-check the performance of the new parametric

approach, scene Rigi was geocoded using the improved, non-parametric rubber-sheet approach (Itten and Meyer, 1993). Table 2 (line 3) presents the result for the improved rubber-sheet approach and shows the better performance of the parametric solution.

The datasets Zug and especially Rigi need georadiometric corrections. Atmospheric corrections using radiative transfer models like MODTRAN-2a (Green et al., 1993) as well as a compensation for the slope-aspect-dependent illumination difference (Meyer et al., 1993a) should complete the preprocessing of the sensor, system and scene related effects of the current data set.

The whole procedure was implemented using the IDL (Interactive Data Language, a proprietary programming language, Research System Inc., 1993).

5. ACKNOWLEDGMENTS

The first author would like to thank the Swiss Research Foundation and NASA for supporting the project and K.I. Itten (RSL), G. Vane, R. O. Green, and E. G. Hansen (JPL) for providing special assistance. The support of the NASA Ames Research Center, the Swiss Air Force, and Litton, Aero Products, Woodlands, CA is gratefully acknowledged. Thanks for technical assistance go to R.O. Green, T. G. Chrien, A. T. Murray, H. I. Novack, M. Solis, P. J. Nielsen, J. J. Genofsky, and C. Chovit (JPL) as well as to T. Kellenberger, M. Schaepman, S. Sandmeier, C. Ehrler, E. H. Meier, S. Veraguth, U. Kurer, and D. Schlaepfer (RSL).

The research described in this paper was carried out at the Jet Propulsion Laboratory, California Institute of Technology, and was sponsored by the Swiss Research Foundation, Project No. 8220-33290.

6. REFERENCES

- Green, R. O., J. E. Conel, T. G. Chrien (1993), Correction of AVIRIS Radiance to Reflectance using MODTRAN-2, in *Proc. International Society for Optical Engineering (SPIE) 1937*, Orlando, FL (in press).
- Itten, K. I., and P. Meyer (1993), Georadiometric correction of TM-Data of mountainous forest areas, *IEEE Transactions on Geoscience and Remote Sensing* (in press).
- Larson, S., P. Meyer, and E. G. Hansen (1994), Topographical and Geometric Correction of Remote Sensing Image Data using Dead Reckoning, *IEEE Transactions on Geoscience and Remote Sensing* (in preparation).
- Meyer, P., K. I. Itten, T. Kellenberger, R. Leu, and S. Sandmeier (1993a), Radiometric and Geometric Correction of TM-Data of Mountainous Forest Areas, *ISPRS Journal of Photogrammetry and Remote Sensing: 48* (in press).
- Meyer, P., R. O. Green, and T. G. Chrien (1993b), Extraction of Auxiliary Data from AVIRIS Distribution Tape for Spectral, Radiometric, and Geometric Quality Assessment, in *Proc. of the Fourth Annual JPL Airborne Geoscience Workshop*, Washington, D.C. Published by Jet Propulsion Laboratory, Pasadena, California (this volume).
- Meyer, P. (1993c), A Parametric Approach for the Geocoding of Airborne Visible/Infrared Imaging Spectrometer (AVIRIS) Data in Rugged Terrain, *Remote Sensing of Environment* (submitted).
- Perrin, D. (1993), Personal communication (fax Jan 28, 1993).
- Research Systems, Inc.®. (1993), IDL User's Guide, Version 3.0, Boulder, CO.
- Thomson-CSF (1987), Radar ADOUR, Modernisation télémétrie et codage, Tome I.

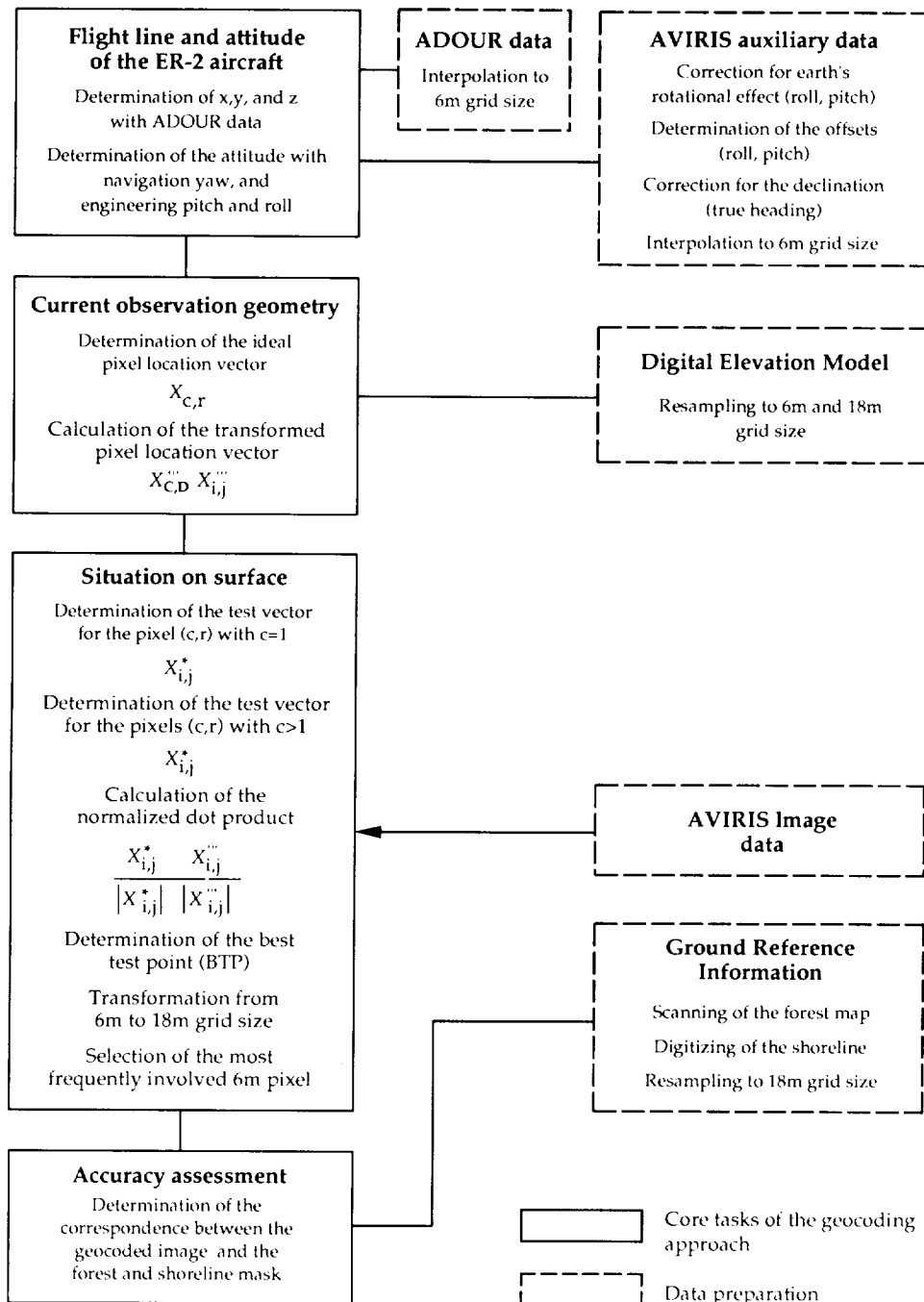


Figure 1: Overview of the data preparation and core tasks of the geocoding approach, where x=latitude, y=longitude, z=altitude of the airplane, and c=column and r=row of the raw file.

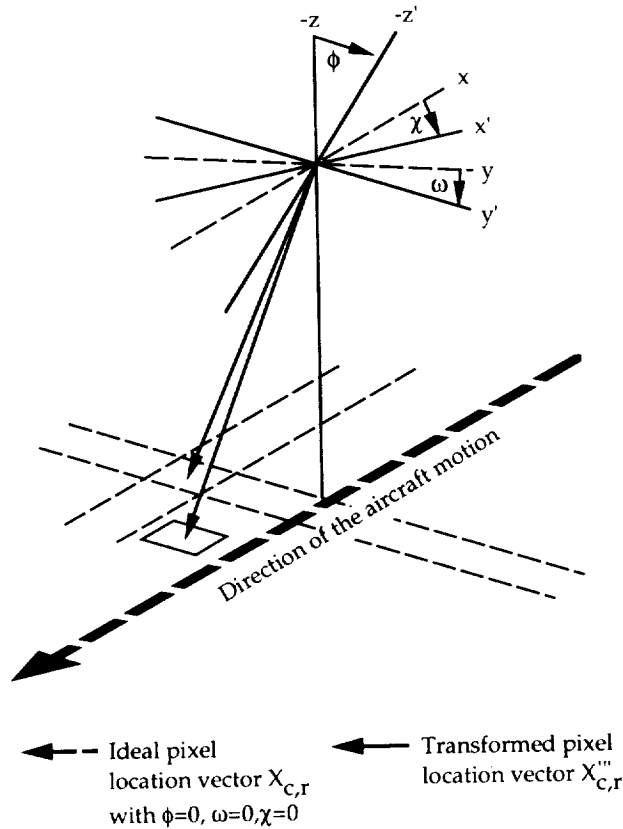


Figure 2: Principal outline of the observation geometry to calculate the transformed pixel location vector where ϕ =pitch, ω =roll, and χ =true heading, and x, y, z defining the coordinate axis for the ideal pixel location vector and x', y', z' for the transformed pixel location vector.

Figure 3 (Slide 7): (A) shows the composite rendered on the digital elevation model with tags (B-E) for the location of the enlarged subareas of the horizontal (non-rendered) composite. (B)-(E) show zoom-up (\approx factor 5) parts with different aspect and slope angles.

Table 1: Result of the quantitative effort for the comparison between the geocoded images and the forest map with the RMS for the east-west direction (i) and north-south direction (j) of the digital elevation model. The check points used for the non-parametric approach for scene Rigi are a selection from the entire number of points used for the parametric approach.

	<i>No. of checkpoints</i>	<i>RMS for i-direction</i>	<i>RMS for j-direction</i>
Scene Zug (parametric approach)	186	0.07 pixel	0.19 pixel
Scene Rigi (parametric approach)	309	0.12 pixel	0.09 pixel
Scene Rigi (non-parametric approach)	249	3.57 pixel	1.37 pixel

The Data Facility of the Airborne Visible/Infrared Imaging Spectrometer (AVIRIS)

Pia J. Nielsen, Robert O. Green, Alex T. Murray, Bjorn T. Eng, H. Ian Novack, Manuel Solis, and Martin Olah

Jet Propulsion Laboratory, California Institute of Technology, Pasadena, CA 91109

ABSTRACT

AVIRIS operations at the Jet Propulsion Laboratory include a significant data task. The AVIRIS data facility is responsible for data archiving, data calibration, quality monitoring and distribution. Since 1987, the data facility has archived over one terabyte of AVIRIS data and distributed these data to science investigators as requested. In this paper we describe recent improvements in the AVIRIS data facility.

1.0 INTRODUCTION

AVIRIS measures spatial images of the upwelling spectral radiance through 224 spectral channels at a rate of 17 megabits per second. On a single flight up to ten gigabytes (11,000 km²) of data may be acquired. During a typical eight month period of flight operations AVIRIS will collect airborne science data on more than 30 flights. This translates to a collection on the order of 200 gigabytes of imaging spectrometer data each year. In the AVIRIS data facility, all of these data as well as ground calibration and engineering data are moved through the steps shown in Table 1. In Table 2, a summary of the AVIRIS data acquired and moved through the data facility since 1991 is given.

The AVIRIS sensor and data facility has been operational since 1989. In each year since, modifications have been pursued in most of the subsystems of the sensor and data facility. These modifications have been designed to improve the rate and the quality of calibrated imaging spectrometer data delivered to the science community. Changes to AVIRIS prior to 1992 have been described previously (Porter et al., 1990 and Hansen et al., 1992). In the following sections of this paper we describe more recent and planned improvements to the AVIRIS data facility.

2.0 AVIRIS DATA FACILITY IMPROVEMENTS**2.1 1992 Data Facility Modifications**

In 1992, with the upgrade of the high density tape recorder in the AVIRIS sensor, a new high density tape recorder was installed in the AVIRIS data facility. Since installation, a sophisticated software interface has been developed between the HDTR and the AVIRIS archiving software. This allows rapid downloading as well as detailed monitoring of the AVIRIS data transferred from the high density data tape.

Prior to the 1992 flight season, a complete rewrite of the software to archive, calibrate and distribute AVIRIS data was undertaken. Typically 200 gigabytes of laboratory and flight AVIRIS data pass through this code each year. Most data distributed to investigators have the calibration algorithms (Green et al., 1992) applied in this code as well. A limited augmentation to the data facility computer hardware was undertaken in conjunction with the software upgrade. Sensor performance and data quality monitoring were designed into this new code as core capabilities. The upgrade was completed in 1992 and resulted in a quadrupling of the data archiving, calibration and distribution performance of the data facility.

As part of the AVIRIS software upgrade, a relational database was integrated into the AVIRIS data facility software to control and record AVIRIS data activities. This data base has significantly improved levels of data trend analysis as well as data acquisition, calibration and distribution tracking.

A policy was established in 1992, with the support of the AVIRIS NASA sponsors, to offer data acquired in previous years to investigators for the marginal cost of reproduction. This has resulted in the exploration of the uses of imaging spectrometry data by additional university, industry and government investigators.

2.2 1993 Data Facility Modifications

An extensive effort has been undertaken to eliminate potential single point failures in the AVIRIS data facility system in 1993. Removal of single point failure has been motivated by the desire to minimize interruptions in data delivery to the AVIRIS investigators. This effort has been largely successful with most of the AVIRIS software capable of operating on two or more computer hardware platforms. At present, the single HDTR at the data facility remains the dominant potential single point of failure.

In 1993, a software subsystem has been pursued to automate the generation of AVIRIS calibration files. This software allows rapid reduction of the gigabytes of radiometric calibration data acquired in the laboratory before and after each flight season. A number of analysis tools have been developed to monitor and validate this process of radiometric calibration file generation.

To allow use of AVIRIS data in calibrating and modeling current and future spaceborne sensors, software has been developed to offer AVIRIS data convolved to the spectral characteristics of a number of satellites. Currently weighted spectral convolution software has been completed for the Optical Sensor (OPS) on board the Japanese Earth Resources Satellite 1. For this spaceborne sensor, AVIRIS data are being used to establish the on orbit calibration of OPS (Green et al., 1993a). In the future, weighted spectral convolution AVIRIS imagery will be available in the AVIRIS spectral range for Landsat TM, Landsat MSS, AVHRR, EOS ASTER, EOS MODIS, EOS MISR, etc.

An improved capability for the monitoring of encoded sensor telemetry has been developed in 1993. The software allows the rapid extraction and trend analysis of telemetry stored in the AVIRIS data base. Monitoring and assessment of the sensor telemetry encoded on the high density data tape are required prior to authorizing subsequent airborne acquisitions of AVIRIS data.

All AVIRIS data are archived, calibrated and distributed through the AVIRIS data facility. Based on the modifications described, the capability of the data facility to fulfill this role has kept pace with the growing demand for calibrated AVIRIS data. A summary of the recent and projected acquisition and distribution of AVIRIS data is given in Table 3. At present, an archive of approximately one terabyte of AVIRIS data acquired since test flights in 1987 is maintained under the cognizance of the data facility.

2.3 Data Facility Future Plans

In 1994 a new archive server computer is planned to be acquired in the AVIRIS data facility. This machine will replace hardware acquired in 1989 that is becoming unmaintainable. With this hardware upgrade, further improvements in data archiving rates and data quality monitoring will be possible. Compatibility with future system and network software releases will also be ensured. In conjunction with the archive server upgrade, the data facility plans to maintain AVIRIS quicklook images on-line for a one year period after acquisition. Maintaining these images on-line will allow investigators to retrieve and examine quicklook data as soon as they are available via modem or Internet. These improvements are consistent with the current goals of the AVIRIS data facility: 1) to deliver quicklook images to investigators within one week of acquisition, and 2) to calibrate and distribute data to investigators within two weeks of request. To exceed these performance goals in the future, on-line storage and direct network distribution of AVIRIS data are being investigated.

Finally, the data facility hopes to pursue the delivery of AVIRIS derived geophysical parameters in addition to the instrument measured signal and calibrated upwelling radiance currently offered. Geophysical parameters that are currently being considered are apparent surface reflectance (Green et al., 1993b), atmosphere water vapor, surface leaf water, cirrus cloud maps, surface oxygen pressure height, etc. Some of these parameters may be offered in the 1994 and 1995 time frame.

3.0 CONCLUSION

Since first becoming operational in 1989, the AVIRIS system has been undergoing incremental improvements. These improvements have occurred in both the sensor and

the data facility components of the AVIRIS project. These modifications and upgrades have been pursued to improve the quality of data provided to the science investigators.

In the data facility, efforts will continue towards improved data delivery rates. For example, network distribution of quicklook images and eventually AVIRIS data will be investigated. In addition, geophysical parameters, such as surface reflectance, may be offered directly from the AVIRIS data facility. By pursuing these improvements and upgrades, AVIRIS will continue to have an important role in providing calibrated imaging spectrometer data to researchers across the Earth science disciplines.

4.0 ACKNOWLEDGMENTS

This research was carried out at the Jet Propulsion Laboratory, California Institute of technology, under contract with the National Aeronautics and Space Administration.

5.0 REFERENCES

Green, Robert O., Steve Larson and Ian Novack, "Calibration of AVIRIS digitized data", Proc. Third Annual AVIRIS Workshop, JPL Publication 91-28, Jet Propulsion Laboratory, Pasadena, CA, pp. 109-118, 1991.

Green, Robert O., James E. Conel, Jeannette van den Bosch, Masanobu Shimada and Masao Nakai, "On-orbit Calibration of the Japanese Earth Resources Satellite-1 Optical Sensor Using the Airborne Visible-Infrared Imaging Spectrometer", IGARSS'93, Tokyo Japan, Optical Sensor and Calibration, in press, 1993a.

Green, Robert O., James E. Conel and Dar A. Roberts, "Estimation of Aerosol Optical Depth and Calculation of Apparent Surface Reflectance from Radiance Measured by the Airborne Visible-Infrared Imaging Spectrometer (AVIRIS) Using MODTRAN2", SPIE Conf. 1937, Imaging Spectrometry of the Terrestrial Environment, in press, 1993b.

Hansen, E. G., Steve Larson, H. Ian Novack, and Robert Bennett, "AVIRIS Ground Data Processing System", Proc. Third Annual Airborne Geoscience Workshop, JPL Publication 92-14, Jet Propulsion Laboratory, Pasadena, CA, pp. 80-82, 1992.

Porter, W. M., T. G. Chrien, E. G. Hansen, and C. M. Sarture, "Evolution of the Airborne Visible/Infrared Imaging Spectrometer (AVIRIS) Flight and Ground Data Processing System", Proceedings of SPIE, Vol. 1298, pp. 11-17, 1990.

6.0 TABLES

Table 1. AVIRIS Operational Characteristics

DATA FACILITY	
Performance monitoring	48 hours from acquisition
Archiving	One week from acquisition
Quicklook distribution	One week from acquisition
Calibration	Two weeks from request
Quality monitoring	Prior to distribution
Distribution	Two weeks from request
Engineering and data analysis	High priority as required

Table 2. Recent and planned AVIRIS data acquisition

	1991	1992	1993*
Months of operations	7	8	7
Aircraft bases	5	4	4
Principle investigators	52(Europe)	32	35
Investigator sites flown	137	172	200
Launches	36	34	35
Calibration experiments	3	3	3
Square kilometers flown	115,000	127,300	140,000
Flight scenes	1150	1273	1400
Gigabytes archived	161	178	196
Scenes calibrated/distributed	498	847	1000
Data turnaround (months)	5	2.5	1

*projected

23-83
41034

**MAPPING OF THE RONDA PERIDOTITE MASSIF (SPAIN) FROM
AVIRIS SPECTRO-IMAGING SURVEY : A FIRST ATTEMPT**

P.C. PINET, S. CHABRILLAT, G. CEULENEER

UPR 234 "Dynamique terrestre et planétaire"/CNRS/Observatoire Midi-Pyrenees,
14 avenue Edouard Belin, F-31400 Toulouse, France

1. INTRODUCTION

1.1. Ronda massif mineralogy

The Ronda peridotite massif is a large exposure (~300 km²) of upper mantle included in the earth's crust. From field observations, Obata (1980) showed that the massif displays a well-developed mineralogical zonation moving away from the basalt thrust contact : 1) garnet lherzolite, 2) ariegite subfacies of spinel lherzolite, 3) seiland subfacies of spinel lherzolite, and 4) plagioclase lherzolite are systematically encountered. Apart from these relatively smooth regional variations, peridotites display local but drastic variations in their modal composition, expressed mostly in their olivine / pyroxene and orthopyroxene (OPX) / clinopyroxene (CPX) ratio (peridotites range in composition from lherzolite to dunite), and in the local development of a pyroxenitic layering. These variations reflect phenomena related to melt migration and/or partial melting. Although these last variations are small scale phenomena, ranging from a few centimeters to a hundred meters, our preliminary field results have shown that their distribution at the scale of the massif is not random. The production of a global map of the distribution of such variations would be extremely useful to understand the petrological history of the massif (Suen and Frey, 1987), but achieving this task from field observations appears extremely difficult and no such map has been yet obtained by means of field geology work. Recent airborne spectro-imaging observations are currently being processed to achieve this objective.

1.2. Mapping by infrared spectro-imagery

Advances in remote sensing technology have led to the development of imaging or mapping spectrometry (Goetz et al., 1985). Mapping spectrometers measure both spatial and spectral information simultaneously with sufficient wavelength resolution such that, in principle, direct mineralogical information may be retrieved. In visible and near-infrared reflectance spectra, pyroxenes are readily identifiable in the laboratory from their characteristic Fe²⁺ electronic transition absorption bands located near 1 μm and 2 μm (e.g., Burns, 1970; Hunt and Salisbury, 1970; Adams, 1974), the center of the absorption band diagnostic of olivine being located at 1-1.05 μm . The spectra of OPX and CPX mixtures have been qualitatively described by previous researchers (Adams, 1974; Singer, 1981; Cloutis and Gaffey, 1991) as having properties that are intermediate to their end-members and estimating the modal abundances from the spectra appears possible (e.g., Sunshine and Pieters, 1993). The absorption band diagnostic of plagioclase is centered at 1.25 μm . Given the existence of discriminant absorption bands for each mineralogical species present in the Ronda massif, the production of a map of the variations in the mineralogical composition is a priori reachable, though challenging objective.

1.3. Airborne campaigns : ARAT/ISM - AVIRIS/TMS

The airborne version of the imaging spectrometer ISM, developed for the Phobos-2 space mission, was operated over Ronda massif, during the July 91 campaign of the ARAT aircraft and about 20 separate ISM axes were flown over Sierra Bermeja on July, 5th, 9th, 10th and 11th. This ARAT/ISM campaign was coupled with an Airborne Visible/Infrared Imaging Spectrometer (AVIRIS) flight over the same site during the European Multispectral Airborne Campaign (Mustard et al., 1992). Three cloud-free, hyperspectral images were acquired on 15th July 91.

Although not developed here, this is a unique opportunity for cross calibration between the two instruments, the main objective being to assess the consistency and the level of

precision one can retrieve from independent spectral observations for the purpose of geological mapping and mineralogical interpretation (Chabrilat et al., 1993).

2. ANALYSIS

1.1 First order analysis

In this work, we use a simple linear mixing model (e.g., Gillespie et al., 1990) to evaluate the spatial distribution of spectroscopically distinct materials across the Aviris mapping of the Ronda massif from the mosaic of the three available images. The mosaic has been binned and is analyzed at the spatial resolution of 160x160m. Based on previous knowledge on the field and on statistical tests, small areas with both high internal spectral homogeneity and distinct respective spectral behavior, are selected to define an endmembers basis in the image.

In parallel with the ISM data analysis, the focus here is placed on the use of uncalibrated spectra for the purpose of mapping different geologic units and determining image endmembers (Smith et al., 1990) which will be later on, related to laboratory spectra and field spectroscopy (Mustard et al., 1992). After removal of the atmospheric absorption windows (0.92-0.98, 1.09-1.17, 1.33-1.5, 1.75-2. micron), the Aviris spectra have been normalized to a standard area selected within the Ronda massif given its large surface proportion of well-exposed bedrock and the normalized relative reflectance values are scaled at 0.80 μm . Then, a spectro-mixing analysis is performed with a selection of endmembers representative of the main geological units previously mapped (Obata, 1980), in order to check whether the observed spectral variability agrees with the geological boundaries. Four endmembers are needed to account for nearly all the spectral variance. One endmember represents the vegetation, two endmembers are taken in the massif, corresponding to two locations within the peridotite massif based on previous knowledge of the area, the last endmember represents a non-peridotite field (sedimentary soil) without vegetation cover. Owing to the situation of the field of study (southern Spain: latitude 36°30'), the period of observation close to the summer solstice, and the time of the observation near local solar noon, the shade effect appears very limited and probably included in what is considered to be our "Vegetation" endmember. A prevailing contribution of peridotite-like rocks is recognized within the whole Sierra Bermeja massif, combined locally with vegetation spots, in agreement with their locations on the ground. The contribution of the "sedimentary soil" endmember corresponds to the geological mapping of the peridotite massif and its surrounding rocks. In this analysis, the endmembers named peridotite, limestone.. are discriminated from their spectral variations in the albedo contrast, from their location on the imaging mapping with respect to the geological map, and from the regional groundtruth, but they are not mineralogically identified yet from the airborne spectral data, although rock samples collected in situ and analyzed with the RELAB facility at Brown University display unambiguous spectroscopic absorption features (Mustard et al., 1992).

Three tests on three different spectral domains are performed :

1- throughout all the useful spectral domain available for AVIRIS, i.e. 0.4-1.8 micron,
2- on the 0.8-1.8 μm domain, in an attempt to reproduce the ISM spectral sampling interval. Geological boundaries of the peridotite massif are identified, and highly vegetated areas and vegetated areas within the massif are discriminated. These two tests lead basically to the same results, with a higher average rms residual over the first spectral domain (1.7%) than over the second one (0.8%). Indeed, after having removed the 0.4-0.8 μm bands, the high rms values in the variance image, which were located over vegetation spots, have disappeared. This means that a great deal of the observed variance arises from the spectral variability associated to the visible domain, with little related to mineralogical information. When we compare the second test with the same analysis applied to the ISM axes, these results are in complete agreement (Chabrilat et al., 1993).

3- Finally, the spectral domain analysis is restricted to 0.7-1.3 micron, which is a significant spectral domain for the mineralogical characterisation of mafic minerals. This corresponds to a residual analysis approach while the previous tests correspond to continuum analyses (see Sabol et al., 1992). The atmospheric absorption windows (0.80-0.84, 0.92-0.97, 1.10-1.17 μm) are removed from the test. This analysis shows similar results than the two previous ones, with a still lower average rms residual 0.6% and is in

favor of a mineralogical contribution in the observed variations between the spectra of the two endmembers located within the massif, although it may also arise from topographic effects and/or vegetation differential contributions.

At this stage of analysis, one sees that, through the spectro-mixing approach undertaken, it is possible for the purpose of mapping geology to discriminate from uncalibrated spectra, vegetated and non-peridotite areas from the peridotitic massif itself. It is very likely that the observed spectral variations are at least partially controlled by the soil and bedrock lithologies. This preliminary conclusion agrees with a recent independent evaluation of AVIRIS data (Mustard, 1993). To go further in the geological understanding and the spatial organisation of the Ronda massif, a "second order" analysis is needed, with the goal of examining whether or not spectrally detectable mineralogical variations may exist within the peridotite massif.

2.2 Second step analysis

The approach consists in building up a numerical mask which allows to reject the pixels in the image in which vegetation and mineralogical effects unrelated to the peridotite massif are present in a significant proportion. We then repeat the mixing analysis on the remaining part of the image. Although one cannot completely exclude that there may be little residual vegetation and/or topographic effects, they should be significantly reduced. Consequently, the results derived from this "second order" mixing should be prevailing related to mineralogical variations occurring within the peridotite massif only. The reason of these two steps approach is that the spectral contribution resulting from the mineralogical variations within the peridotite massif has a much more subtle effect upon the spectrum than first order reflectance variations resulting from : i- the vegetation cover, and ii- the large mineralogical contrast between the massif itself and the surrounding geological units.

With the criteria of rejection that we have chosen (pixels with fractions of vegetation or non-peridotite field higher than 20%), based on the test over the 0.7-1.3 spectral domain described previously, 18% of the Aviris image mosaic over the Sierra Bermeja massif (i.e., ~2200 spectra) is kept with a sufficient spatial connectivity between the pixels for the purpose of geological mapping. A check with the fieldwork observations shows that it corresponds to the well-exposed bedrock and soil areas distributed across the massif. Within these areas, four endmembers are requested, the level of the average rms residual being 0.43%. One identifies a well-exposed area where land denudation occurred due to a forest fire; another maps the summit and northern part of Mount Reales but also the south part of the top of a well-exposed bedrock elongated crest located in the eastern side of the massif. The third endmember fraction image reveals an encircling pattern around Mount Reales, and the last one mainly maps out the north part of the previously described eastern exposed crest. As suggested by the variations between the relative reflectance spectra, this distribution might be related to different content and/or type of pyroxene in the lithology of the well-exposed bedrock and soil areas.

3. CONCLUSION

In both AVIRIS and ISM data, through the use of mixing models, geological boundaries of the Ronda massif are identified with respect to the surrounding rocks. We can also yield first-order vegetation maps. ISM and AVIRIS instruments give consistent results. On the basis of endmember fraction images, it is then possible to discard areas highly vegetated or not belonging to the peridotite massif. Within the remaining part of the mosaic, spectro-mixing analysis reveals spectral variations in the peridotite massif between the well-exposed areas. Spatially organized units are depicted, related to differences in the relative depth of the absorption band at 1 micron, and it may be due to a different pyroxene content. At this stage, it is worth noting that, although mineralogical variations observed in the rocks are at a sub-pixel scale for the airborne analysis, we see an emerging spatial pattern in the distribution of spectral variations across the massif which might be prevalently related to mineralogy. Although it is known from fieldwork that the Ronda peridotite massif exhibits mineralogical variations at local scale in the content of pyroxene, and at regional scale in different mineral facies, ranging from garnet-, to spinel-

to plagioclase-herzolites, no attempt has been done yet to produce a synoptic map relating the two scales of analysis. The present work is a first attempt to reach this objective, though a lot more work is still required. In particular, for the purpose of mineralogical interpretation, it is critical to relate the airborne observation to field work and laboratory spectra of Ronda rocks already obtained, with the use of image endmembers and associated reference endmembers (e.g., Smith et al., 1990). Also, the pretty rough linear mixing model used here is taken as a "black-box" process which does not necessarily apply correctly to the physical situation at the sub-pixel level (see Sabol et al., 1992). One may think of using the ground-truth observations bearing on the sub-pixel statistical characteristics (texture, structural pattern, surface distribution and vegetation contribution (grass, ...)) to produce a more advanced mixing model, physically appropriate to the geologic and environmental contexts.

Acknowledgments. We express our thanks to C. Sotin for his efforts in the dispatching of the Aviris data relative to the coordinated ISM/AVIRIS data analysis over Ronda.

References

- Adams, J.B., 1974, Visible and near-infrared diffuse reflectance : Spectra of pyroxenes as applied to remote sensing of solid objects in the solar system, *J. Geophys. Res.*, 79, 4829-4836.
- Burns, R.G., Mineralogical Application to Crystal Field Theory, 224pp., Cambridge university Press, London, 1970.
- Chabrilat, S., P.C. Pinet, G. Ceuleneer, B. Gondet, J.P. Bibring, 1993, Mapping of the Ronda massif (Spain) by infrared spectro-imagery, *Proc. of 25th Intern. Symposium on Rem. Sens. and Global Environ.*, Graz (Austria), in press.
- Cloutis, E.A., and M.J. Gaffey, 1991, Pyroxene spectroscopy revisited : Spectral-compositional correlations and relationships to geothermometry, *J. Geophys. Res.*, 96, 22, 809-22, 826.
- Gillespie, A.R., M.O. Smith, J.B. Adams, S.C. Willis, A.F. Fischer III, and D.E. Sabol, 1990, Interpretation of residual images : Spectral mixture analysis of AVIRIS images, Owens Valley, California, *Proc. of the Airborne Science Workshop*, JPL Publ. 90-54, 243-270.
- Goetz, F.H., G. Vane, J.E. Solomon, B.N. Rock, 1985, Imaging spectrometry for earth remote sensing, *Science*, 288, 1147-1153.
- Green, R.O., Larson, S.A., Novack, H.I., 1991, Calibration of AVIRIS digitized data, *Proc. of the Third Airborne Visible/Infrared Imaging Spectrometer (AVIRIS) Workshop* (R.O.Green, editor), JPL Publication, 91-28, 109-118.
- Hunt, G.R., and J.W. Salisbury, 1970, Visible and near-infrared reflectance spectra of minerals and rocks, I, Silicate minerals, *Mod. Geol.*, 1, 219-228.
- Mustard, J.F., S. Hurltrez, P. C. Pinet, C. Sotin, 1992, First results from analysis of coordinated AVIRIS/TMS, and ISM (French) data for the Ronda (Spain) and Beni Boussera (Morocco) peridotites, *Summaries of the Third Annual JPL Airborne Geoscience workshop June 1-5, 1992*, AVIRIS Workshop (R.O. Green, editor), JPL Publication 92-14, vol 1, 26-28.
- Mustard, J.F., 1993, Relationships of soil, grass, and bedrock over the Kaweah serpentinite melange through spectral mixture analysis of AVIRIS data, *Rem. Sens. Environ.*, 44, 293-308.
- Obata M., 1980, The Ronda peridotite : garnet-, spinel-, and plagioclase-herzolite facies and the P-T trajectories of a high-temperature mantle intrusion, *J. Petrol.*, 21, 533-572.
- Singer, R.B., 1981, Near-infrared spectral reflectance of mineral mixtures : Systematic combinations of pyroxenes, olivine, and iron oxides, *J. Geophys. Res.*, 86, 7967-7982.
- Sabol, D.E., Adams, J.B., Smith, M.O., 1992, Quantitative subpixel spectral detection of targets in multispectral images, *J. Geophys. Res.*, 97(E2), 2659-2672.
- Smith, M.O., S.L. Ustin, J.B. Adams, and A.R. Gillespie, 1990, Vegetation in deserts: I. A regional measure of abundance from multispectral images, *Remote Sens. Environ.*, 31, 1-26.
- Suen, C.J., and F.A. Frey, 1987, Origins of the mafic and ultramafic rocks in the Ronda peridotite, *Earth and Planetary Science Letters*, 85, 183-202.
- Sunshine, J.M. and C.M. Pieters, 1993, Estimating modal abundances from the spectra of natural and laboratory pyroxene mixtures using the modified gaussian model, *J. Geophys. Res.*, 98, E5, 9075-9087.

11/035
1**SPECTRAL VARIATIONS IN A COLLECTION OF AVIRIS IMAGERY**

John C. Price

USDA Agricultural Research Service
 Beltsville Agricultural Research Center
 Beltsville, Maryland 20705

1. INTRODUCTION

The advent of AVIRIS presents to the scientific community the first opportunity to examine high quality hyperspectral image data over areas of interest (Vane, 1987), while recent developments promise even better data in the future. With these data we may address questions such as: 1) Is such high spectral resolution ($0.01\mu\text{m}$) necessary?, and 2) How can we take advantage of the AVIRIS experience in specifying an improved future Landsat satellite? In this paper we describe the use of relatively broadband measurements (20-50 nm) to represent spectral variability (Price, 1990, 1991). The problem of generality is addressed through consideration of 28 AVIRIS scenes, although analysis of additional areas is clearly desirable. Section 2 defines the expansion of spectra in terms of basis functions, section 3 describes the application to AVIRIS data, and the conclusion, section 4, relates these preliminary results to possible future remote sensing instrumentation such as the planned Landsat 8.

2. DESCRIPTION BY BASIS FUNCTIONS

From inspection most visible near infrared reflectance spectra vary in a relatively smooth, continuous fashion, implying that correlations exist between measurements at nearby wavelengths. Thus a measurement in a limited spectral range provides information about values over a wider spectral range. Let $\mathbf{x}^\alpha(\lambda) = (x_1^\alpha, x_2^\alpha, \dots, x_n^\alpha)$ represent a measured spectrum for the $n = 224$ wavelength values $\lambda = (\lambda_1, \lambda_2, \lambda_3, \dots, \lambda_n)$ of the AVIRIS instrument, with superscript α denoting an individual spectrum (pixel). We describe reflectance spectra, i. e. the ratio of reflected energy to the solar constant, as this tends to equalize the wavelength contributions, which are otherwise heavily weighted toward the visible region of the spectrum where reflected radiation is strongest. We represent spectra by a set of spectral basis functions φ :

$$\mathbf{x}^\alpha \approx \sum_{i=1}^M S_i^\alpha \varphi_i(\lambda), \quad (1)$$

where the $\varphi(\lambda_1, \lambda_2, \lambda_3, \dots, \lambda_n)$ are spectral shapes obtained by statistical analysis of AVIRIS spectra, and the coefficients S_i^α are wavelength integrals relating to the original spectra \mathbf{x}^α . Each basis function φ_i has an

associated spectral interval $[\lambda_i(\min), \lambda_i(\max)]$ representing the domain of integration for specifying the coefficients S_i . Each φ has essentially unit value in its spectral interval (more precisely has mean value of 1.0 in this interval), then decreases according to the degree of wavelength correlation in the ensemble of measured spectra. The expansion represents successive approximations to the original spectra. Evidently the number of basis functions M which is required to describe the \mathbf{x}^α to within small residuals must be much less than 224, or else the expansion is not useful. Thus let $\delta\mathbf{x}_i^\alpha$ be the difference between a measured spectrum and the sum to order i of the expansion (eq. 1), and let S_i^α be the mean of $\delta\mathbf{x}_i^\alpha$ over a selected spectral interval $[\lambda_i(\min), \lambda_i(\max)]$

$$S_i^\alpha = \frac{1}{[\lambda_i(\max) - \lambda_i(\min)]} \int_{\lambda_i(\min)}^{\lambda_i(\max)} \delta\mathbf{x}_i^\alpha d\lambda \quad (2)$$

At the beginning $\delta\mathbf{x}_1 = \mathbf{x}$. Since S_i is correlated with the value of $\delta\mathbf{x}$ over a wider spectral interval, we define the basis function φ_i by

$$\varphi_i(\lambda) = \langle \delta\mathbf{x}_i S_i \rangle / \langle (S_i)^2 \rangle. \quad (3)$$

where the brackets represent an average over the ensemble of N spectra, e. g. $\langle \mathbf{x} \rangle = 1/N \sum_{\alpha=1}^N \mathbf{x}^\alpha$. From the definition of S , the normalization of φ is given by

$$\frac{1}{[\lambda_i(\max) - \lambda_i(\min)]} \int_{\lambda_i(\min)}^{\lambda_i(\max)} \langle \delta\mathbf{x}_i S_i \rangle / \langle (S_i)^2 \rangle d\lambda = 1 \quad (4)$$

so that φ has a mean value of one within the integration interval. At each iteration level i the residual vector $\delta\mathbf{x}_i^\alpha$ is approximated by $\delta\mathbf{x}_i^\alpha \approx S_i^\alpha \varphi_i(\lambda)$, leaving a new residual $\delta\mathbf{x}_{i+1}^\alpha$. Then the procedure moves to $\delta\mathbf{x}_{i+1}$. From the definition $\delta\mathbf{x}_i$ and all higher order residuals have the value 0 somewhere within the wavelength interval $[\lambda_i(\min), \lambda_i(\max)]$. Thus successive residuals $\delta\mathbf{x}_i$ pass through zero at more and more wavelength values as the order of the expansion increases, and the magnitude of the residuals $\int (\delta\mathbf{x})^2 d\lambda$ decreases. The criterion for terminating the expansion of basis functions is based on the examination of the residuals. Let percent error R , given M basis functions, be defined by

$$R(M) = 100\% \cdot \left\langle \int (\mathbf{x} - \sum_{i=1}^M s_i \boldsymbol{\varphi}_i)^2 d\lambda \right\rangle / \left\langle \int (\mathbf{x}^2) d\lambda \right\rangle \quad 15)$$

where integration extends over the AVIRIS wavelength interval. The residual R provides an indication of the remaining signal plus noise after subtraction of the basis function series. Given enough basis functions the residual is dominated by instrument noise. Thus at a mean signal to noise ratio of 30:1, the residual R is $(1/30)^2 = 1/900 \approx 0.1\%$. The description of spectra in terms of reflectance as opposed to radiance greatly increases the importance to longer wavelengths where the signal to noise of AVIRIS is poorer.

3. APPLICATION TO AVIRIS SPECTRA

Table 1 lists the data sets used in these calculations, and the general type of scene. The selection attempts to span the natural variability represented throughout the AVIRIS data sets, with the exception of clouds. Only after the fact was it noticed that #17 and 27 cover largely the same area. Scenes were selected using the quick look data at the Jet Propulsion Laboratory. I am indebted to the staff for their cooperation.

Table 1. AVIRIS Data Scenes and Identifiers

Flight	Run	Scene	Catalog name	type of scene
1 920602A	9	8	Moffett Field	suburb, shallow water
2 920826B	3	2	Maricopa farm	agriculture
3 920828B	13	1	Los Alamos	geology, town
4 920827B	2	5	Rodgers Dry Lake	geology
5 921119B	9	8	Tampa Bay	city, water
6 920603B	2	3	Cuprite	geology
7 920826B	5	1	Camp Pendleton	water, military base
8 920615B	2	3	Harvard Forest	forest
9 920612B	2	5	Indian Pines	agriculture, forest
10 920531C	6	1	Death Valley	geology
11 920603B	14	3	Cima volcanic field	geology
12 920708B	1	2	Gainesville, FL	lake, vegetation
13 920819B	2	1	Denver	suburb, agriculture
14 920828B	2	5	San Juan Mtns	snow, geology
15 920602A	6	2	Jasper Ridge	suburb, vegetation
16 920826B	4	1	Fort Huachuca	a.f.base, geology
17 920616B	2	1	Spruce forest	forest, clear cuts
18 920820B	6	1	Pleasant Grove	agriculture
19 921117D	2	30	Jackson, TN	agriculture, forest
20 921119B	5	4	Tampa Bay	island, shallow water
21 920826B	6	2	San Joaquin	agriculture
22 920531C	2	1	Owens Valley	geology
23 920820B	7	1	Dunnigan, CA	agriculture
24 920819B	10	14	San Bernardino	agriculture
25 920708B	5	1	Gainesville, FL	town, vegetation
26 920621C	2	1	Blackhawk Island	ag, forest, water
27 920615B	8	1	Spruce forest	forest, clear cuts
28 920820B	8	3	Davis, Webster	agriculture, town

Since 28 AVIRIS images represent 4 gigabytes of data, some care was needed in devising an efficient analysis strategy. First a scene showing considerable variability in surface types (Moffet Field) was analyzed. It was found that 9 variables (spectral intervals) described the signal variation to within 0.1% (Table 2, column 1). Then a 1% sample of the 28 scenes (every 100th pixel) was analyzed, with results as shown in column 2 of Table 2. Finally, the basis function expansion to level 20 was used to select "bad" pixels, with the worst 1% being saved from each scene. Then these were added to the original 1% sample, so that the effect of poorly described spectra was exaggerated by a factor of 50. Even this requires only approximately 20 basis functions to describe the AVIRIS signal very well.

Table 2. **Variables Required to Meet Varying Accuracies**

Accuracy (1-R)	# variables Moffet field (1 scene)	# variables 1% sample (28 scenes)	#variables 1% sample +1% bad (28 scenes)
90%	1	1	1
99%	3	3	4
99.9%	9	8	12
99.95%	-	15	19
99.96%	-	20	23
99.97%	-	28	31

Finally, each of 34 coefficient images (S_i) for each of the 28 scenes was studied visually. Small variance images ($i > 25$) still showed signals at a level of a few tenths of a percent. Possible explanations include instrument noise, spectral misregistration, broad atmospheric variations between images (aersols), and true scene to scene variability. Little or no evidence was found for isolated surface types with extraordinary spectral features.

4. CONCLUSION AND OUTLOOK

From examination of 28 scenes it appears that approximately 20-25 measurements are adequate to define the spectral variability of the 20 meter data from AVIRIS. This result will simplify treatment of atmospheric effects, assist in the identification of remotely sensed spectra from a spectral library, and may guide the design of future instrumentation, such as the number of spectral channels to consider for Landsat 8.

5. REFERENCES

- Vane, G. T., "First Results of the Airborne Visible/Infrared Imaging Spectrometer (AVIRIS), SPIE, Vol 834 Imaging Spectroscopy, 166 (1987)
- Price, J. C., "Information content of soil spectra", Remote Sensing Environment, 33, 113 (1990).
- Price, J. C., "Variability of high resolution crop reflectance spectra", Int. J. of Remote Sensing, 13, 2593 (1992).

41036

MONITORING LAND USE AND DEGRADATION USING SATELLITE AND AIRBORNE DATA

Terrill W. Ray

Division of Geological and Planetary Sciences
California Institute of Technology
Pasadena, CA 91125

Thomas G. Farr, Ronald G. Blom, and Robert E. Crippen

Jet Propulsion Laboratory
California Institute of Technology
Pasadena, CA 91109

1. Introduction

In July 1990 AVIRIS and AIRSAR data were collected over the Manix Basin Area of the Mojave Desert to study land degradation in an arid area where center-pivot irrigation had been in use. The Manix Basin is located NE of Barstow, California, along Interstate-15 at $34^{\circ}57'N$ $116^{\circ}35'W$. This region was covered by a series of lakes during the Late Pleistocene and Early Holocene. Beginning in the 1960's, areas were cleared of the native creosote bush-dominated plant community to be used for agricultural purposes. Starting in 1972 fields have been abandoned due to the increased cost of electricity needed to pump the irrigation water, with some fields abandoned as recently as 1988 and 1992. These circumstances provide a time series of abandoned fields which provide the possibility of studying the processes which act on agricultural fields in arid regions when they are abandoned. Ray *et al.* (1992) reported that polarimetric SAR (AIRSAR) could detect that the concentric circular planting furrows plowed on these fields persist for a few years after abandonment and then disappear over time and that wind ripples which form on these fields over time due to wind erosion can be detected with polarimetric radar. Ray *et al.* (1993) used Landsat Thematic Mapper (TM) bandpasses to generate NDVI images of the Manix Basin which showed that the fields abandoned for only a few years had higher NDVI's than the undisturbed desert while the fields abandoned for longer time had NDVI levels lower than that of the undisturbed desert. The purpose of this study is to use a fusion of a time series of satellite data with airborne data to provide a context for the airborne data. The satellite data time series will additionally help to validate the observation and analysis of time-dependent processes observed in the single AVIRIS image of fields abandoned for different periods of time.

2. Methods

Fourteen Landstat Multispectral Scanner (MSS) images of the Manix Basin Area covering the years 1973-75 and 1978-1988 were acquired from the EROS Data Center. Images acquired between the end of May and mid-August were selected in order that the images would be compatible with the AVIRIS data (July 1990) in terms of the season when the data were acquired. For the years prior to 1979, only a few images acquired each year are available in digital form, so some of the images are not totally satisfactory in terms of data quality, cloud cover, and areal coverage. Additionally, an image collected by the Russian Resource satellite in January 1991

was acquired through the generosity of Arnold Selivonov of the Institute of Space Devices.

The MSS images consist of four bands (0.5–0.6 μm , 0.6–0.7 μm , 0.7–0.8 μm , and 0.8–1.1 μm) with a nominal resolution of 79 m by 57 m for pre-1979 images and 57 m by 57 m for the post-1978 images. The Russian Resource data consist of three bands (0.5–0.6 μm , 0.6–0.7 μm , and 0.8–0.9 μm) with a nominal resolution of 30 m by 30 m; however, the pixels appear to cover a slightly larger area than Landsat TM pixels, yielding a pixel spacing of approximately 32 m by 32 m for the Resource data. AVIRIS data consist of 224 bands between .4 μm and 2.5 μm with .01 μm -wide bands all with a nominal resolution of 20 m by 20 m.

It was necessary to co-register all fourteen images to remove image distortions due to changes in the spacecraft attitude and to match the pixel spacings. The co-registration was performed on 1001-sample by 801-line subimages which contain the region of interest. The Russian Resource data were also co-registered with the MSS data. The AVIRIS data were resampled spectrally using the MSS bandpasses and then co-registered with the satellite data. A video of the co-registered imagery has been produced with the aid of the JPL digital animation laboratory.

Instead of the standard NDVI we have chosen to use the infrared percentage vegetation index (IPVI) developed by Crippen (1990) in which the subtraction of the red radiance (reflectance) is recognized as irrelevant and is eliminated, yielding: $IR/(IR + Red)$. IPVI is related to NDVI by:

$$IPVI = \frac{1}{2} (NDVI + 1)$$

IPVI ranges from 0 to 1, never taking on negative values, as can NDVI. It is also quicker to calculate than NDVI.

3. Preliminary Results

Even without the removal of the relative biases between the images and instruments and the atmospheric offset corrections, the IPVI trends seen on the abandoned fields in the AVIRIS data seem to be confirmed with the combined MSS/AVIRIS/RESOURCE data set. In figure 1a we see a plot of IPVI of three abandoned fields in the northernmost part of the study area; the IPVI has been normalized by dividing the values from the abandoned fields by the average IPVI for a large region of the undisturbed desert. This normalization (NIPVI) was performed in an attempt to remove biases which may be due to annual variability in rainfall and other growth parameters. Another important factor may be the harvesting schedule of the alfalfa, which is not considered in these examples but merits attention in the future. This set of fields was not covered by either the 1975 MSS image or the July 1990 AVIRIS data.

The solid line in figure 1a represents the farthest upwind of the set of three fields (referred to as field 9), the dotted line is the field which is farthest downwind (field 11), and the dashed line is the field between them (field 10). The location of the fields with respect to the wind direction is important, because an abandoned field may be a potential source of aeolian sediment which may affect areas downwind of the field. In 1978 both fields 10 and 11 appear to be in cultivation. The fields were likely taken out of cultivation in 1979, but the substantially lower NIPVI for that year might alternatively be due to poorer production on these fields. Interviews with local residents and water well records indicate that irrigation on these fields stopped in 1980. After 1978, both fields show a strong, nearly-exponential decline in NIPVI, with field 11, which is downwind, declining more sharply than field 10. In 1981, cultivation on field 9 seems to begin; the NIPVI curve for field 10, which is immediately downwind, shows an inflection as the drop in plant cover seems to slow. In 1982 the cultivation on field 9 is either suspended for the year, or a strong downturn in productivity occurs, and the NIPVI levels on both fields 10

continue to drop. Cultivation resumes or productivity increases on field 9 in 1983, which correlates with a halt in the decay of NIPVI values on field 10 and an increase on field 11. In 1984 field 9 is abandoned and NIPVI values for it drop dramatically, which is coupled with a fairly steep drop in NIPVI values for fields 10 and 11. Between 1985 and 1991 the highest NIPVI values are generally associated with the most upwind field and the lowest with the most downwind field, and by 1991 all three fields have NIPVI levels very similar to those of the background desert. Interestingly, water well records suggest that irrigation on field 9 was halted in 1980 which seems to be inconsistent with the high vegetation levels in 1981–1983. This land is owned by St. Anthony's Monastery, and one of the monks stated that the field was last irrigated in 1982, which is more compatible with the IPVI data.

Figure 1b shows NIPVI curves for two other fields in the study area. These fields were covered by the 1990 AVIRIS data, but not by the 1975 MSS data. The solid line is the curve for field 6a which is the upwind field in this pair, and the dotted line is for field 6b which is the downwind field. Both fields seem to be active in 1978, but in 1979 field 6a is abandoned and a substantive drop in NIPVI occurs to levels which are still higher than for the desert. In 1981, both fields are in active cultivation. Field 6b is abandoned in 1982 and NIPVI sharply drops while field 6a remains in cultivation. It is interesting to note that the 1982 NIPVI values for field 6b are higher than those for field 6a in 1979. Field 6a is abandoned in 1983 and NIPVI on both fields come to similar levels which are slightly higher than those of the desert. The NIPVI values for these fields remain about the same with the field 6b values typically lower than those for field 6a. In 1990, a sharp drop in NIPVI occurs for field 6b while field 6a drops only slightly. The 1990 AVIRIS data show what appears to be a very large area of blown sand extending up to 2 kilometers downwind of field 6b. The NIPVI value for field 6b in 1991 has increased significantly to just below that for field 6a. The downwind sandblow seems to be less extensive in the 1991 Resource image. Interviews with the local people give 1983 or 1984 as the date of final abandonment, and there was mention that irrigation on one of the fields had stopped in 1978 or 1979. The dates inferred from the imagery seem to agree with these statements.

The data presented in figure 1 show that a time sequence of remote sensing data incorporating both airborne and satellite borne data can be used to observe and potentially quantify changes in land cover due to changes in land use. These changes are both direct, as in the case of the vegetation level dropping steeply when cultivation stops, and indirect, as in the cases illustrated above where downwind fields lose less vegetation and, in some cases, gain vegetation when they are protected by an upwind field, and lose more vegetation when an abandoned field is immediately upwind. This more substantive loss in vegetation on the downwind fields is probably due to the fact that sand eroding from the upwind field abrades, damages, and buries plants on the downwind field. Ray *et al.* (1992, 1993) mention extensive wind ripples on several of these fields as evidence of substantial wind erosion, and there were observations of sand drifting off of field 11 made in early December 1990. NDVI data presented in Ray *et al.* (1993) also show that, in two pairs of upwind/downwind fields, the downwind field was less well vegetated than the upwind field. Ray *et al.* (1993) also mention "plumes" of lower NDVI values extending downwind of several abandoned fields.

4. Future Work

Crippen (1988) demonstrated the importance of atmospheric corrections for the analysis of band ratio images. The NDVI image calculated from the MSS-subsampled AVIRIS radiance data has a substantially different appearance as compared to the NDVI image calculated from the MSS-subsampled AVIRIS data corrected to apparent reflectance using the empirical line calibration technique described by Conel *et al.* (1987). It is apparent from an examination of the co-

registered MSS data that there are substantial differences in the instrument gains between the periods 1973–1978 and 1979–1988 which need to be removed in order to properly analyze the time sequence of data. The relative gains and offsets will be determined based on the assumption that there was little change in the spectral characteristics of alluvial fan deposits. IPVI images based on the uncorrected MSS data indicated that vegetation levels on these deposits were extremely low, which is also borne out by the IPVI values from the AVIRIS data. Crippen (1987) described a technique for calculating the atmospheric offset corrections for satellite data called the Regression-Intersection Method (RIM). Once the relative corrections between each image and the image selected as a reference have been applied, it is only necessary to apply RIM to one of the MSS images. The Russian Resource image will be corrected by directly using RIM. Other methods of correcting the data will be explored. The corrected data will be assembled into a video with sequences showing the corrected and uncorrected IPVI. The extension of these techniques into other areas where such sequences of data can be assembled is also anticipated.

5. References

- Conel, J. E., R. O. Green, G. Vane, C. J. Bruegge, R. E. Alley and B. J. Curtiss, Airborne imaging spectrometer-2: Radiometric spectral characteristics and comparison of ways to compensate for the atmosphere, in *Imaging Spectroscopy II, Proc. SPIE*, 834:140-157, 1987.
- Crippen, R. E., Calculating the vegetation index faster, *Remote Sens. Environ.*, 34:71-73, 1990.
- Crippen, R. E., The dangers of underestimating the importance of data adjustments in band ratioing, *Int. J. Remote Sens.*, 9:767-776, 1988.
- Crippen, R. E., The regression intersection method of adjusting image data for band ratioing, *Int. J. Remote Sens.*, 8:137-155, 1987.
- Ray, T. W., T. G. Farr, and J. J. van Zyl, Study of land degradation with polarimetric SAR and visible/near-infrared imaging spectroscopy, *Proc. of Top. Symp. on Combined Optical-Microwave Earth and Atmosphere Sensing*, 228-231, 1993.
- Ray, T. W., T. G. Farr, and J. J. van Zyl, Detection of land degradation with polarimetric SAR, *GRL*, 19:1587-1590, 1992.

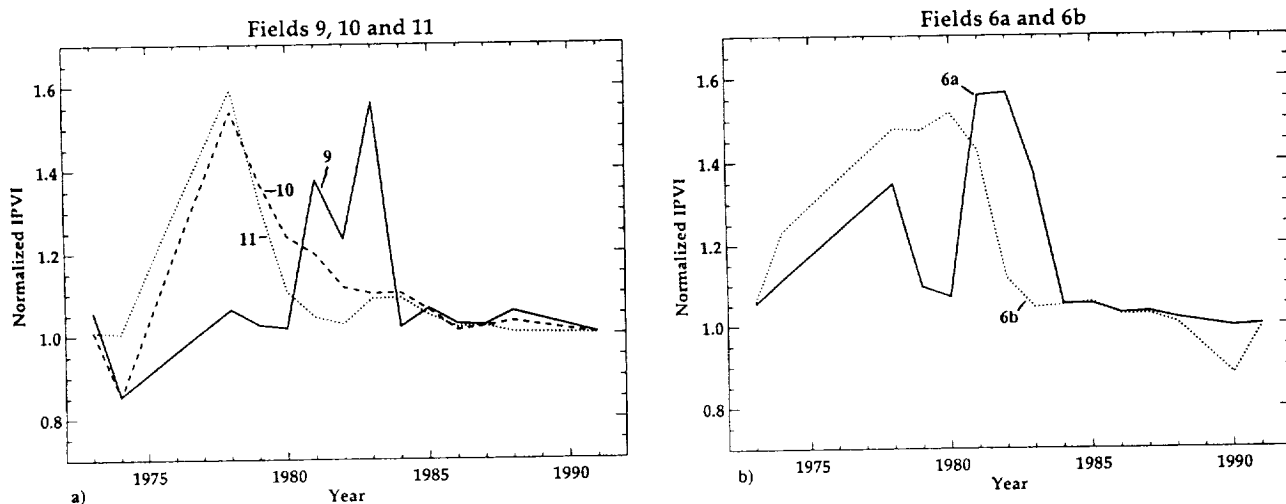


Figure 1: Plots of the normalized infrared percentage vegetation index (NIPVI) over time. Undisturbed desert values would fall along the line $NIPVI = 1.0$. This normalization is an attempt to minimize seasonal and rainfall variations which affect the entire region. No data from 1975, 1976 or 1977 are available for these fields. High values of NIPVI ($NIPVI > 1.3$) are believed to correspond to active cultivation. Note how NIPVI values relate to the position of the field relative to the wind. a) Field 9 (solid line) is farthest upwind, field 11 (dotted line) is farthest downwind, and field 10 (dashed line) is immediately between them. Note that no remote sensing data from 1990 are available for these fields. b) Field 6a (solid line) is upwind and field 6b (dotted line) is immediately downwind.

407-12
11037

THE RED EDGE IN ARID REGION VEGETATION: 340–1060 nm SPECTRA

Terrill W. Ray and Bruce C. Murray
Division of Geological and Planetary Sciences
California Institute of Technology
Pasadena, CA 91125

A. Chehbouni and Eni Njoku
Jet Propulsion Laboratory
California Institute of Technology
Pasadena, CA 91109

1. Introduction

The remote sensing study of vegetated regions of the world has typically been focused on the use of broad-band vegetation indices such as NDVI. Various modifications of these indices have been developed in attempts to minimize the effect of soil background, e.g., SAVI (Huete, 1988), or to reduce the effect of the atmosphere, e.g., ARVI (Kaufman and Tanré, 1992). Most of these indices depend on the so-called "red edge", the sharp transition between the strong absorption of chlorophyll pigment in visible wavelengths and the strong scattering in the near-infrared from the cellular structure of leaves. These broadband indices tend to become highly inaccurate as the green canopy cover becomes sparse (Huete *et al.*, 1985; Elvidge and Lyon, 1985; Huete and Tucker, 1991).

The advent of high spectral resolution remote sensing instruments such as the Airborne Visible and Infrared Imaging Spectrometer (AVIRIS) has allowed the detection of narrow spectral features in vegetation and there are reports of detection of the red edge even for pixels with very low levels of green vegetation cover by Vane *et al.* (1993) and Elvidge *et al.* (1993). High spectral resolution data have led to the use of derivative-based techniques to improve the measurement of low green vegetation levels (Chen *et al.*, 1993) and to characterize algal biomass in coastal areas (Goodin *et al.*, 1993). Spectral mixing approaches similar to those of Smith *et al.* (1990) can be extended into the high spectral resolution domain allowing for the analysis of more endmembers, and, potentially, discrimination between materials with narrow spectral differences.

Vegetation in arid regions tends to be sparse, often with small leaves such as the creosote bush. Many types of arid region vegetation spend much of the year with their leaves in a senescent state, i.e., yellow, with lowered chlorophyll pigmentation. The sparseness of the leaves of many arid region plants has the dual effect of lowering the green leaf area which can be observed and of allowing more of the sub-shrub soil to be visible which further complicates the spectrum of a region covered with arid region vegetation. Elvidge (1990) examined the spectral characteristics of dry plant materials showing significant differences in the region of the red edge and the diagnostic ligno-cellulose absorptions at 2090 nm and 2300 nm. Ray *et al.* (1993) detected absorption at 2100 nm in AVIRIS spectra of an abandoned field known to be covered by a great deal of dead plant litter. In order to better study arid

region vegetation using remote sensing data, it is necessary to better characterize the reflectance spectra of *in situ*, living, arid region plants.

2. Materials and Method

Field spectra were collected from several characteristic types of desert plants present in the Manix Basin Area of the Mojave Desert, which lies NE of Barstow, California along Interstate-15. The plants were creosote bush (*Larrea divaricata*); bursage (*Artemisia dumosa*); Russian thistle (*Salsola Kali*, commonly "tumbleweed") which was only present as dry balls trapped against creosote or bursage by the wind; and a small grass which is ubiquitous in the area and which has been tentatively identified as fluffgrass (*Erioneuron pulchellum*). Additional spectra were acquired of a few minor plants which were present in the area, as well as a spectrum of an active alfalfa field. These spectra were collected on July 23 and 24, 1993 to correspond to the same time of the year as the AVIRIS data collected on July 24, 1990. A significant potential difference between 1990 and 1993 is the fact that 1990 was a very dry year, while 1993 was a very wet year. The data were collected using a Personal Spectrometer 2 (PS-2) which uses a silicon detector to measure a spectral range from 335 to 1064 nm in 512 channels which are approximately 1.4 nm wide.

Spectra of shrub-type plants were collected in two different modes. The first is the plant spectra that include both canopy and underlying soil contributions. For the second mode a dark background was placed underneath the shrub so as to cover the sub-shrub soil. This dark background consisted of railroad board painted with ultra-flat black Krylon spray paint which has a very low reflectivity from the ultraviolet through 20 μm .¹ Five spectra were collected at each target. Photographs were also taken of each target to allow estimates of how much soil or dark target were visible in each case. Each target was located using chain and a Brunton compass.

3. Preliminary Results

Figure 1 shows the spectra of the alfalfa field and of the most common native plants in the area. In each case, the field of view of the spectrometer is effectively filled by the plant(s). In figure 1a the classic green vegetation reflectance spectrum is readily apparent in the case of the irrigated alfalfa field. The chlorophyll "bump" between .5 and .6 μm is clear and distinct, and there is a sharp red edge at the transition between red and near-infrared leading to a high reflectance plateau. The NDVI value from this spectrum is 0.8686.

Creosote bush is shown in figure 1b. This spectrum is the average spectrum based on the spectra recorded for four different individuals with the soil as the background. The chlorophyll "bump" is not nearly as distinct, although it is still present in a somewhat suppressed form. The red edge is still a fairly sharp step to a plateau of moderate near-infrared reflectance, but the step is significantly smaller than that for the alfalfa field. The NDVI which results in this case is 0.7264. When the creosote is recorded against the dark background, the chlorophyll "bump" is more pronounced and a slightly higher NDVI of 0.7314 results.

Figure 1c shows the average spectrum of four bursage shrubs. In this case, the chlorophyll "bump" is very indistinct and forms part of a plateau of slightly elevated reflectance which stretches from .55-.65 μm . The red edge transition is much smaller than in the case of either creosote bush or alfalfa. Additionally, the reflectance in the .4-.5 μm region is higher than seen in figures 1a and 1b. The NDVI computed from this spectrum is 0.4253.

A spectrum of a senescent grass which is ubiquitous in this area is shown in figure 1d. The spectrum is an average of two different sites. None of the fea-

¹ Westphal, personal comm., 1993.

tures typically associated with vegetation are apparent in this spectrum; there is no chlorophyll "bump" nor is there a perceptible red edge. The NDVI calculated from this spectrum is 0.1316, which is a value which could correspond to completely bare soil. This means that an area completely covered with this grass at this time of year would appear nearly barren. This grass has been tentatively identified as fluff grass, which is a perennial.

The examples shown in figure 1 clearly demonstrate that NDVI is not a satisfactory method for observing and quantifying vegetative cover in arid regions. The examples in this paper are based on cases where the instrument field of view is completely filled by the particular plant in question, and this problem will be greatly magnified when the vegetation cover is sparse. Additionally, these spectra are atmospherically corrected while measurements of NDVI from spaceborne systems often depend on data without an atmospheric correction, which tends to decrease the red-near-infrared contrast and further suppress NDVI.

4. Future Work

The spectra collected in this experiment will be used in analysis of AVIRIS and Landsat data which cover the Manix Basin area and other areas of the southwestern U.S. Repeat spectra of each target will be collected in October 1993, January 1994, April 1994, and July 1994 to characterize seasonal changes in spectral characteristics. In the case of annual plants, such as Russian Thistle, a representative plant from the immediate area of the original target will be chosen. The repeat observations may include measurements with a PIMA spectrometer which covers the 1300 to 2500 nm range. This work may lead to the development of a better index for monitoring vegetation dynamics in arid regions.

5. Acknowledgements

The authors would like to thank Curtiss Davis at JPL for the use of the PS2 spectrometer. Lisa Gaskell and Becky Zaske, undergraduates in Caltech's Division of Geological and Planetary Sciences, were instrumental in the collection of the field data.

6. References

- Chen, Z., C. D. Elvidge, and W. T. Jansen, Description of derivative-based high spectral-resolution (AVIRIS) green vegetation index, unpublished manuscript, 1993.
- Elvidge, C. D., Visible and near infrared reflectance characteristics of dry plant materials, *Int. J. Remote Sens.*, 11:1775-1795, 1990.
- Elvidge, C. D., Z. Chen, and D. P. Groeneveld, Detection of trace quantities of green vegetation in 1990 AVIRIS data, *Remote Sens. Environ.*, 44:271-279, 1993.
- Elvidge, C. D. and R. J. P. Lyon, Influence of rock-soil spectral variation on the assessment of green biomass, *Remote Sens. Environ.*, 17:265-279, 1985.
- Goodin, D. G., L. Han, R. N. Fraser, D. C. Rundquist, W. A. Stebbins, and J. F. Shalles, Analysis of suspended solids in water using remotely sensed high resolution derivative spectra, *Photo. Eng. Remote Sens.*, 49:505-510, 1993.
- Huete, A. R., A soil-adjusted vegetation index (SAVI), *Remote Sens. Environ.*, 25:295-309, 1988.
- Huete, A. R. and C. J. Tucker, Investigation of soil influences in AVHRR red and near-infrared vegetation index imagery, *Int. J. Remote Sens.*, 12:1223-1242, 1991.
- Huete, A. R., R.D. Jackson, and D. F. Post, Spectral response of a plant canopy with different soil backgrounds, *Remote Sens. Environ.*, 17:37-53, 1985.

- Kaufman, Y. J. and D. Tanré, Atmospherically resistant vegetation index (ARVI) for EOS-MODIS, *IEEE Trans. Geosci. Remote Sens.* 30:261-270, 1992.
- Ray, T. W., T. G. Farr, and J. J. van Zyl, Study of land degradation with polarimetric SAR and visible/near-infrared spectroscopy, *Proceedings of Topical Symposium on Combined Optical-Microwave Earth and Atmosphere Sensing*, 228-231, 1993.
- Smith, M. O., S. L. Ustin, J. B. Adams, and A. R. Gillespie, Vegetation in deserts: I. A regional measure of abundance from multispectral images, *Remote Sens. Environ.*, 31:1-26.
- Vane, G., R. O. Green, T. G. Chrien, H. T. Enmark, E. G. Hansen, and W. M. Porter, The airborne visible/infrared imaging spectrometer (AVIRIS), *Remote Sens. Environ.*, 44:127-143, 1993.

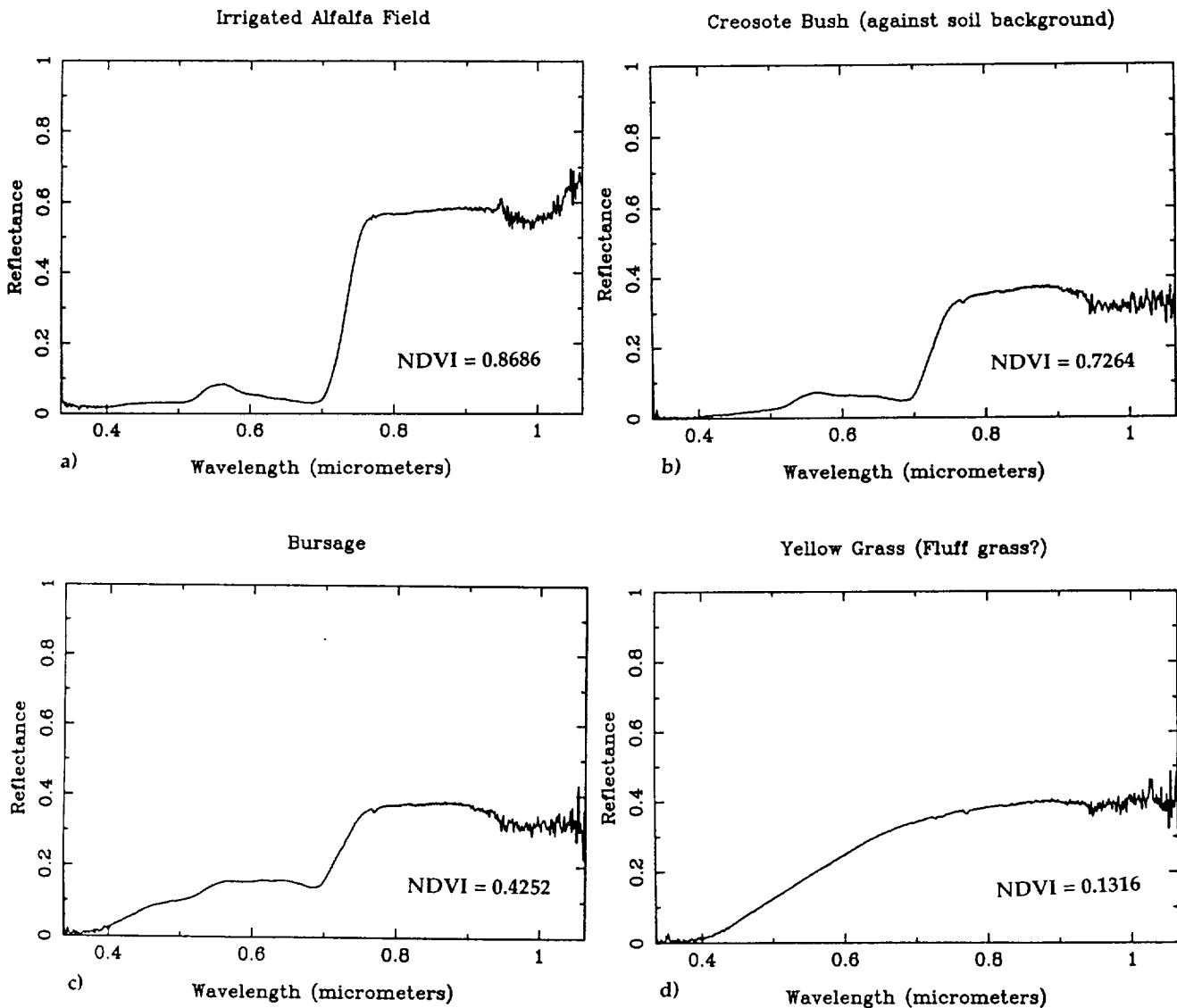


Figure 1: Spectra for some common Mojave Desert plant types and for an active irrigated alfalfa field in the Manix Basin area. In each case, the instrument field of view is completely filled by the vegetation being measured (100% vegetation cover). Compare the shapes of the spectra in the visible region and the nature of the red edge. NDVI values for each spectrum are listed to illustrate the poor performance of NDVI when looking at arid region vegetation. **a)** Irrigated alfalfa field. **b)** Creosote Bush. **c)** Bursage. **d)** An extremely common grass which is yellow most of the year; tentatively identified as fluff grass.

23-43
11038

TEMPORAL CHANGES IN ENDMEMBER ABUNDANCES, LIQUID WATER AND WATER VAPOR OVER VEGETATION AT JASPER RIDGE

Dar A. Roberts¹, Robert O. Green², Donald E. Sabol¹, John B. Adams¹

1. Department of Geological Sciences, AJ-20
University of Washington, Seattle, WA 98195

2. Jet Propulsion Laboratory, California Institute of Technology, Pasadena, CA 91109

1. INTRODUCTION

Imaging spectrometry offers a new way of deriving ecological information about vegetation communities from remote sensing. Applications include derivation of canopy chemistry (e.g., Wessman et al., 1989), measurement of column atmospheric water vapor and liquid water (Green et al., 1992), improved detectability of materials (Sabol et al., 1992), more accurate estimation of green vegetation cover and discrimination of spectrally distinct green leaf, non-photosynthetic vegetation (NPV: litter, wood, bark etc.) and shade spectra associated with different vegetation communities (Roberts et al., 1993).

Much of our emphasis has been on interpreting Airborne Visible/Infrared Imaging Spectrometry (AVIRIS) data as spectral mixtures. Two approaches have been used, simple models, where the data are treated as a mixture of 3 to 4 laboratory/field measured spectra, known as reference endmembers (EMs), applied uniformly to the whole image, to more complex models where both the number of EMs and the types of EMs vary on a per-pixel basis (Roberts et al., 1992). Where simple models are applied, materials, such as NPV, which are spectrally similar to soils, can be discriminated on the basis of residual spectra (Roberts et al., 1993). One key aspect is that the data are calibrated to reflectance and modeled as mixtures of reference EMs, permitting temporal comparison of EM fractions, independent of scene location or data type. In previous studies the calibration was performed using a modified-empirical line calibration (Roberts et al., 1993), assuming a uniform atmosphere across the scene.

In this study, a Modtran-based calibration approach was used to map liquid water and atmospheric water vapor and retrieve surface reflectance from three AVIRIS scenes acquired in 1992 over the Jasper Ridge Biological Preserve (see Green et al., 1993). The data were acquired on June 2nd, September 4th and October 6th. Reflectance images were analyzed as spectral mixtures of reference EMs using a simple 4 EM model. Atmospheric water vapor derived from Modtran was compared to elevation, and community type. Liquid water was compared to the abundance of NPV, Shade and Green Vegetation (GV) for select sites to determine whether a relationship existed, and under what conditions the relationship broke down. Temporal trends in endmember fractions, liquid water and atmospheric water vapor were investigated also. The combination of spectral mixture analysis and the Modtran based atmospheric/liquid water models was used to develop a unique vegetation community description.

2. RESULTS

Atmospheric water vapor, liquid water and the abundance of soil, NPV, GV and photometric shade, were determined for 14 sites of known elevation from the 3 dates (Fig. 1). A comparison of atmospheric water vapor to elevation demonstrated a good linear relationship for all 3 dates, with September having the highest water vapor concentrations, June intermediate and October the lowest (Fig. 2). Atmospheric water vapor was negatively correlated to increased elevation. The steepest gradient occurred at intermediate water vapor concentrations in June, producing the highest contrast between elevations. The relationship between elevation and atmospheric water vapor showed a marked departure from predicted water vapor over heavily vegetated areas in June and September. In all of these regions, except the Stanford Golf Course (C in Fig. 1), the atmospheric water vapor was higher over the vegetated regions. These departures may represent evapotranspired water vapor, trapped water vapor in canyons or an incomplete separation of liquid water from atmospheric water vapor. The latter, however, is unlikely, because liquid water and atmospheric water vapor, although positively correlated, were not directly correlated in all areas. Liquid water was mapped as showing very sharp gradients between vegetated and non-vegetated areas. Atmospheric water vapor, on the other hand, had

gradational boundaries. Heavily vegetated sites did not show above normal water vapor concentrations on the driest date, in October, potentially attributable to low transpiration rates at that time.

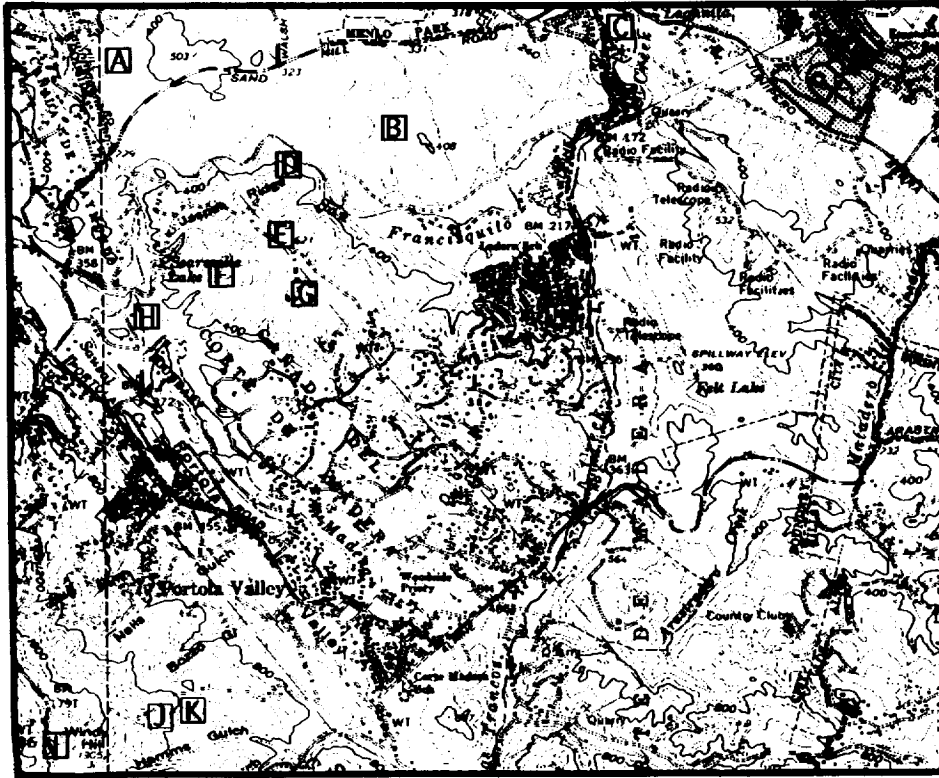


Figure 1. Index map showing the location of some of the study sites. These include a Horse Ranch (A), Webb Ranch (B), Stanford Golf Course (C), Evergreen Broadleaf Forest (D), Serpentine Grassland (E), Chaparral (F), Annual Grassland (G), Forested Wetland (H) and 3 high elevation grasslands (I, J and K). Four forested areas in the Santa Cruz Mountains, one at Alambique Creek (317 m), and three along an elevational transect in Martín Creek, at 183, 262 and 390 m, respectively, were off the map.

The EM fractions changed among the three dates, primarily due to a decrease in the solar elevation and senescence, producing an increase in the shade and NPV fractions and a decrease in the GV fraction (Fig. 3, Site locations, Fig. 1). For a more detailed discussion of the relationship between endmember abundances, vegetation communities, and temporal trends see Sabol et al. (1993).

Fractions of NPV, GV and shade were compared to liquid water absorptions for the three dates (Fig. 4a-c). The best relationships occurred in June, where shade and GV were positively correlated to liquid water and NPV was negatively correlated. The best fit was for NPV and liquid water. The only major departure was in the Serpentine site (E on Fig. 1), where the soil fraction was high. GV showed departures at two sites, the Stanford Golf Course, where the GV fraction was high, but the liquid water concentration low, and in the Santa Cruz Mountains (Martín and Alambique Creeks), where the highest liquid water absorptions occurred but GV was low due to a high shade fraction (>0.60). In these areas, shade showed a high correlation with liquid water. The difference between GV and liquid water absorptions is due, most likely, to the low leaf area of the golf course grasses. The relationship between the EM fractions was similar for the other two dates, although the fit was poorer. Liquid water absorption showed a systematic change between the three dates; values for September were higher than June by 20, whereas the October values were lower for the lowest sites (by approximately 10) and slightly higher for the sites with the highest absorptions. Whether these differences are real (due to rainfall in September), or due to modeling errors (e.g., slight wavelength miscalibrations) requires further investigation.

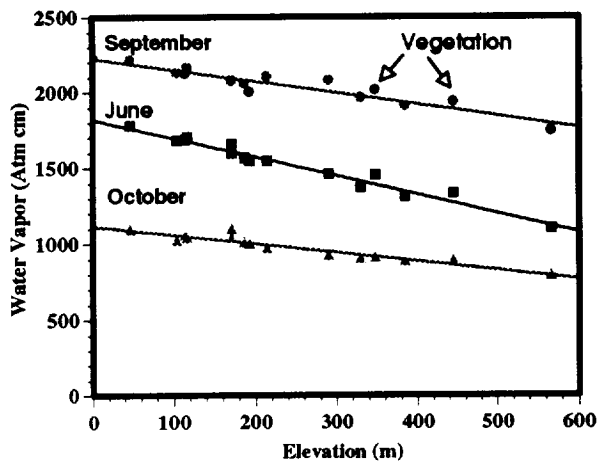


Figure 2. Comparison between atmospheric water vapor and elevation for all of the study sites over the three dates. Water vapor was negatively correlated with elevation (June: $Y = -1.236 \cdot X + 1820$, $R^2 = 0.966$; Sept.: $Y = -0.759 \cdot X + 2225$, $R^2 = 0.875$; Oct.: $Y = -0.576 \cdot X + 1117$, $R^2 = 0.896$).

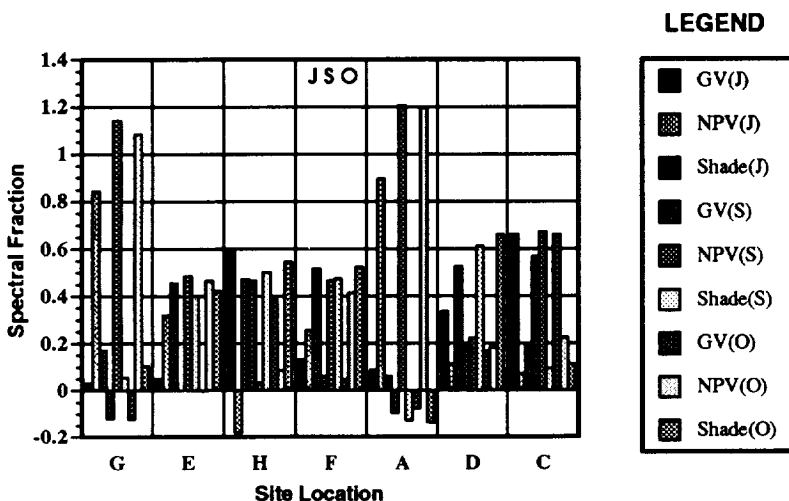


Figure 3. Changes in endmember fractions at 7 sites on three dates. The first, second and third columns are for June, next three for September and last three for October. Negative and super-positive (>1.0) fractions are due to limitations in the simple model (see Sabol et al., 1993).

3. SUMMARY

AVIRIS provides information about vegetation that cannot be obtained using other sensors. In this paper we mapped temporal and spatial patterns in liquid water, atmospheric water vapor, shade, GV, NPV and soil, relating these parameters to vegetation types. Examples included atmospheric water vapor which was modeled as higher, for a given elevation, over vegetated sites than non-vegetated sites for June and September, but not for October, on a dryer day. Liquid water was correlated with GV on all three dates except for highly shaded areas, where shade showed a better relationship, and areas with low leaf area but a high GV fraction, such as the Stanford Golf Course. Under these instances, liquid water estimates and mixture models provide complementary, but different information about vegetation. Through this analysis, we offer a new way to characterize vegetation communities through their physical attributes (EM fractions and liquid water) and associated atmospheric properties (water vapor).

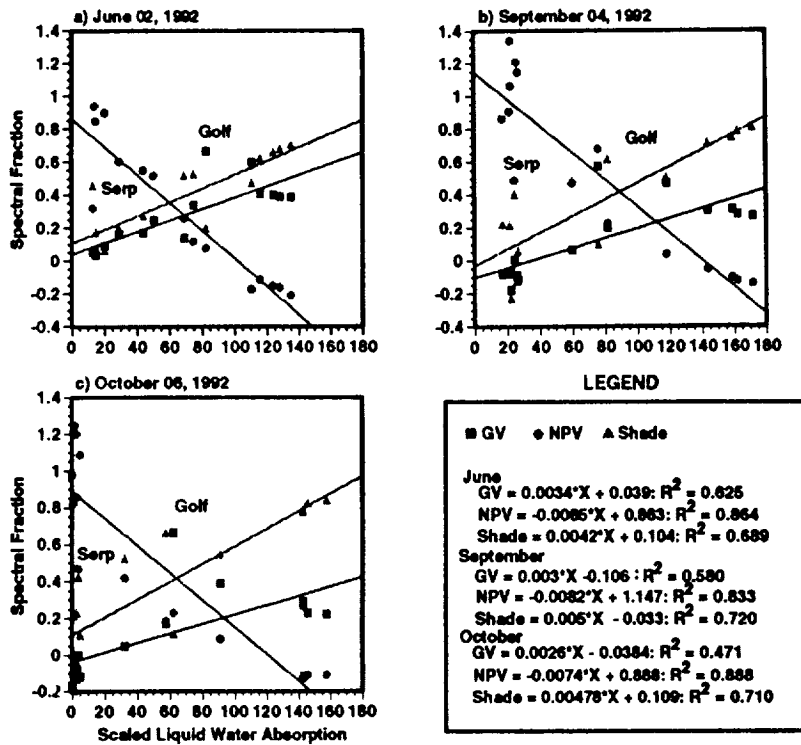


Figure 4. Scatterplot between scaled liquid water absorption and NPV, GV and Shade fractions. For all three dates, NPV was negatively correlated and shade and GV were positively correlated.

4. REFERENCES

- Green, R.O., Conel, J.E., Margolis, J.S., Bruegge, C.J., and Hoover, G.L., An Inversion Algorithm for Retrieval of Atmospheric and Leaf Water Absorption From AVIRIS Radiance With Compensation for Atmospheric Scattering. *Summaries of the 3rd Annual JPL Airborne Geoscience Workshop, vol.1, AVIRIS Workshop* (Green ed.), JPL Publication 92-14, Jet Propulsion Laboratory, Pasadena, CA, June 1, 1992, pp. 51-61.
- Green, R. O., Conel, J.E., and Roberts, D.A., 1993, Estimation of Aerosol Optical Depth and Calculation of Apparent Surface Reflectance from Radiance Measured by the Airborne Visible-Infrared Imaging Spectrometer (AVIRIS) Using MODTRAN2, *SPIE Conf. 1937, Imaging Spectrometry of the Terrestrial Environment*, in press, 12 p.
- Roberts, D.A., Smith, M.O., Sabol, D.E., Adams, J.B., and Ustin, S., Mapping the Spectral Variability in Photosynthetic and Non-photosynthetic Vegetation, Soils and Shade Using AVIRIS, *Summaries of the 3rd Annual JPL Airborne Geoscience Workshop, vol.1, AVIRIS Workshop* (Green ed.), JPL Publication 92-14, Jet Propulsion Laboratory, Pasadena, CA, June 1, 1992, pp. 38-40.
- Roberts, D.A., Smith, M.O., and Adams, J.B., 1993, Green Vegetation, Nonphotosynthetic Vegetation, and Soils in AVIRIS Data. *Remote Sens. Environ.*, 44:255-269.
- Sabol, D.E., Adams, J.B., and Smith, M.O., 1992, Quantitative Subpixel Spectral Detection of Targets in Multispectral Images. *J. Geophys. Res.*, 97(E2): 2659-2672.
- Sabol, D.E., Roberts, D.A., Adams, J.B., and Smith, M.O., 1993, Mapping and Monitoring Changes in Vegetation Communities of Jasper Ridge, CA, Using Spectral Fractions, this volume.
- Wessman, C.A., Aber, J.D., and Peterson, D.L. 1989. An Evaluation of Imaging Spectrometry for Estimating Forest Canopy Chemistry. *Int. J. Remote Sens.*, 10(8): 1293-1316.

23883
1/10/39
44

**MAPPING AND MONITORING CHANGES IN VEGETATION
COMMUNITIES OF JASPER RIDGE, CA, USING SPECTRAL
FRACTIONS DERIVED FROM AVIRIS IMAGES**

Donald E. Sabol Jr., Dar A. Roberts,
John B. Adams, and Milton O. Smith

Department of Geological Sciences, AJ-20
University of Washington
Seattle, Washington 98195

Introduction:

An important application of remote sensing is to map and monitor changes over large areas of the land surface. This is particularly significant with the current interest in monitoring vegetation communities. Most traditional methods for mapping different types of plant communities are based upon statistical classification techniques (i.e. parallel piped, nearest-neighbor, etc.) applied to uncalibrated multispectral data. Classes from these techniques are typically difficult to interpret (particularly to a field ecologist / botanist). Also, classes derived for one image can be very different from those derived from another image of the same area, making interpretation of observed temporal changes nearly impossible. More recently, neural networks have been applied to classification (Ridd et al., 1992). Neural network classification, based upon spectral matching, is weak in dealing with spectral mixtures (a condition prevalent in images of natural surfaces).

Another approach to mapping vegetation communities are based on spectral mixture analysis, which can provide a consistent framework for image interpretation (Gillespie et al., 1990). Roberts et al. (1990) mapped vegetation using the band residuals from a simple mixing model (the same spectral endmembers applied to all image pixels). Sabol et al. (1992b) and Roberts et al. (1992) used different methods to apply the most appropriate spectral endmembers to each image pixel, thereby allowing mapping of vegetation based upon the different endmember spectra. In this paper, we describe a new approach to classification of vegetation communities based upon the spectral fractions derived from spectral mixture analysis. This approach was applied to three 1992 AVIRIS images of Jasper Ridge, California to observe seasonal changes in surface composition.

Methods:

AVIRIS images of Jasper Ridge, CA from three dates were used for this study: 2 June 1992, 4 September 1992, and 6 October 1992. Each of these images was: 1) calibrated using the approach of Green et al., 1993 (this issue), 2) registered with the USGS 7.5 minute digital-terrain-map (DTM), and 3) modeled as mixtures of four spectral components (samples collected in the study area and measured in the laboratory): green vegetation, soil, non-photosynthetic vegetation (NPV), and shade. Each image was then classified based upon the endmember fractions. The boundaries for the various classes were initially determined interactively by relating pixel fraction clusters (in fraction space) to their spatial distribution in the image using TM data of Brazil (Adams et al., in preparation) and subsequently adapted to the Jasper Ridge data.

The architecture of the various plant canopies causes different shade fractions; a key to their classification. It is, therefore, important to isolate the shade fraction caused by surface composition from that caused by topographic effects. To do this, we used the DTM and the solar elevation information for each image to calculate the shade due to topography (assuming a lambertian surface). The shade fraction was then adjusted so that only the shade fraction due to surface texture was used in classification.

Results and Discussion:

Endmember fractions describe the physical characteristics of plant communities as interpreted by spectral mixture analysis. For example, the group of pixels labeled A in Figure 1 correspond to the forested wetland in the image. Here, high fractions of

vegetation (greater than 100%) occur because the spectral contrast between the actual green vegetation in the forested wetland and mixtures of the soil and NPV endmembers is greater than that of the green vegetation endmember used to model the scene. The high shade fraction is also distinctive of the forested wetland. The fractions labeled B in Figure 1 are characteristic of senescent grassland (low shade and high fractions of NPV). This ability to relate spectral fractions to surface composition facilitates a meaningful classification of the scene.

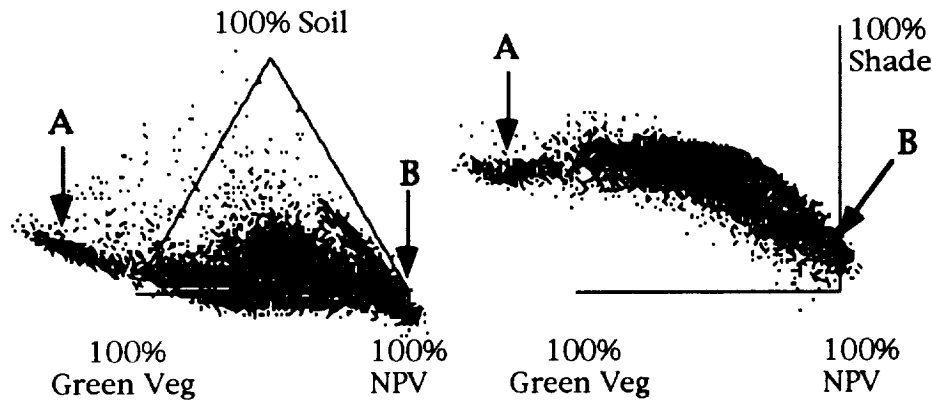


Figure 1: Distribution of fractions for a subset of the June 2, 1992 AVIRIS image of Jasper Ridge. Fractions indicative of the forested wetlands is labeled A and those for the grasslands, B.

The classification scheme is shown in the ternary diagram in Figure 2. Class boundaries in this scheme are linear and may appear arbitrary. In early investigations of this approach to classification, the boundaries were mapped as being slightly curved. It was subsequently determined that linearizing the boundaries simplified application of the classification with little change in the final results. Although not shown in Figure 2, the shade fraction (a relative measure of canopy architecture of plant communities) was used in the classification. For example, pixels containing tall bushes and trees (i.e. forested wetland, chaparral, and deciduous oak woodland) typically contained greater than 35 percent shade at the time of image acquisition.

Images classified using this approach closely matched vegetational maps of the surface. Figure 3 (Slide 11 in the pocket attached to the cover) shows the classified June 2nd image next to a vegetation map (mapped in the field) for comparison. The classes (and colors) are the same for both maps. The degraded grassland, however, was not mapped separately from grassland in the field map, as it was in the classification image.

Preliminary results show that observation of temporal changes in the fractions can be useful in monitoring surface processes. Temporal changes in the fractions of the forested wetland, chaparral, and grasslands are shown in Figure 4. The raw fractions (open symbols) are those calculated from spectral mixture analysis. Most of the vegetation communities had low fractions of soil. Detection-threshold analysis (Sabot et al., 1992a) was used to determine whether the low soil fractions were within detectable limits. If the observed soil fraction was less than the minimal fraction of soil necessary to be detectable, soil is not considered to be present. The fractions are then adjusted for interpretation.

Examination of the temporal changes in the fractions shows some interesting trends (Figure 4). For example, a distinct increase in the NPV fraction was observed in the forested wetland from June to October. This is probably due to the increasing fraction of bark and stems as the deciduous trees in the forested wetland drop their leaves. The chaparral and grasslands also show the trend toward increasing NPV as well as having detectable soil fractions in June. This trend in the chaparral may be explained by leaf drop in September and October, which increased exposure of the bark and stems while fallen leaves obscured the soil that had been visible through the canopy in June. The same trend observed in the grassland was most likely caused by other processes. Here,

the grass had senesced but was still standing upright in June; allowing some soil to be observed. Later, the grass began to fall over thereby reducing exposure of the soil.

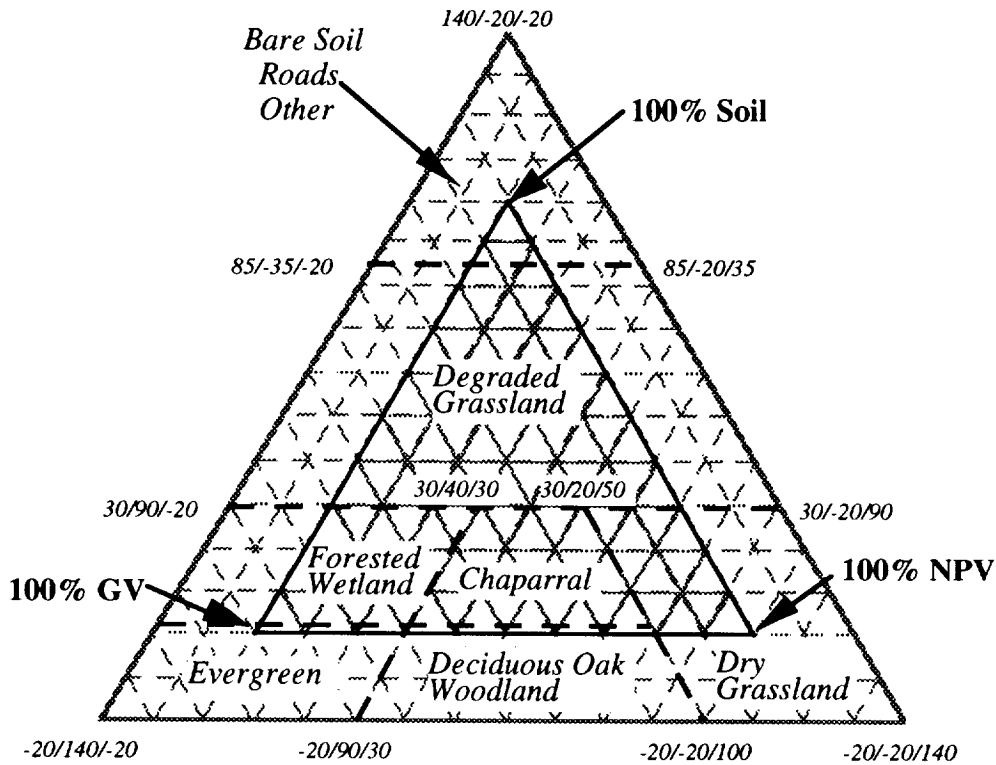


Figure 2: Ternary classification diagram used to classify the Jasper Ridge images.

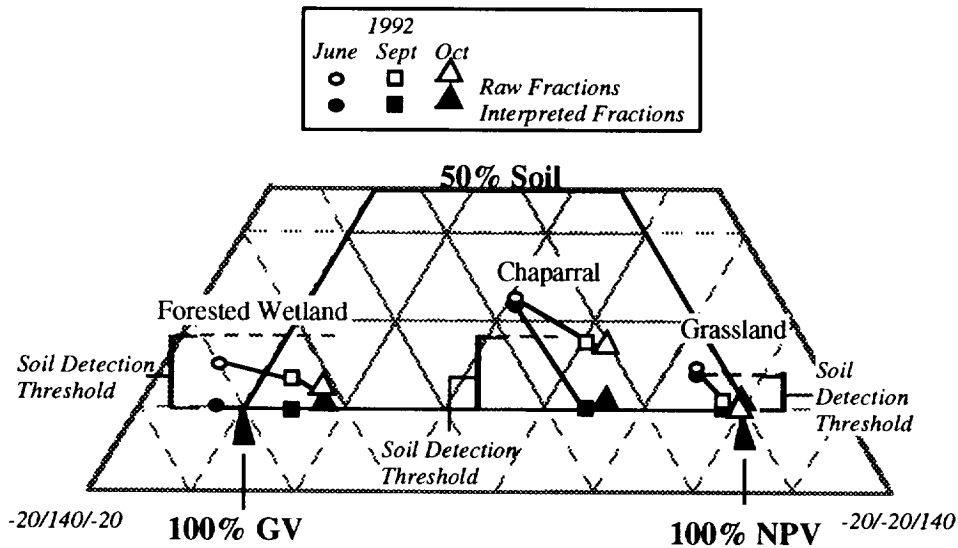


Figure 4: Temporal changes in fractions of three different plant communities of Jasper Ridge. Fractions plotted are of representative pixels representative of each community.

These seasonal trends were only observed over a part of the year, and, in the case of the grasslands, most of the growing season was missed. With the addition of image data from March or April, a more complete map of seasonal fractional variability may be produced and related to the seasonal growing cycle of various vegetational communities. With higher temporal resolution, these seasonal changes can be incorporated into the classification scheme as a way to separate spectrally similar communities with different growing cycles.

Conclusions:

- 1) Spectral mixture analysis provides a consistent framework for image interpretation, thereby allowing image classification based upon spectral fractions as well as observation of temporal changes.
- 2) Because the shade fraction is an important factor in classification of vegetational communities, it is necessary to separate the shade fraction caused by topographic effects from that caused by surface texture (for example, differential shading and shadows caused by various plant communities).
- 3) This classification scheme has yielded encouraging results in a variety of heavily vegetated images, including TM images of Brazil, MSS and TM images of northern California, and AVIRIS images of Jasper Ridge.
- 4) A clear understanding of the spectral changes in vegetation communities throughout the growing season may aid identifying spectrally similar communities with different growing cycles
- 5) Long term monitoring of any given area will allow separation of seasonal changes from longer term changes that may indicate a long-term cyclic (or permanent) changes in surface composition.

References:

- Adams, J.B., Sabol, D.E., Kapos, V., Almeida Filho, R., Roberts, D.A., Smith, M.O., and Gillespie, A.R., in preparation, Classification of multispectral images based on fractions of endmembers: Application to land-use change in the Brazilian Amazon, to be submitted to Remote Sensing of Environment.
- Gillespie, A.R., Smith, M.O., Adams, J.B., Willis, S.C., Fischer, A.F. III, and Sabol, D.E., 1990, Interpretation of residual images: Spectral mixture analysis of AVIRIS images, Owens Valley, California, Proc. Second Visible/Infrared Imaging Spectrometer (AVIRIS) Workshop. JPL Pub. 90-54, 243-270.
- Green, R.O., Conel, J.E., and Roberts, D.A., 1993, Estimation of aerosol optical depth and calculation of apparent reflectance from radiance measured by the Airborne Visible Infrared Imaging Spectrometer (AVIRIS) using MODTRAN2a, Proc. Forth Annual Airborne Geosci. (AVIRIS) Workshop, this issue.
- Ridd, M.K., Ritter, N.D., Byrant, N.A., and Green, R.O., 1992, AVIRIS data and neural networks applied to an urban ecosystem, Proc. Third Annual Airborne Geosci. (AVIRIS) Workshop. JPL Pub. 92-14, vol. 1, 129-131.
- Roberts, D.A., Smith, M.O., Adams, J.B., Sabol, D.E., and Gillespie, A.R., 1990, Isolating woody plant material and senescent vegetation from green vegetation in AVIRIS data, Proc. Second Visible/Infrared Imaging Spectrometer (AVIRIS) Workshop. JPL Pub. 90-54, 42-57.
- Roberts, D.A., Smith, M.O., Sabol, D.E., Adams, J.B., and Ustin, S., 1992, Mapping the spectral variability in photosynthetic and non-photosynthetic vegetation, soils, and shade using AVIRIS, Proc. Third Annual Airborne Geosci. (AVIRIS) Workshop. JPL Pub. 92-14, vol. 1, 38-40.
- Sabol, D.E., Adams, J.B., and Smith, M.O., 1992a, Quantitative subpixel spectral detection of targets in multispectral images, *J. Geophys. Res.* 97, 2659-2672.
- Sabol, D.E., Roberts, D.A., Smith, M.O., and Adams, J.B., 1992b, Temporal variation in spectral detection thresholds of substrate and vegetation in AVIRIS images, Proc. Third Annual Airborne Geosci. (AVIRIS) Workshop. JPL Pub. 92-14, vol. 1, 132-134.

THE EFFECT OF SIGNAL NOISE ON THE REMOTE SENSING OF FOLIAR BIOCHEMICAL CONCENTRATION

Geoffrey M. Smith.

Department of Geography, University College of Swansea,
Singleton Park, Swansea SA2 8PP, United Kingdom.

and

Paul J. Curran.

Department of Geography, University of Southampton,
Highfield, Southampton SO9 5NH, United Kingdom.

41040
11

1. INTRODUCTION

Spectral measurements made using an imaging spectrometer contain systematic and random noise, whilst the former can be corrected the latter remains a source of error in the remotely sensed signal (Curran, 1989). A number of investigators have tried to determine the signal-to-noise-ratio (SNR) of the instrument (Green *et al.*, 1992), or the resultant imagery (Curran and Dungan, 1989; Gao, 1993). However, the level of noise at which spectra are too noisy to be useful is not usually determined. The first attempt was by Goetz and Calvin (1987), who suggested that the depth of the absorption feature should be at least an order of magnitude greater than the noise and more recently Dekker (1993) suggested a SNR of around 600:1 was required in visible/near infrared wavelengths to measure a 1 g l^{-1} change in chlorophyll *a* concentration in water. The wide range of applications of imaging spectroscopy make it difficult to set SNR specifications as they are dependent on a number of factors, one of the most important being reflectance of a particular target. For example, the SNR of imagery for vegetated targets is relatively low simply because vegetation has a relatively low level of reflectance.

The Airborne Visible/Infrared Imaging Spectrometer (AVIRIS) is being used to estimate the concentration of biochemicals within vegetation canopies. This paper reports a study undertaken to identify first, wavebands that were highly correlated with foliar biochemical concentration and second, to determine how sensitive these correlations were to sensor noise.

2. DATA SET

The foliar samples were collected from a slash pine (*Pinus elliottii* var. *elliottii*) plantation in north central Florida (Gholz *et al.*, 1991). Ten samples of needles were collected in July 1991 from two fertilised and two control plots, these were subdivided into new and old needles giving a total of eighty samples. In the laboratory the spectral reflectance of a single layer of fresh whole needles was measured in the 400 - 2400nm wavelength range using a GER Infrared Intelligent Spectroradiometer (IRIS) and a controlled light source. The needles were then assayed using wet chemical techniques to determine the concentrations of nitrogen, lignin and cellulose.

The IRIS spectra were spectrally degraded to match AVIRIS spectra. The 400 - 1100nm spectral region was removed from further analysis as it contained wavebands that were highly correlated with the three biochemical concentrations but not at explicable wavebands. The spectra were converted to 1st and 2nd derivatives

using a Lagrangian three-point interpolation (Hildebrand, 1974).

3. THE SELECTION OF WAVEBANDS BY CORRELATION ANALYSIS

The wavebands that had the largest correlation with biochemical concentration were selected by comparing the two derivative reflectances of each waveband with the concentration of each biochemical (Ebdon, 1985). For each biochemical and derivative combination a correlogram of correlation coefficient (r) against waveband was produced. From these correlograms the wavebands with the largest r 's were selected (table 1).

Table 1. The wavebands with the largest explicable correlation between derivative reflectance and foliar biochemical concentration.

Reflectance derivative	Biochemical	Selected waveband(nm)	Explaining feature(nm)	r
1st	Nitrogen	1491	1485 Protein	0.53
	Lignin	1689	1690 Lignin	0.44
	Cellulose	1281	1275 Cellulose	-0.39
2nd	Nitrogen	1195	1187 Protein	0.41
	Lignin	1709	1696 Lignin	-0.40
	Cellulose	1719	1706 Cellulose	-0.34

The biochemical explanation of the wavebands selected in table 1 were suggested by Williams and Norris (1987), Curran (1989) and Peterson (1991). The selected wavebands did not always have the largest r . The wavebands with the largest r 's were sometimes unexplained or within the major water absorption bands. For both derivatives nitrogen gives the largest r and cellulose the smallest.

4. SENSITIVITY OF THE SELECTED WAVEBANDS TO NOISE

To determine the noise sensitivity of the wavebands selected in table 1, noise of increasing amplitude was added to the spectra. The noise was random, normally distributed and scaled by the average reflectance of all the spectra. At each step the noise was added to the original spectra and the derivatives recalculated. The correlation analysis, described above, was then repeated to reselect the wavebands and rank them by their absolute r 's. As the amplitude of the added noise increased a point was reached when the rank of the selected waveband in table 1 began to change. At this point the selected waveband was deemed to be sensitive to the added noise. The SNR ratio for this noise amplitude was calculated by dividing the mean of the reflectances in the selected waveband, the signal, by the amplitude of the added noise, the noise. The process of determining this SNR was repeated five times with different randomisation seeds for the noise and then averaged to give a representative SNR (table 2).

Initially the noise present in the IRIS spectra was assumed to be zero. To estimate the SNR of the IRIS a sample of dry slash pine needles were scanned fifty times. These spectra were degraded to AVIRIS spectral resolution and the SNR calculated by dividing the mean reflectance of each waveband, the signal, by its

standard deviation, the noise. The SNR estimates for the IRIS were much lower than expected. Therefore the SNR's from the analysis were corrected for the noise in the IRIS spectra (table 2).

The SNR predictions in table 2 have similar trends to the r's in table 1 except for the 2nd derivative nitrogen waveband at 1195nm. The SNR's from the analysis were very variable and supported the decision to correct for the inherent noise in the IRIS spectra. The corrected SNR's from the analysis were all of a similar magnitude. In the 1st derivative spectra nitrogen is the least sensitive to noise and cellulose the most. Except for nitrogen, the 2nd derivative seem to be less noise sensitive than the 1st derivative, possibly due to the smoothing effect of a second derivative calculation.

Table 2. The SNR at which wavebands selected as having a large correlation between biochemical concentration and derivative reflectance (table 1) become sensitive to the addition of noise.

Reflectance derivative	Biochemical	Selected waveband (nm)	SNR from analysis	Corrected SNR from analysis
1st	Nitrogen	1491	48:1	37:1
	Lignin	1689	114:1	50:1
	Cellulose	1281	525:1	65:1
2nd	Nitrogen	1195	1765:1	61:1
	Lignin	1709	108:1	46:1
	Cellulose	1719	198:1	48:1

5. COMPARISON WITH JPL SNR ESTIMATES

The Jet Propulsion Laboratory (JPL) estimate SNR for the AVIRIS on the assumption of a 50% reflectance (Green *et al.*, 1992), however this level of reflectance is not reached by vegetation in the spectral regions that correlate strongly with biochemical concentration. The JPL SNR values for the start of the 1993 flight season (Green, *pers comm.*) were converted, albeit approximately, to values that would be obtained when recording vegetation (table 3) and compared to the results of this study. The AVIRIS data appeared to have large enough SNR's for the estimation of foliar biochemical concentrations except for the 1st derivative nitrogen waveband which is close to the threshold (table 3).

6. CONCLUSIONS

Laboratory studies using instruments with SNR's in the thousands have indicated that near infrared spectroscopy of foliar biochemical concentrations is possible (Marten *et al.*, 1989). The results of this study suggest that the AVIRIS is now near or just beyond the SNR threshold that is required in order to estimate foliar biochemical concentrations. However, the spectral data for this study had a much simpler origin than those recorded by the AVIRIS; atmospheric effects were reduced by the close proximity of the source, sample and detector and the sample arrangement was not as complex as that of vegetation and background in an actual canopy. This suggests that the AVIRIS data of a vegetation canopy will have a SNR that is barely adequate for the remote sensing of foliar biochemical concentration.

Table 3: A comparison of the SNR achieved by AVIRIS and the SNR required for the spectral estimation of foliar biochemical concentration.

Reflectance derivative	Biochemical	Selected waveband (nm)	JPL SNR @ vegetation reflectance	Corrected SNR from analysis
1st	Nitrogen	1491	25:1	37:1
	Lignin	1689	100:1	50:1
	Cellulose	1281	240:1	65:1
2nd	Nitrogen	1195	210:1	61:1
	Lignin	1709	95:1	46:1
	Cellulose	1719	90:1	48:1

REFERENCES

- Curran, P.J., 1989, The remote sensing of foliar chemistry. *Remote Sensing of Environment*, 29, 271-278.
- Curran, P.J. and Dungan, J.L., 1989, Estimation of signal-to-noise: A new procedure applied to AVIRIS data. *IEEE Transactions in Geoscience and Remote Sensing*, 27, 620-628.
- Dekker, A.G., 1993, *Detection of Optical Water Quality Parameters for Eutrophic Water by High Resolution Remote Sensing*. Ph.D. thesis, Proefschrift Vrije Universiteit, Amsterdam.
- Ebdon, D., 1985, *Statistics in Geography*. Basil Blackwell, Oxford.
- Gao, B-C, 1993, An operational method for estimating signal to noise ratios from data acquired with imaging spectrometers. *Remote Sensing of Environment*, 43, 23-33.
- Gholz, H.L., Vogel, S.A., Cropper, W.P.Jr., McKelvey, K., Ewel, K.C., Teskey, R.O. and Curran, P.J., 1991, Dynamics of canopy structure and light interception in *Pinus elliotii* stands, North Florida. *Ecological Monographs*, 61, 33-51.
- Goetz, A.F.H. and Calvin, W.M., 1987, Imaging spectrometry: Spectral resolution and analytical identification of spectral features. *Imaging spectroscopy II, SPIE 834*, Bellingham, WA, 158-165.
- Green, R.O., Conel, J.E., Bruegge, C.J., Margolis, J.S., Carrere, V., Vane, G. and Hoover, G., 1992, In-flight calibration of the spectral and radiometric characteristics of AVIRIS in 1991. *Summaries of the Third Annual JPL Airborne Geoscience Workshop*, JPL publication 92-14, Pasadena, CA, 1-4.
- Hildebrand, F.B., 1974, *Introduction to Numerical Analysis*. McGraw Hill, New York.
- Marten, G.C., Shenk, J.S. and Barten II, F.E., 1989, *Near Infrared Reflectance Spectroscopy (NIRS): Analysis of Forage Quality*. USDA, Agricultural Handbook 643, Washington DC.
- Peterson, D.L., 1991, *Report on the Workshop: Remote Sensing of Plant Biochemical Content: Theoretical and Empirical Studies*. NASA White Paper, NASA Ames Research Centre, CA.
- Williams, P. and Norris, K., 1987, *Near-infrared technology in the agricultural and food industries*. American Association of Cereal Chemists Inc., St. Paul, MN.

41041
7 4

**APPLICATION OF MAC-EUROPE AVIRIS DATA TO THE ANALYSIS OF
VARIOUS ALTERATION STAGES IN THE LANDDMANNALAUGAR
HYDROTHERMAL AREA (SOUTH ICELAND)**

S. Sommer, G. Lörcher & S. Endres

**AGF - Institute f. General & Applied Geology
Ludwig-Maximilians-Universität München
Luisenstr. 37, D-80333 München, Germany**

1. INTRODUCTION

In June 1991 extensive airborne remote sensing data-sets have been acquired over Iceland in the framework of the joint NASA/ESA Multisensor Airborne Campaign Europe (MAC-Europe).

The study area is located within the Torfajökull central volcanic complex in South Iceland. This complex is composed by anomalously abundant rhyolitic acid volcanics, which underwent intensive hydrothermal alteration. Detailed studies of surface alteration of rhyolitic rocks in the area showed that all the major elements are leached as the rock is affected by complex mineralogical changes. Montmorillonite appears during the earliest stages of alteration. In the ultimate alteration product montmorillonite is absent and the rock consists mostly of amorphous silica, anatase, up to a volume of 50% kaolinite and variable amounts of native sulphur and pyrite (ARNORSON et al., 1987).

The case study presented shall contribute to assess the potential of MAC-Europe AVIRIS and TMS data to determine a possible zonation of hydrothermal alteration in relationship to the active geo-thermal fields and structural features. To this end, the airborne data is analysed in comparison with laboratory spectral measurements of characteristic rock, soil and vegetation samples collected in the study area in summer 1992. Various spectral mapping algorithms as well as unmixing approaches are tested and evaluated. Detailed geological and structural mapping as well as geochemical analysis of the main rock and soil types were performed to underpin the analysis of the airborne data.

2. TEST SITE DESCRIPTION AND AVAILABLE DATA SETS

The test site is part of the Torfajökull rhyolitic complex (S. Iceland) and covers an area of approximately 100 km² around the center coordinate 64°N 19°W. The geology is characterized by a caldera structure built up by tertiary to recent acidic volcanics (mainly rhyolites) in the interior. At the margins of the caldera pleistocene hyaloclastites and postglacial basic and intermediate lavas are predominant. Hot springs are the recent expression of the hydrothermal activity, which intensively altered the rhyolites.

The hilly to mountainous area is covered by sparse mossy vegetation. Dense algae and moss canopies are concentrated around the wells of hot water.

The following data sets have been included in the investigations:

- Remote Sensing Data: AVIRIS, TMS; Acquisition date 17 June 1991
- Atmospheric Measurements: In-flight P, T, HV, radiosonde profile Keflavik airport
- Ground Truth: Geological maps 1 : 20 000, 1 : 250 000; laboratory spectral measurements and geochemical analysis of field samples
- Structural Data: Structural maps derived from Landsat-TM and aerophotographs

3. ANALYSIS OF FIELD SAMPLES

Field samples of all rock units and relevant vegetation types were collected in summer 1991 and 1992. Furthermore, a 500 m cross section through a thermal field was taken with sampling every 25 m.

Field and laboratory spectral measurements were performed with a GER S-FOV IRIS spectroradiometer.

Fluorescence X-ray analysis was used for element geochemistry.

X-ray diffractometry (XRD) was applied to the determination of various clay minerals, respectively phyllosilicates, in the alteration facies.

Spectroradiometer measurements clearly exhibit that spectral reflectance is an excellent parameter to distinguish altered rhyolite from unchanged volcanic rocks. In all spectral regions from 400 to 2500 nm alteration leads to an increase of reflectance and more prominent absorption features can be observed, due to recrystallisation and formation of oxides, sulphates and OH-bearing minerals. However, the differentiation of various clay fractions, potentially characterizing different stages of alteration, definitely requires spectral information from the 2000 to 2500 nm part of the spectrum. XRD analysis revealed abundances of typical alteration minerals like alunite, chlorite, kaolinite and nontronite in the samples from the thermal field transect. In fact, these

minerals show characteristic absorption features around 2200 nm, at 2270 nm and around 2300 nm. Consequently, the fourth AVIRIS spectrometer is of utmost importance for mineral mapping inside the alteration zone.

4. ANALYSIS OF AVIRIS DATA

According to the findings of field sample analysis the investigations concentrated on the SWIR II module (channels 172-224) of AVIRIS. Unfortunately, this spectrometer was damaged in early June and therefore strongly affected by throughput reduction (GREEN et. al., 1992).

4.1. Data Quality

Data quality assessment was based on visual inspection of all channels and a simple scene dependent approach to determine SNR. Assuming that for a homogeneous target sample

$$\text{SNR} = \text{Average Signal/Standard Deviation}$$

the following average SNR values were estimated:

VIS (Channels 1-32)	50 - 100
NIR (Channels 36-96)	50 - 100
SWIR I (Channels 102-160)	60 - 100
SWIR II (Channels 172-224)	<1 - 12

The data of the first three modules could be used without any constraints. In the SWIR II region only channels 185 to 215 (2060 nm - 2360 nm) were considered usable, although with limitations.

4.2. Data Processing and Analysis

Data processing and analysis were performed using LOWTRAN7, the SIPS software package (CSES/CIRES 1992) and the AGF SPEX spectral analysis tool, both developed under IDL.

For calibration to apparent reflectance, the LOWTRAN7 code as well as the empirical line method were used. Due to the lack of reliable in-flight field spectral measurements and the availability of consistent atmospheric/weather information of the flight day, better results were achieved applying the atmospheric model.

The usable SWIR II channels (185-215) were spatially and spectrally filtered. In a first step spikes were set to the average value of the surrounding pixels. Spatial noise was smoothed applying a low pass filter, in the spectral domain fft filtering was applied.

From this data set reference spectra for known sample points were extracted and interactively compared to the field sample spectra using SPEX. Two AVIRIS and four field sample spectra were selected as "endmembers" representing abundances of "altered material", "phyllosilicates" and "amorphous silica". The Spectral Angle Mapper provided with SIPS was used to determine pixels with high spectral similarity to these "endmembers". The quality of fit is currently being analysed by merging the SAM images with detailed geological/petrographical maps (1 : 25000) in a GIS.

5. CONCLUSIONS

- Even though affected by severe radiometric defects, the 1991 AVIRIS SWIR II channels seem to bear information about absorption features of alteration minerals.
- Mixture modelling including SWIR II channels will probably be hindered due to noise constraints.
- Full use of spectral information will be taken by merging it with other spatial data sets such as geological and structural maps in a GIS system.

6. REFERENCES

ARNORSON S., CUFF K.E., IVARSSON G. & SAEMUNDSSON K., 1987:

Geothermal Activity in the Torfajökull Field, South Iceland: Summary of Geochemical Studies. Jökull 37. pp 1-10, Reykjavik.

GREEN R.O., CONEL J.E., BRUEGGE C.J., MARGOLIS J.S., CARRERE V., VANE G. & HOOVER G., 1992: In-flight Calibration of the Spectral and Radiometric Characteristics of AVIRIS in 1991. Summaries of the Third Annual JPL Airborne Geoscience Workshop, June 1-5, 1992, Volume 1 AVIRIS Workshop, JPL Publication 92-14, pp 1-4, Pasadena June 1, 1992.

CSES/CIRES, 1992: SIPS Users's Guide. Spectral Image Processing System Version 1.2, September 1992, University of Colorado, Boulder.

ESTIMATION OF CROWN CLOSURE FROM AVIRIS DATA USING REGRESSION ANALYSIS

K. Staenz¹, D.J. Williams², M. Truchon¹, and R. Fritz³

¹Canada Centre for Remote Sensing
588 Booth Street, Ottawa, Ontario, Canada K1A 0Y7

²MacDonald Dettwiler and Associates Ltd.
13800 Commerce Parkway, Richmond, British Columbia, Canada V6V 2J3

³University of Freiburg
Werderring 4, 7800 Freiburg, Germany

1. INTRODUCTION

Crown closure is one of the input parameters used for forest growth and yield modelling. Preliminary work by Staenz et al. (1991) indicates that imaging spectrometer data acquired with sensors such as the Airborne Visible/Infrared Imaging Spectrometer (AVIRIS) have some potential for estimating crown closure on a stand level. The objectives of this paper are (a) to establish a relationship between AVIRIS data and the crown closure derived from aerial photography of a forested test site within the Interior Douglas Fir biogeoclimatic zone in British Columbia, Canada, (b) to investigate the impact of atmospheric effects and the forest background on the correlation between AVIRIS data and crown closure estimates, and (c) to improve this relationship using multiple regression analysis.

2. DATA ACQUISITION

AVIRIS data of the test scene used for this investigation were collected in British Columbia, Canada, on August 14, 1990. Additional information includes aerial photography of 1:25000 scale and British Columbia Ministry of Forests's Geographic Information System (GIS) on a 1:20,000 scale encompassing forest inventory maps and forest attribute information. This flat area mainly covered by douglas fir (*Pseudotsuga mensiesii* var. *latifolia* (Mirb.) Franco) with inclusion of lodgepole pine (*Pinus contorta* Dougl.) and yellow pine (*Pinus ponderosa* Laws.) is situated between the Columbia and Kootenay Rivers. The 30 to 200 year old forest stands were selectively logged several times over the years resulting in a full range of crown closures. The open forested areas are mainly covered by dry grass while the background material for stands with high crown closure consists of a mixture of soil and litter.

3. ANALYSIS SCHEME

Radiometrically calibrated AVIRIS data were corrected for atmospheric effects using in a first step an altitude dependent version of the 5S code (Teillet and Santer, 1991) for a viewing angle dependent removal of the scattering effects and, secondly, the flat field approach for a first order correction of the gaseous transmittance. The combination of these procedures for the removal of atmospheric effects was first successfully demonstrated by Staenz et al. (1991) and is shown in Figure 1 for spectra of different crown closure classes. A total of 159 bands (508.40 - 2357.80 nm) were processed for subsequent analysis after eliminating the strong water vapour absorption bands around 1400 nm and 1900 nm as well as the first few bands predominated by noise patterns and the last ones due to a low signal-to-noise ratio (SNR). Overlapping bands between the spectrometers were also eliminated keeping the bands of the spectrometer with the higher SNR.

Homogeneous forest stands with different crown closures were initially

selected from the forest cover maps using in addition the GIS attribute information characterizing each forest stand (polygon). For this purpose, the forest cover maps were registered to the AVIRIS scene with the nearest neighbour resampling technique resulting in an RMS error of ± 1.50 pixels in the pixel direction and ± 0.95 pixels in the line direction. The percent crown closures of these stands were then checked with black and white aerial photography on 1:25,000 scale and re-adjusted where necessary. Additional samples were selected from the aerial photography and transferred to the AVIRIS scenes to cover the full range of percent crown closure. Spectra as shown in Figure 1 were then extracted for each of the 26 sample sites encompassing between 27 and 199 pixels, and grouped into 10 crown closure classes (0, 10, 20, 30, 40, 50, 70, 80, 90, and 100 percent).

Linear regression analysis was first applied to the radiance and relative reflectance data (atmospherically corrected) to determine their relationship with crown closure at each band. In addition, spectral derivatives (first-order, second order) to reduce the background noise were calculated from atmospherically corrected data and included in the regression analysis as well. In a second attempt, an exhaustive stepwise multiple regression procedure STEPWISE from S-PLUS (1991) was used to find band combinations with significantly higher correlation than with the univariate analysis.

4. RESULTS

Coefficients of determination (R^2) calculated at each spectral band are shown in Figure 2 for the radiance and the relative reflectance (atmospherically corrected) data, as well as the first-order derivative of the relative reflectance spectra. The R^2 values exceed 0.8 in many of the non-derivative spectral bands as shown, for instance, for band 204 (2258.3 nm) in Figure 3. It can also be seen from Figure 2 that the application of the atmospheric correction procedure significantly increased the R^2 values in most of the bands within the 700 to 1350 nm region. The procedure produces in addition slightly higher R^2 values between 500 nm and 580 nm and lower R^2 values between 580 nm and 700 nm. The non-derivative-band R^2 values generally outperform the derivative-band R^2 values considerably except between 750 nm and 860 nm for the radiance data. The high spectral variability in the derivative-based R^2 values is expected since derivatives are sensitive to high frequency noise and spectra with a similar shape produce similar values (zero-crossing points) at specific wavelengths along the derivative curves (Gong et al., 1992). These effects could reduce the correlation between derivative spectra and crown closure.

Stepwise multiple regression analyses of relative reflectance (159 bands) spectra were applied to the entire data set as well as to a reduced set of nine bands (Table 1). These bands were selected based on their known relationships with biomass, chlorophyll, liquid water content, cellulose, etc. It can be seen from Table 1 that the multivariate analysis improves the correlation between the AVIRIS data and crown closure for both data sets. R^2 values larger than 0.9 can be achieved with this procedure as shown graphically in Figure 4 for the best five-band subset of the nine-band data. Furthermore, the prediction of crown closure improves using the entire data set in the analysis procedure. However, the R^2 values should be interpreted with caution since an inflation of R^2 occurs when the predictor variables (159 bands) outnumber the sample size (26) (Wessman et al., 1989). Significance tests at the 0.95 confidence interval for R^2 values obtained with the stepwise multiple regression techniques were therefore based on adjusted values of R^2 (Rechner and Pun, 1980).

The correlation achieved with the regression procedures could be affected by noise in the data caused by the sensor system and the atmospheric correction procedure. However, the robustness of the regression results with respect to noise is not known, but will be considered for future analysis.

5. CONCLUSION

Univariate as well as multivariate regression analyses were applied to an AVIRIS data set acquired over a forested test site in British Columbia, Canada to investigate the relationships between crown closure and the AVIRIS data. Values of R^2 larger than 0.8 were achieved in many spectral bands for the atmospherically corrected data. Results for the original (radiance) data were similar except within the 700 nm to 1350 nm wavelength region. In addition, the non-derivative-band R^2 values clearly outperformed the derivative-band R^2 values. A stepwise multiple regression technique was applied to the entire data set (159 bands) and to a reduced set of nine bands known to be linked with physical parameters. R^2 values improved to over 0.9 in both cases. The best subset extracted from the nine-band data includes bands 12(508.4 nm), 17(557.4 nm), 43(776.6 nm), 64(978.2 nm), and 138(1648.5 nm).

6. ACKNOWLEDGEMENT

The authors wish to thank NASA and the Inventory Branch of the British Columbia Ministry of Forests for their support of the AVIRIS data acquisition and A. Kalil for wordprocessing the manuscript.

7. REFERENCES

- Gong, P., R. Pu, and J.R. Miller, 1992, "Correlating Leaf Area Index of Ponderosa Pine with Hyperspectral CASI Data", Canadian Journal of Remote Sensing, Vol.18, No.4, pp.275-282.
- Rechner, A.C., and F.L. Pun, 1980, "Inflation of R^2 in Best Subset Regression", Technometrics, Vol.22, pp.49-53.
- S-PLUS, 1991, "S-PLUS Reference Manual", Version 3.0, Statistical Sciences, Inc., Seattle, Washington, U.S.A.
- Stanz, K., D. Schanzer, and C. Kushigbor, 1991, "Classification of Forest Stands in British Columbia Using AVIRIS Data: A Preliminary Investigation", Proceedings of the Third Airborne Visible/Infrared Imaging Spectrometer (AVIRIS) Workshop, JPL Publication 91-28, Pasadena, California, pp.173-182.
- Teillet, P.M. and R. Santer, 1991, "Terrain Elevation and Sensor Altitude Dependence in a Semi-Analytical Atmospheric Code", Canadian Journal of Remote Sensing, Vol.17, No.1, pp.36-44.
- Wessman, L.A., J.D. Aber, and D.L. Peterson, 1989, "An Evaluation of Imaging Spectrometry for Estimating Forest Canopy Chemistry", International Journal of Remote Sensing, Vol.10, No.8, pp.1293-1316.

Table 1: Multi-band analysis of the relative reflectance data using the stepwise multiple regression technique. The band combinations were selected from (A) 159 bands (entire data set) and (B) 9 bands (12(508.4 nm), 17(557.4), 29(675.1), 43(776.6), 52(863.0), 64(978.2), 87(1199.0), 138(1648.5), and 196(2198.7)).			
Bandset (# of bands)	Band Subsets (Wavelength in nm)	Coefficient of Determination (R^2)	Standard Error of Percent Crown Closure
A (1)	204(2258.3)	0.852*	13.869
(2)	84(1170.2), 93(1256.6)	0.913*	10.840
(3)	55(891.8), 58(920.6), 213(2347.8)	0.938*	9.361
(4)	52(863.0), 68(1016.6), 90(1227.8), 179(2009.7)	0.962*	7.501
(5)	52(863.0), 68(1016.6), 84(1170.2), 149(1757.3), 190(2119.1)	0.976*	6.069
B (1)	198(2198.7)	0.840*	14.408
(2)	52(863.0), 198(2198.7)	0.862*	13.670
(3)	52(863.0), 87(1199.0), 138(1648.5)	0.886*	12.708
(4)	17(557.4), 52(863.0), 87(1199.0), 138(1648.5)	0.891*	12.761
(5)	12(508.4), 17(557.4), 43(776.6), 64(978.2), 138(1648.5)	0.903*	12.294

* passed significance test at 0.95 confidence level.

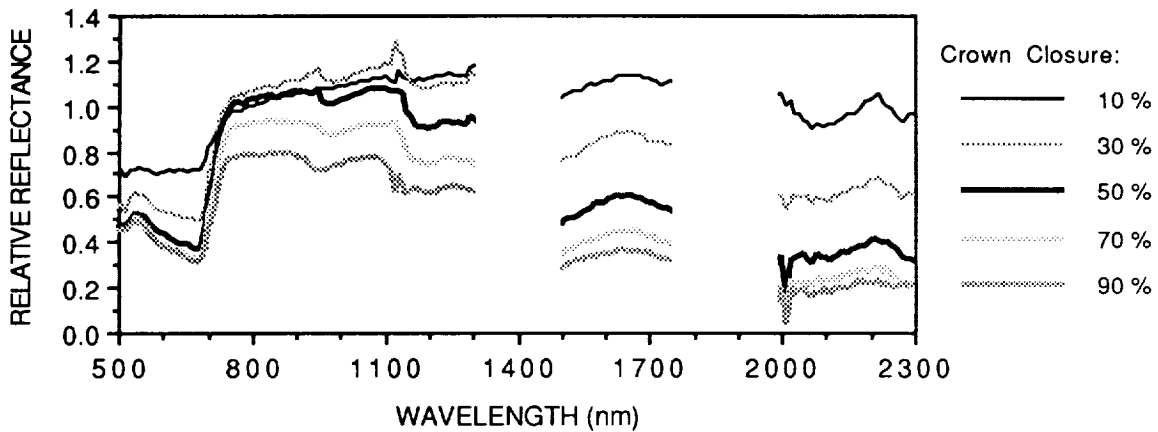


Figure 1: Relative reflectance spectra of different crown closure classes.

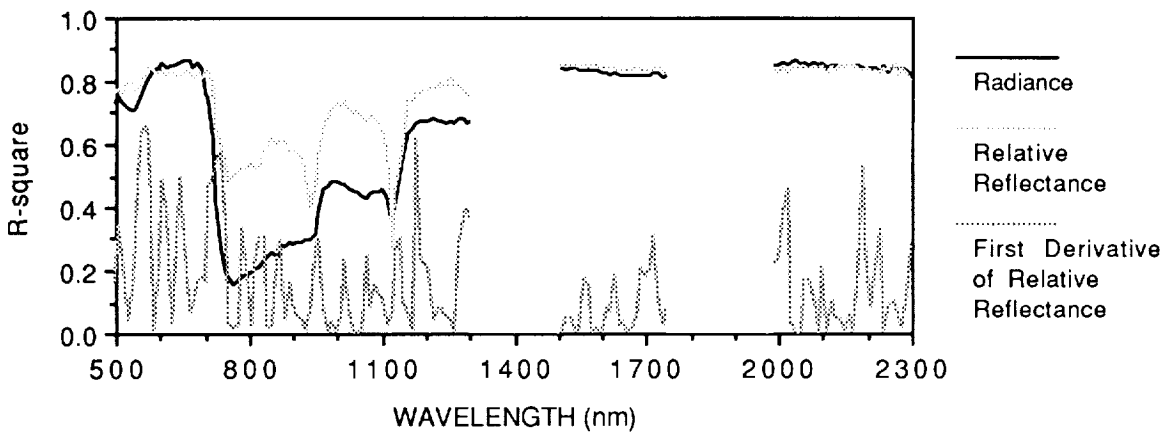


Figure 2: Correlation between percent crown closure and radiance, relative reflectance, and first-order derivative of the relative reflectance data.

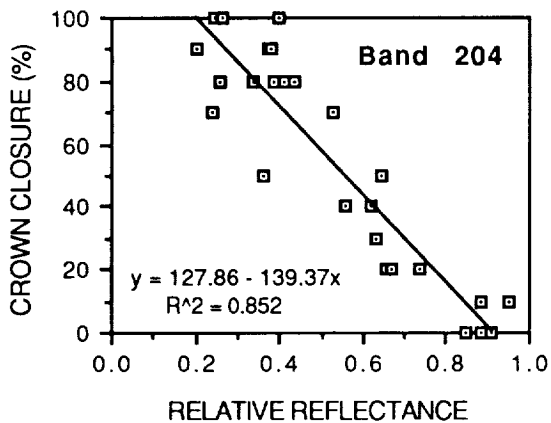


Figure 3: Crown closure as a function of the relative reflectance (atmospherically corrected data) for band 204 (2258.3 nm).

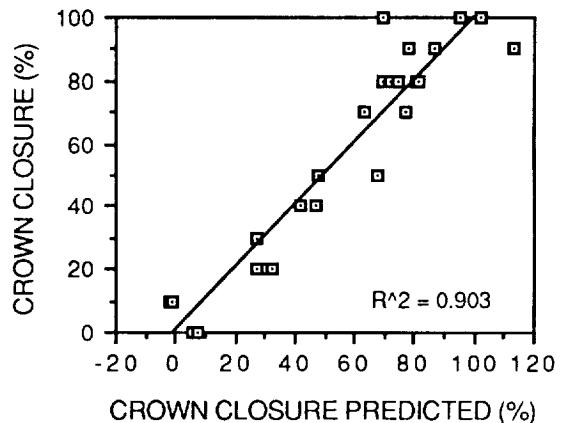


Figure 4: Prediction of crown closure derived with the stepwise multiple regression technique involving bands 12(508.4 nm), 17(557.4 nm), 43(776.6 nm), 64(978.2 nm), and 138(1648.5 nm).

243 93

41043

2 1

OPTIMAL BAND SELECTION FOR DIMENSIONALITY REDUCTION OF HYPERSPPECTRAL IMAGERY

Stephen D. Stearns, Bruce E. Wilson and James R. Peterson

ESL Incorporated, a subsidiary of TRW
P.O. Box 3510
Sunnyvale, CA 94088-3510
steve_stearns@smt.esl.com

1. INTRODUCTION

Hyperspectral images have many bands requiring significant computational power for machine interpretation. During image pre-processing, regions of interest that warrant full examination need to be identified quickly. One technique for speeding up the processing is to use only a small subset of bands to determine the "interesting" regions. The problem addressed here is how to determine the fewest bands required to achieve a specified performance goal for pixel classification. The band selection problem has been addressed previously by Chen et al. (1987, 1988, 1989), Ghassemian et al. (1988), Henderson et al. (1989), and Kim et al. (1990).

Some popular techniques for reducing the dimensionality of a feature space, such as principal components analysis, reduce dimensionality by computing new features that are linear combinations of the original features. However, such approaches require measuring and processing all the available bands before the dimensionality is reduced. Our approach, adapted from previous multidimensional signal analysis research, is simpler and achieves dimensionality reduction by selecting bands. Feature selection algorithms are used to determine which combination of bands has the lowest probability of pixel misclassification. Two elements required by this approach are a choice of objective function and a choice of search strategy.

2. OBJECTIVE FUNCTIONS

A variety of objective functions have been proposed for feature selection optimization, including the Shannon equivocation $H(\Omega | X)$, the Shannon mutual information $I(\Omega; X)$ that the feature vector X gives about the class Ω , the Bhattacharyya distance $B(\Omega, X)$, and the divergence $J(\Omega, X)$. The latter two quantities are defined for classes taken in pairs.

The two-class Bayes error probability P_e^* is bounded above and below in terms of these quantities.

$$P_e^* \leq \frac{1}{2} H(\Omega | X) \leq \frac{1}{2} \log M - \frac{1}{2} I(\Omega; X) \leq \frac{1}{2} \exp(-B),$$

$$\frac{1}{4} \exp(-J/2) \leq \frac{1}{4} \exp(-2B) \leq \frac{1}{2} (1 - \sqrt{1 - \exp(-2B)}) \leq P_e^*.$$

The M-class Bayes error probability is upper bounded by a weighted sum of the two-class Bayes error probabilities between all pairs of classes.

3. FEATURE SELECTION PARADOXES AND ALGORITHMS

The theory of feature selection is a history of the discovery of paradoxes and of increasingly sophisticated algorithms designed to overcome these paradoxes (Cover, 1974; Cover et al., 1977; Narendra et al, 1977).

The (m, n) feature selection algorithm was developed as a means to handle a large number of candidate features (Stearns, 1976). This technique avoids having to evaluate all possible combinations of 200 or more features. It is resistant to the feature selection paradoxes, although not immune. At present, it is one of the most powerful and practical methods for selecting near-optimal subsets of features from a large set of candidates, e.g. automatic selection of hyperspectral bands.

Recently, a variant of the (m, n) feature selection algorithm, called the Greedy (m, n) algorithm, was applied to the problem of determining minimal band sets for hyperspectral imagery. Experimental results are summarized here. A companion paper provides theoretical discussion (Stearns et al., 1993).

4. EXPERIMENTAL RESULTS

An experiment was performed to compare three algorithms for automatically selecting subsets of bands for pixel classification. The three algorithms compared were the Best Individual Features algorithm, the Forward Sequential or (1, 0) algorithm, and the Greedy (2, 1) algorithm. The data for the experiment was a 224-band AVIRIS scene of the southern San Francisco peninsula. Regions of the scene were selected and used to form a library of 224-element feature vectors for the six classes: open water, evaporation ponds, marsh, green grass, brown grasslands, and urban. Portions of the scene not belonging to these six classes were not used.

The objective function used by the three feature selection algorithms was the minimum Bhattacharyya distance between any two of the six classes. The minimum Bhattacharyya distances were converted to upper bounds on the Bayes error probability according to

$$P_e^* \leq \frac{1}{M} \sum_{i > k} \exp(-B_{i,k}) \leq \frac{M-1}{2} \exp(-\min(B_{i,k})).$$

The three feature selection algorithms determined sets of one through nine bands. The results are shown in Tables 1 - 3. The Best Individual Features algorithm did poorly. This algorithm does not consider feature interactions. Consequently, the bands selected by this algorithm are grouped around the best individual band, 139. Each additional band

Table 1. Bands Selected by the Best Individual Features Algorithm.

Number of Bands	Bands	Upper Bound on P_e^*
1	139	0.688
2	137, 139	0.623
3	137, 138, 139	0.598
4	137, 138, 139, 140	0.575
5	137, 138, 139, 140, 143	0.558
6	136, 137, 138, 139, 140, 143	0.452
7	136, 137, 138, 139, 140, 141, 143	0.417
8	136, 137, 138, 139, 140, 141, 143, 144	0.405
9	136, 137, 138, 139, 140, 141, 142, 143, 144	0.393

conveys little or no new information over that provided by the bands selected already. The class separability does not increase much as the number of bands increases.

The Greedy (2, 1) algorithm produces identical subsets of bands as the Forward Sequential algorithm for the first eight sets, but the search paths start to diverge at nine bands. The Greedy (2, 1) algorithm is expected to yield a superior band set for subset sizes greater than nine.

Table 2. Bands Selected by the Forward Sequential (1, 0) Algorithm.

Number of Bands	Bands	Upper Bound on P_e^*
1	139	0.688
2	120, 139	3.86×10^{-2}
3	33, 120, 139	1.43×10^{-2}
4	33, 120, 139, 154	5.74×10^{-4}
5	33, 120, 139, 154, 174	2.07×10^{-4}
6	33, 108, 120, 139, 154, 174	2.72×10^{-5}
7	33, 108, 120, 139, 154, 174, 217	6.90×10^{-6}
8	25, 33, 108, 120, 139, 154, 174, 217	7.20×10^{-7}
9	25, 33, 40, 108, 120, 139, 154, 174, 217	3.95×10^{-7}

Table 3. Bands Selected by the Greedy (2, 1) Algorithm.

Number of Bands	Bands	Upper Bound on P_e^*
1	139	0.688
2	120, 139	3.86×10^{-2}
3	33, 120, 139	1.43×10^{-2}
4	33, 120, 139, 154	5.74×10^{-4}
5	33, 120, 139, 154, 174	2.07×10^{-4}
6	33, 108, 120, 139, 154, 174	2.72×10^{-5}
7	33, 108, 120, 139, 154, 174, 217	6.90×10^{-6}
8	25, 33, 108, 120, 139, 154, 174, 217	7.20×10^{-7}
9	33, 40, 77, 108, 120, 139, 154, 174, 217	3.20×10^{-7}

5. SUMMARY AND CONCLUSIONS

Band selection has been shown here and elsewhere to be a practical method of data reduction for hyperspectral image data. Moreover, band selection has a number of advantages over linear band combining for reducing the dimensionality of high-dimensional data. Band selection eliminates the requirement that all bands be measured before data dimensionality is reduced. Bands that are uninformative about pixel classification need not be measured or communicated. Band sets can be tailored to specific classification goals (classes, error rates, etc.). Band selection reduces data link requirements, yet retains a tunable capability to collect as many bands as required for a specific application. Feature selection algorithms developed for statistical pattern classifier design can be used to perform band selection. The Greedy (2, 1) feature selection algorithm has been shown to be a practical means of selecting bands. In

addition this algorithm has theoretical advantages over the Forward Sequential algorithm, making it the method of choice for hyperspectral applications.

6. ACKNOWLEDGEMENTS

The authors wish to thank David A. Landgrebe and Carl Salvaggio for helpful discussions that contributed to this paper.

7. REFERENCES

- Cover T.M., 1974, "The best two independent measurements are not the two best," *IEEE Trans. Syst., Man, and Cybernetics*, (correspondence), vol. SMC-4, no. 1, pp. 116-117.
- Cover T.M. and J.M. van Campenhout, 1977, "On the possible orderings in the measurement selection problem," *IEEE Trans. Syst., Man, and Cybernetics*, vol. SMC-7, no. 9., pp. 657-661.
- Chen C.-C.T. and D.A. Landgrebe, 1987, "Spectral feature design for data compression in high dimensional multispectral data," *Proc. IEEE Int'l Geoscience and Remote Sensing Symp. (IGARSS'87)*, Ann Arbor, MI, pp. 685-690.
- Chen C.-C.T. and D.A. Landgrebe, 1988, *Spectral feature design in high dimensional multispectral data*, Ph.D. thesis and Tech. Rep. TR-EE 88-35, School of Electrical Engineering, Purdue University, West Lafayette, IN, 140 pp.
- Chen C.-C.T. and D.A. Landgrebe, 1988, "A spectral feature design system for high dimensional multispectral data," *Proc. IEEE Int'l Geoscience and Remote Sensing Symp. (IGARSS'88)*, Edinburgh, Scotland, pp. 891-894.
- Chen C.-C.T. and D.A. Landgrebe, 1989, "A spectral feature design system for the HIRIS/MODIS era," *IEEE Trans. Geoscience and Remote Sensing*, vol. 27, no. 6, pp. 681-686.
- Ghassemian H. and D.A. Landgrebe, 1988, "An unsupervised feature extraction method for high dimensional image data compaction," *Proc. IEEE Int'l Conf. on Syst., Man, and Cybernetics*, George Mason Univ., Alexandria, VA, October 20-23, 1987, pp. 540-544, also appeared in *IEEE Control Systems Magazine*, vol. 8, no. 3, pp. 42-48.
- Henderson T.L., A. Szilagyi, M.F. Baumgardner, C.-C.T. Chen, and D. Landgrebe, 1989, "Spectral band selection for classification of soil organic matter content," *J. Soil Science Society of America*, vol. 53, no. 6, pp. 1778-1784.
- Kim B. and D.A. Landgrebe, 1990, "Prediction of optimal number of features," *Proc. IEEE Int'l Geoscience and Remote Sensing Symp., (IGARSS'90)*, Washington, D.C., pp. 2393-2396.
- Narendra P.M. and K. Fukunaga, 1977, "A branch and bound algorithm for feature subset selection," *IEEE Trans. Computers*, vol. C-26, no. 9, pp. 917-922.
- Stearns, S.D., 1976, "On selecting features for pattern classifiers," *Proc. Third Int'l Joint Conf. on Pattern Recognition*, pp. 71-75.
- Stearns, S.D., B.E. Wilson, and J.R. Peterson, 1993, "Dimensionality reduction by optimal band selection for pixel classification of hyperspectral imagery," *Proc. SPIE 38th Int'l Symp. on Optical Applied Science and Engineering*, San Diego.

45
11044
1

OBJECTIVE DETERMINATION OF IMAGE END-MEMBERS IN SPECTRAL MIXTURE ANALYSIS OF AVIRIS DATA

Stefanie Tompkins, John F. Mustard, Carle M. Pieters, Donald W. Forsyth
Dept. Geol. Sci., Box 1846, Brown University, Providence, RI 02912

INTRODUCTION

Spectral mixture analysis has been shown to be a powerful, multifaceted tool for analysis of multi- and hyper-spectral data (Adams et al., 1986; Smith et al., 1990). Applications to AVIRIS data have ranged from mapping soils and bedrock to ecosystem studies (e.g. Gamon et al., 1993; Roberts et al., 1993; Mustard et al., 1993; Kruse et al., 1993). During the first phase of the approach, a set of end-members are selected from an image cube (image end-members) that best account for its spectral variance within a constrained, linear least squares mixing model. These image end-members are usually selected using *a priori* knowledge and successive trial and error solutions to refine the total number and physical location of the end-members. However, in many situations a more objective method of determining these essential components is desired. We approach the problem of image end-member determination objectively by using the inherent variance of the data. Unlike purely statistical methods such as factor analysis, this approach derives solutions that conform to a physically realistic model.

DAMPED LEAST SQUARES MODEL

The underlying assumption of spectral mixture analysis is that each pixel on the surface is a physical mixture of several components, and the spectrum of the mixture is a linear combination of the end-member reflectance spectra. The spectral variability of a scene is thus modeled as a linear combination of a small number of image end-members. The fundamental equations of spectral mixture analysis are:

$$\sum_b R_b = \sum_b \sum_i r_{ib} f_i + \sum_b E_b \quad (1) \quad \text{and} \quad \sum_i f_i = 1.0 \quad (2)$$

where f_i is the fractional abundance of end-member i in the pixel, R_b is the total reflectance of the pixel in band b , r_{ib} is the reflectance of end-member i in band b , and E_b is the residual error in band b . In a typical spectral mixing analysis, the end-members are prescribed and the fractional abundances and errors are then calculated for each pixel, through a simple least squares inversion of the form:

$$\underline{m} = (\underline{G}^T \underline{G})^{-1} \underline{G}^T \underline{d} \quad (3)$$

The matrix \underline{G} consists of the partial derivatives of the model equations given by (1) and (2). The vectors \underline{d} and \underline{m} represent the data (R_b) and the model parameters (f_i) respectively. A two-dimensional graphical representation of mixture analysis is shown in Figure 1. The image end-members (indicated by squares) should reside as close as possible to the boundaries of the data cloud. Fractions that are >1.0 or <0.0 occur for data points that lie outside the region defined by the end-members, and cannot be entirely eliminated no matter how well chosen the image end-members.

Consider, instead, an approach where the end-member spectra are not prescribed, but are treated as unknowns along with the fractional abundances. The model equations are the same as stated above, but because F_i and r_{ib} are both unknowns, they must be

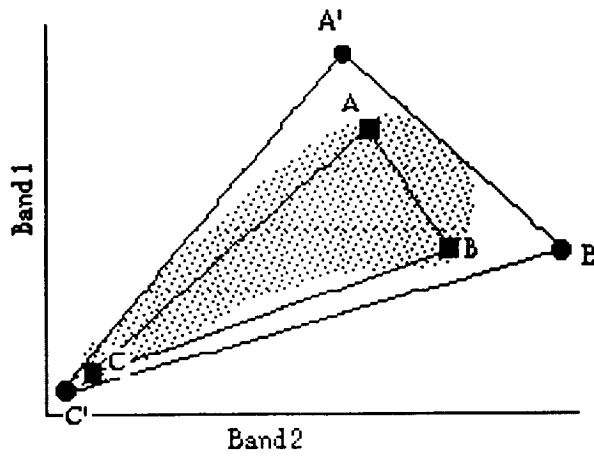


Figure 1: A, B, and C indicate image end-members. A', B', and C' are the model-derived end-members.

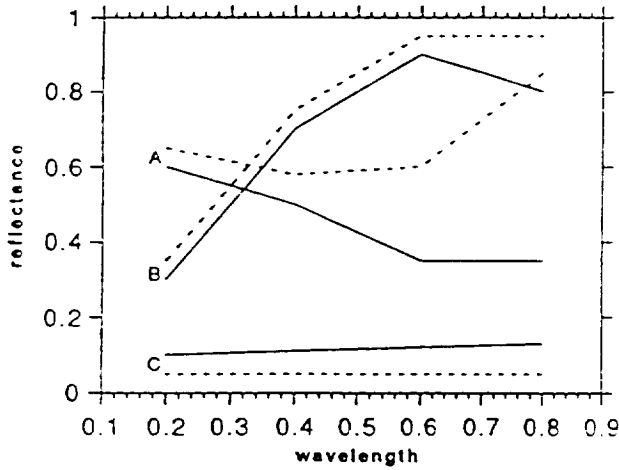


Figure 2: Solid lines represent image end-member spectra. Dashed lines are model-derived virtual end-members.

solved non-linearly. The approach we have chosen employs a damped least squares non-linear inversion technique as presented by Tarantola and Valette (1982). In short, a starting model is provided (a suite of possible end-member spectra, estimated fractional abundances, and the image data to be modeled). Constraints on the solutions are imposed as additional equations (i.e. fractions must sum to 1.0) or as allowable deviations from the starting model (damping of solutions). Both the starting model and the constraints are based on *a priori* knowledge. Each successive iteration of the equations results in a calculated change to the previous model that will reduce the error of the fit. These changes are incorporated and the inversion is run successively until a prescribed error threshold is surpassed, as given by:

$$\underline{m}_{j+1} = \underline{m}_j + \left[\underline{G}_j^T \underline{C}_{nn}^{-1} \underline{G}_j + \underline{C}_{mm}^{-1} \right]^{-1} \left[\underline{G}_j^T \underline{C}_{nn}^{-1} (\underline{d} - \underline{g}(\underline{m}_j)) - \underline{C}_{mm}^{-1} (\underline{m}_j - \underline{m}_0) \right] \quad (4)$$

In this case, the model parameters and G-matrix change with each iteration (\underline{m}_j is the model parameter vector at the j th iteration) and include both f_j and r_{ib} from equations (1) and (2). \underline{C}_{nn} and \underline{C}_{mm} are covariance matrices for the data and the model parameters, respectively. The term $\underline{g}(\underline{m}_j)$ is the predicted value of the data vector when the forward

model is run, so $(\underline{d} - g(\underline{m}_j))$ simply describe the residual error. The starting model parameters, found in \underline{m}_0 , are included at each iteration to penalize large deviations from the starting model and thus damp the final solution.

The model results are therefore intimately guided by the inherent spectral variability of the data, the starting model, and the constraints imposed on the solutions. The calculated end-member spectra are driven to better bound the data cloud. This is shown in Figure 1 (new end-members indicated by circles). The effects in a spectral sense are illustrated conceptually in Figure 2 (initial end-member spectra are shown by solid lines and calculated end-members by dashed lines). Although the new end-member spectra are not necessarily identical to any pixel spectrum (they can lie outside the data cloud), they provide the best mathematical fit to the whole data set and are determined using a model which is based on a physically realistic description of the surface. One might think of these as *virtual end-members*.

PRELIMINARY RESULTS

Artificial Data Set

This model was developed and refined on a test data set where the end-members and their abundances are known perfectly. This data set provides a working template for establishing the necessary conditions under which the best solution can be derived. The model successfully reproduces the true end-member spectra in the test data sets for a variety of initial conditions, provided that the model is minimally constrained. An additional step in spectral mixture analysis is determining the optimum number of end-members. Using the test data set, model solutions for fewer than and greater than the correct number of spectral end-members were analyzed. When too few end-members were used, the solution failed to meet the original constraints on the model. The residual error steadily declined as the number of end-members increased until the optimum number was reached; thereafter, the improvement in error was statistically insignificant. Thus, the evolution of error and successful satisfaction of model constraints as a function of the number of end-members can be used to threshold the optimum solution. We continue to use the artificial data sets to develop a better understanding of the model, and establish limits on the amount of *a priori* information that is needed to calculate the true end-member spectra.

Lunar CCD Images

The model has also been applied to 8-band CCD images of the lunar crater Bullialdus (Tompkins et al., 1992). This required some restructuring of the program due to the increased number of spectral channels and pixels; however, the model is the same. The starting model is guided by previous investigations (Tompkins et al., 1992; Pieters, 1991). Initial results on small data sets within the image show generally the same results as were obtained with the traditional mixing approach, but provide a much lower rms error and only very rare occurrences of superpositive (>100%) or negative abundances. In mixing models, the best image end-members can be considered those that best describe the data cloud (Figure 1), for all bands simultaneously. As was found with the test data, the nonlinear inversion defines virtual end-members that are outside the data cloud, while still providing a physically reasonable solution.

AVIRIS Data

The model is now applied to an AVIRIS image from the western foothills of the Sierra Nevada. Materials found within the data include dry, grass-covered hills, irrigated

orchards, and a complex substrate with rapidly changing bedrock composition (Mustard, 1993). Because the memory requirements for the model increase multiplicatively with the number of pixels and spectral channels in a data set, the initial application will be to a subset of the image, using a limited number of channels. The fraction images that result from using virtual end-members will be compared to those derived through the traditional mixing model.

One of the strengths of spectral mixture analysis is the ability to calibrate raw data to reflectance by linking the image end-members to reference end-members from a spectral library. This can be especially advantageous when using data from systems with poorly defined characteristics or areas lacking well characterized reference end-members. Though this can lead to non-unique solutions for the reference end-members, common sense and geologic context help govern the choice of library end-members to which the image end-members are calibrated. The data inversion approach presented here may confer a distinct advantage for proceeding to the calibration stage. The virtual end-members are thought to be more spectrally pure than the image end-members, thereby reducing the number of non-unique solutions. Future work will involve testing this type of calibration using the AVIRIS images, as well as further constraining the mixture model.

REFERENCES

- Adams, J.B., M.O. Smith, and P.E. Johnson, 1986, "Spectral mixture modeling: a new analysis of rock and soil types at Viking Lander 1," *J. Geophysical Research*, vol. 91, pp. 8113-8125.
- Gamon, J., C.B. Field, D.A. Roberts, S.L. Ustin, and R. Valentini, 1993, "Functional Patterns in an Annual Grassland during an AVIRIS Overflight," *Rem. Sens. Env.*, vol. 44, pp. 239-253.
- Kruse, F.A., A.B. Lekhoff, and J.B. Dietz, 1993, "Expert System-Based Mineral Mapping in Northern Death Valley, California/Nevada, Using the Airborne Visible/Infrared Imaging Spectrometer (AVIRIS)," *Rem. Sens. Env.*, vol. 44, pp. 309-335.
- Mustard, J.F., 1993, "Relationships of Soil, Grass, and Bedrock Over the Kaweah Serpentine Melange through Spectral Mixture Analysis of AVIRIS Data," *Rem. Sens. Env.*, vol. 44, pp. 293-308.
- Pieters, C.M., 1991, "Bullialdus: Strengthening the case for lunar plutons," *Geophys. Res. Lett.*, vol. 18, pp. 2129-2132.
- Roberts, D.A., M.O. Smith, and J.B. Adams, 1993, "Green Vegetation, Non photosynthetic Vegetation, and Soils in AVIRIS Data," *Rem. Sens. Env.*, vol. 44, pp. 254-269.
- Smith, M.O., S.L. Ustin, J.B. Adams, and A.R. Gillespie, 1990, "Vegetation in deserts: I. A regional measure of abundance from multispectral images," *Remote Sensing of Environment*, vol. 31, pp. 1-26.
- Tarantola and Valette, 1982, "Generalized nonlinear inverse problems solved using the least squares criterion," *Rev. Geophys. Space. Phys.*, vol. 20, pp. 219-232.
- Tompkins, S., C.M. Pieters, J.F. Mustard, and P. Pinet, 1992, "Distribution of the materials around the lunar crater Bullialdus: A spectral mixing analysis" (abstract), *Lunar Planet. Sci. XXIII*, pp. 1435-1436.
- Tompkins, S.T., J.F. Mustard, C.M. Pieters, and D.W. Forsyth, 1993, "Objective determination of image end-members in spectral mixture analysis" (abstract), *Lunar Planet. Sci. XXIV*, pp. 1431-1432.

2/5/93
41045
7-4

Relationships Between Pigment Composition Variation and Reflectance for Plant Species from a Coastal Savannah in California

by

**Susan L. Ustin, Eric W. Sanderson, Yaffa Grossman, Quinn J. Hart,
and Robert S. Haxo**

Department of Land, Air, and Water Resources
University of California, Davis, CA 95616

Introduction

Advances in imaging spectroscopy have indicated that remotely sensed reflectance measurements of the plant canopy may be used to identify and quantify some classes of canopy biochemicals (Wessman et al, 1988a); however the manner in which differences in biochemical compositions translate into differences in reflectance measurements is not well understood. Most frequently, multiple linear regression routines have been used to correlate narrow band reflectance values with measured biochemical concentrations (e.g., see Wessman et al, 1988b, Card et al, 1988). Although some success has been achieved with such methods for given data sets, the bands selected by multiple regression are not consistent between data sets, nor is it always clear what physical or biological basis underlies the correlation (Curran, 1989).

To examine the relationship between biochemical concentration and leaf reflectance signal we chose to focus on the visible spectrum where the primary biochemical absorbances are due to photosynthetic pigments. Pigments provide a range of absorbance features, occur over a range of concentrations in natural samples, and are ecophysiologicaly important. Concentrations of chlorophyll, for example, have been strongly correlated to foliar nitrogen levels within a species (Evans, 1989) and to photosynthetic capacity across many species (Field and Mooney, 1986). In addition, pigments effectively absorb most of the photosynthetically active radiation between 400-700 nm, a spectral region for which silicon detectors have good signal/noise characteristics. Our strategy has been to sample a variety of naturally occurring species to measure leaf reflectance and pigment compositions. We hope to extend our understanding of pigment reflectance effects to interpret small overlapping absorbances of other biochemicals in the infrared region. For this reason, selected samples were also tested to determine total nitrogen, crude protein, cellulose and lignin levels. Leaf reflectance spectra measured with AVIRIS bandwidths and wavelengths were compared between species and within species and for differences between seasons, for changes in the shape of the spectra. We attempted to statistically correlate these shape changes with differences in pigment composition.

In parallel with our comparisons of pigment composition and leaf reflectance, we have modified the PROSPECT leaf reflectance model to test the contributions of pigments or pigment group concentrations (Jacquemoud and Baret, 1990, Jacquemoud, 1993). PROSPECT considers a leaf as a multi-layer dielectric plane with an uneven surface. Jacquemoud adapted the basic analysis of Allen (1973, 1968) for surface effects, a leaf thickness factor, and the absorption of water and chlorophyll (actually all pigments) and the plant matrix. Our modifications to PROSPECT in the forward direction include

breaking out the pigment concentration parameter into separate components for chlorophyll a and b and a number of xanthophylls and carotenes, and introducing a shift and convolution function to model the spread and shift from their *in vitro* measurements to their *in vivo* state. Further we have considered how the matrix elements (i.e., all biochemicals and structural effects not modeled explicitly) vary with species.

Currently we are inverting PROSPECT using our modifications to process measured leaf reflectance spectra from a wide variety of non-cultivated plant species for which pigment compositions and water contents are known. PROSPECT in the backward direction was embedded in an optimization routine which estimates concentration shift and spread parameters for each pigment based on measured spectra. The means by which PROSPECT might be scaled up to canopy level measurements like AVIRIS will be discussed.

Materials and Methods

Leaf samples were collected from approximately fourteen species representing different ecological groupings commonly found in plant communities of the Central Coast Range of California to provide a wide range of reflectance and biochemical variation, including photosynthetic pigments and other important biochemicals. The individual plants were identified and resampled repetitively in different seasons over the course of one year. Reflectance and transmittance spectra of ten excised leaves for each sample were measured either with NIRS or Varian CARY 5E spectrometers between 400-2500 nm using bandwidths similar to AVIRIS.

Concurrently obtained bulk leaf samples were analysed in the laboratory for their pigment compositions (chlorophyll a and b, phaeophytin a and b, chlorophyllide, β -carotene, cis- β -carotene, lutein, neoxanthin, zeaxanthin, violaxanthin, and antheraxanthin) by HPLC (Wright et al, 1991). Specific leaf absorption curves were determined for each of the pigments from the HPLC diode array detector. Some samples were also analysed for crude protein (Pierce, 1993), total nitrogen, hydrolyzed cellulose and non-acid hydrolyzable lignin contents (Effland, 1977). Both the bulk (biochemistry) samples and the leaf disks were assumed to be representative of the same population of leaves from a given plant sample.

Discussion

Statistical comparisons (F test) of the reflectance spectra of the excised leaves and the first derivatives of the reflectance spectra show significant (98% confidence level above thin bar on figure) differences between the green foliage of different species, even species of the same genus. For example, *Quercus agrifolia* (Live Oak) and *Quercus lobata* (Valley Oak) (Figure 1). Differences in the visible region were detected in the derivative spectra indicating that pigment compositions has greater effect on spectral shape than albedo effects. Concomitant changes in pigment concentration were also detected (Figure 2). Parallel comparisons of the biochemical and leaf reflectance were made for the species and seasonal effects. The deciduous and evergreen oaks shown here are more similar than many other comparisons. The ranges of pigment concentration found across the sample

species are listed in Table 1. Similar statistical differences in spectral features in the SWIR region were found.

Figure 1: Leaf reflectance spectra for *Quercus lobata* (Valley Oak) and *Quercus agrifolia* (Live Oak) and values of F test of significance for comparisons of first derivative spectra.

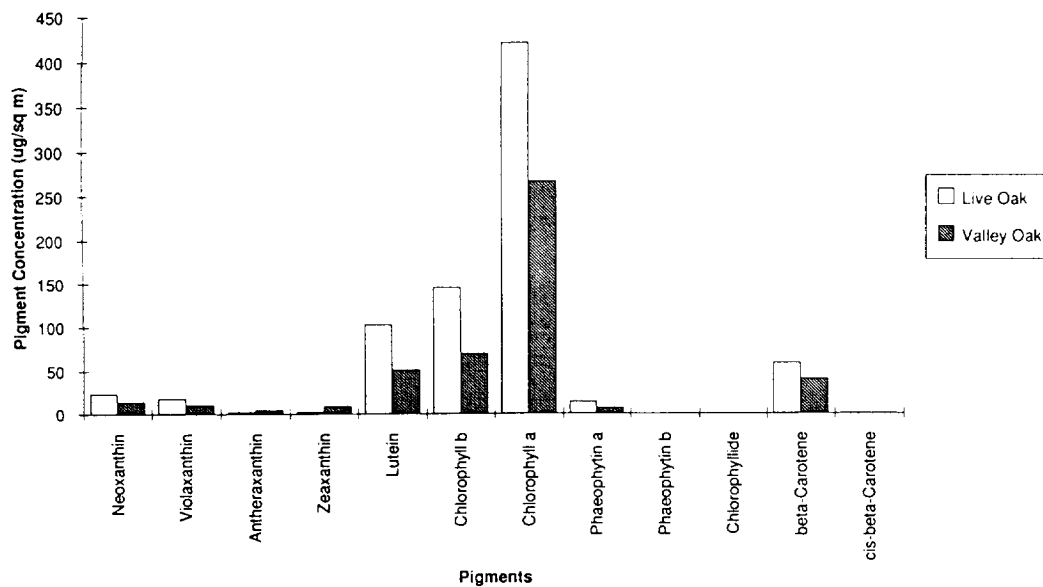
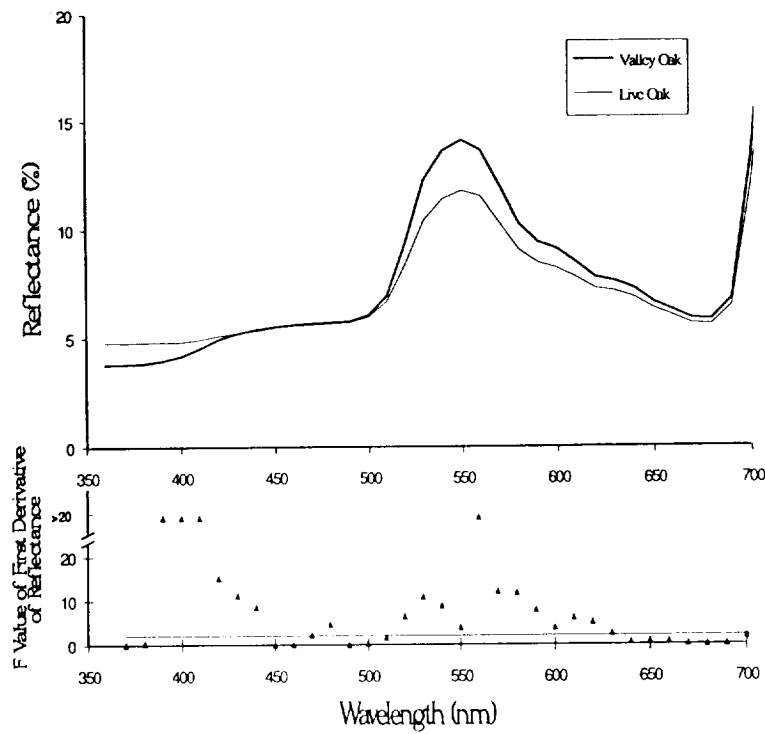


Figure 2. Pigment composition and concentration for mature leaves of *Quercus lobata* (Valley Oak) and *Quercus agrifolia* (live oak).

We adapted the PROSPECT leaf reflectance model to accept the coefficients of multiple pigments and have evaluated the contribution of each pigment to the spectrum using specific absorbance curves developed from our study. We are interested in how different reflectances/biochemistries are expressed between communities and whether ranges within a species are greater than ranges between similarly adapted species. Species differences

in biochemistry and reflectance appear to vary by ecological categories (e.g., community type or guild) and by season more than within species differences at a single point in time. The former differences result from evolutionary convergences of form and functional traits. The latter differences result from ecophysiological adjustments made in the foliage with regard to season and environmental conditions.

Table 1. Concentration Ranges ($\mu\text{mol}/\text{m}^2$) for Thirteen Leaf Pigments for Nine Species^{a,b}

	Concentration Range ($\mu\text{mol}/\text{m}^2$)	Fold Difference	Minimum Value Species	Maximum Value Species
Chlorophyll a	55-883	16	<i>Quercus lobata</i>	<i>Quercus douglasii</i>
Chlorophyll b	15-290	19	<i>Quercus lobata</i>	<i>Quercus douglasii</i>
Phaeophytin a	1-90	90	<i>Quercus lobata</i>	<i>Umbellularia californica</i>
Phaeophytin b	0-12	--	several	<i>Umbellularia californica</i>
Chlorophyllide	0-41	--	several	<i>Umbellularia californica</i>
Lutein	12-194	16	<i>Quercus lobata</i>	<i>Quercus douglasii</i>
Neoxanthin	3-48	16	<i>Quercus lobata</i>	<i>Eriodictyon californicum</i>
Violaxanthin	1-41	41	<i>Acer macrophyllum</i>	<i>Eriodictyon californicum</i>
Antherxanthin	0.2-29	145	<i>Acer macrophyllum</i>	<i>Eriodictyon californicum</i>
Zeaxanthin	1-42	42	<i>Arbutus menziesii</i>	<i>Eriodictyon californicum</i>
β -carotene	8-150	19	<i>Quercus lobata</i>	<i>Eriodictyon californicum</i>
cis- β -carotene	0.1-3	30	<i>Quercus lobata</i>	<i>Eriodictyon californicum</i>

^aSome species were sampled twice in different habitats. The sampled species were *Acer macrophyllum*, *Arbutus menziesii* (2x), *Eriodictyon californicum* (2x), *Heteromeles arbutifolia*, *Ludwigia pacifica*, *Quercus agrifolia*, *Quercus douglasii*, *Quercus lobata* (2x) and *Umbellularia californica*.

^bSpecies sampled in late May 1993 at Jasper Ridge Biological Preserve, Stanford University.

References

- Card, D. H., D. L. Peterson, P. A. Matson, J. D. Aber, 1988. Prediction of Leaf Chemistry by the Use of visible and near infrared reflectance spectroscopy, *Remote Sens. Environ.* 26: 123-147.
- Curran, P.J., 1989. Remote Sensing of Foliar Chemistry, *Remote Sens. Environ.* 30:271-278.
- Effland, M., 1977. Modified procedure to determine acid-insoluble lignin in wood and pulp. *TAPPI* 6: (10).
- Evans, J.R., 1989. Photosynthesis and nitrogen relationships in leaves of C3 plants. *Oecologia* 78: 9-19.
- Field, C. and H.A. Mooney, 1986. The photosynthesis-nitrogen relationship in wild plants. in: T.J. Givnish, *On the Economy of Plant Form and Function*, Cambridge University Press, New York.
- Jacquemoud, S., 1993. Inversion of the PROSPECT + SAIL canopy reflectance model from AVIRIS equivalent spectra: Theoretical study, *Remote Sens. Environ.* 44:281-292.
- Jacquemoud, S., and F. Baret, 1990. PROSPECT: a model of leaf optical properties spectra. *Remote Sens. Environ.* 34: 75-91.
- Pierce, A. 1993. BCA protein assay reagent protocol. Pierce Corp. P.O. Box 117, Rockford, IL 61105, Handbook No. 23225X, p. 16.
- Verhoef, W., 1984. Light scattering by leaf layers with application to canopy reflectance modeling: the SAIL model, *Remote Sens. Environ.* 16: 125-141.
- Wessman, C.A., J.D. Aber, D.L. Peterson, and J.M. Melillo, 1988a. Remote sensing of canopy chemistry and nitrogen cycling in temperate forest ecosystems. *Nature* 335: 154-156.
- Wessman, C.A., J.D. Aber, D.L. Peterson, and J.M. Melillo, 1988b. Foliar analysis using near infrared reflectance spectroscopy. *Can. J. For. Res.* 18:6-11.
- Wright, S.W., S.W. Jeffrey, R.F.C. Mantoura, C.A. Llewellyn, T. Borland, D. Repeta, and N. Welschmeyer, 1991. Improved HPLC method for the analysis of chlorophylls and carotenoids from marine phytoplankton. *Marine Ecol. Prog. Ser.* 77: 183-196.

43
11/24/6
p. 4

ATMOSPHERIC CORRECTION OF AVIRIS DATA OF MONTEREY BAY CONTAMINATED BY THIN CIRRUS CLOUDS

Jeannette van den Bosch, Curtiss O. Davis, Curtis D. Mobley and W. Joseph Rhea
Jet Propulsion Laboratory/California Institute of Technology, Pasadena, CA

1. INTRODUCTION

Point source measurements (e.g. sun photometer data, weather station observations) are often used to constrain radiative transfer models such as MODTRAN/LOWTRAN7 when atmospherically correcting AVIRIS imagery. The basic assumption is that the atmosphere is horizontally homogeneous throughout the entire area. If the target area of interest is located a distance away from the point measurement position, the calculated visibility and atmospheric profiles may not be characteristic of the atmosphere over the target.

AVIRIS scenes are often rejected when cloud cover exceeds 10 percent. However, if the cloud cover is determined to be primarily cirrus rather than cumulus, in-water optical properties may still be extracted over open ocean. High altitude cirrus clouds are non-absorbing at 744 nm (Reind, *et al*, 1992). If the optical properties of the AVIRIS scene can be determined from the 744 nm band itself, the atmospheric conditions during the overflight may be deduced.

2. STUDY SITE

AVIRIS imagery of Monterey Bay, CA (Figure 1) was acquired 4 September 1992 at 14:00 PDT in support of a larger experiment which involved shipboard measurements of photosynthetic pigment concentrations. Monterey Bay, a designated National Marine Sanctuary, is an ecologically important area that has been the subject of intense research for over 15 years due to the diversity of underwater habitats, increased bioproductivity from upwelling coastal waters and anthropogenic impact.

3. IN-SITU MEASUREMENTS AND PROCESSING

The Monterey Bay Aquarium Research Institute (MBARI) maintains a permanent mooring, M1, in the Bay. The mooring includes Biospherical Instruments MER-2020 underwater spectroradiometers at depths of 10 and 20 m which measured downwelling irradiance and upwelling radiance at six wavelengths and a surface sensor which measured surface irradiance at five wavelengths. A GPS is deployed on the mooring giving exact geographic coordinates at the time of the overflight. The MER-2020 data at 10 and 20 m were converted to water-leaving radiance at each of the five wavelengths. Instrumentation problems prevented use of the surface irradiance values.

Cloud profiling was performed simultaneously with Reagan sun photometer measurements at the Presidio in Monterey, CA, over 20 km away from the mooring location. The sky was characterized by an increasing coverage of stratocirrus and cirrus clouds from sunrise to the time of the overflight. A halo was detected around the sun indicating ice crystals at an altitude of approximately 12 km. The sun photometer data was reduced using a modified Langley approach (Bruegge, *et al*, 1990), yielding a calculated visibility of 36 km and atmospheric water profiles. Ancillary

meteorological data were supplied by the Naval Post Graduate School's Doppler radar wind profiler (wind speed and wind direction) and the NPGS weather station (surface pressure and temperature).

4. ANALYSES AND RESULTS

A correction factor was applied to the radiometrically corrected AVIRIS data based on the ratio of the in-flight calibration to the laboratory calibration (Robert O. Green, JPL, personal communiqué). The 557 and 1382 nm bands of the corrected, calibrated AVIRIS scene were used to determine cloud type (Gao and Goetz, 1992). Cumulus clouds (low elevation water clouds), if present, will be visible in the 557 nm scene but will not be detected in the 1382 nm scene, where the observed radiance results only from the scattering by the cirrus clouds. The cloud cover, estimated at 20 percent, was entirely cirrus.

Apparent reflectance, ρ_{app} , of the cirrus clouds was calculated as

$$\rho_{app} = \frac{L_{AV744}}{L_{TOA744}} \quad (1)$$

where L_{AV744} is the radiance from AVIRIS 744 nm band and L_{TOA744} is the solar radiance at 744 nm above the top of the atmosphere (Iqbal, 1983).

Since the cirrus clouds are non-absorbing at 744 nm and the reflectance of the ocean surface is negligible at this wavelength, the radiance measured represents mainly the scattering of the ice crystals and the ocean aerosols. Transmission at 744 nm may then be approximated as

$$T_{AV744} = 1.0 - \rho_{app} \quad (2)$$

and represents transmission of solar energy in the presence of aerosols.

MODTRAN was iteratively run at visibilities ranging from 30-100 km. The total optical depth at each visibility was separated into the individual components of Rayleigh [scattering], Mie [scattering] and ozone. At 70 km visibility, the MODTRAN predicted total aerosol optical depth matched within 2.55% the calculated optical depth from the AVIRIS 744 nm image.

A 50 x 50 pixel area at the location of M1 mooring was atmospherically corrected to water-leaving radiance with MODTRAN and incorporated a continuum interpolated band ratio (CIBR) correction for water vapor, an ozone correction factor and a visibility of 70 km (Davis, *et al.*, 1993). The resulting spectrum demonstrates closer agreement with the calculated water-leaving radiance from the mooring data than L_w from 36 km visibility (Figure 2). The negative and low values between 400-450 nm are due to the insensitivity of AVIRIS to detect radiance values from dark [ocean] targets in these wavelengths.

In the absence of near-surface profiling measurements of the underwater light field, the mooring data represent a crude approximation when computing water-leaving radiance values. Profile measurements are typically binned to 1 m intervals. The depth-rate of spectral attenuation is fit with a polynomial, extrapolated to just below the surface, and transformed to a value just above the surface using an empirical relationship. With measurements only at 10 and 20 m, the attenuation curve is highly skewed toward lower attenuation values due to the fact that most of the absorption and scattering affecting water-leaving radiance occurs in the uppermost optical depth. This leads to artificially high calculations of water-leaving radiances.

C. Mobley's radiative transfer model (Mobley, 1989) was initialized with the irradiance calculated by MODTRAN, the vertical profile of chlorophyll-a concentration at mooring M1, the solar zenith angle and the recorded wind speed at the time of

the AVIRIS overflight. The calculated water-leaving radiance at the six MER wavelengths (Figure 2) was rescaled by a factor of 0.4. This factor may be associated with the uncertainties in the irradiance calculated by MODTRAN, the absorption and scattering coefficients calculated for the open ocean versus coastal waters and the method of converting *in situ* MER measurements at 10 and 20 m to water-leaving radiance. The radiance distribution calculated by the radiative transfer model depends both on the inherent optical properties of the water column and on the sea state and sky radiance distribution. The model is applicable to general ocean waters. In these model runs, the absorption and scattering coefficients were calculated as functions of wavelength and chlorophyll using empirical relationships developed for clear ocean waters (Morel, 1988). In view of the fact that these relationships are not specific to Monterey Bay, the results are encouraging.

The above outlined method of retrieving atmospheric parameters from an AVIRIS scene demonstrates that there are caveats for using point source measurements for initializing MODTRAN and that AVIRIS scenes contaminated by optically thin cirrus clouds may still be atmospherically corrected.

5. ACKNOWLEDGEMENTS

The authors wish to thank Dick Lind and Mark Boothe (Department of Meteorology, Naval Postgraduate School, Monterey, CA), Francisco Chavez (MBARI), David Glover and Dan Repeta (Woods Hole Oceanographic Institute), and Mike Hamilton and Stu Pilorz (JPL) for the ancillary data and technical discussions.

6. REFERENCES

- Bruegge, C.J., J.E. Conel, J.S. Margolis, R.O. Green, G. Toon, V.E. Carrère, R.G. Holm, G. Hoover. 1990. In-Situ Atmospheric Water-Vapor Retrieval in Support of AVIRIS Validation, *Imaging Spectroscopy of the Terrestrial Environment*, Gregg Vane, Editor, Proc. SPIE 1298, Orlando, Florida, pp. 150-163.
- Davis, C.O., M.K. Hamilton, W.J. Rhea, J.M. van den Bosch, K.C. Carder and R. Steward. 1993. Spectral Analysis of an AVIRIS Image of San Pedro Channel. *Imaging Spectroscopy of the Terrestrial Environment*, Gregg Vane, Editor, Proc. SPIE, Orlando, Florida (in press).
- Gao, B.C. and A.F.H. Goetz. 1992. Detection of Thin Cirrus Clouds from AVIRIS Data using Water Vapor Channels near 1.38 μm . *International Geoscience and Remote Sensing Symposium, Houston, TX*, 91-72810, v. 1, pp. 719-721.
- Iqbal, M. 1983. *An Introduction to Solar Radiation*, Academic Press, pp. 44-50.
- Mobley, C.D. 1989. A Numerical Model for the Computation of Radiance Distributions in Natural Waters with Wind-Roughened Surfaces. *Limnology and Oceanography*, 34(8), pp. 1473-1483.
- Morel, A. 1988. Optical Modeling of the Upper Ocean in Relation to its Biogenous Matter Content (Case I Waters). *Journal of Geophysical Research*, v. 93 C9, pp. 10749-10768.
- Reind, R.E., S.A. Christopher and R.M. Welch. 1992. The Effect of Spatial Resolution upon Cloud Optical Property Retrievals. Part I: Optical Thickness. *International Geoscience and Remote Sensing Symposium, Houston, TX*, 91-72810, v. 1, pp. 722-725.

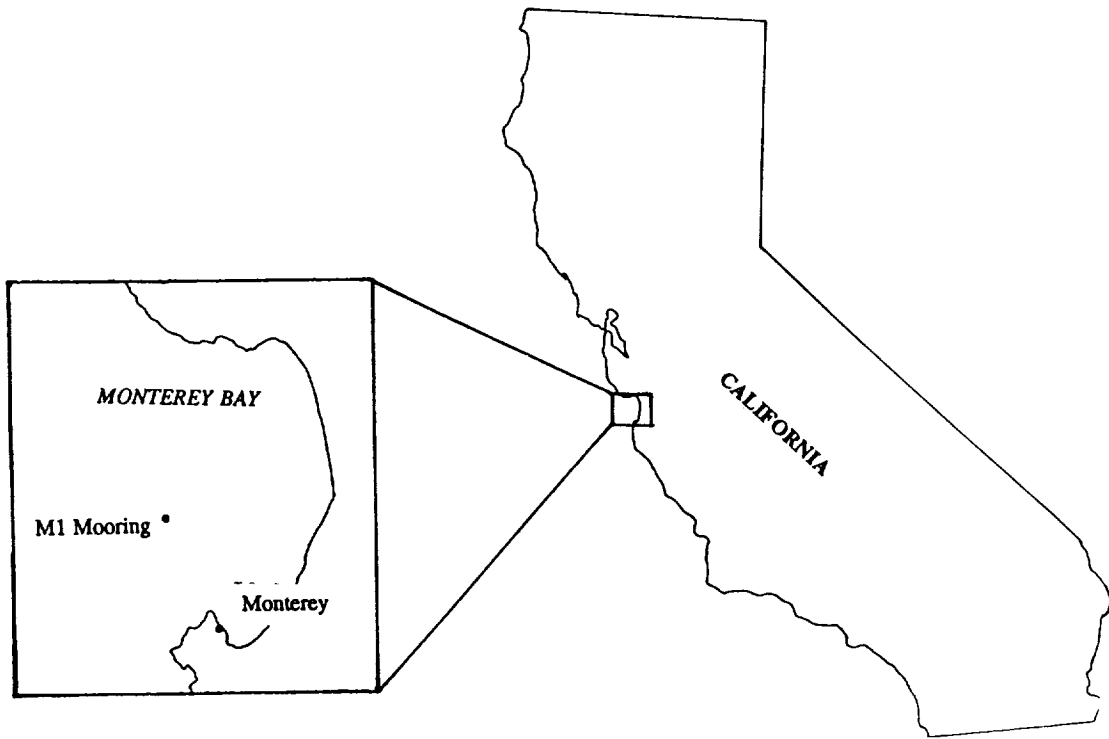


Figure 1. Study Site

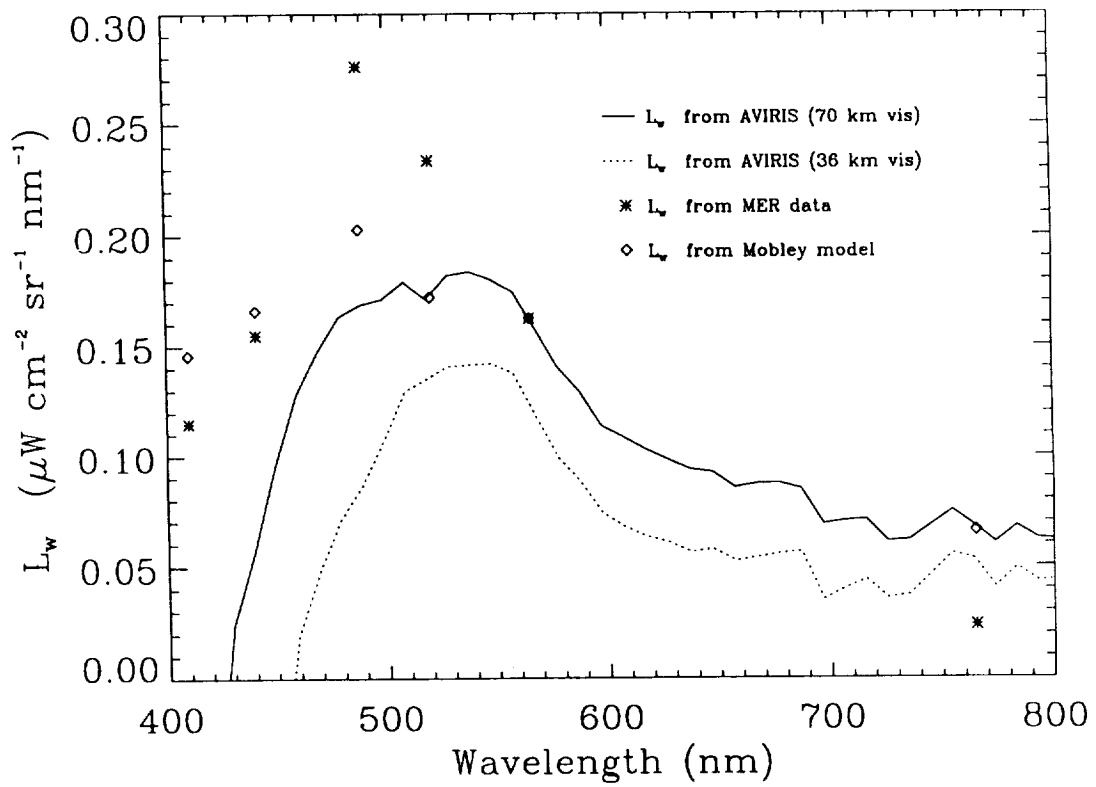


Figure 2. M1 Water-Leaving Radiance

47/43
11047

INVESTIGATIONS ON THE 1.7 μm RESIDUAL ABSORPTION FEATURE IN THE VEGETATION REFLECTION SPECTRUM.

J. Verdebout, S. Jacquemoud, G. Andreoli, B. Hosgood and A. Sieber

Commission of the European Communities
Joint Research Centre – Institute for Remote Sensing Applications
21020 – Ispra – Italy

1. INTRODUCTION

The detection and interpretation of the weak absorption features associated with the biochemical components of vegetation is of great potential interest to a variety of applications ranging from classification to global change studies. This recent subject is also challenging because the spectral signature of the biochemicals is only detectable as a small distortion of the infrared spectrum which is mainly governed by water. Furthermore, the interpretation is complicated by the complexity of the molecules (lignin, cellulose, starch, proteins) which contain a large number of different and common chemical bonds.

In this paper, we present investigations on the absorption feature centred at 1.7 μm ; these were conducted both on AVIRIS data and laboratory reflectance spectra of leaves.

2. ANALYSIS ON AVIRIS DATA

The ground reflectance has been first obtained by using the "Atmosphere Removal program" developed at the CSES/CIRES – University of Colorado. The pixel reflectance ($R_p(\lambda)$) is then unfolded as a linear mixture of a soil and a vegetation spectrum ($R_s(\lambda)$ and $R_v(\lambda)$):

$$R_p(\lambda) = a_s \cdot R_s(\lambda) + a_v \cdot R_v(\lambda) \quad (1)$$

The soil spectrum is taken from the scene as the mean spectrum of a small area known to be bare soil. The vegetation spectrum is modelled with a Kubelka–Munk formula for an optically thick homogeneous medium:

$$R_v(\lambda) = \frac{2 - \omega_0(\lambda) - 2 \cdot \sqrt{1 - \omega_0(\lambda)}}{\omega_0(\lambda)} \quad (2) \quad \text{with} \quad \omega_0(\lambda) = \frac{s}{s + k(\lambda)} = \frac{1}{1 + \frac{k(\lambda)}{s}} \quad (3)$$

where $\omega_0(\lambda)$ is the single scattering albedo, s is the scattering coefficient (as the scattering in leaf tissue is mainly due to multiple reflection and refractions, it can reasonably be assumed to be wavelength independent) and $k(\lambda)$ is the absorption coefficient of the medium

We further assume that the absorption in vegetation is due to chlorophyll and water and write:

$$\frac{k(\lambda)}{s} = \frac{1}{s} \cdot (c_{chl} \cdot k_{chl}(\lambda) + c_w \cdot k_w(\lambda)) = a_{chl} \cdot k_{chl}(\lambda) + a_w \cdot k_w(\lambda) \quad (4)$$

where $k_{chl}(\lambda)$ is the specific absorption coefficient of chlorophyll; the in vivo absorption coefficient (expressed in $\text{cm}^2 \cdot \mu\text{g}^{-1}$) of the PROSPECT model was used; $k_w(\lambda)$ is the specific absorption coefficient of water (expressed in cm^{-1}) (the measurement of Curcio and Petty was used); c_{chl} and c_w are the chlorophyll and water concentration; a_{chl} and a_w are the above concentrations divided by the scattering coefficient and are the independent parameters of the vegetation spectrum model

By combining formula (1), (2), (3) and (4), one obtains a model of the pixel reflectance as a non linear function of four parameters: a_s , a_v , a_{chl} and a_w , which are determined by least mean square fitting on the AVIRIS pixel reflectance by using a Marquardt algorithm. Two spectral windows were used in the fitting: 0.5 to 0.73 μm where the chlorophyll absorption is dominant and 1.5 to 1.65 μm which is governed by water while excluding the 1.7 μm absorption feature.

Once the inversion is performed, a measured spectrum of the vegetation fraction ($R_{vm}(\lambda)$) is extracted as:

$$R_{vm}(\lambda) = \frac{R_p(\lambda) - a_s \cdot R_s(\lambda)}{a_v} \quad (6)$$

If we assume that the 1.7 μm feature is an absorption due to a component of vegetation, we logically evaluate its magnitude from the absorptance corresponding to the measured and fitted vegetation spectra (A_{vm} and A_v). The absorptance is defined here as k/s , and obtained from the reflectance by inverting equations (2) and (3):

$$A(\lambda) = \frac{(R(\lambda) + 1)^2}{4 \cdot R(\lambda)} - 1 \quad (7)$$

The residual has then been evaluated in the 1.65 to 1.76 μm spectral interval as:

$$res = \frac{1}{N} \cdot \sum (A_{vm} - A_v) \quad (8)$$

where the average is taken on the N AVIRIS channels in the spectral window.

Figure 1 shows a result obtained with the above procedure applied to a fraction of the Freiburg test site which contains both forested and agricultural areas. The following comments can be made:

- the residual amplitude is markedly higher on the forest than on the agricultural fields
- well defined structures are seen inside the forest both in the residual amplitude and in the water parameter (a_w), these may reflect the mixed species composition (conifers/deciduous); a recently obtained composition map will allow to verify this hypothesis

- over the forest, the residual amplitude is positively correlated with the water parameter while this correlation breaks on the agricultural zones

Figure 2 shows the residual amplitude over a small fraction of the Black Forest which is completely composed of conifers, Norway spruce being the dominant species. When compared with an age class map, a positive correlation of the residual amplitude with the forest age can be distinguished.

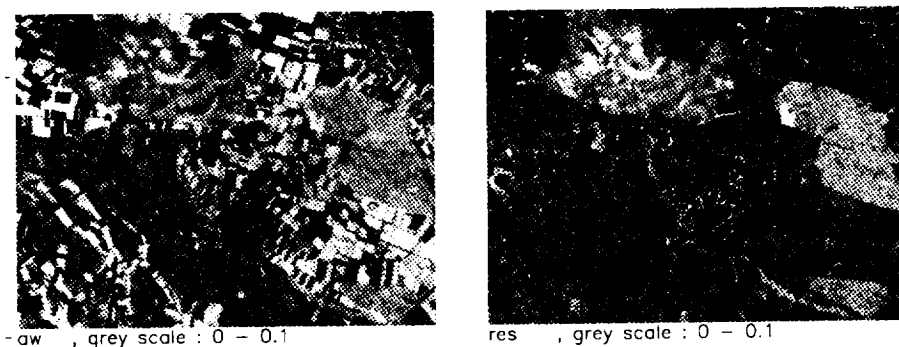


Figure 1. The water parameter (left) and the residual amplitude (right) over the Freiburg test site ; the brighter areas in the residual image are the forested zones.

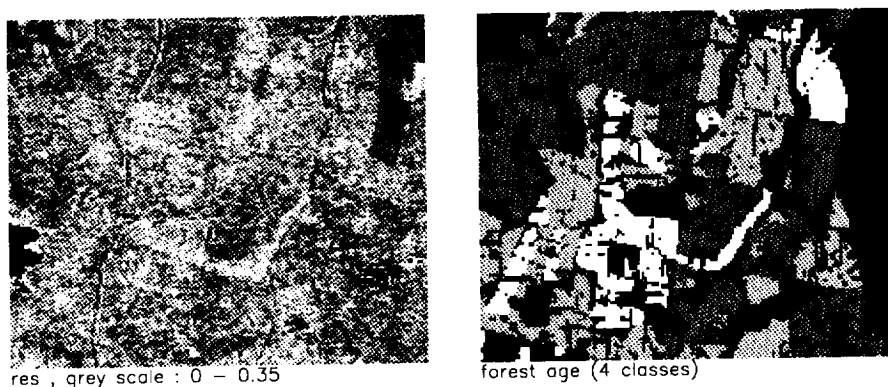


Figure 2. The residual image of a fraction of the Black Forest test site (left) and the age class map (right) of the same area (lighter grey corresponds to older forest).

3. LABORATORY STUDIES

To support the interpretation of the airborne sensor data, we have undertaken to build a data set associating VIS-IR spectra of vegetation elements (leaves, stems, bark) with physical measurements and chemical analyses.

In order to have a wide range of variation of the leaf internal structure, pigmentation, water content and biochemical components, plant species with different types of leaves have been collected outdoor. About 30 species of woody and herbaceous plants were obtained from trees grown within the JRC and from crops. For each sample, 5 representative leaves were selected: we immediately measured the blade thickness and the fresh weight of 4.10 cm² discs which were placed in a drying oven in order to determine the water content, the equivalent water thickness, and the specific leaf area. Samples of leaf material have been also kept to perform later some measurements of photosynthetic pigments, lignin, cellulose, starch and nitrogen concentration. A Perkin Elmer Lambda 19 spectrophotometer equipped with an

integrating sphere was used for the measurements of the directional-hemispherical reflectance and transmittance of the upper faces of the 5 leaves. Moreover, the reflectance of an optically thick sample was obtained by stacking leaves in order to magnify the radiometric signal and minimise the leaf to leaf variability. Spectra were scanned over the 400–2500 nm wavelength interval with 1 nm step and special attention has been paid to the calibrations problems. Finally, we dried some leaves of each species and repeated the above procedure. Conifer needles, bark, stems and substances such as powdered starch or proteins have also been included in the data set.

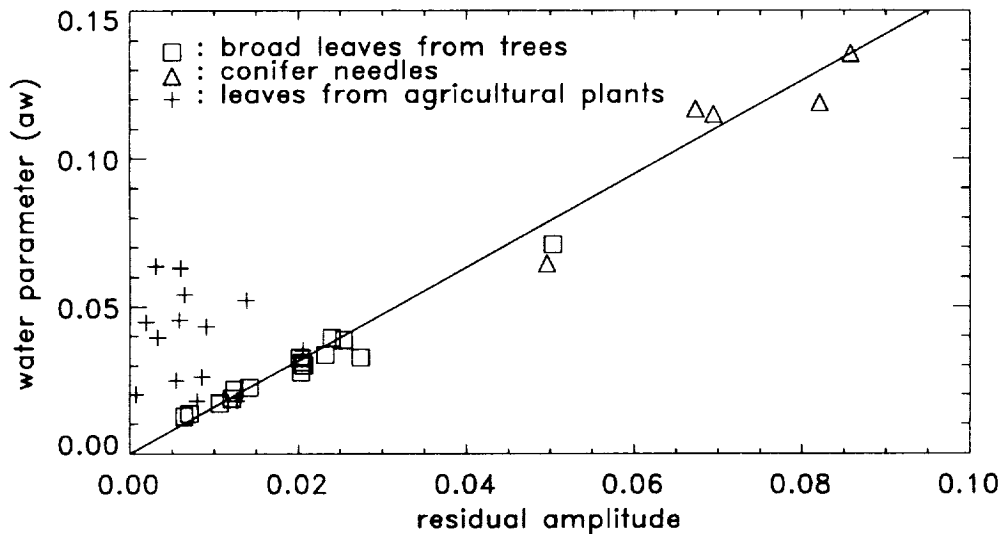


Figure 3. Water parameter and residual obtained from laboratory spectra of optically thick stacks of leaves and needles of various types of vegetation.

The analysis performed on the vegetation fraction spectra of AVIRIS was conducted on the reflectance of optically thick stacks of leaves and needles with the idea that the Kubelka-Munk formula might also be applicable in this case. Figure 3 shows the results obtained for the water parameter and the residual amplitude. Interestingly, these results are coherent with those obtained on the AVIRIS data:

- for tree leaves and conifer needles, a remarkable linear correlation is found between the residual amplitude and the water parameter
- this correlation does not exist for leaves from agricultural plants
- the residual amplitude is lower for leaves from agricultural plants

4. CONCLUSION

This study has established that the 1.7 μm absorption residual shows systematic behaviours with respect to the vegetation type. These behaviours have been independently found from the analysis of AVIRIS spectra and laboratory reflectance spectra of optically thick stacks of leaves and needles. The underlying explanation is not clear at present but, once complemented by chemical analyses, the laboratory data set will allow deeper investigations.

A COMPARISON OF SPECTRAL MIXTURE ANALYSIS AND NDVI FOR ASCERTAINING ECOLOGICAL VARIABLES

Carol A. Wessman^{1,2}, C. Ann Bateson², Brian Curtiss² and Tracy L. Benning^{1,2}

¹ Environmental, Population and Organismic Biology Department

² Cooperative Institute for Research in Environmental Science
University of Colorado, Boulder, Colorado 80309-0449

1. INTRODUCTION

In this study, we compare the performance of spectral mixture analysis to the Normalized Difference Vegetation Index (NDVI) in detecting change in a grassland across topographically-induced nutrient gradients and different management schemes. The Konza Prairie Research Natural Area, Kansas, is a relatively homogeneous tallgrass prairie in which change in vegetation productivity occurs with respect to topographic position in each watershed (Schimel et al. 1991). The area is the site of long-term studies of the influence of fire and grazing on tallgrass production and was the site of the First ISLSCP (International Satellite Land Surface Climatology Project) Field Experiment (FIFE) from 1987 to 1989.

Vegetation indices such as NDVI are commonly used with imagery collected in few (<10) spectral bands. However, the use of only two bands (e.g. NDVI) does not adequately account for the complex of signals making up most surface reflectance. Influences from background spectral variation and spatial heterogeneity may confound the direct relationship with biological or biophysical variables (Choudhury 1987, Huete and Jackson 1988). High dimensional multispectral data allows for the application of techniques such as derivative analysis and spectral curve fitting, thereby increasing the probability of successfully modeling the reflectance from mixed surfaces. The higher number of bands permits unmixing of a greater number of surface components, separating the vegetation signal for further analyses relevant to biological variables.

2. METHODS

AVIRIS imagery was acquired for the Konza Prairie in August 1990. Field data were collected from 12 watersheds in 1990 as part of the annual primary production measurements made by the NSF Long-Term Ecological Research (LTER) program. The LTER watershed estimates are derived as an average of biomass values collected from sites on the ridges and lowlands. (Values are not acquired in the slope regions; sampling in this way does not consider the variation in production across the watersheds.) These estimates are broken down into components of: live (grass), forbs (herbs), current dead, litter, total live (live + forbs) and biomass (total live + current dead).

The AVIRIS image cube was atmospherically corrected using the ATmospheric REMoval Program (ATREM) (Version 1.1, 1992) and filtered in the frequency domain using a Butterworth filter (Hamming 1989). ATREM retrieves "scaled surface reflectance" from image spectrometer data using atmospheric absorption features of atmospheric gases.

The endmembers for the mixture analysis were selected manually using an interactive tool to explore the eigenvector space for endmembers (Bateson and Curtiss 1993). The AVIRIS cube was unmixed twice. Wavelengths were restricted to the visible region (bands 5 to 30 and 33 to 43) for the first unmixing and the shortwave-infrared region (SWIR; bands 45 to 56, 62 to 76, 82 to 89, 104 to 148, 179 to 186) for the second. NDVI was computed using bands 28 (665 nm) and 43 (776 nm) for the entire image.

The concentrations computed from the unmixed data and the NDVI values were regressed against the ground data. The ground data were normalized by dividing all values by the sum of biomass and litter to derive concentration values comparable to the scene component concentrations and NDVI. Sensitivity of the remote sensing data to spatial variation in surface characteristics was tested by plotting values for endmember concentrations and NDVI along transects extracted from unburned and burned watersheds. Comparisons were also made between the images for each endmember fraction and a map of the Konza Prairie research treatments (including fire and grazing treatments).

3. RESULTS AND DISCUSSION

Five scene endmembers (soil, vegetation, litter, shade, and a second vegetation) were selected in fourth dimensional space of the visible portion of the spectrum using the endmember selection tool (Figure 1). These endmembers were identified by visual comparison with known library and field endmembers.

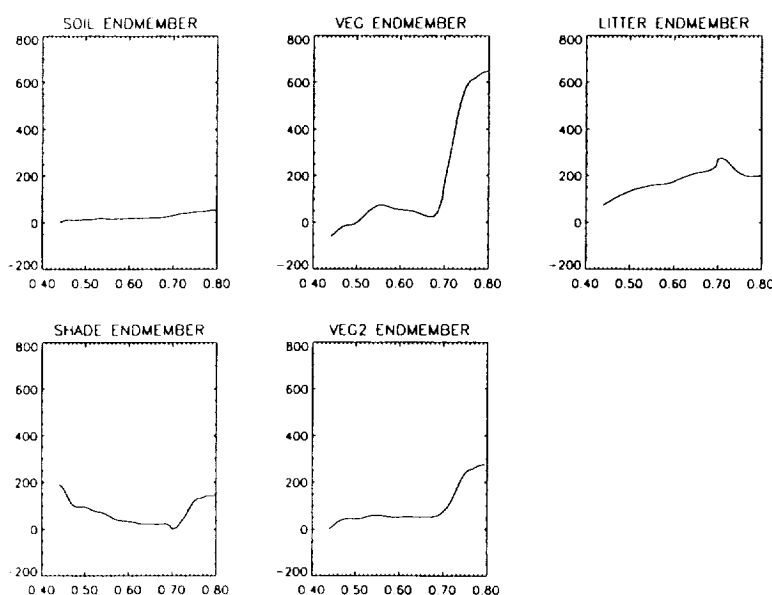


Figure 1. Five endmembers derived from the Konza image cube using the manual endmember selection tool.

The SWIR region consists of more subtle absorption features, necessitating less subjective identification methods. Four endmembers were differentiated: one resembling liquid water, a second resembling leaf "lignin" and two of unknown origin. To verify the identity of the "lignin" and liquid water endmembers, the endmember spectra derived from the image were curve fitted to various laboratory endmember spectra. To do this curve fitting, we used a variant of the method in McKenzie and Johnston (1982). In the curve fit, we assume there is only one endmember, since we are trying to identify each derived endmember with one library endmember. The logs of both the library and derived endmembers are computed to obtain the absorption coefficients. In McKenzie and Johnston (1982), a regression line is fitted to the absorption coefficients of the derived endmember over a short wavelength interval and the deviations of the coefficients from the line are regressed against the deviations similarly computed for the library endmember. Since the endmembers in our analysis span several band segments, we fit separate lines to each segment.

Two of the derived endmembers were fitted with various library endmembers. To identify the endmembers, we used two criteria: small RMS and large correlation

coefficient. The derived water endmember best fit to the library water spectrum with $r = 0.96$ and $RMS = 12.25$ (Fig. 2a). The best fit for the "lignin" endmember was a spectrum from weathered, highly leached leaves believed to consist largely of highly recalcitrant materials such as lignin ($r = 0.52$ and $RMS = 7.06$; Fig. 2b). Although the correlation coefficient is not impressive, the plot of the fit is very convincing. The reason for this discrepancy lies in the fact that the correlation coefficient is computed in log-log space. The next closest fit was with a laboratory starch spectrum with $r = 0.51$ and $RMS = 7.03$. Although r and RMS of the starch spectrum are close to that of the "grey leaves" spectrum, the relative positions of the curve segments in the laboratory starch spectrum do not agree with those of the "lignin" endmember.

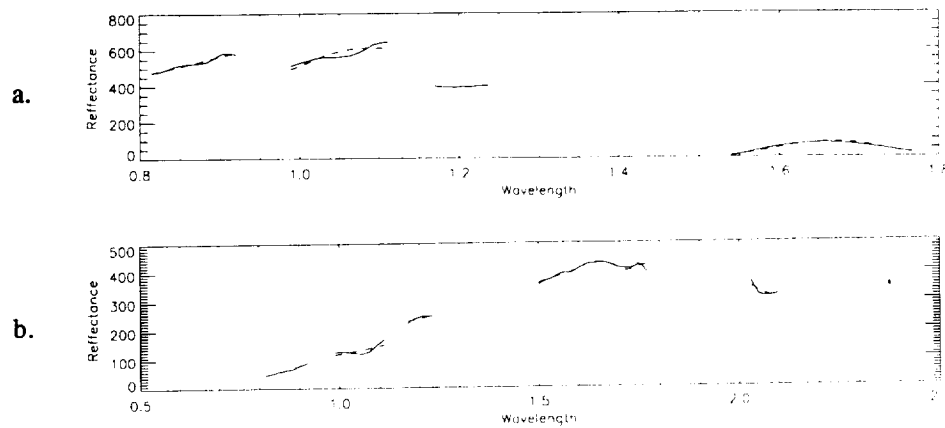


Figure 2. Curve fit of (a) water laboratory spectrum to derived water endmember and (b) "grey leaves" laboratory spectrum to the derived "lignin" spectrum.

Endmember concentrations and NDVI were regressed against the ground data. Green vegetation had a correlation coefficient with total live biomass of $r = 0.73$ ($p = 0.007$) compared with an r of 0.56 ($p = 0.059$) for NDVI. Hence, a significant correlation was achieved by removing background influences through spectral unmixing. The "lignin" concentration had a significant correlation with litter ($r = 0.73$, $p = 0.007$) and a highly significant correlation with biomass + litter ($r = 0.82$, $p = 0.001$). This suggests that the "lignin" endmember is tracking green and standing dead vegetation as well as litter; lignin is present in live and dead plant material.

Concentration images for the landscape constituents exhibit spatial patterns that reflect expected distributions with respect to the research treatments. For example, figure 3 shows transect plots of green vegetation, water, litter, soil and "lignin" concentrations for the burned watershed 1B. The drainage channel of the watershed occurs between coordinate positions 250 and 260. As expected, vegetation and water endmember fractions are highest in the drainage channel. Litter, "lignin", and soil fractions are highest on the ridges. There are notably strong correlations between "lignin" and litter concentrations ($r = 0.87$) and between water and vegetation concentrations ($r = 0.88$). The transect plots for the unburned watershed UB show similar relationships except that the correlation between litter and "lignin" concentrations is stronger ($r = 0.91$) and the correlation between water and vegetation concentrations is weaker ($r = 0.67$). In the Konza image, vegetation concentrations are generally higher in the burned and ungrazed areas and in the lowlands of each watershed. The litter endmember is sensitive to many of the unburned areas and the soil concentrations are highest on the ridge tops.

The most remarkable image is that of the "lignin" endmember, which clearly distinguishes between the research treatments. Higher concentrations are seen in the unburned, ungrazed watersheds just as expected. We conjecture that the sensitivity of the "lignin" endmember to actual lignin concentrations is due to the fact that it is based on more than a narrow wavelength interval, as is the case with other methods for detecting

lignin. Figure 4 (Slide 6) is a two-band image showing the spatial relationship between the derived lignin and water fractions across the site. While the two variables covary to a certain degree, the combination discriminates among fire and grazing research treatments in a unique way:

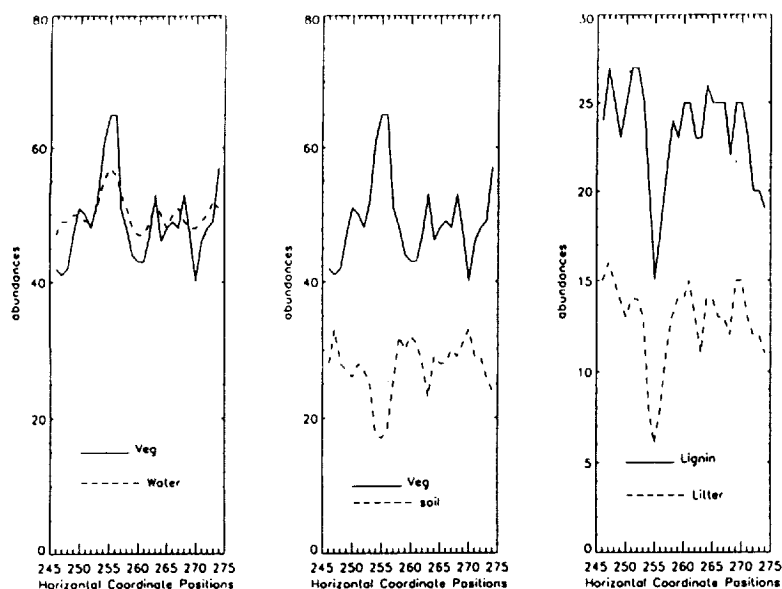


Figure 3. Transect plots of fraction values of green vegetation, water, soil, lignin and litter endmembers for the burned watershed. Drainage channel occurs between coordinate positions 250 and 260.

4. SUMMARY

Spectral image analysis using visible wavelengths and endmembers derived from the AVIRIS image produced more meaningful information about the Konza research area than did the vegetation index NDVI. However, the most promising results were obtained by using shortwave-infrared wavelengths to obtain information on the chemistry within the scene. The so-called "lignin" endmember appears to be responding to variable conditions induced by different fire and grazing regimes. Our separation of the visible and infrared wavelengths for mixture analysis of the AVIRIS imagery revealed possible inroads to the ecological structural of the Konza landscape not present other image transformations.

5. REFERENCES

- Choudhury, B.J. 1987. Relationships between vegetation indices, radiation absorption, and net photosynthesis evaluated by a sensitivity analysis. *Remote Sensing of Environment*, 22: 209-233.
- Huete, A.R. and R.D. Jackson. 1988. Soil and atmosphere influences on the spectra of partial canopies. *Remote Sensing of Environment*, 25: 89-105.
- Hamming, R.W. 1989. *Digital Filters*. Prentice Hall, New Jersey. p. 246.
- McKenzie, R.L. and Johnston, P.V. 1982. Seasonal variations in stratospheric NO₂ at 45 S. *Geophys. Res. Lett.* 9:1255-1258.
- Schimel, D.S., et al. 1991. Physiological interactions along resource gradients in a tallgrass prairie. *Ecology*, 72(2): 672-684.

USING AVIRIS FOR IN-FLIGHT CALIBRATION OF THE
SPECTRAL SHIFTS OF SPOT-HRV AND OF AVHRR?

Veronique Willart-Soufflet and Richard Santer

Laboratoire d'Optique Atmospherique
Universite du Littoral
Station Marine de Wimereux
62930 Wimereux , France

24-113
41049
1 4

1. INTRODUCTION

The response of a satellite sensor varies during its life time; internal calibration devices can be used to follow the sensor degradation or in flight calibration are conducted from estimations of the radiance at satellite level for well predictable situations. Changes in gain are evaluated assuming that the spectral response of the sensor is stable with time; i.e., that the filter response as well as the optics or the electronics are not modified since the pre-launch determinations. Nevertheless, there is some evidences that the SPOT interferometer filters are affected by outgasing effects during the launch : tests in vacuum chambers indicated a narrowing of the filters with a shift of the upper side towards the blue of about 10 nm which is more over consistant with the lost of gain observed during the launch. Also, during the life time of SPOT, the relationship between the lost of sensitivity and the filter band width may correspond to this effect. On the other hand, the unconsistency of the NOAA7 calibration between two methods(desert and ocean) having a different spectral sensitivity may indicate a spectral problem (Santer and Roger, 1993) with a shift of the central wavelenght of -20 nm. The basis idea here is to take advantage of the good spectral definition of AVIRIS to monitor these potential spectral degradations with an experimental opportunity provided by a field campaign held in La Crau (S.E. of France) in June 1991 which associated ground-based measurements and AVIRIS, SPOT2, NOAA-11 overpasses both over the calibration site of La Crau and an agricultural area.

2. METHOD

The method will consist of cross-calibrating a given sensor with AVIRIS. In other words, we want to compare SPOT, for example, to AVIRIS in the same conditions in terms of spectral response, of identical targets viewed under the same geometry and for the same atmospheric conditions. Figure 1 suggests how to reconstruct the spectral responses: the dots on the SPOT-HRV filter responses represent the AVIRIS central wavelenghts with the corresponding weighting coefficients. Then, we have to intercalibrate AVIRIS and SPOT in absolute value. A cross-calibration method will be conducted

over La Crau for which we have two SPOT overpasses on June 23th and 25th and one AVIRIS overpass on June 28th. To account for differences in geometries, we have BRDF archives on the test site. More over, the POLDER instrument (a CCD camera) overflow the site with typically 12 different view angles for each pixel acquired along track. On the other hand, we measured from a ground based station the different atmospheric parameters (aerosol model and loading, water vapor,..) to account for the differences in the atmospheric corrections.

When the radiometric calibration is achieved over La Crau, we want to check if any spectral shift can be made apparent. We first identified both on the AVIRIS and SPOT images different kinds of targets, having different spectral responses, and presenting a spatial homogeneity on several pixels in order to eliminate MTF problems, to overlap more accurately the images, to reduce the instrumental noise. Areas were selected and identified from in situ inventories. Figure 2 reports for some of them their spectral signatures; all the agricultural fields will present the same relative feature characteristic from the chlorophyll but with different amplitudes easily illustrated by the NDVI. What we are expected is that the spectral behaviour of our new sites will be enough different between each of them and from the calibration site. We also have to account for the difference in geometries and atmospheric conditions between AVIRIS and the other sensor. Notice that at shorter wavelengths, the signal is quite identical over water and vegetation which typically indicates that the atmospheric path radiance dominates; or in other words, that the atmospheric corrections towards the blue are a difficult task in the comparison. More over, we need to refer to POLDER to normalize the bi-directional effects for each kind of targets.

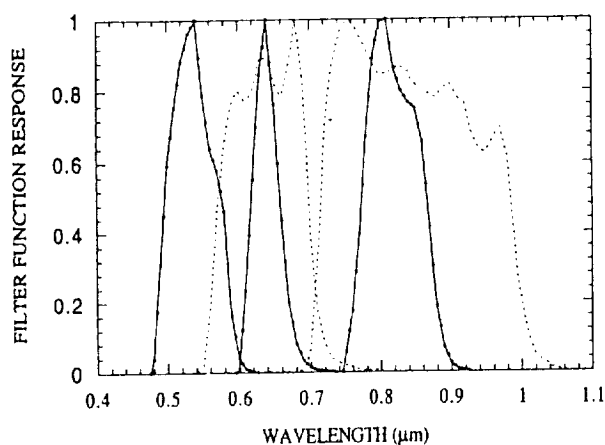


Figure 1. Spectral response for NOAA11 channels 1 and 2 and for SPOT2-IRV

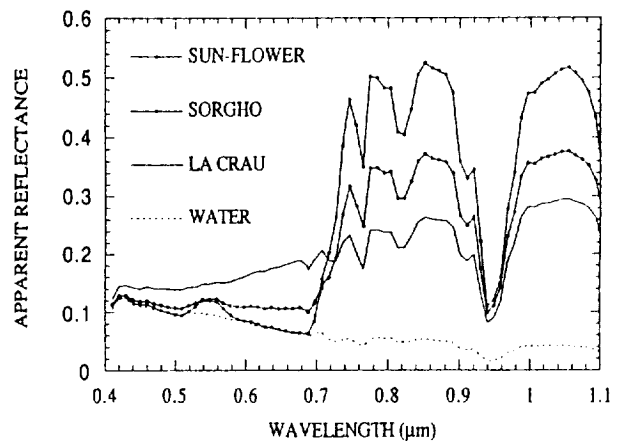


Figure 2. Spectral signatures from AVIRIS on different targets

3. PRELIMINARY RESULTS

Before investigating the different steps proposed in section 2 we want to check how potential changes in spectral response for SPOT or AVHRR can modify the response of the system. We have selected several scenarios indicated in section 1 with first a narrowing of the filters towards the blue of 10 nm (a) and 20 nm (b) We also consider a shift of -10 nm (c) and of -20 nm(d) of the entire filter in agreement with what we observed for NOAA-7. AVIRIS data were used to simulate the different filter responses over the selected areas and table 1 gives the relative variation of the radiance from the nominal value of the different bands of AVHRR and SPOT. For cases (a) and (b), the radiances decreased quite proportionally with the filter bandwidth with a maximum for IIRV2 which is the narrowest filter. Compared with the lost of sensitivity of SPOT-2 in three years which is around 20 percent, the spectral shift proposed for cases (a) and (b) are realistic. For cases (c) and (d), the influence is less pronounced and depends on the target.

sites	NOAA11-1				NOAA11-2			
	(a)	(b)	(c)	(d)	(a)	(b)	(c)	(d)
Crau	7.1	11.4	-0.9	-1.5	3.8	7.2	-1.3	-2.7
Sunflower	8.2	12.8	-3.3	-8.8	3.6	6.7	1.2	2.9
Maize	7.4	11.7	-3.9	-9.3	3.7	6.9	1.6	3.5
Sorghum	7.2	11.5	0.0	-2.3	3.7	7.0	0.8	1.7
Vine	6.8	10.9	6.8	10.9	3.6	6.8	-0.6	-1.1
Corn	7.2	11.5	7.2	11.5	3.7	6.9	-0.9	-1.8
Orchard	7.6	11.9	7.6	11.9	3.6	6.8	1.3	2.9
Foliage	7.3	11.5	7.3	11.5	3.7	6.9	1.7	3.6
Rize	6.5	10.2	6.5	10.2	2.8	5.2	-2.6	-4.9
Water	5.4	8.6	5.4	8.6	3.0	5.6	-4.2	-8.9

	IIRV-1				IIRV-2				IIRV-3			
	(a)	(b)	(c)	(d)	(a)	(b)	(c)	(d)	(a)	(b)	(c)	(d)
11.4	20.6	0.2	0.1	19.0	31.0	-1.0	-1.8	10.2	19.4	-0.6	-0.9	
10.4	19.1	-0.3	-0.6	17.3	28.4	-6.4	-13.4	10.0	19.1	-1.0	-1.4	
9.9	18.3	-2.1	-4.3	17.4	28.5	-6.0	-12.6	10.0	19.1	-0.7	-0.6	
10.8	19.8	-0.2	-0.6	18.3	29.9	-3.2	-6.5	10.0	19.2	-0.7	-0.8	
11.0	20.0	-0.2	-0.5	18.5	30.2	-2.6	-5.0	10.1	19.3	-0.9	-1.2	
10.8	19.6	-1.2	-2.8	18.8	30.7	-1.5	-2.8	10.5	19.9	0.0	0.3	
10.1	18.6	-1.8	-8.7	17.3	28.5	-6.0	-12.3	10.2	19.4	-0.6	-0.4	
9.7	17.7	-3.5	-7.2	17.2	28.2	-6.6	-13.8	10.2	19.5	-0.4	0.1	
10.5	19.2	-1.2	-2.6	17.2	28.4	-6.0	-12.1	8.9	17.2	-2.6	-4.6	
10.2	18.6	-2.1	-4.3	17.2	28.4	-6.1	-12.7	9.4	18.0	-1.9	-3.5	

Table 1. Relative variations (in percent) of the sensor radiances for AVHRR and SPOT when the filter response varies from its nominal values to the four cases described in the text.

The influence of the filter response modifications is attenuated by the in-flight calibration if we suppose that, for example, the sensor degradation is monitor over the calibration test site of La

Crau. Table 2 gives the relative discrepancies observed over the different sites for the assumed spectral response changes. The reference to La Crau eliminates the effect of the variation on the integrated value over the filter response of the solar irradiance but still illustrated the relative difference in spectral response between La Crau and the others targets. The results are then quite different between the different bands and depend on the type of surface. Nevertheless, the effects may be some what substantial as height as 10 percents then more important that the specifications in terms of calibration accuracy. We can then plan the second step with the comparison with SPOT, trying to reduce the differences if exists by adjusting the SPOT spectral responses.

sites	NOAA11-1				NOAA11-2			
	(a)	(b)	(c)	(d)	(a)	(b)	(c)	(d)
Sunflower	1.2	1.6	-2.4	-7.2	-0.2	-0.5	2.5	5.5
Maize	0.3	0.3	-3.0	-7.7	-0.1	-0.3	2.8	6.0
Sorghum	0.1	0.1	0.9	-0.8	-0.1	-0.2	2.0	4.3
Vine	-0.3	-0.5	7.6	12.2	-0.1	-0.4	0.7	1.6
Corn	0.1	0.1	8.0	12.8	-0.1	-0.3	0.4	0.9
Orchard	0.5	0.6	8.4	13.2	-0.1	-0.4	2.5	5.4
Foliage	0.2	0.2	8.1	12.8	-0.1	-0.3	2.9	6.2
Rize	-0.7	-1.3	7.3	11.5	-1.0	-2.2	-1.4	-2.2
Water	-1.8	-3.1	6.2	10.0	-0.8	-1.7	-2.9	-6.0

HRV-1				HRV-2				HRV-3			
(a)	(b)	(c)	(d)	(a)	(b)	(c)	(d)	(a)	(b)	(c)	(d)
-1.2	-1.9	-0.5	-0.7	-2.2	-3.9	-5.4	-11.5	-0.2	-0.3	-0.4	-0.5
-1.7	-3.0	-2.3	-4.4	-1.9	-3.6	-5.0	-10.7	-0.2	-0.4	-0.1	0.2
-0.6	-1.1	-0.4	-0.7	-0.9	-1.6	-2.2	-4.6	-0.1	-0.3	-0.1	0.0
-0.5	-0.8	-0.4	-0.6	-0.7	-1.2	-1.6	-3.2	-0.1	-0.1	-0.3	-0.4
-0.7	-1.3	-1.5	-2.9	-0.3	-0.5	-0.6	-1.0	0.3	0.7	0.5	1.2
-1.4	-2.6	-2.0	-8.8	-2.1	-3.8	-5.0	-10.3	0.0	0.0	0.0	0.4
-2.0	-3.7	-3.7	-7.3	-2.2	-4.2	-5.6	-11.8	0.0	0.1	0.2	1.0
-1.0	-1.7	-1.4	-2.7	-2.2	-3.9	-4.9	-10.1	-1.4	-2.7	-2.0	-3.7
-1.4	-2.6	-2.3	-4.4	-2.2	-3.9	-5.1	-10.7	-0.8	-1.8	-1.3	-2.6

Table 2. Same as Table 1. but after correction for gain changes as monitor over the La Crau calibration site

4. REFERENCE

Santer R. and Roger J.C. (1993) On AVHRR calibration. SPIE proceedings, Vol. 1938, Orlando, Florida, 12-16 April, 1993444

11/10/80
p. 4

LABORATORY SPECTRA OF FIELD SAMPLES AS A CHECK ON TWO ATMOSPHERIC CORRECTION METHODS

Pung Xu and Ronald Greeley

Department of Geology
Arizona State University
Box 871404
Tempe, Arizona 85287-1404

1. INTRODUCTION

Atmospheric correction is the first step toward quantitative analysis of imaging spectroscopy data. Two methods, MODTRAN model (Bosch et al., 1990) and the empirical line (Conel et al., 1987), were used to convert AVIRIS radiance values to reflectance values. A set of laboratory spectra of field samples corresponding to AVIRIS coverage was used to assess these methods. This will also serve to select bands for future quantitative analyses.

2. STUDY SITE AND DATA

The study site was Kelso Dune, California. It is covered by two segments, 01 and 02, of AVIRIS Kelso/Afton flight line flown on Sept. 28, 1989. The AVIRIS data are radiometrically calibrated. The input parameters for the MODTRAN model are the same as a previous LOWTRAN-7 study (Xu et al., 1992). The ground measurements used in the empirical line methods are DAEDALUS spectra taken during the Geologic Remote Sensing Field Experiment (GRSFE) (Arvidson et al., 1989) July, 1989 field campaign. The measurements were taken on a bright target located at the parking area on the road to the Dune and a dark gravel target located at the power station on the KelBaker road. Field samples which are mainly sand were also taken from different places on or near the Dune. The laboratory spectra were obtained by Brown University's RELAB facility using the same phase angle as AVIRIS.

3. METHODS

The MODTRAN model atmospheric correction method is the same as the LOWTRAN-7 method (Bosch et al., 1990) except the MODTRAN model is used instead of LOWTRAN-7 model. MODTRAN model maintains complete compatibility with LOWTRAN-7 but has higher resolution and a better band model than LOWTRAN-7. The DAEDALUS raw data were first calibrated (Xu et al., 1992) before they were used in the empirical line method (Conel et al., 1987). Pixel DN values of AVIRIS for bright and dark targets were also needed to calculate the gain and offset for each band in the empirical line method.

In order for different data set to be compared, all the data were convolved to AVIRIS wavelength.

4. RESULTS

Only the laboratory spectra of samples taken on the homogenous and less than 1% vegetation dune surface were used in this study, so that samples were representative of more than one pixel area and so that the corrected AVIRIS reflectance are close to laboratory reflectance values. Nine RELAB spectra were selected for comparison with atmospherically-corrected AVIRIS data. Among the nine cases, only the best case

(sample X-93-20) and the worst case (sample X-93-1) are shown in Figure 1 and Figure 2 respectively. In general, the MODTRAN-corrected AVIRIS data are closer to the RELAB spectra than DAEDALUS-corrected AVIRIS data (Figure 1 and Figure 2). Moreover, statistics show that the means of the differences between MODTRAN-corrected AVIRIS data and RELAB spectra are smaller than the means of the differences between DAEDALUS ground measurement corrected AVIRIS data and RELAB spectra in both cases (Table 1,2,3,4). The big spikes of MODTRAN-corrected AVIRIS data in Figure 1 and Figure 2 are partially due to MODTRAN's over-estimation of water absorption in this study site. The big spike at around 800 to 900 nm of DAEDALUS-corrected AVIRIS data results from saturation in the electronics of DAEDALUS in the wavelength range 730 to 970 nm. The MODTRAN model gives poorly corrected reflectance values in the range 1300 to 1500 nm, 1750 to 1950 nm, and 2300 to 2400 nm. However, ground DAEDALUS measurements are better at some bands in those wavelength ranges.

Table 1. Statistics of the Differences between
MODTRAN and RELAB for X-93-1

Minimum	0.009411
Maximum	26.299393
Points	159
Mean	6.8869764
Median	6.4395862
Std Deviation	5.3408877

Table 2. Statistics of the Differences between
MODTRAN and RELAB for X-93-20

Minimum	0.027324
Maximum	17.657913
Points	159
Mean	2.6246841
Median	1.568169
Std Deviation	2.9924431

Table 3. Statistics of the Differences between
DAEDALUS and RELAB for X-93-1

Minimum	0.219814
Maximum	66.139587
Points	159
Mean	16.245166
Median	11.820717
Std Deviation	14.138695

Table 4. Statistics of the Differences between
DAEDALUS and RELAB for X-93-20

Minimum	0.9868810
Maximum	49.386105
Points	159
Mean	10.424899
Median	6.7065701
Std Deviation	10.513931

5. CONCLUSIONS

In this study, the MODTRAN-corrected AVIRIS data is generally better than ground DAEDALUS measurement corrected AVIRIS data. The ground DAEDALUS measurement is better in the water absorption wavelength ranges.

6. ACKNOWLEDGMENT

The authors would like to thank Tom Farr for identifying the pixels of the dark target on the AVIRIS image and Robert O. Green for his convolution program.

7. REFERENCES

- Arvidson, R.E. and D.L. Evans, 1989, "Geologic Remote Sensing Field Experiment", *Geol. Soc. Amer, Abstracts with Programs*, 21, pp.A121.
- Bosch, J.M. van den and R.E. Alley, 1990, "Application of lowtran 7 as an atmospheric correction to airborne visible/infrared imaging spectrometer (AVIRIS) data", *Proceedings, IGARSS '90*, pp.175-177.
- Conel, J.E., R.O. Green, G. Vane, C.J. Bruegge, R.E. Alley and B.J. Curtis, 1987, "Radiometric spectral characteristics and comparison of ways to compensate for the atmosphere", *Imaging Spectroscopy II, Proceedings of SPIE*, 834, pp.140-157.
- Xu, P. and R. Greeley, 1992, "A comparison of LOWTRAN-7 corrected Airborne Visible/Infrared Imaging Spectrometer (AVIRIS) data with ground spectral measurements", In *Summaries of the Third Annual JPL Airborne Geoscience Workshop, vol 1*, pp.144-146.

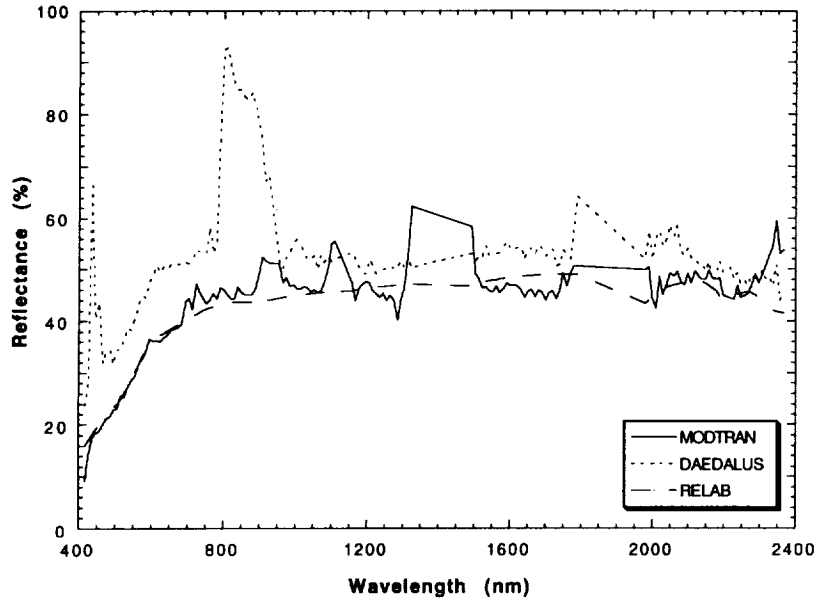


Figure 1. MODTRAN model corrected AVIRIS data (solid line) and ground DAEDALUS measurements corrected AVIRIS data (shorter dashed line) compared with RELAB reflectances of field sample X-93-20 (longer dashed line).

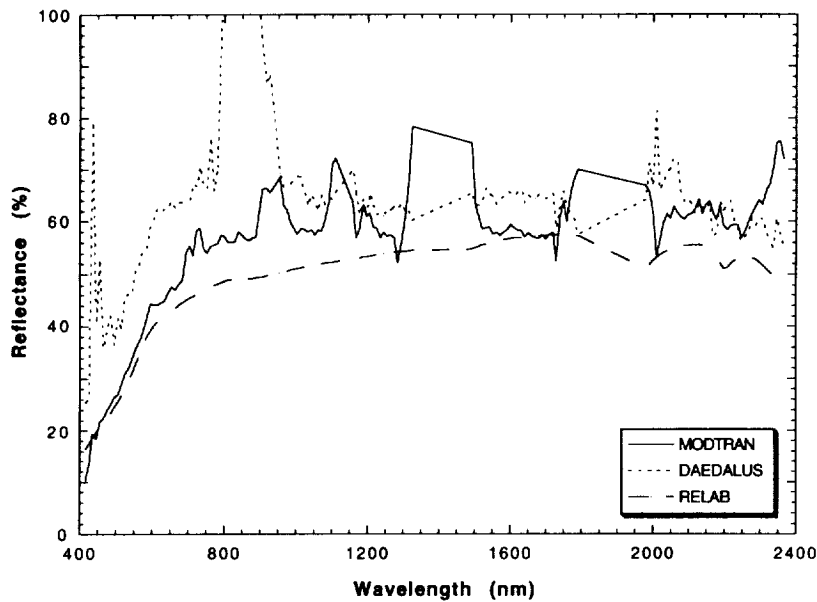


Figure 2. MODTRAN model corrected AVIRIS data (solid line) and ground DAEDALUS measurements corrected AVIRIS data (shorter dashed line) compared with RELAB reflectances of field sample X-93-1 (longer dashed line).

41051

**DETERMINATION OF SEMI-ARID LANDSCAPE ENDMEMBERS AND
SEASONAL TRENDS USING CONVEX GEOMETRY SPECTRAL UNMIXING
TECHNIQUES**

Roberta H. Yuhas ^{1,2}, Joseph W. Boardman ¹, and Alexander F.H. Goetz ^{1,2}

¹ Center for the Study of Earth from Space (CSES)
Cooperative Institute for Research in Environmental Sciences (CIRES)

² Department of Geological Sciences
Campus Box 449, University of Colorado
Boulder, Colorado 80309-0449

1. INTRODUCTION

Airborne Visible/Infrared Imaging Spectrometer (AVIRIS) data were acquired during three consecutive growing seasons (26 September 1989, 22 March 1990, and 7 August 1990) over an area of the High Plains east of Greeley, Colorado (40° 20' N and 104° 16' W). A repeat visit to assess vegetation at its peak growth was flown on 6 June 1993. This region contains extensive eolian deposits in the form of stabilized dune complexes (small scale parabolic dunes superimposed on large scale longitudinal and parabolic dunes). Due to the dunes' large scale (2-10 km) and low relief (1-5 m), the scaling and morphological relationships that contribute to the evolution of this landscape are nearly impossible to understand without the use of remote sensing. Additionally, this area and regions similarly situated could be the first to experience the effects caused by global climate change (Hansen *et al.*, 1988). During the past 10,000 years there were at least four periods of extensive sand activity due to climate change, followed by periods of landscape stability, as shown in the stratigraphic record of this area (Forman, *et al.*, 1992).

2. STUDY SITE CHARACTERISTICS

The dune complexes found along the South Platte River of northeastern Colorado occupy a region of semi-arid grasslands. It is this vegetation that currently stabilizes the dunes and prevents reactivation of the underlying sands. Due to the low mean annual precipitation (33 cm) of the region, the dominant vegetation community is that of the shortgrass prairie. Species commonly found include blue grama, needle-and-thread, and buffalo grass, along with other graminoids and perennial forbs (sage, yucca, and cacti).

The soils in the uplands are predominantly sandy, ranging from sand to sandy clay loam, while those along the terraces of the South Platte River range from clay loams to clays. The latter soils are much thicker and are used for commercial dryland and irrigated farming (alfalfa, corn, etc.), while the former soils cover proportionally more area but are used primarily for grazing due to their infertile nature. Because these soils occur adjacent to each other, the AVIRIS images analyzed in this study contain a wide range of vegetation cover amounts (ranging from 0% in overgrazed, fallow field, or blowout areas to 100% in irrigated fields).

3. METHODS

3.1 Atmospheric Correction/Conversion to Apparent Reflectance

The radiance values of all four of the AVIRIS scenes used in this study were converted to apparent reflectance and atmospherically corrected using the scaled surface reflectance method of Gao known as ATREM (Gao, *et al.*, 1993). In this method a

modeled path radiance spectrum is subtracted from the AVIRIS radiance spectrum. This result is then divided by the solar irradiance curve above the atmosphere to obtain the apparent reflectance spectrum. Next, the integrated water vapor amount is derived from the 0.94 μm and 1.14 μm water vapor absorption features of the corrected spectrum on a pixel-by-pixel basis. This is done using a three-channel ratioing technique. Finally, the calculated atmospheric water vapor transmittances are divided into the apparent reflectance value of each pixel, resulting in an atmospherically corrected image across the entire 0.4-2.5 μm region.

3.2 Spectral Unmixing Using Convex Geometry

A new method of spectral unmixing (Boardman, 1993) was used for the analyses of the apparent reflectance spectra. This new method, based upon the concepts of convex geometry, is unique because it derives estimates of the number of endmembers and their pure spectral signatures using only the data contained in the AVIRIS image. In this application, the data were spatially and spectrally subsetting. A 256x256 pixel region, covering approximately the same area on the ground, was extracted from each atmospherically corrected dataset. Then a nearly-homogeneous area was identified within each subscene. Bands with high standard deviations (denoting high noise content) in this subregion were eliminated from further processing. Also, spatial regions that were cloud-covered or otherwise not of interest were masked out. These areas appear black in the output images.

The convex-geometric unmixing takes advantage of the scatter of the points in spectral-space introduced by spectral mixing. The method is briefly outlined here. Its goal is to geometrically determine the lowest dimensional subspace that spans the data. The data are subjected to a modified principal components transformation, to separate signal from isotropic noise and to determine the inherent dimensionality of the data. Then the data are projected into this lower-dimensional subspace for analysis. If the data prove to be n -dimensional, $n+1$ endmembers are needed to unmix them. Those points that lie as outermost points in the data cluster are used to define a multidimensional polygon (simplex) of $n+1$ points. The best-fit simplex determines the correct endmembers (simplex vertices) which enclose all data points and gives estimates of the spectra of the pure endmember materials. In order to interpret the results, the projected spectra must be transformed back to the original coordinate system (224-band space). The analyst then interprets the spectra and associated grayscale endmember fractional abundance images, where the abundances are positive and sum to unity.

4. RESULTS

The four datasets were examined for both seasonal and temporal changes. These results are given below.

4.1 22 March 1990 Results

Because of the lower signal-to-noise ratio and lack of a D-spectrometer signal in this data, only 117 original bands were used in this analysis. After running the procedure outlined above, 63,913 datapoints were clustered in a 3-dimensional simplex. Therefore, the number of inherent endmembers needed to describe this scene was four. These were spectrally determined from the vertices of the simplex to be: shade/water, sand/soil, vegetation with some chlorophyll absorption (i.e., photosynthesizing, and thus, alive), and dried grass (standing dead). When the fractional abundance image of each endmember was viewed, the results were shown to correspond well with ground observations and prior knowledge of the area. The sand/soil endmember was most abundant in the barren areas of the dunes, and the photosynthesizing vegetation was present in low-lying areas where the water table is high, and, thus, where the plants begin to grow early in the spring. Through ground observation, this was determined to be grass species normally found in a tallgrass community. The dried grass endmember was found in the majority of the scene

and reflects the dead shortgrass prairie species that were left standing from the previous year's growing season. The shade/water endmember shows both water in an irrigation ditch (brighter, but fewer, pixels on this fractional abundance image) and the shade caused by the topographic relief of the area (minimal). Because the topography of the landscape is quite varied between dune and interdune areas, the shade/water endmember shows the morphology of the landscape well.

4.2 7 August 1990 Results

151 original bands were used in this analysis, resulting in a simplex encompassing 62,626 datapoints in 5-dimensional space. The six endmembers derived from this analysis were interpreted as: shade/water, sand/soil, dried grass (standing dead), very green vegetation, moderately green vegetation, and a minimally green vegetation (woody plant) (see Slide 8). Due to the higher signal-to-noise ratio of the data and all 224 bands present, the spectra show much better structure and a higher information content. By looking at the spatial representation of the results in the form of fractional abundance images, four endmembers were determined to be the same endmembers as derived in the 22 March 1990 data. The shade/water endmember is very similar to the previous result, as is the sand/soil endmember. Some of the landscape originally covered by only sand/soil has been replaced by vegetation and appears less bright in this fractional abundance image. The dried grass (standing dead) endmember was once again represented, although the spatial pattern has changed to become less dominant, especially on and in the areas immediately surrounding the largest dunes. The final endmember to be represented again appeared in the previous image as the tallgrass community vegetation. Now, however, instead of appearing just weakly photosynthesizing, this endmember is the most green vegetation in the scene (very green vegetation). Its abundance has spread out to the areas immediately surrounding the dunes where water tends to pool due to a high water table level. Because this image was taken in August, during the vegetation growing season, two more endmembers are present in the landscape. These are the moderately and the minimally green vegetation endmembers. The moderately green endmember represents growing shortgrass vegetation species, while the minimally green endmember represents sage, a woody forb. Different range management practices are clearly seen on this set of images, too, especially the boundary between sage and shortgrass dominated landscapes.

4.3 26 September 1989 Results

In the analysis of this data, 149 original bands were used. Assuming that the landscape did not change much between 1989 and 1990, the results were analyzed to see if the onset of vegetation senescence could be detected due to seasonal change, even though this dataset is not in time order with the ones above. 60,490 datapoints were located within a 5-dimensional simplex, and the six endmembers found were interpreted to match those found in the 7 August 1990 data. This is not to say that the spatial distribution or the spectral signature of these endmembers did not change, however. The chlorophyll absorption is reduced in all of the growing vegetation species except those found in the high water table areas. However, even these species showed changes in their SWIR regions beyond 1.45 μm . These effects are caused by the onset of senescence in the vegetation due to seasonal change. The sand/soil endmember shows greater reflectance in the 1.0 μm region and decreased reflectance in the region beyond 1.5 μm when compared with the August results. The standing dead shortgrass endmember has much greater reflectance across the spectrum. Spatially this endmember does not appear to be as distinct as in either of the other two scenes because the vegetation that is on the dunes has evolved into this endmember. This is the same reason that the sand/soil endmember appears spatially similar to the results seen in March 1990 (before a lot of vegetation began to grow on the dunes). The tallgrass species are also not showing up spatially as well, possibly due to senescence. The shortgrass species appear to be more mixed in with the sage in this image, possibly due to the longer time that they had to grow (almost two months additional time since the August scene). Sage areas have also been taken over by the standing shortgrass dead, another indicator that this hypothesis may be correct.

4.4 6 June 1993 Results

178 original bands were used to derive a 6-dimensional simplex with seven endmembers, enclosing 54,405 datapoints. Because the data had higher signal-to-noise than any other dataset analyzed here, and this was the time of peak growth for the vegetation (thus creating more ephemeral endmembers), the analysis indicated a very high inherent dimensionality in the data. At least fifteen endmembers were indicated, but limitations in the current unmixing routine result in inefficiency above 6-dimensions. Because of this, incomplete unmixing resulted. At least four of the endmembers showed signs of being vegetation, two appeared to be water or shadow related, while the final one was a new sand/soil endmember never before seen. When the data were viewed after the first part of the analysis was complete, many different areas of the dunes, corresponding to potentially different vegetation regimes, were observed. The scene also had more cloud cover than any of the others analyzed, and complete removal of the atmospheric water features may not have occurred. By using the fractional abundance endmember images, the seven endmembers were tentatively named: water/shadow/water vapor, wet sand/soil, very green vegetation (tallgrass?), growing sage, moderately green vegetation (sunflower?), growing shortgrass species, and new sand/soil. More work needs to be done to understand the complexity of this scene and to permit higher dimensional analyses.

4.5 Conclusions

The results derived from the scenes above show the power of this approach. Seasonal change can be detected well, both spatially and, more importantly, spectrally. As the winter landscape progresses to that of summer, the number of landscape endmembers also reflects that change. Then as the season turns to fall, the vegetation senescences, the endmembers once again become more similar, and the landscape composition becomes simpler. Temporal changes are also detected well by this method.

The benefit of this approach is that the entire process is independent of user-provided data. The conversion to reflectance and removal of atmospheric effects can be done without the input of field measurements taken concurrently with the overflight of the AVIRIS sensor. The automated spectral unmixing scheme described above also stands alone with no need for observer data. This is a great plus since in traditional spectral unmixing, the set of endmembers is determined by the user, and therefore the success of the results depends on the accuracy of this dataset to the actual physical system being observed. With the scheme outlined above, there is at least a first approach to understanding imaging spectrometry data without necessarily having to visit the field site first.

5. ACKNOWLEDGMENTS

This work was supported by NASA grants NAGW-2070 and NAS5-30552.

6. REFERENCES

- Boardman, J.W., 1993, "Automating Spectral Unmixing of AVIRIS Data using Convex Geometry Concepts," in *Summaries of the Fourth Annual JPL Airborne Geoscience Workshop*, vol. 1. AVIRIS Workshop (this volume).
- Forman, S.L., A.F.H. Goetz, and R.H. Yuhas, 1992, "Large-scale stabilized dunes on the High Plains of Colorado: Understanding the landscape response to Holocene climates with the aid of images from space," *Geology*, vol. 20, pp. 145-148.
- Gao, B.-C., K.B. Heidebrecht, and A.F.H. Goetz, 1993, "Derivation of scaled surface reflectances from AVIRIS data," *Remote Sensing of Environment*, vol. 44, pp. 165-178.
- Hansen, J., I. Fung, A. Lacis, D.S. Rind, R. Ruedy, and G. Russell, 1988, "Global climate changes as forecast by Goddard Institute for Space Studies three-dimensional model," *Journal of Geophysical Research*, vol. 93, pp. 9341-9364.

SLIDE CAPTIONS

<u>Slide No.</u>	<u>Caption</u>	<u>Senior Author</u>
1	3-component RGB image of the study area; AVIRIS data collected in August 1990. Blue = AVIRIS band 12; green = band 48; red = band 213.	Beratan
2	Jasper Ridge example: The five endmember spectra and their corresponding abundance images.	Boardman
3	Color composites of the simulated and actual TM scenes.	Kalman
4	Selected linear spectral unmixing results for both the empirical line and atmospheric-model calibrated data.	Kruse
5	Classification map, produced by a self-organizing ANN.	Merényi
6	A two-band image showing the spatial relationship between the derived lignin and water fractions across the site.	Wessman
7	(A) shows the composite rendered on the digital elevation model with tags (B–E) for the location of the enlarged subareas of the horizontal (non-rendered) composite. (B)–(E) show zoom-up (\approx factor 5) parts with different aspect and slope angles.	Meyer
8	Fractional abundance images and associated spectra of semi-arid landscape endmembers, August 7, 1990.	Yuhas
9	AVIRIS image cube of Rogers Dry Lake, CA, calibration site.	Green
10	AVIRIS image cube of Moffett Field, CA, data set showing San Francisco Bay and Moffett Field runways.	Green
11	The classified June 2nd image next to a vegetation map (mapped in the field) for comparison.	Sabol, Jr.
12	AIRSAR views of Aeolian terrain.	Blumberg

